Mesure des muons de décroissance des saveurs lourdes ouvertes et des particules associées aux jets dans les collisions p-Pb et Pb-Pb avec ALICE au LHC

Siyu Tang

CENTRAL CHINA NORMAL UNIVERSITY
UNIVERSITÉ CLERMONT AUVERGNE

P H D T H E S I S

présentée pour obtenir le grade de

DOCTOR OF UNIVERSITY

Spécialité : PARTICULES, INTERACTIONS, UNIVERS

Par

Siyu TANG

Measurements of muons from open heavy-flavour hadron decays and jet particles in p–Pb and Pb–Pb collisions with ALICE at the LHC

defended on May 27th, 2022

Jury :

Rapporteurs:	C. CHESHKOV	-	IP2I, Lyon
	P. ZHUANG	-	THU, Beijing
Examinateurs:	L. CHEN	-	SJTU, Shanghai
	Y. MA	-	FDU, Shanghai
Membre invité:	A. OHLSON	-	University of Lund, Lund
	Z. YIN	-	CCNU, Wuhan
Directeurs de thèse:	N. BASTID	-	LPC, Clermont-Ferrand
	P. CROCHET	-	LPC, Clermont-Ferrand
	X. ZHANG	-	CCNU, Wuhan
	D. ZHOU	-	CCNU, Wuhan

分类号_____ 密级_____

U D C _____ 编号_____

华中师范大学

博 士 学 位 论 文

LHC/ALICE 实验中重夸克衰变缪子及喷注粒子产生研究

学 位 申 请 人 姓 名: 汤 思 宇

申请学位学生类别: 全日制博士

申请学位学科专业: 粒子物理与原子核物理

指 导 教 师 姓 名: 周代翠 教授

张晓明 副教授

Philippe Crochet 研究员

Nicole Bastid 教授

博士学位论文

LHC/ALICE 实验中重夸克衰变缪子及喷注粒子产生研究

论文作者： 汤思宇

指导教师： 周代翠　　教授

张晓明　　副教授

菲利普•胡克　资深研究员

妮可•巴斯蒂　教授

学科专业： 粒子物理与原子核物理

研究方向： 高能重离子碰撞实验

华中师范大学物理科学与技术学院

2022 年 5 月

博士学位论文
DOCTORAL DISSERTATION

Dissertation

Measurements of muons from open heavy-flavour hadron decays and jet particles in p–Pb and Pb–Pb collisions with ALICE at the LHC

By

Siyu Tang

Supervisors: Prof. Daicui Zhou

Prof. Xiaoming Zhang

Dr. Philippe Crochet

Prof. Nicole Bastid

Specialty: Particle Physics and Nuclear Physics

Research Area: Heavy-Ion Collision Experiment

College of Physical Science and Technology

Central China Normal University

05, 2022

华中师范大学学位论文原创性声明和使用授权说明

原创性声明

本人郑重声明：所呈交的学位论文，是本人在导师指导下，独立进行研究工作所取得的研究成果。除文中已经标明引用的内容外，本论文不包含任何其他个人或集体已经发表或撰写过的研究成果。对本文的研究做出贡献的个人和集体，均已在文中以明确方式标明。本声明的法律结果由本人承担。

作者签名：　　日期：　　年　　月　　日

学位论文版权使用授权书

学位论文作者完全了解华中师范大学有关保留、使用学位论文的规定，即：研究生在校攻读学位期间论文工作的知识产权单位属华中师范大学。学校有权保留并向国家有关部门或机构送交论文的复印件和电子版，允许学位论文被查阅和借阅；学校可以公布学位论文的全部或部分内容，可以允许采用影印、缩印或其它复制手段保存、汇编学位论文。（保密的学位论文在解密后遵守此规定）

保密论文注释：本学位论文属于保密，在 ____年解密后适用本授权书。

非保密论文注释：本学位论文不属于保密范围，适用本授权书。

作者签名：　　导师签名：

日期：　　年　　月　　日　　日期：　　年　　月　　日

本人已经认真阅读“CALIS 高校学位论文全文数据库发布章程”，同意将本人的学位论文提交“CALIS 高校学位论文全文数据库”中全文发布，并可按“章程”中的规定享受相关权益。同意论文提交后滞后：□半年；□一年；□二年发布。

作者签名：　　导师签名：

日期：　　年　　月　　日　　日期：　　年　　月　　日

摘 要

组成这个物质世界的基本粒子是什么？这些基本粒子之间的相互作用又有怎么样的特性？这是人类在几千年来探索宇宙奥秘的过程中一直孜孜不倦地研究的两个基本问题。早在公元前 6 世纪 ~ 5 世纪，古希腊哲学家流西普斯、德谟克里特斯和伊比鸠鲁等人建立了 “原子论”，就提出物质是由基本粒子组成的猜测。但直到 1897 年，英国物理学家约瑟夫 • 汤姆孙通过对阴极射线的磁偏转与质荷比的研究，人类才第一次发现基本粒子——电子。在之后的近百年时间里，随着质子，中子等大量新粒子被发现，人们对微观世界中物质的结构与性质的认识逐步深入，现代粒子物理学被建立。在 20 世纪 70 年代，基于量子力学和狭义相对论的发展，粒子物理学建立了一个能够描述除引力以外的三种基本相互作用及所有基本粒子（夸克、轻子、规范玻色子、希格斯玻色子）的规范理论——标准模型。在 2012 年，欧洲核子研究组织（CERN）宣布在大型强子对撞机（LHC）上发现了希格斯粒子，这证实了标准模型对最后一种被发现的基本粒子预言。因此，标准模型被认为是迄今为止描述基本粒子以及其相互作用的最成功的理论。

根据标准模型的描述，夸克和轻子组成了宇宙中所有的可见物质，它们也被称为费米子。而费米子之间的相互作用则通过玻色子来传播，比如胶子，光子，W/Z 玻色子以及希格斯玻色子。其中，胶子用来传递夸克之间的强相互作用，并将夸克连接在一起形成强子。作为标准模型的一个基本组成部分，量子色动力学（QCD）被提出来描述强相互作用的各向性质，并已经得到了大量实验证据的证实。QCD 有两种特有属性，禁闭与渐进自由。禁闭意味着自由的夸克与胶子无法在普通实验条件下被观测到。因为当强子中的两个夸克的距离变大时，在胶子场中的能量将足够产生一个夸克对，从而将夸克一直以强子的形式束缚在一起。渐进自由则发现在能量尺度变得任意大的时候，或等效地，距离尺度变得任意小的时候，夸克与夸克之间的相互作用非常微弱。根据格点量子色动力学（lQCD）的计算，在极端高温或者高重子数密度的条件下，普通强子物质将发生相变。强子中的夸克和胶子将退禁闭成为自由的状态，并一起形成一种新的物质形态——夸克胶子等离子体（QGP）。在自然界中，QGP 目前被认为只存在于正在塌陷的中子星内部（高重子数密度）或者宇宙大爆炸 20 微秒之后的宇宙初期（极端高温）。基于上述事实，对于 QGP 的性质的研究，不仅可以研究多粒子体系下强相

互作用的产生机制，还有助于揭示宇宙早期的演化规律。因此，如何在现有的实验条件下，产生并研究 QGP 的特性也成为了科学家一直研究的问题。

事实证明，高能重离子对撞是在实验室条件下产生 QGP 最便捷有效的方法。在加速器中，两个被剥离带电的原子核被加速到接近光速，随即相互进行对撞。巨大的动能在短时间内转换成热能并沉积在一个极小的对撞区域内，从而形成了一个极端高温的环境并达到退禁闭条件，自由的夸克与胶子产生并形成 QGP 物质。之后，随着系统的膨胀与内部温度的降低，这些自由的夸克被强子化成末态粒子，并被粒子探测器所观测到。自上个世纪七十年代以来，世界各国科学家建立了一系列的粒子对撞机来进行重离子对撞实验，包括位于欧洲核子研究中心（CERN）的超级质子同步加速器（SPS）和大型强子对撞机（LHC）、美国布鲁克海文国家实验室（BNL）的交变梯度加速器（AGS）和极端相对论对撞机（RHIC）。其中，LHC 作为世界上最大的粒子对撞机于 2009 年正式运行，服务于在其上工作的四个大型高能物理实验（ALICE，ATLAS，CMS，LHCb）。大型重离子碰撞实验（ALICE）是 LHC 上唯一专门致力于研究高能重离子碰撞中的夸克物质信号及其性质的实验。自 2009 年起，ALICE 通过研究质心能量 2.76 TeV，5.02 TeV 铅核-铅核碰撞数据，5.02 TeV，8.16 TeV 质子-铅核碰撞数据，2.76 TeV ，5.02 TeV，13 TeV 质子-质子碰撞数据以及 5.44 TeV 氙核-氙核碰撞数据，观测到了大量与 QGP 形成相关的实验现象，包括高横动量粒子产额的压低以及喷注淬火，奇异粒子产额的增强，各向异性流对组分夸克的标度，光子产额的提高等。这些实验观测结果与相应理论描述一致，都证明了 QGP 物质的存在。同时通过与理论计算的定量比较，这些观测量也能反映 QGP 物质的各项物理性质，因此也被称为研究 QGP 的探针。

在对众多反映 QGP 性质的末态探针的研究当中，产生于部分子（夸克和胶子）硬散射过程的硬探针，如高横动量强子，喷注和重夸克（粲夸克，顶夸克），一直是高能核物理界的一个研究焦点。硬探针的主要特点是其产生过程中具有较大的动量转移（通常用四动量转移的平方 Q^2 表示），或者探针本身具有较大的横动量或者质量。由于硬散射通常发生在碰撞初期，因此这些硬探针早于 QGP 的形成，并随后经历整个 QGP 物质的演化过程，记录了各个阶段 QGP 的性质。在这些硬探针当中，重夸克由于其独特的性质而在对 QGP 的研究当中有着非常重要的地位。在初态硬散射发生之后，重夸克在穿越 QGP 介质时，与介质中的组分发生相互作用并进行动量交换，从而损失能量，进而影响末态观测到的重味

强子以及其衰变产物的分布。通过测量重味强子的核修正因子 R_{AA}，即重味强子在重离子碰撞中约化为一对核子碰撞的产额与在质子-质子碰撞中的产额之比，我们可以定量地研究重夸克在介质中的能量损失。根据理论上的预言，相比于轻夸克，重夸克的胶子辐射会在与其夸克质量相关的锥角内压低，从而导致重夸克辐射能量损失比轻夸克小，这一效应被称为死角效应。因此，重味强子的 R_{AA} 将大于轻味强子。在实验上，对向前快度区间内重味强子及其衰变产物的测量还有助于把对重夸克的研究拓展到更小的 Bjorken-x 值区间。另一方面，除了能量损失之外，重夸克在与 QGP 介质发生相互作用时，会产生热化效应。这使得重夸克获取集体性并导致其末态产物的各向异性流（如椭圆流）的出现。在低横动量区间内，对重夸克末态产物的各向异性流的测量主要是研究重夸克的热化自由度，而在高横动量区间内，这种测量主要反映的是重夸克能量损失对穿越路径长度的依赖性。因此，结合对重夸克核修正因子以及各向异性流的测量，我们可以对研究重夸克与 QGP 相互作用机制以及其背后所蕴含的 QGP 本身的物理性质提供一个完备的实验限制。

相较于重离子碰撞，在小系统碰撞中（如质子-质子碰撞，质子-铅核碰撞），我们一般认为其沉积的能量密度不足以产生 QGP。事实上，在质子-铅核碰撞中，所观测到的包括重夸克，高横动量粒子，喷注在内的各类硬探针的核修正因子也的确没有表现出压底效应，这也表明硬部分子在穿越整个系统时并没有产生显著的能量损失。然而，近些年来，随着在小系统碰撞中对各向异性流的提取方法的不断改进，显著非零的高横动量带电粒子椭圆流被观测到，这似乎又预示着部分子能量损失的存在。因此，对小系统碰撞中高横动量粒子集体流的产生机制的解释，与观测的核修正因子产生了矛盾。这需要我们进一步地，尤其是在一个更大的横动量区间内，对小系统碰撞中各类硬探针的各向异性流进行更加精确的测量。这将为寻找小系统碰撞中各向异性流的起源提供更多的实验观测量。

本文的工作围绕 ALICE 实验对硬探针（重夸克，喷注）的测量而展开，包含了在铅核-铅核碰撞中重味衰变缪子的核修正因子的测量，和在质子-铅核碰撞中测量缪子与喷注粒子椭圆流的测量三个分析工作。在第一章中，本文叙述了标准模型，量子色动力学，QGP 相变等理论背景，介绍了高能重离子碰撞实验以及各类探寻 QGP 性质的探针，如喷注淬火，重夸克和各向异性流等。第二章介绍了在高能物理实验上各类测量各向异性流的方法，以及这些方法的优缺点与适用范围。第三章则介绍了 ALICE 实验探测器的结构、原理和性能，以及未来的探测器升级

计划。此外还介绍了在 ALICE 实验上数据的采集和重建的过程。第四、五、六章则分别聚焦于三项独立的数据分析工作。第四章讨论了在质心系能量为 $\sqrt{s}$ =2.76 TeV 和 $\sqrt{s}$ =5.02 TeV 的铅核-铅核碰撞中，重夸克衰变缪子的产额以及其核修正因子的测量。结果显示在两种质心系能量下，重夸克衰变缪子的产额均被明显压低。相较于 ALICE 在 Run 1 中发表的结果，该分析首次将测量范围推广到高横动量区间，这为精确标定底夸克在热密介质中能量损失提供了实验限制。第五章介绍了在质心系能量为 $\sqrt{s}$ =8.16 TeV 质子-铅核碰撞中缪子的椭圆流的测量。两粒子关联和两粒子矩的方法首次被应用到对重味粒子的各向异性流的测量中，并给出相互吻合的结果。此分析还首次对 ALICE 质子-铅核碰撞中的长程和短程非流关联进行了完整的研究。结果显示，在小系统碰撞中，重味粒子有着明显的各向异性，这为我们理解这种类流长程关联的起源提供了新的视角。第六章介绍了在铅核-铅核和质子-铅核碰撞中，对喷注粒子的各向异性的测量。该分析采用了一种全新的三粒子关联的方法，首次在 ALICE 实验上测量了喷注伴随粒子的各向异性流。结果显示，在小系统碰撞中即使喷注淬火效应不存在，喷注粒子依然表现出与重离子碰撞中类似的集体性。这为理解硬部分子如何在小系统碰撞中获取各向异性的现象提供了重要的实验限制。第七章则对本文所有的工作进行了一个系统性的总结。

关键词：夸克胶子等离子体（QGP）；大型强子对撞机（LHC）；大型重离子碰撞实验（ALICE）；核修正因子（R_{AA}）；各向异性流；重味衰变缪子；喷注粒子

Abstract

Within the Standard Model, the strong interaction between quarks is described by the theory of quantum chromodynamics (QCD). Due to the presence of color confinement, the isolated quarks and gluons cannot be seen in normal conditions. On the other hand, one of the features of QCD, the asymptotic freedom, tells us that the free quarks and gluons can be produced in an environment of extreme high temperatures and/or high densities, which results in a new phase of matter, the quark–gluon plasma (QGP). Nowadays, ultra-relativistic heavy-ion collisions are regarded as an effective way to produce the QGP and study its properties.

ALICE (A Large Ion Collider Experiment) is one of the four experiments operating at the largest particle collider in the world, the Large Hadron Collider (LHC). It is the only LHC experiment which is dedicated to the study of heavy-ion physics. In past decades, many important probes to study the properties of the QGP were measured by the ALICE collaboration. Among them, the hard probes, such as heavy flavours, high transverse momentum (p_{T}) particles, jets, are of particular interest since they are believed to be produced in hard scattering processes during the early stage of the collision and subsequently undergo the whole evolution of the hot and dense medium. The suppression observed in the production of open heavy flavours in heavy-ion collisions relative to that in binary-scaled proton-proton collisions can be characterized in terms of the nuclear modification factor (R_{AA}), which is a crucial observable to understand the mechanism of in-medium energy loss of heavy quarks. The measurement of the anisotropic flow of heavy flavours provides additional insights on the possible thermalization of heavy quarks in the medium at low p_{T} and the path-length dependent in-medium energy loss at high p_{T}. On the other hand, in small collision systems, the QGP is thought not to exist due the absence of suppression observed in the measurement of the nuclear modification factor. However, recent measurements of anisotropic flow indicate a significant collective behaviour in small collision systems, especially for high-p_{T} particles. It challenges our understanding about the small collision systems, which need to be further studied via more specific and precise measurements.

This thesis presents three measurements with hard probes at both midrapidity ($|y|$ <0.8) and forward rapidity (2.5< y <4) in p–Pb collisions at $\sqrt{s_{\mathrm{NN}}}$ = 5.02 and 8.16 TeV, and Pb–Pb collisions at $\sqrt{s_{\mathrm{NN}}}$ = 2.76 and 5.02 TeV, with the ALICE detector at the LHC. The first chapter of the thesis is dedicated to an introduction about the theoretical background of quantum chromodynamics and heavy-ion collisions, and the latest experimental findings in both large and small collision systems. Chapter 2 presents the current anisotropic flow analysis methods, including the event-plane, scalar-product, cumulants and pair-wise azimuthal correlation methods. Chapter 3 gives an overview of the ALICE experiment with a particular emphasis on the description of the detectors relevant for the analyses discussed in this thesis. Data processing and reconstruction based on the online and offline systems are also introduced. Chapter 4 presents the measurement of the R_{AA} of muons from heavy-flavour hadron decays in Pb–Pb collisions at $\sqrt{s_{\mathrm{NN}}}$ = 2.76 and 5.02 TeV. The strategy to obtain the muon distribution normalized to minimum bias events

and the subsequent subtraction of background muons is introduced. The results concerning the measurement of the R_{AA} as a function of p_{T} in various centrality classes are discussed and compared to the model calculations. Chapter 5 addresses the measurement of the azimuthal anisotropy of inclusive muons in p–Pb collisions at $\sqrt{s_{\mathrm{NN}}} = 8.16$ TeV. Several non-flow subtraction strategies are also discussed. Chapter 6 shows the measurement of the azimuthal anisotropy of particles associated with jets down to low p_{T} in p–Pb and Pb–Pb collisions at $\sqrt{s_{\mathrm{NN}}} = 5.02$ TeV. A novel three-particle correlation method is developed to separate the contributions from hard and soft components in flow measurements for the first time. A summary of the three analysis is given in Chapter 7. In addition, a brief introduction about the ALICE rivetization service work is given in appendix.

Keywords: quark-gluon plasma (QGP); A Large Ion Collider Experiment (ALICE); Large Hadron Collider (LHC); Heavy-ion collisions; Small collision systems; Nuclear modification factor; Anisotropic flow; Open heavy flavours; Jet particles.

Contents

List of Figures

List of Tables

CHAPTER 1

Introduction

The purpose of physics is to study the world around us, and two of the most important aspects are the understanding of the elementary constituents of matter and the interactions between them. From Thomson's discovery of the electron in 1897 [1] to the observation of the Higgs boson at CERN (European Organization for Nuclear Research) in 2012 [2, 3], people made giant strides in exploring the micro-world for more than a century. Nowadays, all known elementary particles and the fundamental forces between them (except for gravity) can be well classified and described by the Standard Model (SM). As an important component of the Standard Model, the quantum chromodynamics (QCD) predicts a transition to a new phase of colour-deconfined matter, the quark-gluon plasma (QGP), which can be created experimentally in high-energy heavy-ion collisions. In this chapter, we start with the introduction to the theory of Standard Model and quantum chromodynamics, described in Sec. 1.1. Then an introduction on the heavy-ion collisions is given in Sec. 1.2, which includes the description of the collision geometry and evolutionary processes. After that, the probes to study the properties of QGP and related experimental findings are introduced in Sec. 1.3. Finally, recent measurements in small collision systems are presented in Sec. 1.4.

1.1 Standard Model

The Standard Model was born out of the two great revolutions of physics in the 20th century: the establishment of quantum mechanics [4–6] and special relativity [7]. The former one provides a description of the physical properties of nature at the scale of atoms and subatomic particles and the latter describes the propagation of light and matter up to high speeds. The development of the Quantum Field Theory (QFT) brings a full description which is consistent with both quantum mechanics and special relativity, where all particles are regarded as excited states of their underlying quantum fields, and are more fundamental than the particles. With many theoretical breakthroughs in QFT, the Standard Model was built step by step. Up to now, all fundamental particles and interactions (except for gravity), and related many predictions, all get remarkable experimental confirmation. Especially after the Higgs boson discovered at the Large Hadron Collider (LHC) in 2012, the existence of all constituents of the Standard Model is fully confirmed.

As shown in Fig. 1.1, 17 elementary particles[1] are described by the Standard Model, which can be divided into several groups: quarks, leptons and bosons. The

[1] Particles and antiparticles are considered together here.

quarks and leptons are also called fermions, they follow Fermi-Dirac statistics and generally have half odd integer spin. The bosons are subdivided into gauge bosons and scalar bosons, both of which obey Bose-Einstein statistics.

Overall, there are six quarks and six leptons. In the case of quarks, we distinguish six flavours, each of them corresponds to a quark type: up (u), down (d), strange (s), charm (c), bottom (b), and top (t). Besides, there are six anti-quarks corresponding to each quark with an opposite electric charge but the same mass: anti-up ($\bar{u}$), anti-down ($\bar{d}$), anti-strange ($\bar{s}$), anti-charm ($\bar{c}$), anti-bottom ($\bar{b}$), anti-top ($\bar{t}$). Their mass increases from left to right. These quarks are bound together to form the hadrons according to the strong interactions. Therefore another property of quarks, the "colour charge", is introduced in quantum chromodynamics to explain how quarks could exist in some observed hadrons, which will be explained in the next section. On the other hand, there are six lepton flavours, consisting of the electron, the muon and the tau and accompanying three types of neutrinos (electron neutrino, muon neutrino and tau neutrino). Different from quarks, leptons have half-integer spin and don't undergo strong interactions, therefore they have no colour charge.

The Standard Model predicts the existence of five types of bosons: gluon (g), photon (γ), Z, W and Higgs (H), all of which are supposed to carry the fundamental interactions between the fermions. There are four fundamental interactions (also called fundamental forces) known to exist in the nature: the gravitational and electromagnetic interactions, which produce significant long-range forces whose effects can be seen directly in daily life, and the strong and weak interactions, which produce forces at subatomic distances and govern nuclear interactions. The quantities coupled to the four fundamental forces and the effective ranges are summarized in Tab. 1.1.

	Strong	Weak	Electromagnetic	Gravitation
Exchange particle	gluon	$W^{\pm}, Z^0$	photon	graviton (hypothetical)
Couples to	colour charge	weak isospin	charge	mass
Relative strength	100	10^{-11}	1	10^{-24}
Range	1 fm	0.01 fm	∞	∞

Table 1.1: The four fundamental forces are listed with their exchange particle, coupling strength relative to the electromagnetic interaction, and effective range. Values are taken from [8].

As mentioned before, except for the gravitational interaction, the other three interactions are well unified in the Standard Model. The gluons act as the exchange particles to carry the strong force between the quarks, which is analogous to the exchange of photons in the electromagnetic force between two charged particles [9]. Differently from photons which act only as a medium in electromagnetic interactions, the gluons participate in the strong interactions in addition mediating it, therefore the gluons also carry the colour charge. The $W^{\pm}$ and Z bosons are exchanged between fermions for weak interactions, which are responsible for the radioactive

decay of atoms since the weak interaction allows quarks and leptons to swap their flavour to another. Last but not least, there is the Higgs boson which is responsible for giving to other massive particles their (inertia) mass according to the Yukawa coupling with the Higgs scalar field [10].

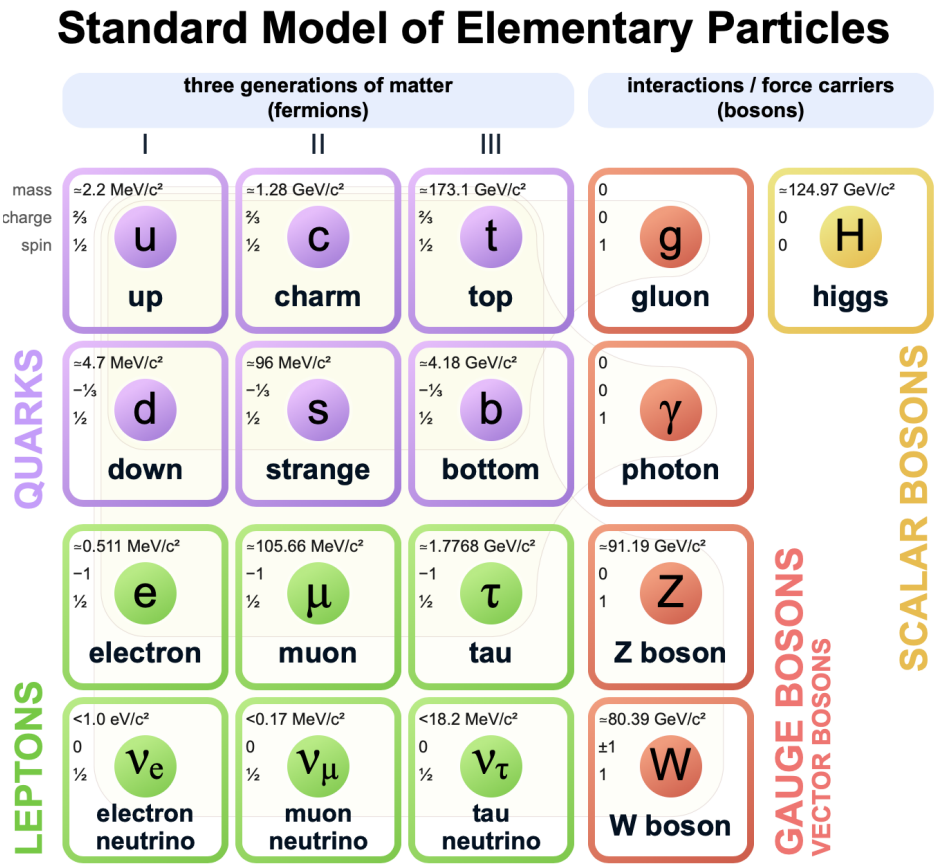

Figure 1.1: Elementary particles in the Standard Model. Figure taken from [11].

1.1.1 Quantum Chromodynamics

Quantum chromodynamics is a non-Abelian quantum gauge theory to describe the strong interaction between quarks and gluons, based on the invariance under local $SU(3)_c$ group transformations. As the concept of electric charge in Quantum Electrodynamics (QED), the conserved charge of QCD is called colour charge, which assumed three values for quarks, commonly referred as red, green, and blue. Anti-quarks have corresponding anti-colour. Gluons also have colour charges and there are eight gluons in total, which are the so-called "color octet".

The Lagrangian of QCD is expressed as [12]:

$$L_{QCD} = \sum_q (\bar{\psi}_{qi} i\gamma^\mu [\delta_{ij}\partial_\mu + ig(G^\alpha_\mu t_\alpha)_{ij}]\psi_{qj} - m_q \bar{\psi}_{qi}\psi_{qi}) - \frac{1}{4} G^\alpha_{\mu\nu} G^{\mu\nu}_\alpha. \quad (1.1)$$

In Eq. 1.1, ψ_{qi} is the Dirac spinor of the quark field of a quark with flavour f, colour charge i, and mass m_q; t_α is the 3×3 Gell-Mann matrices; γ^μ are Dirac $\gamma-$matrices which expresses the vector nature of the strong interaction with μ being a Lorentz vector index; g is the strong coupling constant, which is also written as $\alpha_s = g^2/4\pi$ ($\hbar = c = 1$). The second term of Eq. 1.1 describes the kinematics and the dynamics of the gluons and, if we make explicit the gluon field tensor:

$$G^{\mu\nu}_\alpha = \partial^\mu G^\nu_\alpha - \partial^\nu G^\mu_\alpha - g f^{\alpha\beta\gamma} G^\mu_\beta G^\nu_\gamma, \tag{1.2}$$

where $f^{\alpha\beta\gamma}$ are the structure constants of SU(3). We find that the non-Abelian term $g f^{\alpha\beta\gamma} G^\mu_\beta G^\nu_\gamma$ produces self-interactions among gluons. The gluon self-coupling is related to two peculiar properties of the QCD theory: confinement and asymptotic freedom.

1.1.2 Confinement and Asymptotic Freedom

Neither quarks nor gluons are observed as free particles. In normal conditions, they always clump together to form hadrons, which have a color charge of zero. The phenomenon is called color confinement, often simply named confinement. However, such phenomenon is not present in QED since when two charged particles are separated somehow, the electric field between them will decreases rapidly, and we can easily find isolated particles. In QCD, once the gluon field between a pair of color charges forms a narrow flux tube (or string), the strong force between the particles is constant regardless of their separation. Then, when two color charges are separated, at some point, it becomes energetically favorable to create a new quark-antiquark pair instead of further extending the tube. Therefore, when quarks are produced experimentally, many color-neutral particles (e.g. mesons and baryons) instead of individual quarks are observed. This process is also called hadronization. Figure 1.2 is an illustration of the process where two new mesons are created when the constituents in a meson are pull apart. In theory, the potential between

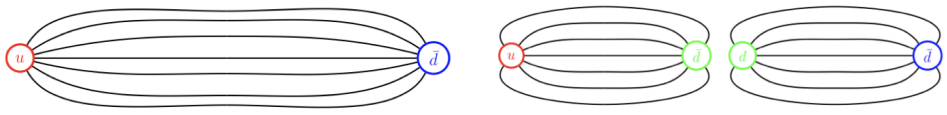

(a) (b)

Figure 1.2: (a) Quark and anti-quark are bounded in a meson. Gluons exchange is represented by the flux tube containing the field lines. (b) Separating the quarks, the energy of the gluon field increases until the flux tube breaks up in a new quark-antiquark pair. Figure taken from [13].

a quark-antiquark pair can be expressed as a function of the distance between the two quarks:

$$V_{\mathrm{QCD}}(r) = -\frac{4}{3}\frac{\alpha_s(r)}{r} + \sigma \cdot r, \tag{1.3}$$

where V_{QCD} is the QCD potential between the quark and antiquark, r is the distance between them, α_s is the QCD gauge coupling parameter and σ is the QCD string

tension. The first term is the Coulomb-like term which has dependence on $1/r$, and the second term rises linearly with the quark-antiquark distance.

For a given energy scale, the actual value of the coupling parameter α_s in Eq. 1.3 cannot be predicted by QCD, but its energy dependence can be determined using perturbative calculations of quantum chromodynamics (pQCD). The running coupling strength α_s can be written as a function of the four-momentum transfer of gluons, Q^2, as follows:

$$\alpha_s = \frac{4\pi}{(11 - \frac{2}{3}n_f)\ln(\frac{Q^2}{\Lambda^2_{\mathrm{QCD}}})}, \tag{1.4}$$

where n_f is the number of active flavours and Λ_{QCD} is the QCD scale parameter, which corresponds to the energy scale below which perturbative coupling becomes divergent. The value of Λ_{QCD} is determined experimentally, and is of order of ~ 200 MeV [14]. Figure 1.3 shows the coupling parameter α_s as a function of the four-momentum transfer, Q^2, measured at different scales using various experimental methods. One can observe that the strong coupling becomes smaller in higher energy reactions. Combining the Eq. 1.3 and Eq. 1.4, we can find that the second term of

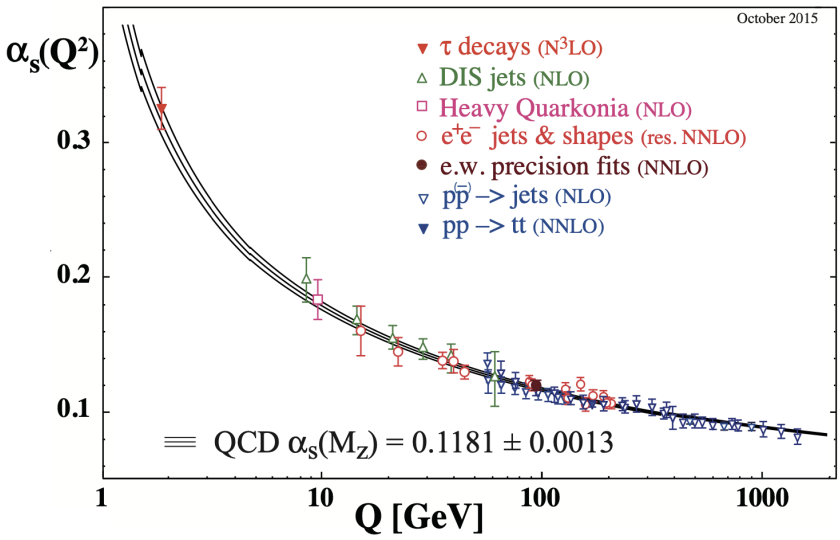

Figure 1.3: The QCD coupling strength α_s as a function of the four-momentum transfer Q^2. The brackets indicate the order to which perturbation theory is used. Figure taken from [14].

Eq. 1.3 (i.e. the string term) dominates with low temperatures and large separation distances between quark and anti-quark, which causes the QCD potential to increase linearly as a function of r. It is impossible to see the free quarks and gluons escaping this potential, which is known as the colour confinement phenomenon, as already discussed. However, as the distance between quark and anti-quark is very small (i.e. $r \to 0$) and the energy of reactions is very high, the string term vanishes and the coupling of the Coulomb term is very weak. In this case, quarks and gluons may behave like free particles. This effect is known as asymptotic freedom [15]. In the

regime of asymptotic freedom, the quark-antiquark potential is screened by the free color charges, then the QCD potential can be parametrized as:

$$V_{\mathrm{QCD}}(r) = (-\frac{4}{3}\frac{\alpha_s}{r} + \sigma \cdot r)e^{-\frac{r}{r_{\mathrm{D}}}}, \tag{1.5}$$

where r_{D} is the Debye radius, which sets the maximum distance at which two quarks can be considered as bound, and it is reduced below the typical hadron size ($\sim$ 1 fm) due to the presence of free colour charges. Thus, the deconfinement occurs and the new state of matter appears, which is known as the quark-gluon plasma (QGP).

1.1.3 QCD Phase Diagram

As mentioned in the previous section, the pQCD framework can be used for hard processes, i.e. those processes with large momentum transfer Q^2. It is done by setting a cut-off of infinite series expanded in powers of the QCD coupling constant α_s. However, for soft processes which have low momentum transfer, the pQCD framework is no longer valid. In this case, the Green's functions of the QCD Lagrangian can still be evaluated on a discrete space-time grid. This method is the so-called lattice QCD (lQCD) [16]. The lQCD approach allows us to study the QCD phase structure at finite temperature and density, meanwhile it can also help us to understand the whole QCD phase diagram based on thermodynamical considerations.

Figure 1.4 shows the phase diagram for QCD matter, as temperature (T) versus baryon chemical potential (μ_{B}), where μ_{B} represents the abundance of matter over anti-matter in the system, so it can be simply considered as the net density of the baryons. In the QCD phase diagram, the region named "hadron gas" in the lower-left corner shows ordinary hadronic matter under confinement conditions. The point at ($\mu_{\mathrm{B}} = 950$ MeV, $T \simeq 0$) corresponds to nuclear matter under natural conditions in the universe. At high baryon chemical potential and low temperatures, a colour-superconductor state is predicted to occur. In this region, the separation between hadrons is smaller than their radius, which implies that quarks can not be meaningfully attributed to any given hadron. The other possible extreme is a high temperature and low baryon chemical potential. In the limit of $\mu_{\mathrm{B}} = 0$, the transition is expected to occur at $T \approx$ 145–165 MeV, corresponding to an energy density of about $\varepsilon \approx$ 0.18–0.5 GeV/fm^3. In this case, the crossover between the hadronic and deconfined state (QGP) is predicted by lQCD calculations [17]. In addition, it is worth to mention that the phase transition is of the first order if it occurs with a discontinuous pattern in the first derivative of the free energy. In a first order transition, entropy varies with discontinuity and latent heat is present. If the phase transition occurs with discontinuous derivatives after the first order, it is of the second order.

Based on the QCD phase diagram, different phase transition paths can be followed to create the QGP, depending on the temperature and the baryon chemical potential. In the early universe (about 10 μs after the Big Bang), the temperature is extremely high and $\mu_{\mathrm{B}} \to 0$, all quarks and gluons are deconfined and form the QGP, which is filled in space like a soup. A few microseconds later, the soup

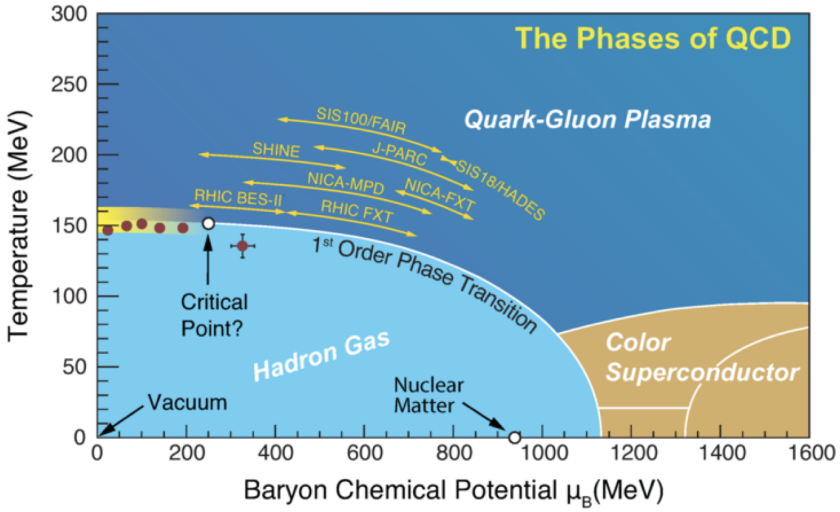

Figure 1.4: Schematic phase diagram of QCD matter. Figure taken from [18].

started to cool down, and when its temperature decreased to the critical value, the phase transition described above happened. The deconfined particles combined into hadrons and consequently into matter. Figure 1.5 shows the evolution of the universe. Fortunately, the QGP can be recreated nowadays in laboratory, using the heavy-ion collisions performed in large hadron colliders. Heavy-ion collisions with the highest energy at RHIC and the LHC lie at the very top-left part of this phase diagram shown in Fig. 1.4, where μ_{B} is almost 0 and T is very high. For this reason, such heavy-ion collisions are also called **Little Bangs** [19].

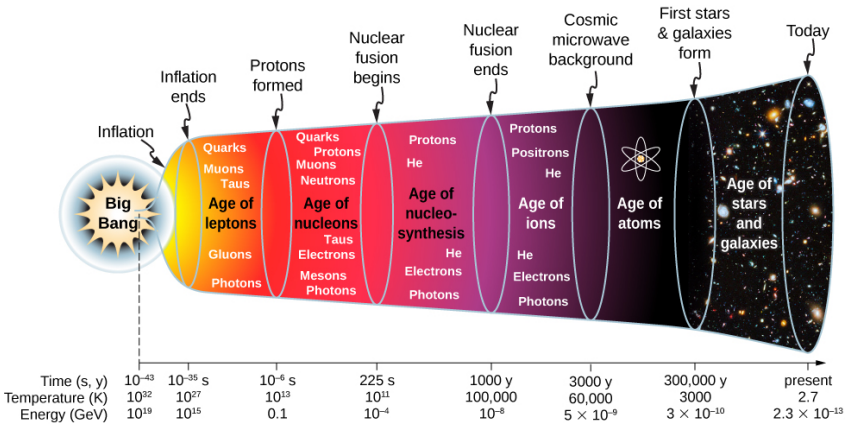

Figure 1.5: The evolution of the universe. Figure taken from [20].

1.2 Heavy-ion Collisions

As mentioned in the previous section, heavy-collision experiments are effective ways to create and study the deconfined QGP matter. They make use of the pow-

erful accelerators to make head-on collisions between massive ions, such as gold or lead nuclei, in order to create the extremely high temperature environment. In this section, we introduce the theoretical background of heavy-ion collisions, which includes the collision geometry and its evolution, as shown in Sec. 1.2.1 and Sec. 1.2.2, respectively.

1.2.1 Collision Geometry and Glauber Model

In heavy-ion collisions, two ions are accelerated to a velocity which is close to the speed of light, thus the Lorentz Factor γ becomes larger than one. In the centre-of-mass frame, due to the Lorentz contraction in the longitudinal direction, the two incoming nuclei can be seen as two thin disks of transverse size $2R_{\mathrm{A}} \simeq 2A^{1/3}$ fm, where R_{A} is the nuclear radius of nuclei A and A is the atomic number. Figure 1.6 shows the collision geometry of a nucleus A and a nucleus B. The quantities used

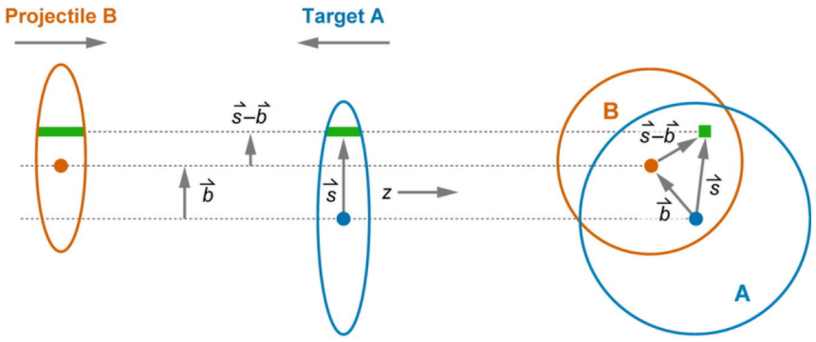

Figure 1.6: Illustration of two incoming nuclei before a collision together with the their geometric construction. Figure taken from [21].

to characterize the collision geometry are introduced as follow:

- The impact parameter, labeled as b. It is the distance between the centres of the two colliding nuclei. One can distinguish central collisions with $b \approx 0$, semi-central collisions with $b > 0$ and peripheral collisions in case of $b \lesssim R_{\mathrm{B}} + R_{\mathrm{A}}$, where R_{B} is the nuclear radius of nucleus B.

- The number of participant nucleons, N_{part}. As the collision happens, the nucleons which suffer at least one nucleon-nucleon interaction are called participants, and the nucleons which do not collide with any nucleon of the other nuclei are called spectators.

- The number of binary collisions, N_{coll}. It is the total number of nucleon-nucleon collisions.

In heavy-ion collisions, the Glauber model [21] is usually used to estimate N_{part} and N_{coll}. In this model, the nuclear reaction is approximated by the superposition of independent nucleon-nucleon interactions. As shown in Fig. 1.6, the two heavy ions A and B separated by an impact parameter vector $\vec{b}$, are going to collide along the

z axis. The position of a given nucleon in the transverse plane of nucleus A (labeled as green tube of ion A) is expressed by the vector $\vec{s}$, and the same position with respect to the centre of the nucleus B is given by $\vec{b} - \vec{s}$. The probability per unit transverse area to find a given nucleon at the transverse coordinate $\vec{s}$ is expressed as:

$$T_{\mathrm{A}}(\vec{s}) = \int_{-\infty}^{+\infty} \mathrm{d}z \cdot \rho_{\mathrm{A}}(\vec{s}, z), \tag{1.6}$$

where $T_{\mathrm{A}}(\vec{s})$ is the so-called nuclear thickness function of nucleus A, ρ is the nuclear density as a function of longitudinal z and transverse $\vec{s}$ positions which is parametrised with a Wood-Saxon function [21]. Similarly, the probability per unit transverse area to find a given nucleon in the same position of nucleus B, can be written as:

$$T_{\mathrm{B}}(\vec{s}) = \int_{-\infty}^{+\infty} \mathrm{d}z \cdot \rho_{\mathrm{B}}(\vec{s}, z). \tag{1.7}$$

Considering a nucleus-nucleus collision, the probability to have an elementary collision between two nucleons taken from the overlap region of nucleus A and B is given by:

$$p(\vec{b}) = \sigma_{\mathrm{inel}}^{\mathrm{NN}} \cdot \int \mathrm{d}^2 s \cdot T_{\mathrm{A}}(\vec{s}) T_{\mathrm{B}}(\vec{b} - \vec{s}) = \sigma_{\mathrm{inel}}^{\mathrm{NN}} \cdot T_{\mathrm{AB}}(\vec{b}), \tag{1.8}$$

where $\sigma_{\mathrm{inel}}^{\mathrm{NN}}$ is the nucleon-nucleon inelastic cross section, and $T_{\mathrm{AB}}(\vec{b})$ is defined as the nuclear overlap function for a given $\vec{b}$, which represents the effective overlap area in which a given nucleon in ion A can interact with a given nucleon in ion B. Furthermore, the probability to have n nucleon-nucleon interactions is given by the binomial distribution:

$$\begin{aligned} P_{n,\mathrm{AB}}(\vec{b}) &= \binom{\mathrm{AB}}{n} \cdot p(\vec{b})^n \cdot (1 - p(\vec{b}))^{\mathrm{AB}-n} \\ &= \binom{\mathrm{AB}}{n} \cdot [\sigma_{\mathrm{inel}}^{\mathrm{NN}} \cdot T_{\mathrm{AB}}(\vec{b})]^n \cdot [1 - \sigma_{\mathrm{inel}}^{\mathrm{NN}} \cdot T_{\mathrm{AB}}(\vec{b})]^{\mathrm{AB}-n}, \end{aligned} \tag{1.9}$$

where A and B are the number of nucleons in the nucleus A and B, respectively. The mean value of the binomial probability distribution can be regarded as the average number of binary nucleon-nucleon collisions, i.e. $\langle N_{\mathrm{coll}} \rangle$:

$$\langle N_{\mathrm{coll}}(\vec{b}) \rangle = AB \cdot \sigma_{\mathrm{inel}}^{\mathrm{NN}} \cdot T_{AB}(\vec{b}). \tag{1.10}$$

One can see that the number of binary collisions in a heavy-ion collision is inversely proportional to the impact parameter. Similarly, the number of participants at an impact parameter $\vec{b}$ can be expressed as:

$$N_{\mathrm{part}} = A \int \mathrm{d}^2\vec{s}\, T_{\mathrm{A}}\{1 - [1 - \sigma_{inel}^{\mathrm{NN}} T_{\mathrm{B}}(\vec{b} - \vec{s})]^B\} + B \int \mathrm{d}^2 s T_{\mathrm{B}}\{1 - [1 - \sigma_{\mathrm{inel}}^{\mathrm{NN}} T_{\mathrm{A}}(\vec{s})]^A\}, \tag{1.11}$$

where the integral over the terms in brackets gives the respective inelastic cross sections for nucleus-nucleus collisions.

The impact parameter, N_{part} and N_{coll} can not be directly measured experimentally. The mean values of such quantities for given classes of measured events can

be extracted by means of Monte Carlo Glauber calculations [21]. This is done by connecting the distribution of the number of charged particles to the average N_{part} and impact parameter b, as shown in Fig. 1.7. We can see that a smaller impact parameter, i.e. a more central collision, will on average lead to a higher particle multiplicity. The centrality is usually expressed in percentiles of the total inelastic hadronic cross section, whose variation from 0% to 100% is corresponding to changes from central to peripheral collisions.

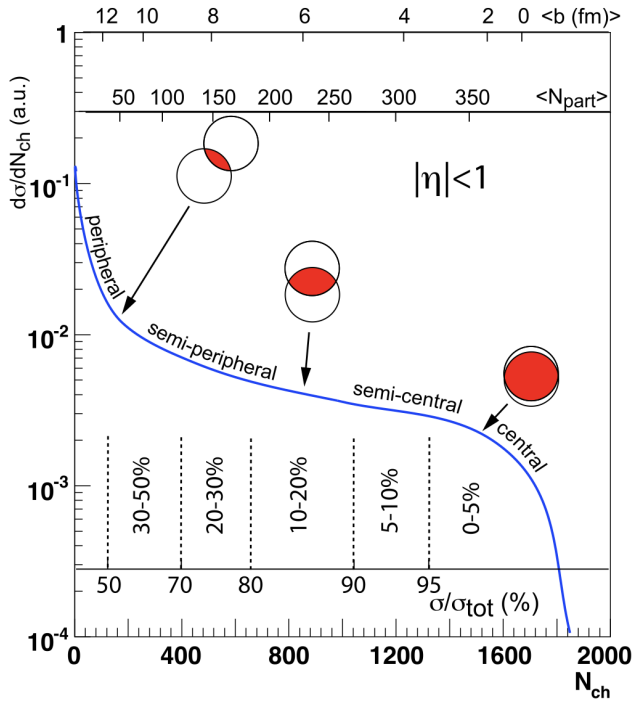

Figure 1.7: Illustration of the correlations between the number of charged particles and impact parameter, $\langle N_{\text{part}} \rangle$ obtained from Monte Carlo Glauber calculations. The figure is taken from [13].

1.2.2 Space-time Evolution

After the initial collision geometry is fixed, the heavy-ion collisions will evolve within a specific way. Figure 1.8 shows the different stages of a heavy-ion collision (top) and its space-time evolution in the Minkowski space coordinate [22].

The longitudinal proper time τ in the Minkowski space coordinate can be defined by:

$$\tau = \sqrt{t^2 - z^2}, \tag{1.12}$$

where t and z are the time and the longitudinal coordinate in the beam direction, respectively. The light cone of the collision, defined by lines of constant proper time τ, is indicated by diagonal black lines, as shown in Fig. 1.8. Some important

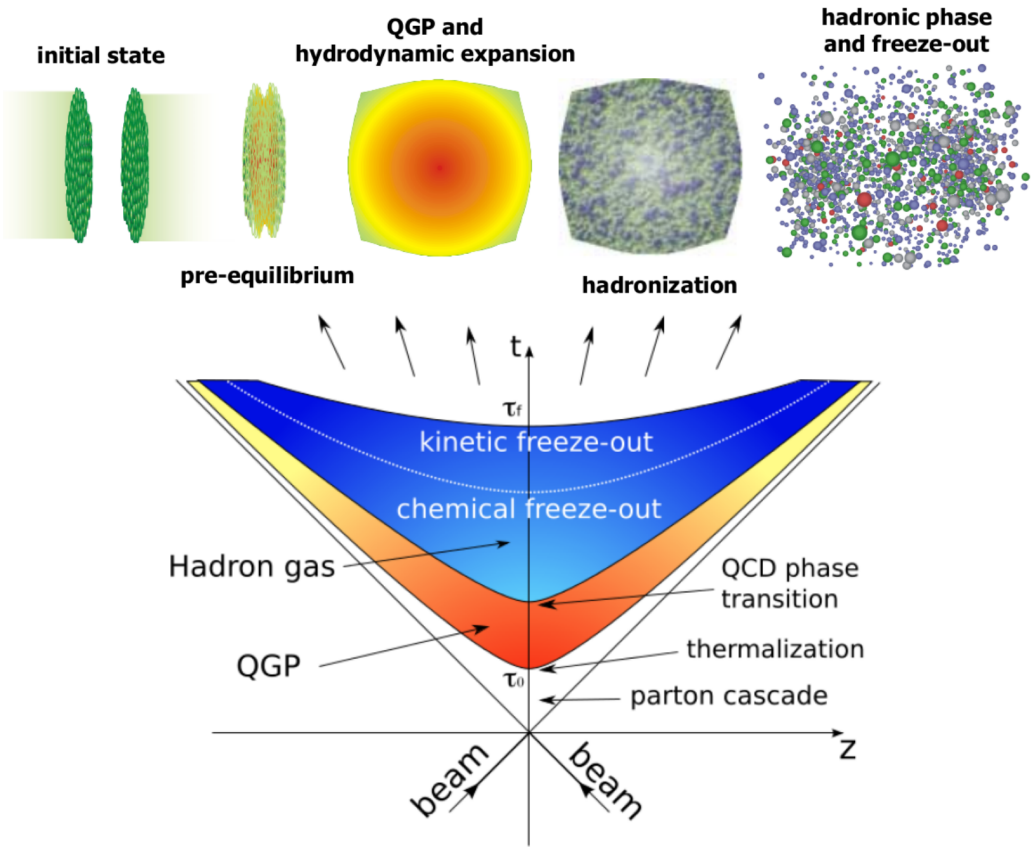

Figure 1.8: Illustration of the different stages of a heavy-ion collision (top) and space-time evolution of heavy-ion collisions (bottom). Figures are taken from [22, 23].

steps are indicated. Generally, the following phases of the collision evolution can be defined:

- Initial stage: the collision between two ions happens in a very short time ($\tau \sim 0.3$ fm/c), and the initial collision conditions are described by the Glauber model, as discussed in Sec. 1.2.1.
- Pre-equilibrium: the energy is deposited in the interaction region by the colliding ions, a pre-equilibrium phase is created by the multiple interactions among the partons. Hard partons (e.g. heavy quarks) are also produced at this stage. The whole process will last $\tau \simeq 0.3$–2 fm/c.
- QGP formation: when the temperature reaches the critical temperature, the system becomes a deconfined phase as described in Sec. 1.1.3, and the QGP is formed. Meanwhile, the whole system starts to expand, and with the expansion, the system starts to cool down. The time scale of this stage is $\tau \simeq 2$–6 fm/c.
- Hadronisation: when the temperature decreases below the critical temperature of the transition crossover, the QGP phase becomes a hadron gas. The quarks

and gluons are not longer deconfined, and they start to hadronize into hadrons. The time scale of this stage is $\tau \simeq 6$–10 fm/c.

- Freeze-out: when $\tau \gtrsim 10$ fm/c, the system evolves into the freeze-out stage. First the inelastic interactions cease, and all the hadron species are fixed, which is the so-called chemical freeze-out. Then, the elastic processes stop, the final momentum spectrum of the produced particles are determined, which is called the kinetic freeze-out.

1.3 Probing the quark-gluon plasma Medium

As mentioned in the previous section, the kinetic freeze-out is reached in about 10 fm/c after the collision, therefore the QGP can not be observed directly. However, the information of the evolution of the system is preserved in the created final-state particles, the so-called **probes**. Based on the momentum scale of the given probe, they can be generally divided into hard and soft probes. The hard probes originate from hard scattering of partons (quarks and gluons) with a large momentum transfer ($1/\mathrm{Q} \ll 1$ fm/c) which occur prior to the QGP formation, therefore the hard partons and the subsequent parton shower experience the entire evolution of the system. Examples of hard probes include high-p_{T} particles, jets, particles with heavy quarks and quarkonia.

One of the most prominent observables of the soft probes is the anisotropic flow, which refers to the collective properties of soft bulk matter. Due to the finite size of the colliding objects (as shown in Sec. 1.2), the initial geometry and fluctuations of a nucleus-nucleus collision will result in the anisotropy of produced QGP matter in the transverse plane. Then with the expansion and the evolution of the QGP, all information is ultimately propagated to the final particles. Therefore the measurement of anisotropic flow can help to understand not only the initial conditions but also the transport properties of the QGP medium.

Recently, the measurement of hard and soft probes are not mutually independent. Some observables, for instance the anisotropic flow of heavy-flavour hadrons and high-p_{T} particles, can provide us an unique way to study the interplay between the initial geometrical anisotropy and energy loss mechanisms during the evolution of the QGP. In this section, we introduce some important observables of heavy-ion physics and the experimental results that supported the current understanding of the properties of QGP.

1.3.1 High-p_{T} Hadrons and Jet Quenching

High-p_{T} partons are usually produced in hard-scattering processes in the early stage of the collision, then they traverse the subsequently formed QGP medium and fragment into experimentally observed high-p_{T} hadrons, or jets [24]. During the travel of these partons in the QGP medium, they interact with the medium constituents and lose energy via inelastic (gluon radiation) and elastic (collisional) processes, which is called **jet quenching**.

A key observable for the study of jet quenching is the nuclear modification factor R_{AA}. It is used to quantify the suppression of the production of particles (possibly identified) or reconstructed jets in heavy-ion collisions, relative to the expectation from binary scaling of the hard interactions in pp collisions. The R_{AA} is defined as

$$R_{\mathrm{AA}} = \frac{\mathrm{d}^2 N_{\mathrm{AA}}/\mathrm{d}y\mathrm{d}p_{\mathrm{T}}}{\langle N_{\mathrm{coll}}\rangle \mathrm{d}N_{\mathrm{pp}}^{\mathrm{INEL}}/\mathrm{d}y\mathrm{d}p_{\mathrm{T}}} = \frac{\mathrm{d}^2 N_{\mathrm{AA}}/\mathrm{d}y\mathrm{d}p_{\mathrm{T}}}{\langle T_{\mathrm{AA}}\rangle \mathrm{d}\sigma_{\mathrm{pp}}^{\mathrm{INEL}}/\mathrm{d}y\mathrm{d}p_{\mathrm{T}}}, \tag{1.13}$$

where N_{AA} and N_{pp} are the charged-particle or reconstructed-jet yields in AA and pp collisions, and $\sigma_{pp}^{\mathrm{INEL}}$ is the inelastic cross section in pp collisions. $\langle T_{\mathrm{AA}}\rangle$ is the nuclear overlap function, which is defined as $\langle T_{\mathrm{AA}}\rangle = \langle N_{\mathrm{coll}}\rangle/\sigma_{pp}^{\mathrm{INEL}}$. According to the Glauber model described in Sec. 1.2.1, the R_{AA} is expected to be equal to unity in the absence of any nuclear effects, while a difference from unity implies that the p_{T} distributions of hadrons or reconstructed jets are modified. The effects of such modifications are usually divided in two classes:

- Initial-state effects, such as nuclear shadowing, gluon saturation and Cronin enhancing [25]. They depend on the size and energy of the colliding nuclei, but not on the presence of the QGP formed in the collision. They are usually studied via the measurement of the nuclear modification factor in pA collisions, which will be introduced in Sec. 1.4.1.

- Final-state effects, such as collisional and radiative energy loss induced by the created medium, which influence the yields and the kinematic distributions of the produced hard partons. They depend strongly on the properties of the medium (e.g. the gluon density, temperature and volume).

Figure 1.9 (left) shows the nuclear modification factor of charged particles as a function of p_{T} measured by ALICE in central (0–5%) and peripheral (70–80%) Pb–Pb collisions at $\sqrt{s_{\mathrm{NN}}} = 5.02$ TeV. One can observe a significant suppression of charged-hadron yields for the most central (0–5%) collisions. The nuclear modification factor exhibits a minimum at around $p_{\mathrm{T}} = 6$–7 GeV/c and a significant rise for $p_{\mathrm{T}} > 7$ GeV/c which reaches a value of about 0.4 for the highest p_{T} bin (30–50 GeV/c), indicating a reduction of the relative energy loss. For peripheral collisions (70–80%), only a moderate suppression and a weak p_{T} dependence is observed. Since at $p_{\mathrm{T}} \gtrsim 3$ GeV/c, the R_{pPb} is consistent with unity, that indicates that the large suppression observed from the R_{AA} measurement at high p_{T} is due to the jet quenching in the QGP instead of initial-state effects. In addition, the nuclear modification factor of particles which are not sensitive to QCD dynamics (such as direct photon, $W^{\pm}$ and Z bosons) measured by ALICE and CMS [26–28], is also found to be compatible with unity. In order to extend the measurement to higher p_{T}, the R_{AA} of reconstructed jets is measured in the 0–10% most central Pb–Pb collisions at $\sqrt{s_{\mathrm{NN}}} = 2.76$ TeV, as shown in Fig. 1.9 (right). As we can see, the production of jets in the measured $p_{\mathrm{T,jet}}$ range is strongly suppressed. The R_{AA} is found to be independent of $p_{\mathrm{T,jet}}$, and its average value reaches 0.28 ± 0.04. In addition, the observed suppression in data is in fair agreement with expectations from two jet quenching model calculations, YaJEM [29] and JEWEL [30].

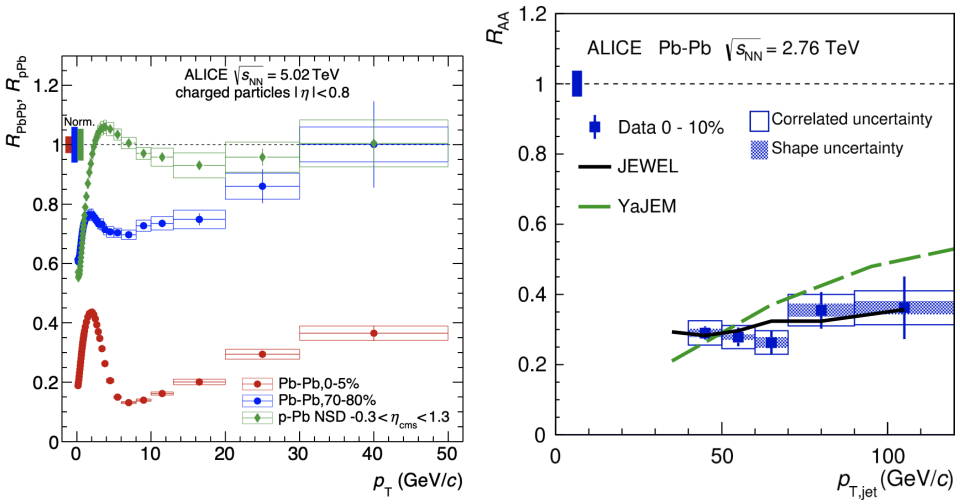

Figure 1.9: Left: the nuclear modification factor a function of p_{T} measured by ALICE in central (0-5%) and peripheral (70-80%) Pb–Pb collisions and in non-single diffractive (NSD) p–Pb collisions at $\sqrt{s_{\mathrm{NN}}} = 5.02$ TeV. Figure taken from [31]. Right: the nuclear modification factor for jets with the leading track requirement of 5 GeV/c in 0–10% most central Pb–Pb collisions at $\sqrt{s_{\mathrm{NN}}} = 2.76$ TeV, compared to calculations from YaJEM [29] and JEWEL [30]. Figure taken from [32].

In summary, the R_{AA} of high-p_{T} particles and jets are sensitive probes of the formation of the QGP and the comparison with the model calculations can used to further characterize the jet-quenching effects.

1.3.2 Heavy Flavours

Similar to the high-p_{T} partons, heavy quarks (charm and beauty)[2] are produced early in the nucleus-nucleus collisions on a time-scale that is shorter than the QGP formation time. Therefore, the kinematic studies of heavy-flavour hadrons and decay particles (muons, electrons) provide insight into the full evolution of the QGP. In this section, we introduce the theoretical background and current experimental results about heavy-flavour production in both pp and AA collisions.

1.3.2.1 Open Heavy-flavour Production in pp Collisions

For hard processes, such as heavy-flavour production, in the absence of nuclear and medium effects, a nucleus-nucleus (AA) collision would behave as a superposition of independent proton-proton (pp) collisions. In pp collisions, due to the large masses of heavy-quark ($m_{\mathrm{c}} \simeq 1.3$ GeV/c^2 and $m_{\mathrm{b}} \simeq 4.2$ GeV/c^2), large momentum transfer is involved in scattering processes, which can be calculated in the

[2]The top quark is also considered to belong to the heavy quarks, but it decays before it can hadronise, which is very different from charm and beauty quarks. Therefore top quark is not mentioned in the following.

framework of perturbative QCD down to low p_{T} [33]. Following the factorization theorem [34], the heavy-flavour hadron production in proton-proton collisions is described by three terms: the parton distribution functions, the hard partonic scattering cross section and the fragmentation function. The inclusive differential cross section for the production of a heavy-flavour hadron H_Q can be expressed as

$$\begin{aligned} \mathrm{d}\sigma^{\mathrm{pp}\to\mathrm{H}_Q\mathrm{X}}(\sqrt{s}, m_{\mathrm{Q}}, \mu_{\mathrm{F}}^2, \mu_{\mathrm{R}}^2) = \sum_{i,j=q,\bar{q},g} & f_i(x_1, \mu_{\mathrm{F}}^2) \otimes f_i(x_2, \mu_{\mathrm{F}}^2) \\ & \otimes \mathrm{d}\hat{\sigma}^{ij\to Q(\bar{Q})\{k\}}(\alpha_s(\mu_{\mathrm{R}}^2), \mu_{\mathrm{F}}^2, m_Q, x_1 x_2 s) \\ & \otimes D_{Q\to\mathrm{H}_Q}(z, \mu_{\mathrm{F}}^2), \end{aligned} \tag{1.14}$$

where $f_i(x_1, \mu_{\mathrm{F}}^2)$ and $f_i(x_2, \mu_{\mathrm{F}}^2)$ are the parton distribution functions (PDFs), which can be interpreted as the probability to find a parton i inside the proton with fraction of momentum $x_1 = p_i/p_p$ ($x_2 = p_i/p_p$). The partonic cross section $d\hat{\sigma}^{ij\to Q(\bar{Q})\{k\}}$ up to a given perturbative order k is calculated as a perturbative series in terms of the strong coupling α_s, where $m_{\mathrm{Q}} > \Lambda_{\mathrm{QCD}}$. Currently, the calculations are performed up to Next-to-Leading Order (NLO [35,36]), or at Fixed Order with Next-to-Leading Logarithms (FONLL [37, 38]). $D_{Q\to\mathrm{H}_Q}$ is the fragmentation function which parametrizes the probability for the scattered heavy quark Q to fragment into a hadron H_Q with a momentum fraction $z = p_{\mathrm{H}_Q}/p_Q$. One can see that both PDFs and the fragmentation functions depend on the energy scale of the process, which is evaluated at a given scale called factorization scale μ_{F}. The renormalization scale μ_{R} and factorization scale μ_{F} are usually taken of the same order of the momentum transfer of the hard process $\mu_{\mathrm{R}} \sim \mu_{\mathrm{F}} \sim \sqrt{m_{\mathrm{Q}}^2 + p_{\mathrm{T,Q}}^2}$. In summary, the whole process can be described as three steps:

- Two partons are extracted from PDFs $f_i(x_1, \mu_{\mathrm{F}}^2)$ and $f_i(x_2, \mu_{\mathrm{F}}^2)$ in the initial stage of nucleon-nucleon collisions.
- The cross section of heavy flavours produced during hard scatterings is computed by pQCD.
- After a heavy quark is formed, it will fragment into an open heavy-flavour hadron based on the fragmentation function $D_Q^{\mathrm{H}_Q}$.

Experimentally, open heavy-flavour production can be studied in various ways. In ALICE, it can be studied either via the full reconstruction of exclusive decays of D and B mesons at midrapidity, e.g. $\mathrm{B}^0 \to \mathrm{J}/\psi K_{\mathrm{S}}^0$ and $\mathrm{D}^0 \to \mathrm{K}^-\pi^+$ and so on, or the semi-leptonic decays of D and B mesons to muons (electrons) at forward (mid-) rapidity. Each approach has its own advantages: the measurement of B and D mesons allows the full kinematic information of the original particle to be reconstructed; the measurement of heavy-flavour decay electrons allows us to separate the contribution of beauty hadrons from the inclusive spectrum by means of a template fit to the impact parameter distribution [39]; the measurement of heavy-flavour hadron decay muons at forward rapidity allows us to cover the region of small

Bjorken-x values. Figure 1.10 (left) shows the measurement of prompt D^0 meson p_T-differential production cross section compared to FONLL calculations. The data can be described within uncertainties by FONLL predictions. The measurement of the p_T-differential production cross section of muons from heavy-flavour hadron decays at forward rapidity ($2.5 < y < 4$) is shown in Fig 1.10 (right), which is compatible with FONLL predictions within uncertainties. The FONLL predictions are also displayed for muons coming from charm and beauty decays, separately. One can see that muons from charm decays dominate in the low-p_T region ($p_T \lesssim 4$ GeV/c), while at high p_T ($p_T \gtrsim 4$ GeV/c) muons from beauty decays are the main contribution. On the other hand, the central values of FONLL predictions systematically appear to underestimate the data, which is observed in both the D-meson and heavy-flavour decay muon production cross section measurements, as shown in Fig. 1.10 (left and right). The measurements bring constraints on pQCD-based calculations and gluon PDF at midrapidity and forward rapidities [40].

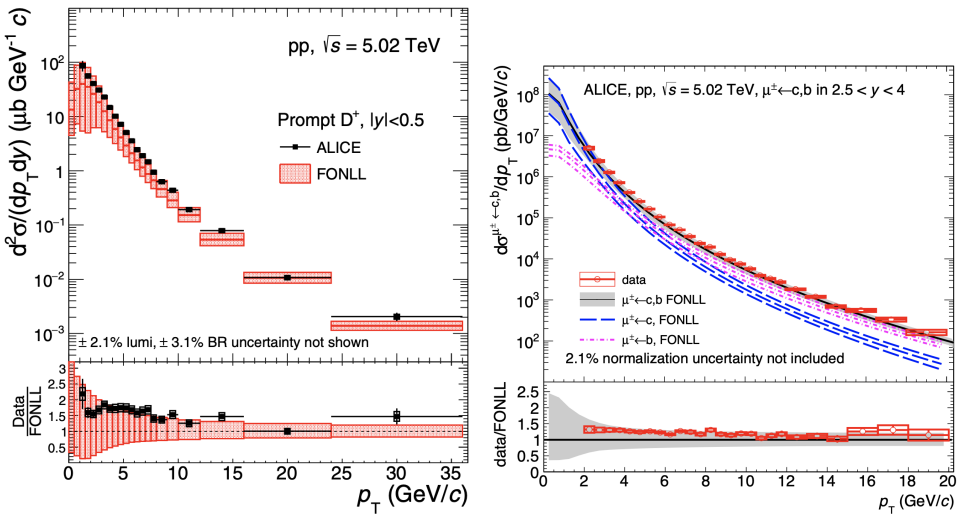

Figure 1.10: Left: p_T-differential production cross sections for prompt D^0 mesons compared to FONLL calculations in pp collisions at $\sqrt{s_{NN}} = 5.02$ TeV. The figure is taken from [41]. Right: p_T-differential production cross section of muons from heavy-flavour hadron decays at forward rapidity compared to FONLL calculations in pp collisions at $\sqrt{s_{NN}} = 5.02$ TeV. The figure is taken from [42].

In summary, measurements of the open heavy-flavour production in pp collisions provide an interesting test of pQCD calculations. Especially, the measured heavy-flavour decay muons in the forward rapidity region allow us to test pQCD predictions in a region of small Bjorken-x down to about 10^{-5}. In addition, the measurement of the heavy-flavour production cross sections in pp collisions provides the necessary baseline for the corresponding measurements in nucleus-nucleus collisions in order to study the nuclear effects related to the hot and dense strongly-interacting medium, which will be introduced in next section.

1.3.2.2 Open Heavy-flavour Production in AA Collisions

As mentioned, heavy quarks are produced before the formation of the QGP medium, then they traverse the QGP and interact with the medium constituents and lose part of their energy via elastic (collisional) and inelastic (gluon radiation) processes. Therefore, following the same notations as in Eq. 1.14, the cross section for the production of a heavy-flavour hadron in AA collisions (with mass number A) can be expressed as:

$$\begin{aligned} \mathrm{d}\sigma^{\mathrm{AA}\to\mathrm{H}_Q\mathrm{X}}(\sqrt{s}, m_\mathrm{Q}, \mu_\mathrm{F}^2, \mu_\mathrm{R}^2) = A\cdot A\cdot \sum_{i,j=q,\bar{q},g} & f_i^N(x_1,\mu_\mathrm{F}^2)\otimes f_i^N(x_2,\mu_\mathrm{F}^2) \\ & \otimes \mathrm{d}\hat{\sigma}^{ij\to Q(\bar{Q})\{k\}}(\alpha_s(\mu_\mathrm{R}^2),\mu_\mathrm{F}^2, m_Q, x_1x_2s) \\ & \otimes R_N^{\mathrm{QGP}}(E, m_Q, T, \alpha, L, ...)\otimes D^N_{Q\to\mathrm{H}_Q}(z,\mu_\mathrm{F}^2). \end{aligned} \tag{1.15}$$

Compared to Eq. 1.14, the PDF $f_i(x_1,\mu_\mathrm{F}^2)$ and fragmentation function $D_{Q\to\mathrm{H}_Q}$ are replaced by nuclear modified PDF $f_i^N(x_1,\mu_\mathrm{F}^2)$ and medium-modified fragmentation function $D^N_{Q\to\mathrm{H}_Q}$, due to the effects from the nuclear environment. In addition, an extra term R_N^{QGP} which represents the modification of the heavy-quark momentum due to energy loss in the medium, is introduced. It shows that the energy loss (labeled as ΔE) depends on the properties of the particle (energy E, mass of quark m_Q) as well as the medium (temperature T, particle-medium interaction coupling α, thickness L). Generally, the total energy loss can be expressed as the sum of two terms:

$$\Delta E = \Delta E_\mathrm{coll} + \Delta E_\mathrm{rad}, \tag{1.16}$$

where ΔE_coll and ΔE_rad represent the collisional energy loss and radiative energy loss, respectively. At low momentum, the collisional energy loss of heavy quarks is dominated according to their elastic scatterings with the medium constituents. For higher momentum, because the mass becomes negligible compared to momentum ($m_Q \ll p$), heavy quarks behave like light particles, which lose energy mainly via gluon radiation, i.e. radiative energy loss. Figure 1.11 shows the comparison of radiative and collisional energy loss for charm and beauty quarks as a function of the quark energy, obtained within the framework of a Langevin equation coupled to a hydrodynamic model that simulates the space-time evolution of the produced hot and dense QCD matter [43].

Collisional Energy Loss

The average collisional energy loss of a elastic scattering in a medium of temperature T can be expressed as:

$$\langle \Delta E_\mathrm{coll}\rangle \approx \frac{1}{\sigma T}\int_{m_\mathrm{D}^2}^{t_\mathrm{max}} t\frac{\mathrm{d}\sigma}{\mathrm{d}t}\mathrm{d}t, \tag{1.17}$$

where $\frac{\mathrm{d}\sigma}{\mathrm{d}t}$ is the parton-parton differential particle-medium interaction cross section, m_D is the Debye mass and t_max is the maximum squared momentum transfer. Considering that the momentum-transfer integral limits are given by the QGP Debye

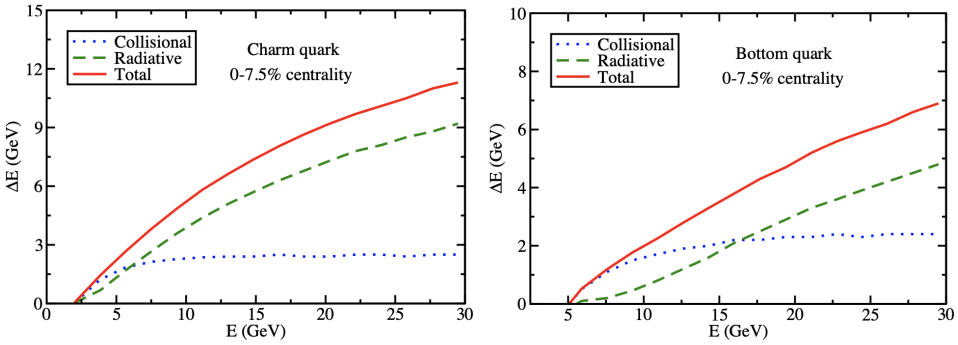

Figure 1.11: Comparison of radiative and collisional energy loss for charm (left) and beauty (right) quarks as a function of the quark energy. Figures are taken from [43].

mass squared: $t_{\min} = m_D^2(\mathrm{T}) \sim 4\pi\alpha_\mathrm{s}\mathrm{T}^2(1+\mathrm{n_f}/6)$ and $t_{\max} = E \cdot T$, the cross section is expressed as:

$$\frac{\mathrm{d}\sigma}{\mathrm{d}t} \approx C_i \frac{4\pi\alpha_\mathrm{s}^2(t)}{t^2} \tag{1.18}$$

where $C_i = 9/4{,}1{,}4/9$ are the colour factors for gg, gq and qq scatterings respectively. The amount of ΔE_{coll} varies linearly with the medium thickness and it has a logarithmic dependence on the initial parton energy.

Radiative Energy Loss

The radiative energy loss is mainly for gluon radiation (gluon bremsstrahlung), which is determined from the corresponding single- or double-differential gluon bremsstrahlung spectrum:

$$\begin{aligned} \langle \Delta E_{\mathrm{rad}} \rangle &= \int_0^E w \frac{\mathrm{d}I_{\mathrm{rad}}}{\mathrm{d}w} \mathrm{d}w \\ &\text{or} \\ \langle \Delta E_{\mathrm{rad}} \rangle &= \int_0^E \int_0^{k_{\mathrm{T,max}}} w \frac{\mathrm{d}^2 I_{\mathrm{rad}}}{\mathrm{d}w \mathrm{d}k_\mathrm{T}^2} \mathrm{d}w \mathrm{d}k_\mathrm{T}^2, \end{aligned} \tag{1.19}$$

where w, k_T are the energy and transverse momentum of the radiated gluon, respectively. Many approximations of Eq. 1.19 are given by several theoretical groups, here we take the general concepts of the BDMPS model [44, 45] as an example. In an energetic collision, a hard parton is produced and then undergoes multiple scatterings in a Brownian-like motion, along its path in the dense medium. The medium is modeled with static scattering centres, which implies that the gluons in the hard parton wave function can pick up transverse momentum k_T and then eventually be decohered from the partonic projectile. The energy of the emitted gluons w_c as a function of a finite path length L traversed by the parton can be expressed as:

$$w_c = \frac{1}{2}\hat{q}L^2, \tag{1.20}$$

where $\hat{q}$ is the transport coefficient of the medium, defined as the average squared transverse momentum transferred to the projectile per unit of path length:

$$\hat{q} = \frac{\langle k_{\mathrm{T}}^2 \rangle}{L}. \tag{1.21}$$

In the case of a static medium, i.e. $w \ll w_c$, the energy distribution of radiated gluons can be obtained as

$$w\frac{\mathrm{d}I_{\mathrm{rad}}}{\mathrm{d}w} \simeq \frac{2\alpha_s C_{\mathrm{R}}}{\pi}\sqrt{\frac{w_c}{2w}}, \tag{1.22}$$

where C_{R} is the Casimir factor for the QCD vertices, which is equal to 4/3 for quark-gluon coupling and 3 for gluon-gluon coupling. Thus the average energy loss $\langle \Delta E_{\mathrm{rad}} \rangle$ of the parton can be expressed as:

$$\langle \Delta E_{\mathrm{rad}} \rangle = \int_0^{w_c} w\frac{dI_{\mathrm{rad}}}{dw} \propto \alpha_s C_{\mathrm{R}} w_c \propto \alpha_s C_{\mathrm{R}} \hat{q} \mathrm{L}^2. \tag{1.23}$$

We can see that the average energy loss is proportional to the path length L^2, to the transport coefficient $\hat{q}$ and to $\alpha_s C_{\mathrm{R}}$, ans thus is larger by a factor 9/4 for gluons than for quarks. Moreover, due to the large masses of heavy quarks, the so-called "dead-cone effect" [46] should be considered in the radiative energy loss. For the heavy quarks with moderate energy, i.e. $m_Q/E \gg 0$, their propagation velocity $\beta = \sqrt{1-(m_Q/E)^2}$ is significantly smaller than the velocity of light ($\beta = 1$). Therefore, the gluon radiation at an angle Θ which is smaller than the ratio of their mass to the energy $\Theta_0 = m_Q/E$ is suppressed. The relatively reduced cone around the heavy-quark direction with $\Theta < \Theta_0$ is called the dead cone. Considering the dead-cone effect, the energy distribution of the radiated gluons for heavy quarks, is estimated to be suppressed by a factor:

$$w\frac{\mathrm{d}I_{\mathrm{rad}}}{\mathrm{d}w}|_{\mathrm{Heavy}} / w\frac{\mathrm{d}I_{\mathrm{rad}}}{\mathrm{d}w}|_{\mathrm{Light}} = (1+\frac{\Theta_0^2}{\Theta^2})^{-2} = \left[1+(\frac{m_Q}{E})^2\sqrt{\frac{w^3}{\hat{q}}}\right]^2 \equiv F_{H/L}(m_Q/E, \hat{q}, w), \tag{1.24}$$

where the expression for the characteristic gluon emission angle $\Theta \simeq (\hat{q}/w^3)^{1/4}$ is used. The dead-cone suppression factor $F_{H/L}$ increases with the increasing energy E of heavy quarks, and decreases at large w, which indicates that high-energy part of the gluon radiation spectrum is drastically suppressed by the dead-cone effect [47].

Based on the above descriptions about collisional and radiative energy loss mechanisms, a hierarchy of flavour-dependent energy loss can be obtained:

$$\Delta E(g) > \Delta E(q) > \Delta E(c) > \Delta E(b), \tag{1.25}$$

where the energy loss is expected to be larger for gluons and light quarks than for beauty and charm quarks. Experimentally, the effects of energy loss can also described by the nuclear modification factor R_{AA}, as defined in Eq. 1.13.

Figure 1.12 (left) shows the nuclear modification factor R_{AA} of D^0 as a function of p_{T} at midrapidity ($|y| < 1$) in the 0–10% central Pb–Pb collisions at $\sqrt{s_{\mathrm{NN}}} = 5.02$

TeV. A strong suppression of the D-meson yields with respect to the binary-scaled pp reference is observed. It reaches a maximal factor of 5 to 6 for p_{T} = 6–10 GeV/c, where the dominant process is the radiative energy loss. The suppression gets smaller with decreasing p_{T} for $p_{\mathrm{T}} < 6$ GeV/c, and R_{AA} increase up to a value of about 0.6 in the p_{T} range 60–100 GeV/c. The general trend of the R_{AA} is qualitatively reproduced by different theoretical models [48–51]. On the other hand, the average R_{AA} of D^0, D^+ and D^{*+} mesons as a function of p_{T} at midrapidity ($|y| < 0.5$) measured by ALICE in the 0–10% central Pb–Pb collisions at $\sqrt{s_{\mathrm{NN}}} = 5.02$ TeV is compared to the R_{AA} of particles originating from pions, charm-hadron and beauty-hadron decays, as shown in Fig. 1.12 (right). One can see that the R_{AA} of D mesons is larger than that of pions for $p_{\mathrm{T}} < 8$ GeV/c, while they are similar at high p_{T} (> 8 GeV/c). It provides the evidence of the hierarchy of flavour-dependent energy loss, as mentioned in Eq. 1.25. In addition, the R_{AA} of prompt D mesons is smaller than that of non-prompt J/Ψ mesons from beauty hadron decays, while the R_{AA} of prompt J/Ψ is consistent with the one of prompt D mesons within uncertainties at high p_{T} (> 10 GeV/c). These comparisons give insights into the properties of the in-medium parton energy loss, especially its dependence on the colour charge and the quark mass.

The measurements of heavy-flavour hadrons are also performed via their semileptonic decay channel. Figure 1.13 (left) shows the nuclear modification factor of electrons from semileptonic heavy-flavour hadron decays measured in the most central 0–10% Pb–Pb collisions at $\sqrt{s_{\mathrm{NN}}} = 5.02$ TeV. A clear suppression is observed, which reaches a minimum of about 0.3 around $p_{\mathrm{T}} = 7$ GeV/c. This suppression of the electron production is due to the partonic energy loss in the QGP medium since the R_{AA} of electrons is consistent with unity in proton-lead collisions [52] where the QGP is not expected to exist. In addition, the R_{AA} of muons from heavy flavour decays in $2.5 < y < 4$, as a function of p_{T} in central 0–10% collisions is also measured, as shown in Fig. 1.13 (right). A strong suppression is also observed at forward rapidity, reaching a factor of about 3-4. However, due to the limits of statistics in Run 1, the R_{AA} of muons from heavy flavour decays can not be extended to higher p_{T} ($p_{\mathrm{T}} > 10$ GeV/c), where the energy loss of beauty quarks is dominant. Based on this, one of the motivations of this thesis is to perform a new measurement of the R_{AA} of muons from heavy flavour decays in a wider p_{T} region with higher collision energy. The analysis will be discussed in Chapter 4.

1.3.2.3 Hadronisation Mechanisms

The heavy quarks produced in the early stage of collisions experience the process that generate the final-state hadrons, which is the so-called hadronisation. In general, there are two kinds of hadronisation mechanisms, the fragmentation and recombination (or coalescence). The fragmentation was described by the fragmentation function, $D_{Q\to \mathrm{H}_Q}(z, \mu_{\mathrm{F}}^2)$, as mentioned in Eq. 1.14, where heavy quarks can be fragmented into a spray of lower momentum hadrons in pp collisions. On the other hand, due to the presence of the hot and dense QGP medium, the hadronisation process will be modified in heavy-ion collisions, as described in Eq. 1.15. The heavy

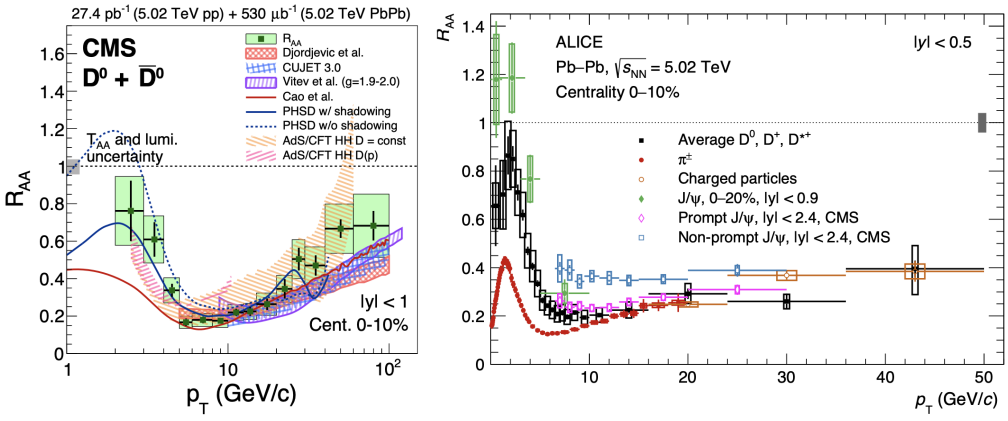

Figure 1.12: Left: R_{AA} as a function of p_{T} in 0–10% most central Pb–Pb collisions at $\sqrt{s_{\mathrm{NN}}} = 5.02$ TeV. The figure is taken from [53]. Right: Average R_{AA} of prompt D mesons in 0–10% most central Pb–Pb collisions at $\sqrt{s_{\mathrm{NN}}} = 5.02$ TeV, compared to R_{AA} of charged pions, charged particles, inclusive J/Ψ. The figure is taken from [54].

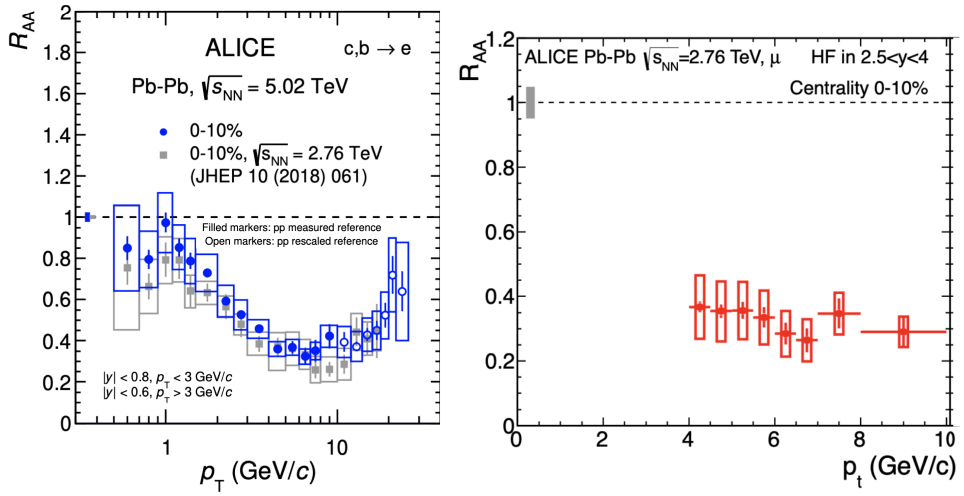

Figure 1.13: Left: R_{AA} of electrons from heavy-flavour hadron decays measured in midrapidity as a function of p_{T} in 0–10% Pb–Pb collisions at $\sqrt{s_{\mathrm{NN}}} = 5.02$ TeV. The figure is taken from [55]. Right: R_{AA} of muons from heavy flavour decays in $2.5 < y < 4$ as a function of p_{T} in 0–10% Pb–Pb collisions at $\sqrt{s_{\mathrm{NN}}} = 2.76$ TeV. The figure is taken from [56].

quarks may recombine with other light quarks in the medium and generate the final state hadrons with momentum higher than one of initial partons. In this case, the fragmentation mixes with the recombination mechanism in heavy-ion collisions, while the former one expected to dominate at high p_{T} [43, 57] and the latter one is related to the production of hadrons at low and intermediate p_{T}.

To obtain a clean environment without any nuclear effects, the fragmentation

functions of heavy quarks are usually studied in e^+e^- and e^-p collisions at the LEP and HERA [58]. A fragmentation universality assumption that the heavy-quark fragmentation into hadrons is the same in e^+e^-, e^-p and pp collisions was proposed in [58]. A traditional way to describe the fragmentation mechanism is the Lund string model [59, 60], which is implemented in the PYTHIA event generator with the default tuning. However, the fragmentation fractions measured in pp collisions at midrapidity are different from the ones measured in e^+e^- and e^-p collisions, as shown in Fig. 1.14 (left). In addition, the relative production of baryons and mesons, i.e. baryon-to-meson ratio is also studied in pp collisions since it is sensitive to the hadronisation mechanisms. As shown in Fig. 1.14 (right), the Λ_c^+/D^0 production ratios measured in pp collisions at $\sqrt{s_{\mathrm{NN}}} = 5.02$ TeV are underestimated significantly by the predictions driven by charm-quark fragmentation processes measured in e^+e^- and e^-p collisions. These results indicate that the production of charm baryons in hadronic collisions can not be described by the assumption of universality also.

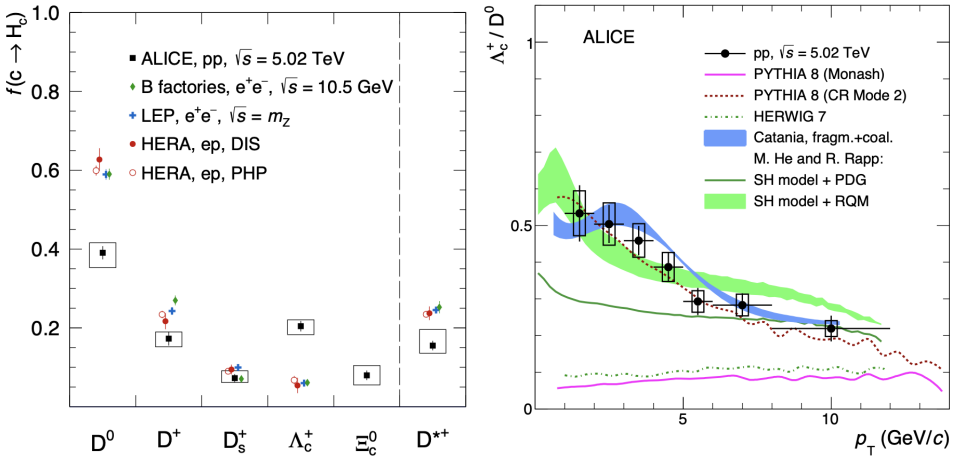

Figure 1.14: Left: the fragmentation fractions of charm quarks into hadrons measured in pp collisions at $\sqrt{s_{\mathrm{NN}}} = 5.02$ TeV in comparison with the measurements performed in e^+e^- collisions at the LEP and at B factories, and in e^-p collisions at HERA [58]. Right: the Λ_c^+/D^0 ratio as a function of p_{T} measured in pp collisions at $\sqrt{s_{\mathrm{NN}}} = 5.02$ TeV in comparasion of several model calculations [61]. Figures are taken from [62].

In heavy-ion collisions, the relative production of Λ_c^+ and D^0 is measured in 0–10% and 30–50% Pb–Pb collisions at $\sqrt{s_{\mathrm{NN}}} = 5.02$ TeV, as shown in Fig. 1.15. Compared to the pp measurement at the same collision energy, the ratio between the production yields of Λ_c^+ and D^0 is higher in Pb–Pb collisions and increases from mid-central to central collisions. A similar enhancement is also observed in the measurements of the proton/π [63] and Λ/K_S^0 [64] ratios. The nuclear modification factor (R_{AA}) of prompt Λ_c is presented in Fig. 1.15 (right). One can see that the R_{AA} is consistent with unity within uncertainties for $p_{\mathrm{T}} < 6$ GeV/c, while a suppression is observed at high p_{T} due to the energy loss of charm quarks in the

QGP medium. These measurements provide a further constrain on the theoretical calculations which include hadronization via both coalescence and fragmentation mechanisms [65, 66].

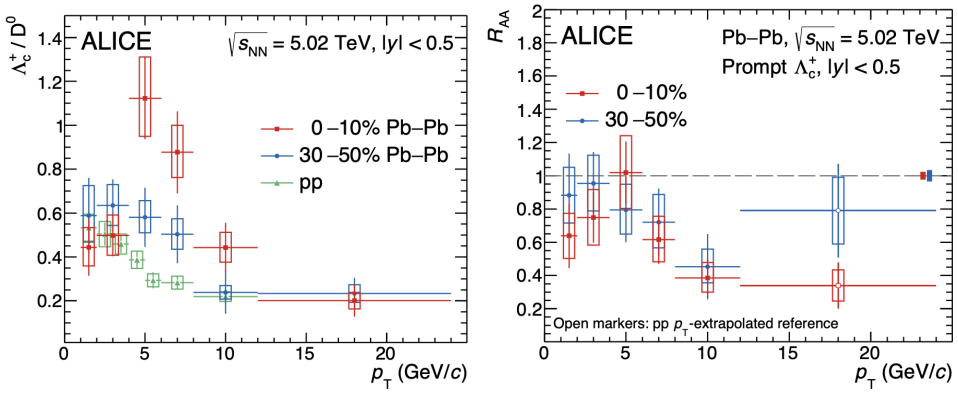

Figure 1.15: Left: Λ_c^+/D^0 ratio in 0–10% and 30–50% Pb–Pb collisions at $\sqrt{s_{NN}}$ = 5.02 TeV in comparison with the results obtained in pp collisions at the same collision energy. Right: the nuclear modification factor of prompt Λ_c as a function of p_T in 0–10% and 30–50% Pb–Pb collisions at $\sqrt{s_{NN}}$ = 5.02 TeV. Figures are taken from [67].

1.3.3 Azimuthal Anisotropy

In non-central collisions, the overlapping region of two colliding nuclei has an almond shape. It creates an initial spatial anisotropy, which results in different expansion rates depending on the azimuthal angle. Such an azimuthal anisotropy is converted into the final momentum anisotropy via multiple interactions with the constituents of the QGP, as shown in Fig. 1.16. Therefore, final-state particles are emitted in preferred direction, this is the anisotropic flow. It is one of the most prominent soft probes of the QGP transport properties and is extensively studied with hard probes.

In reality, the geometry of the overlapping region is not a perfect ellipse, since the colliding nuclei are composed of nucleons whose positions may fluctuate in each collision, which results in the initial geometry fluctuations, as shown in Fig. 1.17. This means that the shape of the overlapping region can be expressed as a superposition of various geometries, which impacts the observed anisotropic flow. In order to unravel the different effects on the final anisotropies and quantify the magnitude of each of them, the measured azimuthal distribution of final-state particles is decomposed into a Fourier series with respect to the common symmetry plane, as

$$\frac{dN}{d\varphi} \propto 1 + 2\sum_{n=1}^{\infty} v_n \cos[n(\varphi - \Psi_n)], \tag{1.26}$$

where φ is particle azimuthal angle and Ψ_n is the azimuthal angle of the symmetry plane for the n^{th} harmonic. The Fourier coefficients v_n characterize the anisotropy

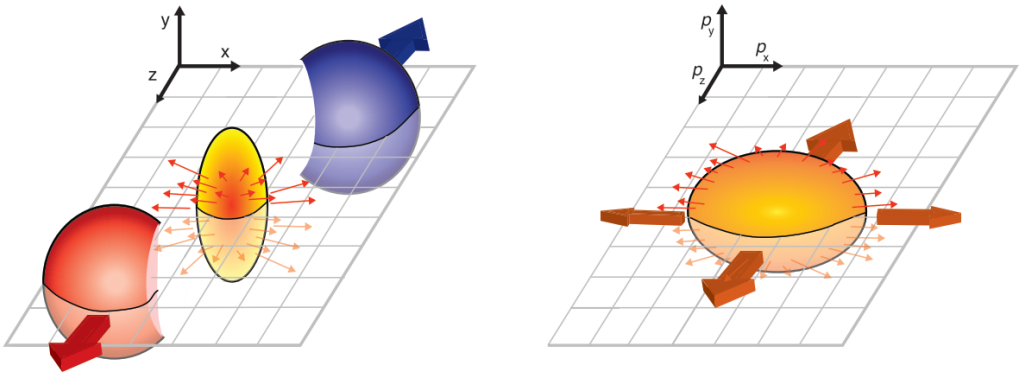

Figure 1.16: Schematic illustration of the process which propagates the initial spatial anisotropy (left) to the final momentum space (right).

of produced particles. They are defined as:

$$v_n = < \cos[\mathrm{n}(\varphi - \Psi_n)] >, \tag{1.27}$$

where the angle brackets represent an average of all particles. Each order of the flow coefficients v_n depends on their different connection to the initial anisotropies.

The second order coefficient v_2, referring as the elliptic flow, originates from the elliptic shape of the interaction region, which is characterized by the eccentricity. It is defined as:

$$\varepsilon = \frac{\langle y^2 - x^2 \rangle}{\langle y^2 + x^2 \rangle}, \tag{1.28}$$

where the brackets represent an average over the transverse plane with the number density of participants used as a weight, x and y are the directions transverse to the beam direction. This initial spatial deformation is converted into the anisotropies in momentum space according to the hydrodynamics [68]. However the efficiency of such conversion is reduced by the viscosity of the fluid, which means that the viscous suppression of the generated final-state momentum anisotropy is related to the specific shear viscosity η/s [69, 70]. Therefore the most common way to study transport properties of the QGP is to investigate the effects of η/s on the elliptic flow in a viscous hydrodynamic model.

In central collisions, the higher order flow coefficients, for instance the triangular flow v_3 and rectangular flow v_4, might become more significant since the overlap geometry is completely driven by the event-by-event fluctuations. Figure 1.17 shows the initial distribution of participating nucleons and the resulting elliptic (left) and triangular (right) shape of the overlapping region in semi-central heavy-ion collisions. In addition, the first-order coefficient v_1, which is called directed flow, arises from the longitudinally tilted particle production due to the asymmetries in the number of forward and backward moving participant nucleons, and can not be neglected in non-central collisions. An overview of various frequently-used methods used to extract the v_n coefficients is presented in Chap. 2.

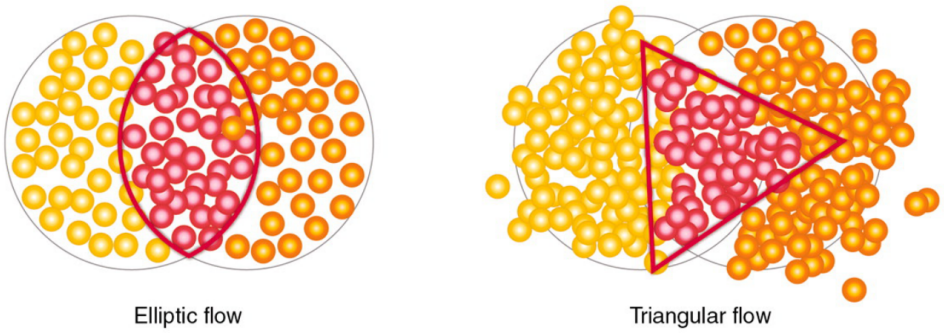

Figure 1.17: Illustration of the initial distribution of participating nucleons (red) and the resulting elliptic (left) and triangular (right) shape of the overlapping region in semi-central heavy-ion collisions. Figure taken from [71].

Many state-of-the-art measurements of anisotropic flow in Pb–Pb collisions with the ALICE experiment were performed in the recent years, which provide us a full picture of collective phenomena. Starting from the correlations between two charged particles, the measurement of di-hadron correlation distributions as a function of the relative difference in azimuth $\Delta\varphi$ and pseudorapidity $\Delta\eta$ shows a clear appearance of azimuthal anisotropy in heavy-ion collisions, as shown in Fig. 1.18. In the left panel of Fig. 1.18, a large peak is observed in the "near-side" region (i.e. $\Delta\varphi \sim 0$), which originates mainly from the contribution of jet-like correlations or high-p_{T} resonance decays. In the away-side region ($\Delta\varphi \sim \pi$), the so-called **ridge** structure spans over the whole rapidity range [72], which comes from low-p_{T} resonance decays, the correlations of di-jets and the collective expansion of the system. The last contribution leading to the anisotropic flow, also exists in the near-side region [73], and can be extracted from a Fourier fit of the $\Delta\varphi$ projection of the di-hadron correlation, as shown in Fig. 1.18 (right). The detailed description of extracting flow coefficients with this method will be discussed in Chapter 2.

The flow coefficients can be also extracted from the measurement of multi-particle cumulants, which is also described in Chap. 2. Figure 1.19 shows the p_{T}-integrated v_{n} of inclusive charged hadrons as a function of centrality in Pb–Pb collisions at $\sqrt{s_{\mathrm{NN}}} = 5.02$ and 2.76 TeV measured by ALICE. One can observe that $v_2\{2, |\Delta\eta| > 1\}$ increases from central to semi-central collisions, then decreases in peripheral collisions, which is compatible with hydrodynamic predictions [74], as shown in Fig. 1.19 (a). In addition, the ratios of the anisotropic flow measured at 5.02 TeV to 2.76 TeV are well described by a different hydrodynamic calculation [75], which employs both a constant $\eta/s = 0.20$ and a temperature dependent η/s, as shown in Fig. 1.19 (b) and Fig. 1.19 (c).

In order to provide tighter constraints on the theoretical models, more detailed measurements of the anisotropic flow are needed. Figure 1.20 shows the anisotropic flow coefficients v_{n} as a function of p_{T} for inclusive charged particles for different centrality classes in Pb–Pb collisions at $\sqrt{s_{\mathrm{NN}}} = 5.02$ TeV, measured with cumulants

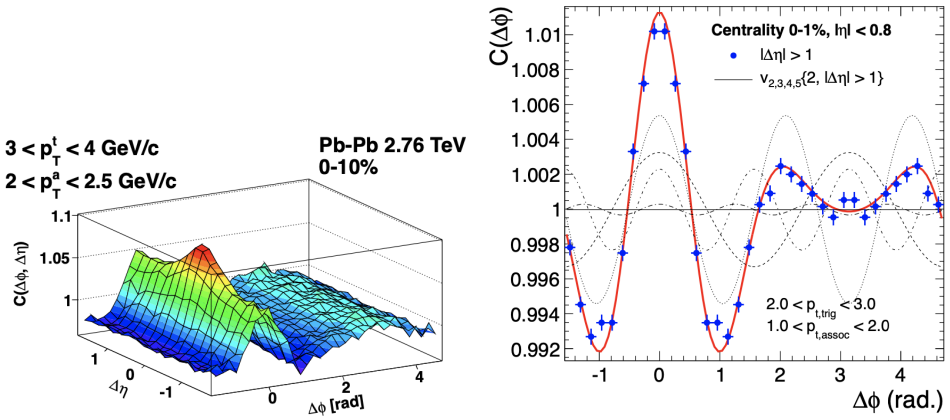

Figure 1.18: Left: di-hadron correlations measured in the 0-10% central Pb–Pb collisions at $\sqrt{s_{\rm NN}}$ = 2.76 TeV. Figure taken from [73]. Right: projection of the di-hadron correlation onto the $\Delta\varphi$ plane in 0–1% central Pb–Pb collisions at $\sqrt{s_{\rm NN}}$ = 2.76 TeV. The condition $|\Delta\eta| < 1$ is applied to remove the near-side jet. Figure taken from [72].

and scalar product methods. The description of these methods will be shown in Chapter 2. The comparison of $p_{\rm T}$-differential flow measurements with different hydrodynamic models in the low- and high-$p_{\rm T}$ regions are also shown. At low $p_{\rm T}$ ($p_{\rm T} < 2$ GeV/c), the anisotropic flow is mostly determined by the collective expansion of the system, which is well described by hydrodynamic models with various initial conditions (for more details, see [75]). At high $p_{\rm T}$ ($p_{\rm T} > 10$ GeV/c), the azimuthal anisotropies are expected to be sensitive to the path-length dependent parton energy-loss mechanisms.

The measurement of the anisotropic flow can be further extended to the identified particles, in both light-flavour and heavy-flavour sectors. The measurement of the $p_{\rm T}$-differential v_2 of identified $\pi^{\pm}$, $\rm K^{\pm}$, $\rm K^0_S$, $p(\bar{p})$, $\Lambda(\bar{\Lambda})$ and ϕ meson using the scalar product method, is shown in Fig. 1.21. For $p_{\rm T} < 2$–3 GeV/c, a clear mass ordering of the v_2 of the different particle species is observed. The lighter particles have a larger v_2 than heavier particles at the same $p_{\rm T}$. This behaviour is expected since the strong radial flow imposes an equal, isotropic velocity boost to all particles, and the particles with larger masses are pushed to higher $p_{\rm T}$. For $3 < p_{\rm T} < 10$ GeV/c, the v_2 of the different hadron species are grouped according to their number of constituent quarks instead of their masses, which supports the hypothesis of particle production via quark coalescence [78]. The measurement of the azimuthal anisotropy of heavy-flavour hadrons was also performed with ALICE, as shown in Fig. 1.22. As an example, the average v_2 and v_3 coefficients of prompt $\rm D^0$, $\rm D^*$ and $\rm D^{*+}$ mesons as a function of $p_{\rm T}$ in the 0–10% most central collisions and 30–50% semi-central collisions is measured with the scalar product method. The D-meson elliptic flow increases significantly from central to semi-central collisions, as expected from the increasing eccentricity of the interaction region. In addition, the $p_{\rm T}$ dependence of

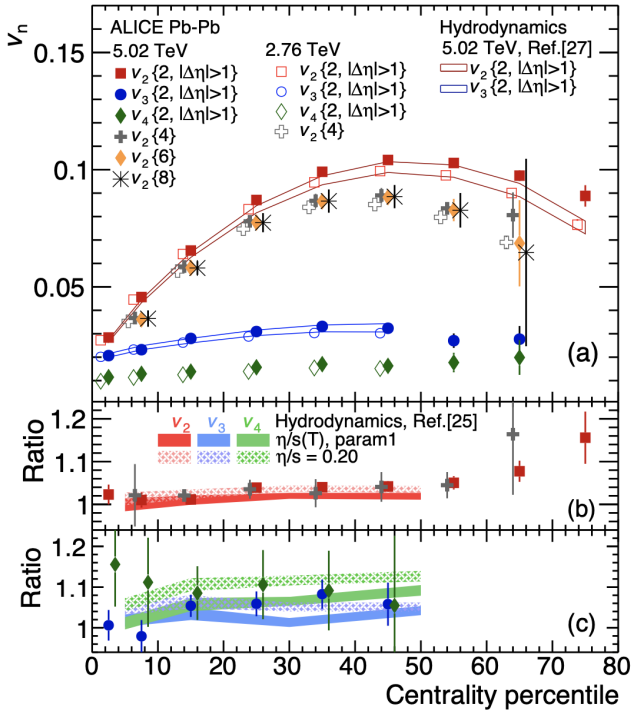

Figure 1.19: Anisotropic flow v_n integrated over the p_T range $0.2 < p_T < 5.0$ GeV/c, as a function of the event centrality in Pb–Pb collisions at $\sqrt{s_{NN}} = 5.02$ and 2.76 TeV, from the two-particle (with $|\Delta\eta| > 1$) and multi-particle cumulant methods. A comparison to hydrodynamic calculations with different options is also performed. Figure taken from [76].

v_n is similar to those of light flavour hadrons. For $p_T < 4$–5 GeV/c, the measured D-meson v_2 (v_3) is lower than that of pions and protons due to the mass ordering effect. For $5 < p_T < 8$ GeV/c, the D-meson v_n coefficients are similar to those of charged pions and lower than those of protons because of the particle production via quark coalescence. The measured v_n coefficients for all the hadron species are compatible within uncertainties for $p_T > 8$ GeV/c, which is explained by the similar path-length dependence of the in-medium parton energy loss for high-p_T charm quarks and gluons.

1.4 Small Collision Systems

The proton-proton collisions or proton-lead collisions, are commonly referred to as collisions of small systems. In the field of heavy-ion physics, the measurements in pp collisions can be provided as the baseline, because no QGP is expected to be formed in pp collisions[3] so that the produced partons evolve without suffering

[3]In recent years, some observables for possible QGP signatures are also observed in high-multiplicity collisions [81]. However, compared to heavy-ion collisions, the hot nuclear effects

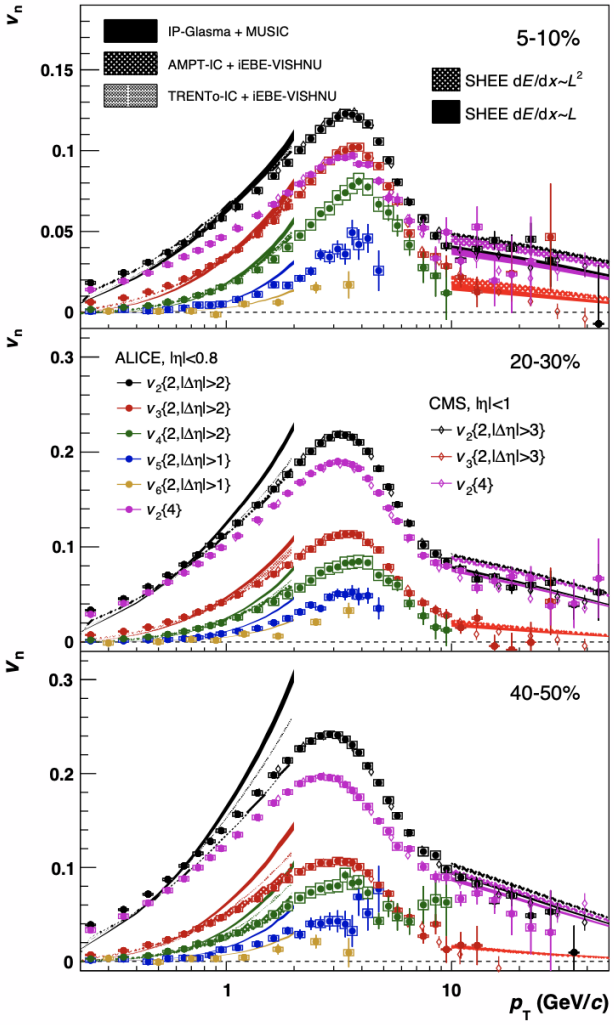

Figure 1.20: The p_{T}-differential v_{n} of inclusive charged particles in the 5–10% (top), 20–30% (middle) and 40–50% (bottom) centrality classes in Pb–Pb collisions at $\sqrt{s_{\mathrm{NN}}} = 5.02$ TeV, measured with cumulant and scalar product methods. Several model calculations and measurements from CMS [77] are shown for comparison. Figure taken from [75].

from the strongly-interacting medium effects. The measurements performed in p–Pb collisions can give the insights into the study of cold nuclear matter (CNM) effects (see Sec. 1.4.1), which originate from the presence of the nucleus before the collisions. CNM effects are present in both p–Pb and Pb–Pb collisions, while hot medium (i.e. QGP) effects also exit in the latter case which are difficult to be distinguished from CNM effect experimentally.

On the other hand, the study of collectivity in small collision systems is a chal-

in pp collisions are very small.

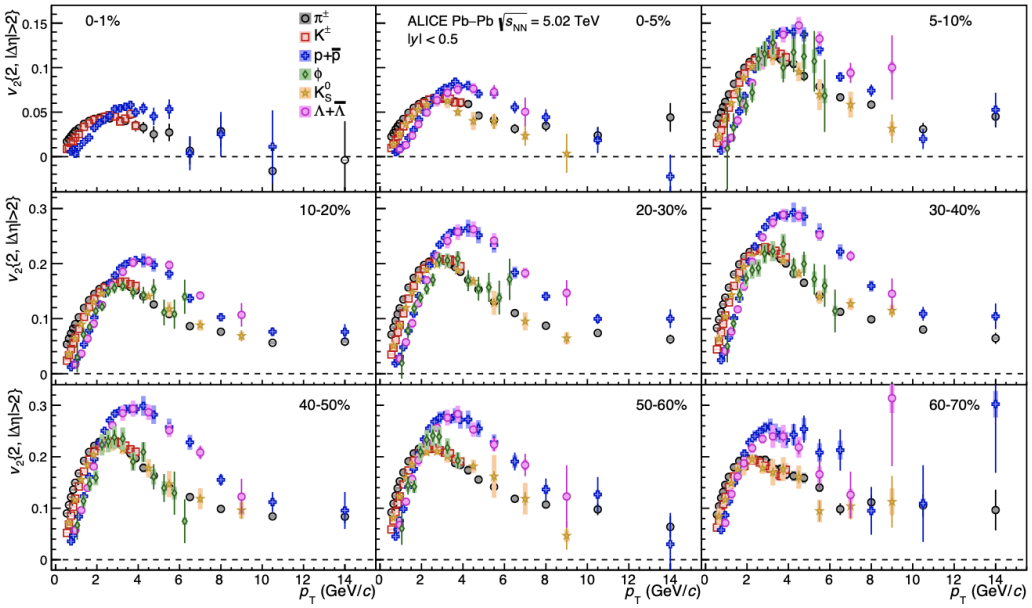

Figure 1.21: The p_{T}-differential v_2 of $\pi^{\pm}$, $\mathrm{K}^{\pm}$, $\mathrm{K}^0_{\mathrm{S}}$, $\mathrm{p}(\bar{\mathrm{p}})$, $\Lambda(\bar{\Lambda})$, and the ϕ-meson for various centrality classes. Statistical and systematic uncertainties are shown as bars and boxes, respectively. The figure is taken from [79].

lenge in recent years. Many measurements in high-multiplicity pp and p–Pb collisions clearly show "collective" phenomena, which are similar to that observed in heavy-ion collisions. It triggered a lot of discussions about the origin of these effects, and how they will affect our previous understanding about large collision systems.

1.4.1 Cold Nuclear Matter Effects

The first experimental evidence for cold nuclear effects was discussed in 1982 [82]. It is found that, the parton distribution functions (PDFs) of isolated nucleons are different from that of nucleons in a nuclear environment, known as nuclear PDFs (nPDFs). The PDFs characterize the density of partons carrying a given momentum fraction x (so-called Bjorken-x) of the total momentum carried by the nucleon to which it belongs. Therefore, the ratio between nPDFs $f_i^{\mathrm{A}}(x, Q^2)$ and PDFs $f_i^{\mathrm{N}}(x, Q^2)$ as a function of x is obtained as:

$$R_i^{\mathrm{A}}(x, Q^2) = \frac{f_i^{\mathrm{A}}(x, Q^2)}{f_i^{\mathrm{N}}(x, Q^2)}, \tag{1.29}$$

where i is the index of partons, such as gluons, valence quarks and sea quarks. The Q^2 scale is the four-momentum squared of the system, which is set by the renormalization scheme used in different models [83]. Figure 1.23 shows a calculation of $R_i^{\mathrm{A}}(x, Q^2)$ as a function of x, under the nPDF parametrization known as Eskola-Paakkinen-Paukkunen-Salgado-2016 (EPPS16) [84]. According to this shape, dif-

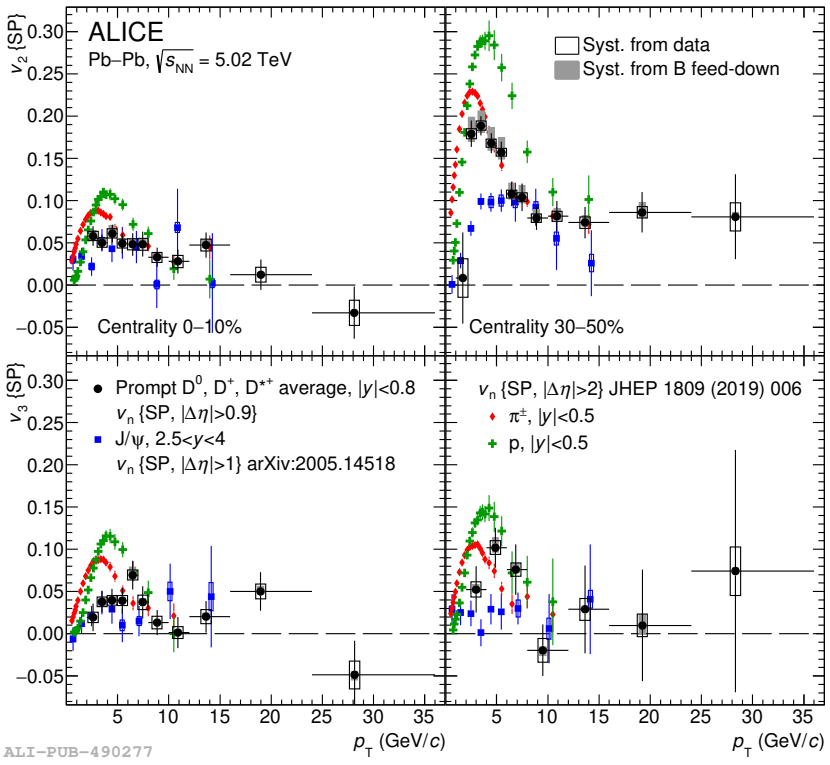

Figure 1.22: Average v_2 (top panels) and v_3 (bottom panels) coefficients of prompt D^0, D^* and D^{*+} mesons as a function of p_T in Pb–Pb collisions at $\sqrt{s_{NN}} = 5.02$ TeV for 0–10% (left panels) and 30–50% (right panels) centrality classes. The comparison with the v_2 and v_3 of $\pi^{\pm}$, $p + \bar{p}$ and inclusive J/ψ is also shown. Figure taken from [80].

ferent cold nuclear effects appear in different Bjorken-x regions. At low x ($x < 0.1$), the number of gluons increases rapidly. It results in more self interactions of gluons and then they can scatter off each other producing destructive interference. Therefore, the incoming nucleon will suffer a decreased flux of gluons relative to a proton. This phenomenon is called "shadowing", as shown in Fig. 1.23. As the x increases, the shadowing diminishes and the region $0.1 < x < 0.3$ is called "anti-shadowing". In the region $0.3 < x < 0.7$, the effect is known as the EMC-effect, which was first observed by the European Muon Collaboration (EMC) [86]. In this case the ratio $R_i^A(x, Q^2)$ is smaller than unity with a minimum at $x \sim 0.7$. In the region $0.7 < x < 1$, the ratio $R_i^A(x, Q^2)$ increases with increasing x, which is explained by the Fermi motion [87]. The Fermi motion is the quantum motion of bounded nucleons inside a nucleus, which can modify the structure of nucleons in a nuclear environment. The Fermi motion can also be explained by a kinematic effect since the free-nucleon PDF vanishes when $x \to 1$. The nuclear-modified parton distribution takes into account the initial longitudinal distribution of partons inside the nuclei within the framework of perturbative QCD collinear factorization. However,

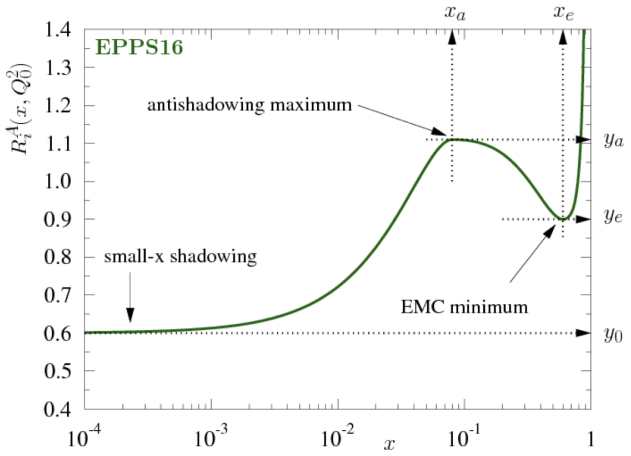

Figure 1.23: EPPS16 calculation of $R_i^{\mathrm{A}}(x, Q^2)$ as a function of x. Figure taken from [85].

in the kinematic region where QCD is non-perturbative the factorization is expected to break down, the gluon density is high enough, which results in a saturation in the gluon phase-space. In such conditions, the partons in the nuclear wave function at small x would act coherently and form a Color Glass Condensate (CGC) [88]. The initial conditions including nPDF functions or CGC models are both used to explain the measurements in small collision systems.

Additionally, cold nuclear effects not only modify the PDFs of free nucleons but also include the momentum broadening of partons, which is called $\boldsymbol{k_{\mathrm{T}}}$ **broadening** or **Cronin enhancement**. The main source for this effect is believed to be the partonic multiple re-scatterings in the initial state, which was first observed in 1970 [25] and it consists of an enhancement of hadron production in pA relative to pp collisions, when scaled by the number of binary nucleon-nucleon collisions.

Various measurements performed in p–Pb collisions by ALICE allow us to extract the information about cold matter nuclear effects. One of the straightforward observables is the charged-particle density in small collisions systems. Figure 1.4.1 shows the pseudorapidity density of charged particles measured in NSD (non single diffractive) p–Pb collisions at $\sqrt{s_{\mathrm{NN}}} = 5.02$ TeV compared to theoretical predictions. We clearly observe the forward-backward asymmetry between the proton and lead hemispheres. The measured charged-particle density is well described by the models which combine perturbative QCD processes with soft interactions, and include nuclear modification of the initial parton distributions. In addition, the saturation models which employ coherence effects can also give a fair description of the results (more details about these models are given in [89]).

Following the definition of the nuclear modification factor R_{AA} in Eq. 1.13, a similar observable R_{pPb} can be also built in p–Pb collisions:

$$R_{\mathrm{pPb}} = \frac{\mathrm{d}^2 N_{\mathrm{pPb}}/\mathrm{d}y\mathrm{d}p_{\mathrm{T}}}{\langle T_{\mathrm{pPb}}\rangle \mathrm{d}\sigma_{\mathrm{pp}}^{INEL}/\mathrm{d}y\mathrm{d}p_{\mathrm{T}}}, \tag{1.30}$$

where $N_{\rm pPb}$ and $\sigma_{\rm pp}^{\rm INEL}$ are the particle yield in p–Pb collisions and inelastic cross-section in pp collisions, $\langle T_{\rm pPb}\rangle$ is the nuclear overlap function defined as $\langle T_{\rm pPb}\rangle = \langle N_{\rm coll}\rangle/\sigma_{\rm pp}^{\rm INEL}$, which is determined from the Glauber model. Figure 1.4.1 shows the nuclear modification factor measured in NSD p–Pb collisions for $|\eta_{\rm cms}| < 0.3$, and compared to theoretical predictions. The $R_{\rm pPb}$ factor exhibits a maximum in the intermediate $p_{\rm T}$ range ($2 < p_{\rm T} < 6$ GeV/c) which is driven by the Cronin enhancement. The model calculations based on the Colour Glass Condensate (CGC) model are consistent with the measurement within uncertainties. In the high $p_{\rm T}$ region ($p_{\rm T} > 8$ GeV/c), the $R_{\rm pPb}$ factor is consistent with unity and is described by NLO calculation with EPS09s PDF's and DSS fragmentation functions [90], while the Leading order (LO) pQCD calculations incorporating cold nuclear matter effects underestimate the data. The HIJING 2.1 model (with shadowing) describes the trend observed in the data. On the other hand, the unity of $R_{\rm pPb}$ demonstrates that the strong suppression of high-$p_{\rm T}$ hadrons observed in central Pb–Pb collisions, as shown in Fig. 1.9, is due to jet-quenching effect in the hot and dense QCD matter rather than to initial-state effects.

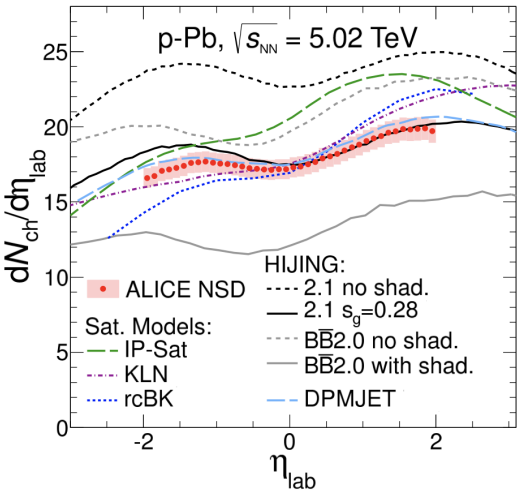

Figure 1.24: Pseudorapidity density of charged particles measured in NSD p–Pb collisions at $\sqrt{s_{\rm NN}} = 5.02$ TeV compared to theoretical predictions. Figure taken from [89].

1.4.2 Collective Flow

As mentioned in Sec. 1.3.3, the features of the observed anisotropic flow in Pb–Pb collisions are understood as a consequence of an initial spatial anisotropy being transferred to a momentum anisotropy via a hydrodynamic expansion of the hot medium. However, the small collision systems are thought to be too small to create the energy density required to form the QGP [31]. In this case, similar "flow-like" observations in small collision systems do not necessarily have the same origin as that in heavy-ion collisions. The "collective" behaviour" may come from the effects

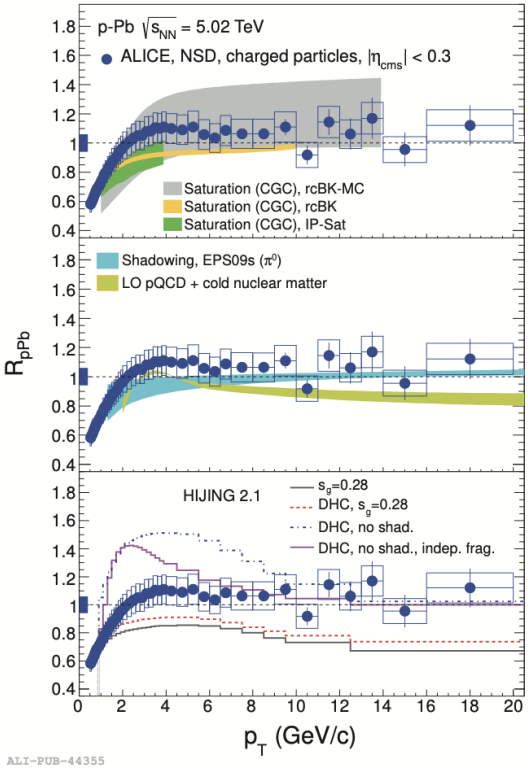

Figure 1.25: Nuclear modification factor measured in NSD p–Pb collisions for $|\eta_{\rm cms}| < 0.3$ at $\sqrt{s_{\rm NN}} = 5.02$ TeV, compared to model calculations. Figure taken from [91].

of the initial stage or interactions in the hadronic stage, or even the effects from new "QGP-like" medium which were never seen before in small collision systems. In order to understand these confusing but fascinating problems, more and more efforts are put into the measurements of collective effects in small collision systems nowadays.

Based on the experience that we have gained in heavy-ion collisions, the measurement of di-hadron correlation distributions can provide us the straightway evidence whether the global collective evolution of all particles exists. Figure 1.26 (left) shows the associated yield per trigger particle as a function of $\Delta\varphi$ and $\Delta\eta$ for di-hadron correlations in high-multiplicity p–Pb collisions at $\sqrt{s_{\rm NN}} = 5.02$ TeV, where the corresponding correlation from the 60-100% event class is subtracted in order to remove the contributions of the correlation due to jets. A double-ridge structure is observed with a near-side ridge located at $\Delta\varphi = 0$ and an away-side ridge centred at $\Delta\varphi = \pi$. In pp collisions, a ridge structure is also clearly visible at $\Delta\varphi = 0$, extending over a range of at least 4 units in $|\Delta\eta|$, as shown in Fig. 1.26 (right). No such long-range correlations are predicted by the PYTHIA event generator [92]. A similar feature also appears in Pb–Pb events as shown in Fig. 1.18, where it is understood to be due to a collective expansion of the hot medium. The origin of these ridge structures

in small collision systems is still puzzling: whether they originate from initial-state effects (e.g. CGC) or from final-state effects is still under debate.

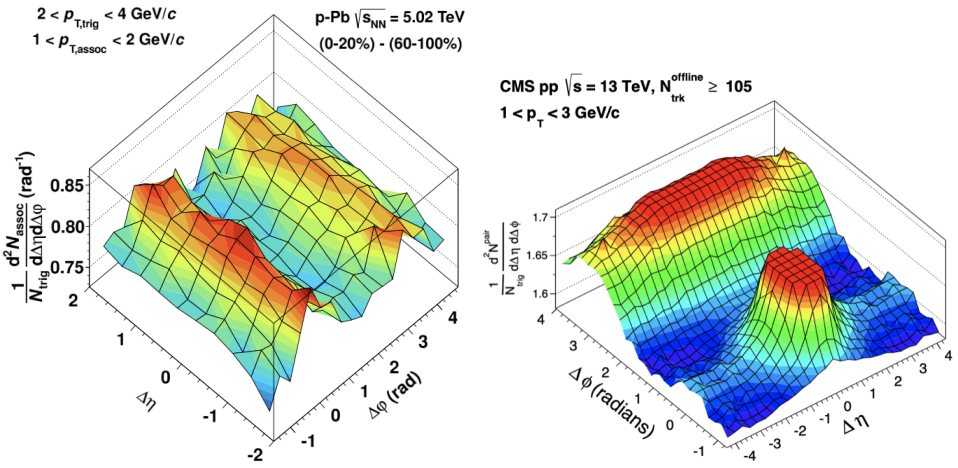

Figure 1.26: Left: associated yield per trigger particle in $\Delta\varphi$ and $\Delta\eta$ for hadron-hadron correlations in p–Pb collisions at $\sqrt{s_{\rm NN}} = 5.02$ TeV for the 0–20% multiplicity class, after subtraction of the associated yield obtained in the 60-100% event class, measured by ALICE. Right: the associated yield per trigger particle in $\Delta\varphi$ and $\Delta\eta$ for hadron-hadron correlations in pp collisions at $\sqrt{s} = 13$ TeV for a high-multiplicity sample ($N_{\rm trk}^{\rm offline} \geq 105$), measured by CMS. Figures are taken from [92, 93].

For a better understanding of the phenomenon, the double ridge structures are extracted from the correlations of identified particles. The $p_{\rm T}$-differential second-order flow coefficient v_2 of identified particles (e.g. $\rm K^{\pm}$, $\pi^{\pm}$, protons) and hadrons can be also obtained, as shown in Fig. 1.27 (left). One can clearly observe that the v_2 of protons is lower than that of $\pi^{\pm}$ and $\rm K^{\pm}$ for $0.5 < p_{\rm T} < 1$ GeV/c. Such mass ordering behaviour is also observed in Pb–Pb collisions, as shown in Fig. 1.21, which can be described by hydrodynamic model calculations [94]. The measurement of the azimuthal anisotropy of heavy-flavour and strange hadrons was also performed, as shown in Fig. 1.27 (right). A clear mass ordering in the v_2 is observed in the low-$p_{\rm T}$ region ($p_{\rm T} < 2.5$ GeV/c), where the heavier particles species have a smaller v_2 signal at a given $p_{\rm T}$ value. For $p_{\rm T} > 2.5$ GeV/c, the v_2 values of Λ, Ξ^- and Ω^- are similar to each other and all are larger than those of $\rm D_0$ and $\rm K^0_S$ mesons. Similar trends are also observed in Pb–Pb collisions [95].

In order to build a clearer connection between the measurements in small collision systems and heavy-ion collisions, the multiplicity dependence of the v_2 coefficient was studied by ALICE [97]. Figure 1.28 shows the v_2 of charged particles measured using two-particle cumulants as a function of the number of produced charged particles $N_{\rm ch}$ at midrapidity ($|\eta| < 0.8$) in pp, p–Pb, Xe–Xe and Pb–Pb collisions. One can observe that in small collision systems, the v_2 coefficient exhibits a weak dependence on multiplicity, and both the trend and magnitude of v_2 can not be described by the PYTHIA8 calculation which does not include any final-state collective effects. At low multiplicities, the values of v_2 from pp and p–Pb collisions

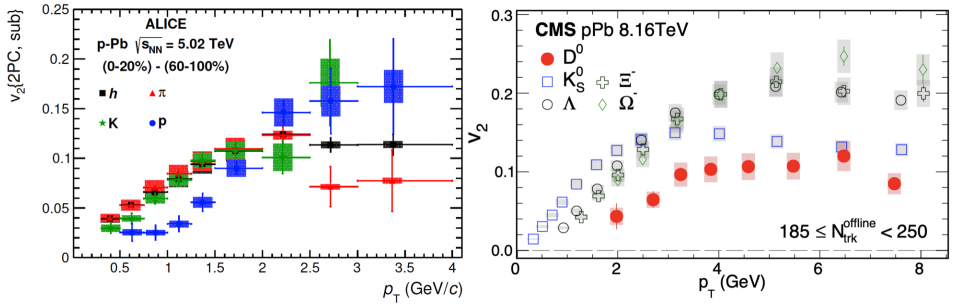

Figure 1.27: Left: the p_{T}-differential v_2 of hadrons, pions, kaons and protons obtained from the two-particle correlations in p–Pb collisions at $\sqrt{s_{\mathrm{NN}}} = 5.02$ TeV for 0–20% multiplicity class, after subtraction of the correlations from the 60–100% multiplicity class, measured by ALICE. Right: the p_{T}-differential v_2 of D^0, $\mathrm{K}^0_{\mathrm{S}}$, Λ, Ξ^- and Ω^- particles in high-multiplicity p–Pb collisions at $\sqrt{s_{\mathrm{NN}}} = 8.16$ TeV, measured by CMS. Figures are taken from [93, 96].

are compatible with those in heavy-ion collisions. It results in a surprising smooth transition from small to large collision systems, which further supports a similar collective behaviour observed in these systems.

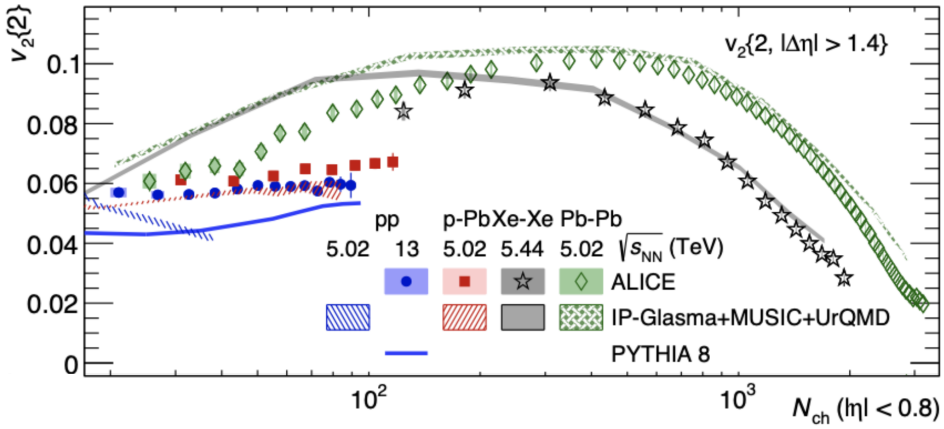

Figure 1.28: Multiplicity dependence of the v_2 using two-particle cumulants in pp, p–Pb, Pb–Pb, and Xe–Xe collisions, compared with various theoretical calculations. Figure taken from [97].

As mentioned in Sec. 1.3.3, the anisotropic flow of high-p_{T} particles in Pb–Pb collisions originates from the path-length dependent energy loss effect in a hot QGP medium, which is also called jet-quenching effect. Such an effect is also observed in the measurement of the R_{AA} of high-p_{T} hadrons in Pb–Pb collisions, as shown in Fig. 1.9. On the other hand, a R_{pPb} comparable with unity is observed in p–Pb collisions at high-p_{T}, as shown in Fig. 1.4.1, which indicates the absence of energy loss in small collision systems. Therefore it is quite necessary to characterize the collective behaviour of high-p_{T} particles in small collision systems. Figure 1.29

(left) shows the v_2 of charged particles in Minimum-Bias Triggered (MBT) events and events with a jet $p_{\mathrm{T}}^{\mathrm{jet}} > 75$ GeV and 100 GeV in 0–5% central p–Pb collisions at $\sqrt{s_{\mathrm{NN}}} = 8.16$ TeV. A significant positive v_2 is observed at high p_{T} ($p_{\mathrm{T}} > 9$ GeV/c), for both MBT and jet events. The p–Pb v_2 values scaled by a empirical factor 1.5, which is the result of slightly different initial spatial deformations and multiplicities between central p–Pb and semi-central Pb–Pb collisions, is also compared with the v_2 measured in 20–30% central Pb–Pb collisions at $\sqrt{s_{\mathrm{NN}}} = 5.02$ TeV, as shown in Figure 1.29 (right). After scaling, the v_2 exhibits similar trends in p–Pb and Pb–Pb collisions, especially at high-p_{T} region where the jet-quenching effect dominates in Pb–Pb collisions. However, the results can not be explained in the theoretical context of jet quenching calculations, since models cannot simultaneously describe R_{pPb} and v_2 of high-p_{T} hadrons in p–Pb collisions. More sophisticated experimental measurements and theoretical calculations are needed in the future.

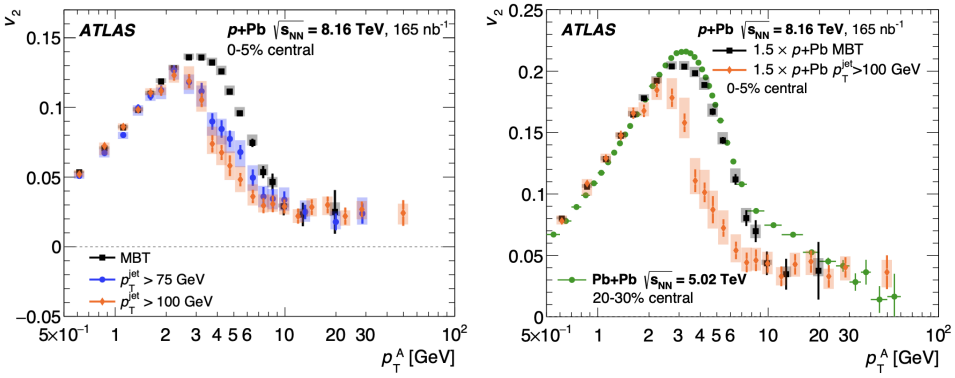

Figure 1.29: Left: distribution of v_2 measured in MBT and jet events as a function of p_{T} in 0–5% central p–Pb collisions at $\sqrt{s_{\mathrm{NN}}} = 8.16$ TeV. Right: scaled p–Pb v_2 values as a function of the p_{T} compared with the v_2 in the 20–30% central Pb–Pb collisions at $\sqrt{s_{\mathrm{NN}}} = 5.02$ TeV. Figure taken from [98].

In summary, recent flow measurements in small collision systems indeed show the existence of the collective behaviour, which is similar to that in heavy-ion collisions at some level. However, its origin is still not clear and the current theoretical calculations usually can not describe all observables simultaneously. It represents one of the biggest open questions in the field of heavy-ion physics [99], and it is also one of the important motivations of this thesis.

CHAPTER 2

Anisotropic Flow

There are many experimental methods to extract the anisotropic flow coefficients v_n [100], each of them has its own advantages and disadvantages. In this chapter, we present several flow analysis methods, which are widely used in both large and small collisions systems. The event plane method and the scalar product method are introduced in Sec. 2.1 and Sec. 2.2, respectively. The two- and multi-particle cumulants methods, including the Q-cumulants and Generic Framework [100], are presented in Sec. 2.3. Finally, we introduce the application of two-particle angular correlations in flow analyses in Sec. 2.4.

2.1 Event Plane Method

The event plane method is the most standard method used in the anisotropic flow analyses. As shown in Eq. 1.26 and Eq. 1.27 (Chap. 1), the calculation of v_n coefficients depends on the determination of the symmetry plane Ψ_n. However, the symmetry plane can not be reliably obtained in each event since it randomly changes event-by-event. The so-called "event plane" is introduced as an approximation of the symmetry plane in the event plane method, which is labeled as $\Psi_{\mathrm{n}}^{\mathrm{EP}}$.

Similarly to Eq. 1.27, with the event plane method, the observed anisotropic flow v_n coefficients for a given harmonic n can be expressed as:

$$v_n^{\mathrm{obs}} = \langle \cos[\mathrm{n}(\varphi - \Psi_n^{\mathrm{EP}})] \rangle. \tag{2.1}$$

In order to calculate the event plane Ψ_n^{EP}, a two-dimensional vector $\boldsymbol{Q}_n$, named the event flow vector, is introduced [101]:

$$\begin{aligned} Q_{n,x} &= \boldsymbol{Q}_n \cos(n\Psi_n^{\mathrm{EP}}) = \sum_j^M w_j \cos(n\varphi_j), \\ Q_{n,y} &= \boldsymbol{Q}_n \sin(n\Psi_n^{\mathrm{EP}}) = \sum_j^M w_j \sin(n\varphi_j), \end{aligned} \tag{2.2}$$

where M is the event multiplicity, the sum goes over all particles j. The φ_j and w_j quantities are the azimuthal angle and weight for particle j. The weights w_j which can be unity [102] or are dependent on φ_j or p_{T}, can be used to correct for non-uniform acceptance and inefficiencies of the detectors, and to optimize the resolution on Ψ_n^{EP}. Furthermore, the complex form of the flow vector Q_n can be defined as:

$$\boldsymbol{Q}_n = Q_{n,x} + iQ_{n,y} = |Q_n| e^{in\Psi_n} = \sum_j^M w_j e^{in\varphi_j}. \tag{2.3}$$

The event plane Ψ_n^{EP} is estimated by the orientation of the Q_n-vector [101]:

$$\Psi_n \simeq \Psi_n^{\mathrm{EP}} = \frac{1}{n}\arctan\frac{Q_{n,y}}{Q_{n,x}} = \frac{1}{n}\arctan\frac{\sum_j w_j \sin(n\varphi_j)}{\sum_j w_j \cos(n\varphi_j)}. \tag{2.4}$$

Considering that the event plane is determined using a finite number of produced particles, the measured event plane angle Ψ_n^{EP} fluctuates about the "real" symmetry plane Ψ_n. As a result, the azimuthal anisotropy of particles with respect to the event plane is smeared compared to its true value. The true flow coefficient v_n^{EP} obtained in the event plane method is evaluated by dividing the observed v_n^{obs} obtained in Eq. 2.1 by a resolution correction factor R_n, as:

$$v_n^{\mathrm{EP}} = \frac{v_n^{\mathrm{obs}}}{R_n} = \frac{v_n^{\mathrm{obs}}}{\langle \cos[n(\Psi_n^{\mathrm{EP}} - \Psi_n)]\rangle}, \tag{2.5}$$

where the average is performed over all events for the denominator. The R_n parameter, the so-called "event-plane resolution factor", is parametrised using modified Bessel function [101]. In practice, it is usually extracted experimentally from the two-subevent method [103, 104]. The measured particles used to calculate the event plane are divided into two subevents (labeled as A and B) covering equal pseudorapidity ranges [103]. The relation between the two event-plane angles $\Psi_n^{\mathrm{EP,A}}$, $\Psi_n^{\mathrm{EP,B}}$ and the symmetry plane can be expressed as:

$$\langle \cos[n(\Psi_n^{\mathrm{EP,A}} - \Psi_n^{\mathrm{EP,B}})]\rangle = \langle \cos[n(\Psi_n^{\mathrm{EP,A}} - \Psi_n)]\rangle \langle \cos[n(\Psi_n^{\mathrm{EP,B}} - \Psi_n)]\rangle, \tag{2.6}$$

where $\Psi_n^{\mathrm{EP,A}}$ and $\Psi_n^{\mathrm{EP,B}}$ are estimated in sub-event A and B, respectively. If the two sub-events have same particle multiplicity[1], such that the two subevents nominally have the same resolution, the event-plane resolution factor R_n is:

$$R_n = \sqrt{\langle \cos[n(\Psi_n^{\mathrm{EP,A}} - \Psi_n^{\mathrm{EP,B}})]\rangle}. \tag{2.7}$$

Alternatively, the three sub-event method can be used to get the resolution [101, 103, 104]. In this case, the R_n value for a given subevent A is obtained from its correlations with two subevents B and C covering different rapidity regions:

$$R_n = \sqrt{\frac{(\langle \cos[n(\Psi_n^{\mathrm{EP,A}} - \Psi_n^{\mathrm{EP,B}})]\rangle)(\langle \cos[n(\Psi_n^{\mathrm{EP,A}} - \Psi_n^{\mathrm{EP,C}})]\rangle)}{\langle \cos[n(\Psi_n^{\mathrm{EP,B}} - \Psi_n^{\mathrm{EP,C}})]\rangle}}, \tag{2.8}$$

where $\Psi_n^{\mathrm{EP,A}}$, $\Psi_n^{\mathrm{EP,B}}$ and $\Psi_n^{\mathrm{EP,C}}$ are estimated in sub-events A, B and C. Differently from the two-subevent method, a same multiplicity and pseudorapidity coverage of each sub-event is not required here.

We can see that the event plane method strongly depends on the estimation of the event plane resolution, which is affected by correlations which are not from the genuine correlation of all particles with respect to the true symmetry plane. It will introduce a bias in the flow estimation event-by-event. In order to suppress this bias, different approaches were proposed. They are introduced in detail in the next sections.

[1] In practice, the two subevents are chosen in equal pseudorapidity ranges in opposite hemispheres, to keep their multiplicity very close [103, 104].

2.2 Scalar Product

The scalar product method is an alternative to the event-plane method in the sense that it measures the anisotropic flow without estimating the symmetry plane explicitly. The first step of the scalar product method is to separate the particles in each event into two equivalent sub-events with the same multiplicity, labeled as a and b. Based on the definition of $\boldsymbol{Q}_n$ in Eq. 2.3, the correlation between the Q_n-vectors measured in the two sub-events (Q_n^a and Q_n^b) is given by [105]:

$$\langle Q_n^a Q_n^{b\,*}\rangle = \langle v_n^2 M_a M_b\rangle, \tag{2.9}$$

where M_a and M_b are the multiplicities for sub-events a and b, respectively. Therefore, one assumes that:

$$\begin{aligned} v_n^a &= v_n^b = v_n, \\ M_a &= M_b \end{aligned} \tag{2.10}$$

The total Q_n-vector is then expressed as:

$$\boldsymbol{Q}_n = \boldsymbol{Q}_n^a + \boldsymbol{Q}_n^b. \tag{2.11}$$

On the other hand, we introduce the unit vector $\mathbf{u}_n = e^{in\varphi}$, which satisfies

$$\boldsymbol{Q}_n = \sum_j^M w_i u_{n,j}. \tag{2.12}$$

Then, the scalar product of the unit vector with n harmonic number and the complex conjugate of the flow vector $\boldsymbol{Q}_n$ is:

$$\langle \boldsymbol{u}_n \cdot \boldsymbol{Q}_n^*\rangle = \frac{1}{M}\sum_{i=k}^{M} \boldsymbol{u}_{k,n} \sum_{j=1,j\neq k}^{M} \boldsymbol{u}_{j,n}^*, \tag{2.13}$$

where $M = M_a + M_b$. In order to remove autocorrelations, the particles employed to construct the $\boldsymbol{u}_n$ vector are subtracted from the particles which are used to calculate $\boldsymbol{Q}_n$ before the scalar product is calculated. As the two sub-events have the same number of particles, i.e. $M_a = M_b$, an estimate of v_n with the scalar product method is obtained with

$$v_n(\mathrm{SP}) = \frac{\langle \boldsymbol{u}_n \boldsymbol{Q}_n^*\rangle}{2\sqrt{\langle \boldsymbol{Q}_n^a \boldsymbol{Q}_n^{b*}\rangle}}. \tag{2.14}$$

In practice, the nonflow contributions, which are mainly from the short-range jet correlations, need to be further removed. Each event is usually divided into three sub-events which are related to the particles in three different rapidity intervals, i.e. forward, backward and central rapidities. Besides that, only the scalar product of unit vector and the Q_n-vector in one sub-event is considered. In this case, the Eq. 2.14 becomes:

$$v_n(\mathrm{SP}) = \frac{\langle \boldsymbol{u}_n \boldsymbol{Q}_n^{a\,*}\rangle}{\sqrt{\frac{\langle \boldsymbol{Q}_n^a \boldsymbol{Q}_n^{b*}\rangle \langle \boldsymbol{Q}_n^a \boldsymbol{Q}_n^{c*}\rangle}{\langle \boldsymbol{Q}_n^b \boldsymbol{Q}_n^{c*}\rangle}}}, \tag{2.15}$$

where the three sub-events are labeled as a, b and c.

In general, the scalar product method can suppress nonflow correlations well by applying a rapidity gap between the two or three sub-events. On the other hand, one can see that the scalar product method strongly relies on the establishment of the assumptions in Eq. 2.10. It means the event-by-event fluctuations could still bias the final v_n.

2.3 Two- and Multi-particle Cumulants

As described in previous sections, any flow analysis method which aims to estimate the symmetry plane experimentally, will introduce the event-by-event bias to the final v_n coefficients inevitably. Alternatively, one can calculate event-averaged two-particle azimuthal correlations without constructing the flow symmetry plane. This is done with the cumulant method described in what follows.

In the first step, we can define the average two- and four-particle azimuthal correlations for a single-event in the following way [106]:

$$\begin{aligned}
\langle 2\rangle &= \langle e^{in(\varphi_1-\varphi_2)}\rangle \\
&= \frac{(M-2)!}{M!}\sum_{\substack{i,j=1\\(i\neq j)}}^{M} e^{in(\varphi_i-\varphi_j)}, \\
\langle 4\rangle &= \langle e^{in(\varphi_1+\varphi_2-\varphi_3-\varphi_4)}\rangle \\
&= \frac{(M-4)!}{M!}\sum_{\substack{i,j,k,l=1\\(i\neq j\neq k\neq l)}} e^{in(\varphi_i+\varphi_j-\varphi_k-\varphi_l)},
\end{aligned} \tag{2.16}$$

where φ_i is the azimuthal angle of the i-th particle measured in the laboratory frame, M is the number of particles in a given event, and $\langle\cdots\rangle$ represents the average over correlations between all particles in one event. In order to remove the contributions coming from auto-correlations, the constraints $i \neq j$ and $i \neq j \neq k \neq l$ are applied in Eq. 2.16. In the second step, we define the all-event average two- and four-particle azimuthal correlations as [106]:

$$\begin{aligned}
\langle\langle 2\rangle\rangle &= \langle\langle e^{in(\varphi_1-\varphi_2)}\rangle\rangle = \frac{\sum_{i=1}^{N}(W_{\langle 2\rangle})_i\langle 2\rangle_i}{\sum_{i=1}^{N}W_{\langle 2\rangle_i}}, \\
\langle\langle 4\rangle\rangle &= \langle\langle e^{in(\varphi_1+\varphi_2-\varphi_3-\varphi_4)}\rangle\rangle = \frac{\sum_{i=1}^{N}(W_{\langle 4\rangle})_i\langle 4\rangle_i}{\sum_{i=1}^{N}W_{\langle 4\rangle_i}},
\end{aligned} \tag{2.17}$$

where N is the number of events, and $\langle\langle\cdots\rangle\rangle$ represents the average first over all particles and then over all events, $(W_{\langle 2\rangle})_i$ and $(W_{\langle 4\rangle})_i$ are the specific weights for the i-th event, which are usually set as the number of distinct two- and four-particle combinations formed in an event with multiplicity M. Using the notation introduced

in Eq. 2.16 and Eq. 2.17, one obtains [106]:

$$\begin{aligned} W_{\langle 2\rangle} &= \frac{M!}{(M-2)!} = M(M-1), \\ W_{\langle 4\rangle} &= \frac{M!}{(M-4)!} = M(M-1)(M-2)(M-3). \end{aligned} \tag{2.18}$$

The third step is to build the relation between multi-particle azimuthal correlations and flow harmonics v_n. As mentioned before, without estimating the symmetry plane Ψ_n explicitly event-by-event, one gets:

$$\begin{aligned} \langle\langle 2\rangle\rangle &= \langle\langle e^{in(\varphi_i-\varphi_j)}\rangle\rangle = \langle\langle e^{in(\varphi_i-\Psi_n)}\rangle\langle e^{-in(\varphi_j-\Psi_n)}\rangle\rangle = \langle v_n^2\rangle, \\ \langle\langle 4\rangle\rangle &= \langle\langle e^{in(\varphi_i+\varphi_j-\varphi_k-\varphi_l)}\rangle\rangle \\ &= \langle\langle e^{in(\varphi_i-\Psi_n)}\rangle\langle e^{jn(\varphi_i-\Psi_n)}\rangle\langle e^{-in(\varphi_k-\Psi_n)}\rangle\langle e^{-in(\varphi_l-\Psi_n)}\rangle\rangle \\ &= \langle v_n^4\rangle. \end{aligned} \tag{2.19}$$

Similarly, for higher-even-order correlations, one can write:

$$\langle\langle 6\rangle\rangle = \langle v_n^6\rangle, \langle\langle 8\rangle\rangle = \langle v_n^8\rangle, \text{ etc.} \tag{2.20}$$

The final step is to introduce the cumulants to calculate these event-averaged quantities. The general formalism of cumulants was introduced firstly in [107,108]. Starting from the two-particle correlation, we define two random observables x_1 and x_2, as:

$$x_1 = e^{in\varphi_1}, x_2 = e^{-in\varphi_2} \tag{2.21}$$

where φ_1 and φ_2 are the azimuthal angles of two particles measured in the laboratory frame. Then, two-particle correlations in a given event can be written as:

$$\langle e^{in(\varphi_1-\varphi_2)}\rangle = \langle e^{in\varphi_1}\rangle\langle e^{-in\varphi_2}\rangle + \langle\langle e^{in(\varphi_1-\varphi_2)}\rangle\rangle, \tag{2.22}$$

where the term $\langle\langle e^{in(\varphi_1-\varphi_2)}\rangle\rangle$ is by definition the second-order cumulant, which is also labeled as $c_n\{2\}$. If x_1 and x_2 are statistically independent, i.e. there is no correlation between particle 1 and 2, $c_n\{2\} = 0$. Otherwise the $c_n\{2\}$ should be positive and represent the magnitude of correlations. On the other hand, the Eq. 2.22 can be also written as:

$$\langle\langle e^{in(\varphi_1-\varphi_2)}\rangle\rangle = \langle e^{in(\varphi_1-\varphi_2)}\rangle - \langle e^{in\varphi_1}\rangle\langle e^{-in\varphi_2}\rangle, \tag{2.23}$$

where $\langle e^{in\varphi_1}\rangle$ and $\langle e^{-in\varphi_2}\rangle$ terms vanish in case of perfect detector with a uniform acceptance. Since the term $\langle\langle e^{in(\varphi_1-\varphi_2)}\rangle\rangle$ is already defined as an all-event average two-particle correlation in Eq. 2.17, one obtains:

$$c_n\{2\} = \langle\langle 2\rangle\rangle. \tag{2.24}$$

Similarly, for four-particle correlations, one obtains:

$$\begin{aligned} \langle e^{in(\varphi_1+\varphi_2-\varphi_3-\varphi_4)}\rangle = \langle e^{in(\varphi_1-\varphi_3)}\rangle\langle e^{in(\varphi_2-\varphi_4)}\rangle + \langle e^{in(\varphi_1-\varphi_4)}\rangle\langle e^{in(\varphi_2-\varphi_3)}\rangle \\ + c_n\{4\}, \end{aligned} \tag{2.25}$$

where

$$c_n\{4\} = \langle\langle 4\rangle\rangle - 2 \cdot \langle\langle 2\rangle\rangle^2. \tag{2.26}$$

Finally, the estimates of the anisotropic flow coefficients can be provided by the calculation of cumulants:

$$\begin{aligned} v_n\{2\} &= \sqrt{c_n\{2\}}, \\ v_n\{4\} &= \sqrt[4]{-c_n\{4\}}. \end{aligned} \tag{2.27}$$

It's worth noting that the particles which we choose to construct the two- or four-particle correlations are not distinguishable. In other words, if the positions of φ_1, φ_2, φ_3, φ_4 in Eq. 2.16 and Eq. 2.17 are switched, the results will not be changed. It means that the flow coefficients measured from Eq. 2.27 are a kind of "integrated values" of v_n for a given group of particles, which is the so-called **reference flow**. The particles which are used to calculate the reference flow are the **reference particles (RPs)**. The cumulants $c_n\{2\}$ and $c_n\{4\}$ are reference cumulants, accordingly. In order to estimate the flow of a subset of correlated particles, typically related to a narrower phase-space region, e.g. p_{T} and η intervals, the measurement of the differential flow is introduced. The particles to construct the **differential flow** are the so-called **particles of interest (POI)**. In the following subsection, the azimuthal angle of the POI is denoted by ϕ, and φ is used for RPs.

The differential correlations are obtained in a very similar way as shown in Eq. 2.16 and Eq. 2.17 [106]:

$$\begin{aligned} \langle 2' \rangle &= \langle e^{\mathrm{i}n(\phi_1 - \varphi_2)} \rangle \\ &= \frac{1}{m_p M - m_q} \sum_{i=1}^{m_p} \sum_{j=1}^{M} e^{\mathrm{i}n(\phi_i - \varphi_j)}, \\ \langle 4' \rangle &= \langle e^{\mathrm{i}n(\phi_1 + \varphi_2 - \varphi_3 - \varphi_4)} \rangle \\ &= \frac{1}{(m_p M - 3m_q)(M-1)(M-2)} \sum_{i=1}^{m_p} \sum_{j,k,l=1}^{M} e^{\mathrm{i}n(\phi_1 + \varphi_2 - \varphi_3 - \varphi_4)}, \end{aligned} \tag{2.28}$$

where m_p is the total number of particles labeled as POI, M is the total number of particles labeled as RPs, m_q is the total number of particles labeled both as RPs and POI, ϕ_i is the azimuthal angle of i-th labeled as POI, and φ_j is the azimuthal angle of j-th particle labeled as RPs. The event averaged two- and four-particle correlations are expressed as [106]:

$$\begin{aligned} \langle\langle 2' \rangle\rangle &= \frac{\sum_{i=1}^{N} \left(w_{\langle 2' \rangle}\right)_i \langle 2 \rangle_i}{\sum_{i=1}^{N} w_{\langle 2' \rangle_i}}, \\ \langle\langle 4' \rangle\rangle &= \frac{\sum_{i=1}^{N} \left(w_{\langle 4' \rangle}\right)_i \langle 4 \rangle_i}{\sum_{i=1}^{N} w_{\langle 4' \rangle_i}}, \end{aligned} \tag{2.29}$$

where the N is the number of events and the $\left(w_{\langle 2' \rangle}\right)_i$ and $\left(w_{\langle 4' \rangle}\right)_i$ are the event weights for the i-th event. They correspond to the number of distinct two- and

four-particle combinations formed in an event. Similar to Eq. 2.18, the $(w_{\langle 2' \rangle})_i$ and $(w_{\langle 4' \rangle})_i$ are defined as:

$$\begin{aligned} w_{\langle 2' \rangle} &= m_p M - m_q, \\ w_{\langle 4' \rangle} &= (m_p M - 3m_q)(M-1)(M-2). \end{aligned} \tag{2.30}$$

Afterwards, the two- and four-particle differential cumulants $d_n\{2\}$ and $d_n\{4\}$ can be calculated from the differential correlations:

$$\begin{aligned} d_n\{2\} &= \langle\langle 2' \rangle\rangle, \\ d_n\{4\} &= \langle\langle 4' \rangle\rangle - 2\langle\langle 2' \rangle\rangle\langle\langle 2 \rangle\rangle. \end{aligned} \tag{2.31}$$

Finally, the differential flow coefficients v_n' are calculated based on the Eq. 2.24, Eq. 2.26 and Eq. 2.31:

$$\begin{aligned} v_n'\{2\} &= \frac{d_n\{2\}}{\sqrt{c_n\{2\}}}, \\ v_n'\{4\} &= \frac{-d_n\{4\}}{(-c_n\{4\})^{3/4}}. \end{aligned} \tag{2.32}$$

The cumulant method has a good ability to overcome the event-by-event bias compared to the event-plane method. However, one of the problems in measuring multi-particle correlations is that the computing power needs to go over all particles, which quickly becomes CPU prohibitive when computing cumulants. For instance, for the calculation of $\langle 2 \rangle$ as shown in Eq. 2.16, $N(N-1)$ operations are needed. So the complexity of this problem is $\mathcal{O}(N^2)$. For the calculation of $\langle 4 \rangle$, the number of combinations become $N(N-1)(N-2)(N-3)$, and the complexity is $\mathcal{O}(N^4)$. The estimate of higher order $\langle n \rangle$ would require the operations with $\mathcal{O}(N^n)$ complexity. In the contest of high-energy physics [109], it becomes very difficult to treat problems with $\mathcal{O}(N^3)$ complexity, considering the huge number of collisions and number of particles produced in each event. Therefore, improvements need to be implemented to resolve this issue. This will be discussed in the next section.

2.3.1 Q-Cumulants

Instead of calculating the contribution of each combination of correlated particles, an alternative approach was proposed in [106]. In such approach, all multi-particle cumulants are expressed analytically in terms of the Q_n-vectors. It is commonly referred to as Q-cumulants (QC) method. In the following, a summary of the main steps of the procedure is reminded.

Starting from the reference flow, in order to obtain the two-particle cumulant, one needs to separate diagonal and off-diagonal terms in $|Q_n|^2$ [106]:

$$|Q_n|^2 = Q_n Q_n{}^* = \sum_{i,j=1}^{M} e^{in(\varphi_i - \varphi_j)} = M + \sum_{\substack{i,j=1 \\ i \neq j}}^{M} e^{in(\varphi_i - \varphi_j)}, \tag{2.33}$$

where the notations are already defined in Eq. 2.16. Then, the average two-particle azimuthal correlation $\langle 2 \rangle$ can be described as [106]:

$$\langle 2 \rangle = \frac{|Q_n|^2 - M}{M(M-1)}. \tag{2.34}$$

For the calculation of four-particle cumulant, the $|Q_n|^4$ can be decomposed as [106]:

$$|Q_n|^4 = Q_n Q_n Q_n^* Q_n^* = \sum_{i,j,k,l=1}^{M} e^{in(\varphi_i + \varphi_j - \varphi_k - \varphi_l)}. \tag{2.35}$$

The average four-particle azimuthal correlation $\langle 4 \rangle$ can be expressed in terms of Q_n [106]:

$$\langle 4 \rangle = \frac{|Q_n|^4 + |Q_{2n}|^2 - 4(M-2)|Q_n|^2 - 2\mathfrak{Re}(Q_{2n}Q_n^*Q_n^*) + 2M(M-3)}{M(M-1)(M-2)(M-3)}. \tag{2.36}$$

After $\langle 2 \rangle$ and $\langle 4 \rangle$ are obtained, the $\langle\langle 2 \rangle\rangle$ and $\langle\langle 4 \rangle\rangle$ can be calculated by making use of Eq. 2.17. Once $\langle\langle 2 \rangle\rangle$ and $\langle\langle 4 \rangle\rangle$ are computed, one can estimate $c_n\{2\}$ and $c_n\{4\}$ (here they are named **two- and four-particle Q-cumulants**) and the related $v_2\{2\}$ and $v_2\{4\}$ coefficients from Eq. 2.24, Eq. 2.26 and Eq. 2.27.

In order to derive the equations for differential Q-cumulants, we have to introduce the p_n- and q_n-vectors. The p_n-vector is computed with all POI, and the q_n-vector is built only with particles labeled both as RPs and POI [106]:

$$\begin{aligned} p_n &= \sum_{i=1}^{m_p} e^{in\phi_i} \\ q_n &= \sum_{i=1}^{m_q} e^{in\phi_i} \end{aligned} \tag{2.37}$$

where all notations are the same as those in Eq. 2.28. The q_n-vector is introduced here to remove the effects from auto-correlations. Using the q_n vectors, the differential correlations in Eq. 2.28 can now be written as [106]:

$$\begin{aligned} \langle 2' \rangle &= \frac{p_n Q_n^* - m_q}{m_p M - m_q} \\ \langle 4' \rangle &= (p_n Q_n Q_n^* Q_n^* - q_{2n} Q_n^* Q_n^* - p_n Q_n Q_{2n}^* \\ &\quad - 2M p_n Q_n^* - 2 \cdot m_q |Q_n|^2 + 7 \cdot q_n Q_n^* \\ &\quad + 2 m_q M - 6 m_q)/[(m_p M - 3 m_q)(M-1)(M-2)] \end{aligned} \tag{2.38}$$

Furthermore the calculations of $\langle\langle 2' \rangle\rangle$, $\langle\langle 4' \rangle\rangle$ and corresponding differential flow coefficients can be performed following the strategy shown in Eq. 2.28–2.32.

Since only Q_n-vector quantities are needed in the calculation of multi-particle correlations, a single pass over all particles is sufficient, instead of using all combinations. It reduces the complexity from $\mathcal{O}(N^n)$ to $\mathcal{O}(N)$, which is feasible with current CPU calculating power. However, as shown in Eq. 2.38, the calculations with Q-cumulants method is still very tedious, in particular for the multi-particle correlations. In this case, a more general way to compute particle correlations analytically is needed. It will be introduced in next section.

2.3.2 Generic Framework

In practice, the anisotropic flow results based on the measurement of azimuthal correlations of particles might be affected by systematic biases [108, 110], due for example to non-uniform acceptance, p_{T}-dependent reconstruction inefficiency, finite detector granularity [100]. The implementation of the Generic Framework (GF) [100] provides an universal method for the calculations of all multi-particle azimuthal correlations in a fast and efficient way, where the non-uniform azimuthal acceptance can be corrected at the level of the Q-vector by introducing the single-particle weights[2]. The so-called "weighted Q-vector" is defined as [100]:

$$Q_{n,p} = \sum_{k=1}^{M} w_k^p e^{\mathrm{i}n\varphi_k}, Q_{-n,p} = Q_{n,p}^*, \tag{2.39}$$

where φ_k is the k-th particle azimuthal angle and w_k is a particle weight of the k-th particle. The weights can depend not only on φ, but also on the dimension in which the inefficiency is present, e.g. the rapidity and transverse momentum. The procedure to obtain the weight will be described in detail in App. C. Similar to the Q-cumulant method, only a fast single pass over particles is needed to calculate the Q-vector for various combinations of harmonic n and power p.

Following the expression of two- and four-particle correlation shown in Eq. 2.16, we can introduce the multi-particle azimuthal correlations in a generic way. The average m-particle correlation is given by the following generic definition:

$$\begin{aligned}\langle m\rangle_{n_1,n_2,\ldots,n_m} &= \langle e^{\mathrm{i}(n_1\varphi_1+n_2\varphi_2+\ldots+n_m\varphi_{k_m})}\rangle \\ &= \frac{\sum_{\substack{k_1,k_2,\ldots,k_m=1 \\ k_1\neq k_2\neq\ldots\neq k_m}}^{M} w_{k_1}w_{k_2}\ldots w_{k_m}e^{\mathrm{i}(n_1\varphi_1+n_2\varphi_2+\ldots+n_m\varphi_{k_m})}}{\sum_{\substack{k_1,k_2,\ldots,k_m=1 \\ k_1\neq k_2\neq\ldots\neq k_m}}^{M} w_{k_1}w_{k_2}\ldots w_{k_m}},\end{aligned} \tag{2.40}$$

where M is the multiplicity of an event. The condition $k_1 \neq k_2 \neq \ldots \neq k_m$ is introduced to remove the trivial contributions from auto-correlations. One can observe that the numerator and denominator in Eq. 2.40 are trivially related. Indeed, the denominator can be derived from the expression of the numerator by setting all harmonics n_1, n_2, ..., n_m to 0. In this case, we can introduce the following notations:

$$\begin{aligned}N\langle m\rangle_{n_1,n_2,\ldots,n_m} &= \sum_{\substack{k_1,k_2,\ldots,k_m=1 \\ k_1\neq k_2\neq\ldots\neq k_m}}^{M} w_{k_1}w_{k_2}\ldots w_{k_m}e^{\mathrm{i}(n_1\varphi_1+n_2\varphi_2+\ldots+n_m\varphi_{k_m})}, \\ D\langle m\rangle_{n_1,n_2,\ldots,n_m} &= \sum_{\substack{k_1,k_2,\ldots,k_m=1 \\ k_1\neq k_2\neq\ldots\neq k_m}}^{M} w_{k_1}w_{k_2}\ldots w_{k_m} \\ &= N\langle m\rangle_{0,0,\ldots,0}.\end{aligned} \tag{2.41}$$

[2]The concept of particle weights was already mentioned in the Appendix of Ref. [106], which is used to improve the Q-cumulant method.

Therefore the Eq. 2.40 can be simplified as:

$$\langle m\rangle_{n_1,n_2,\ldots,n_m} = \frac{N\langle m\rangle_{n_1,n_2,\ldots,n_m}}{D\langle m\rangle_{n_1,n_2,\ldots,n_m}} = \frac{N\langle m\rangle_{n_1,n_2,\ldots,n_m}}{N\langle m\rangle_{0,0,\ldots,0}}. \tag{2.42}$$

Following the same strategy used in Q-cumulants method, $N\langle m\rangle_{n_1,n_2,\ldots,n_m}$ and $D\langle m\rangle_{n_1,n_2,\ldots,n_m}$ can be expressed in terms of $Q_{n,l}$-vectors. For two-particle correlations, one gets:

$$\begin{aligned} N\langle 2\rangle_{n_1,n_2} &= Q_{n_1,1}Q_{n_2,1} - Q_{n_1+n_2,2}, \\ D\langle 2\rangle_{n_1,n_2} &= N\langle 2\rangle_{0,0} \\ &= Q_{0,1}^2 - Q_{0,2}. \end{aligned} \tag{2.43}$$

Additionally, for four-particle correlations, one obtains:

$$\begin{aligned} N\langle 4\rangle_{n_1,n_2,n_3,n_4} =& Q_{n_1,1}Q_{n_2,1}Q_{n_3,1}Q_{n_4,1} - Q_{n_1+n_2,2}Qn_3Q_{n_4,1} \\ &- Q_{n_2,1}Q_{n_1+n_3,2}Q_{n_4,1} - Q_{n1_1}Q_{n_2+n_3}Q_{n_4,1} \\ &+ 2Q_{n_1+n_2+n_3,3}Q_{n_4,1} - Q_{n_2,1}Q_{n_3,1}Q_{n_1+n_4,2} \\ &+ Q_{n_2+n_3,2}Q_{n_1+n_4,2} - Q_{n_1,1}Q_{n_3,1}Q_{n_1+n_4,2} \\ &+ Q_{n_1+n_3,2}Q_{n_2+n_4,2} + 2Q_{n_3,1}Q_{n_1+n_2+n_4,3} \\ &- Q_{n_1,1}Q_{n_2,1}Qn_3+n_4,2 + Q_{n_1+n_2,2}Q_{n_3+n_4,2} \\ &+ 2Q_{n_2,1}Q_{n_1+n_3+n_4,3} + 2Q_{n_1,1}Qn_2+n_3+n_4,3 \\ &- 6Q_{n_1+n_2+n_3+n_4,4}, \\ D\langle 4\rangle_{n_1,n_2,n_3,n_4} =& N\langle 4\rangle_{0,0,0,0} \\ =& Q_{0,1}^4 - 6Q_{0,1}^2Q_{0,2} + 3Q_{0,2}^2 \\ &+8Q_{0,1}Q_{0,3} - 6Q_{0,4}. \end{aligned} \tag{2.44}$$

Then the two-particle and four-particle reference cumulants ($\langle\langle 2\rangle\rangle$ and $\langle\langle 4\rangle\rangle$) and the reference flow value ($v_n\{2\}$ and $v_n\{4\}$) are obtained following the strategy shown in Eq. 2.24–2.27.

On the other hand, for the calculations of differential cumulants, the weighted p- and q-vector are introduced:

$$\begin{aligned} p_{n,l} &= \sum_{k=1}^{m_p} w_k^l e^{\mathrm{i}n\phi_k}, \\ q_{n,l} &= \sum_{k=1}^{m_q} w_k^l e^{\mathrm{i}n\phi_k}, \end{aligned} \tag{2.45}$$

where the weighted $p_{n,l}$-vector is constructed out of all POI in a narrow differential bin of interest in an event (m_p in total) and the weighted $q_{n,l}$-vector, employed to remove the contribution from auto-correlations, is constructed from the particles in an event which are labeled as both POI and RPs (m_q in total). Similarly, for two- and four-particle differential correlations, the $\langle 2'\rangle$ and $\langle 4'\rangle$ differential cumulants can

be expressed in terms of the $Q_{n,l}$, $q_{n,l}$, $p_{n,l}$ vectors. It follows:

$$\begin{aligned} N\langle 2'\rangle_{\underline{n_1},n_2} =& p_{n_1,1}Q_{n_2,1} - q_{n_1+n_2,2}, \\ D\langle 2'\rangle_{\underline{n_1},n_2} =& N\langle 2'\rangle_{\underline{0},0} \\ =& p_{0,1}Q_{0,1} - q_{0,2}, \end{aligned} \tag{2.46}$$

and

$$\begin{aligned} N\langle 4'\rangle_{\underline{n_1},n_2,n_3,n_4} =& p_{n_1,1}Q_{n_2,1}Q_{n_3,1}Q_{n_4,1} - q_{n_1+n_2,2}Q_{n_3,1}Q_{n_4,1} \\ & - p_{n_1,1}Q_{n_{2+3},2}Q_{n_4,4} + 2q_{n_1+n_2+n_3,3}Q_{n_4,1} - q_{n_1+n_4,2}Q_{n_2,1}Q_{n_3,1} \\ & + q_{n_1+n_4,2}Q_{n_2+n_3,2} - p_{n_1,1}Q_{n_3,1}Q_{n_2+n_4} + q_{n_1+n_3,2}Q_{n_2+n_4,2} \\ & + 2q_{n_1+n_2+n_4}Q_{n_3,1} - p_{n_1,1}Q_{n_2,1}Q_{n_3+n_4,2} + q_{n_1+n_2,2}Q_{n_3+n_4,2} \\ & + 2q_{n_1+n_3+n_4,3}Q_{n_2,1} + 2p_{n_1,1}Q_{n_2+n_3+n_4,3} - 6q_{n_1+n_2+n_3+n_4,4}, \\ D\langle 4'\rangle_{\underline{n_1},n_2,n_3,n_4} =& N\langle 4'\rangle_{\underline{0},0,0,0} \\ =& p_{0,1}Q_{0,1}^3 - 3q_{0,2}Q_{0,1}^2 - 3p_{0,1}Q_{0,1}Q0,2 + 3q_{0,2}Q_{0,2} + 6q_{0,3}Q_{0,1}, \end{aligned} \tag{2.47}$$

where the underline indicates which harmonic index corresponds to the differential flow vector. Finally, the differential flow coefficients can be derived from Eq. 2.32.

2.4 Pair-wise Azimuthal Correlation

The two-particle correlations can provide an alternative way to estimate the anisotropic flow, which is the so-called "pair-wise azimuthal correlation method" [101].[3] Similar to Eq. 1.26, the two particle azimuthal correlation of N^{pairs} emitted particle pairs (with each particle labeled as a and b) as a function of relative angle $\Delta\varphi = \varphi^a - \varphi^b$ can be expanded in a Fourier series as:

$$\frac{\mathrm{d}N^{\text{pair}}}{d\Delta\varphi} \propto 1 + 2\sum_{n=1}^{\infty} V_{n\Delta}(p_{\mathrm{T}}^a, p_{\mathrm{T}}^b)\cos[n(\Delta\varphi)], \tag{2.48}$$

where $V_{n\Delta}$ is the two-particle n-th order harmonic. In a pure hydrodynamic picture, due to the particle emission is independent, the two-particle distribution can be factorized based on

$$\langle\frac{\mathrm{d}N^{\text{pairs}}}{\mathrm{d}\Delta\varphi^{ab}}\rangle = \langle\frac{\mathrm{d}N}{\mathrm{d}\varphi^a}\frac{\mathrm{d}N}{\mathrm{d}\varphi^b}\rangle, \tag{2.49}$$

where the bracket $\langle\cdot\rangle$ represents the average over all events. Following Eq. 1.26, the azimuthal distribution of single particle a and b can be expressed as:

$$\begin{aligned} \frac{\mathrm{d}N}{\mathrm{d}\varphi^a} &\propto 1 + 2\sum_{n=1}^{\infty} v_n^a\cos[n(\varphi^a - \Psi_n^a)], \\ \frac{\mathrm{d}N}{\mathrm{d}\varphi^b} &\propto 1 + 2\sum_{n=1}^{\infty} v_n^b\cos[n(\varphi^b - \Psi_n^b)], \end{aligned} \tag{2.50}$$

[3] Here the name is used to distinguish the "two-particle correlations" in the cumulant method. However, in many papers [111–113], they are not distinguished. In this case, we still use "two-particle correlation method" to present this method which is used for the analyses described in this thesis.

where the $\Psi_n^{a(b)}$ and $v_n^{a(b)}$ are the symmetry plane and flow coefficients for particle a (b). Combining Eq. 2.48, Eq. 2.49 and Eq. 2.50, we can get the connection between the single- and two-particle harmonics:

$$\langle V_{n\Delta}(p_{\mathrm{T}}^a, p_{\mathrm{T}}^b)\rangle = \langle v_n^a v_n^b \cos[n(\Psi_n^a - \Psi_n^b)]\rangle \leq \langle v_n^a v_n^b\rangle. \tag{2.51}$$

We can see that the factorization is valid when $\cos[n(\Psi_n^a - \Psi_n^b) = 1$. This scenario is possible in most cases since in principle the symmetry plane always acts as a global phase. However, the factorization may break down experimentally, due to for example the nonflow effects, event-by-event initial-state fluctuations. Previous measurements have shown a significant breakdown of factorization at high p_{T} in central Pb–Pb collisions [114]. A smaller effect was also seen in high-multiplicity p–Pb collisions [115].

Based on the factorization assumption, and averaging Eq. 2.48 over all events within a given reference p_{T} interval, one can write:

$$\begin{aligned}\langle \frac{dN^{\mathrm{pair}}}{d\Delta\varphi}\rangle &\propto 1 + 2\sum_{n=1}^{\infty} V_{n\Delta}(p_{\mathrm{T}}^{\mathrm{ref}}, p_{\mathrm{T}}^{\mathrm{ref}})\cos[n(\Delta\varphi)] \\ &= 1 + 2\sum_{n=1}^{\infty} v_n^2 \cos[n(\Delta\varphi)],\end{aligned} \tag{2.52}$$

where v_2 is the integrated reference flow which can be calculated as

$$v_n = \sqrt{V_{n\Delta}(p_{\mathrm{T}}^{\mathrm{ref}}, p_{\mathrm{T}}^{\mathrm{ref}})}. \tag{2.53}$$

For the differential flow as a function of p_{T}, one gets

$$v_n(p_{\mathrm{T}}) = \frac{V_{n\Delta}(p_{\mathrm{T}}, p_{\mathrm{T}}^{\mathrm{ref}})}{v_n} = \frac{V_{n\Delta}(p_{\mathrm{T}}, p_{\mathrm{T}}^{\mathrm{ref}})}{\sqrt{V_{n\Delta}(p_{\mathrm{T}}^{\mathrm{ref}}, p_{\mathrm{T}}^{\mathrm{ref}})}}. \tag{2.54}$$

In practice, the $V_{n\Delta}$ coefficients of Eq. 2.48 are affected by the non-uniform acceptance and inefficiencies of the detector and can be defined as:

$$V_{n\Delta}(p_{\mathrm{T}}^a, p_{\mathrm{T}}^b) = \langle \cos(n\Delta\varphi)\rangle_{\mathrm{S}} - \langle \cos(n\Delta\varphi)\rangle_{\mathrm{B}} \tag{2.55}$$

where $\langle \cos(n\Delta\varphi)\rangle_{\mathrm{S}}$ is the two-particle anisotropic flow signal where the correlated particles belong to the same event, and $\langle \cos(n\Delta\varphi)\rangle_{\mathrm{B}}$ corresponds to the background and accounts for the effect of the imperfect detector.

To correct for this background in Eq. 2.55, the so-called **event-mixing technique** is introduced. Using same notations as in Eq. 2.48, the particle a is defined as the trigger particle and the particle b as associated particle. The number of particle-pairs in same events is normalized to the number of trigger particles, and expressed as a function of $\Delta\varphi$ and $\Delta\eta$ (the difference between the pseudorapidity of trigger and associated particles):

$$S(\Delta\varphi, \Delta\eta) = \frac{1}{N_{\mathrm{trig}}} \frac{\mathrm{d}^2 N_{\mathrm{same}}}{\mathrm{d}\Delta\eta \mathrm{d}\Delta\varphi} \tag{2.56}$$

where $N_{\rm trig}$ is the total number of trigger particles. Figure 2.1 (left) shows an example of the associated yield per trigger particle as a function of $\Delta\varphi$ and $\Delta\varphi$ in same events. One can clearly observe a significant triangular structure along $\Delta\varphi$, which arises from non-uniform acceptance and inefficiencies of detectors. On the other hand, the associated yield as a function of $\Delta\varphi$ and $\Delta\varphi$ can be also obtained in mixed events, which is the so-called background distribution:

$$B(\Delta\varphi, \Delta\eta) = \alpha \frac{\mathrm{d}^2 N_{\rm mixed}}{\mathrm{d}\Delta\eta \mathrm{d}\Delta\varphi} \tag{2.57}$$

where "mixed" indicates that the correlations are made between trigger particles from any event and associated particles from different events. The factor α is used to normalize the background distribution to unity in the $\Delta\eta$ region of maximal pair acceptance. In this way, only trivial pair acceptance correlations will be present as there can be no physics correlation, as shown in Fig 2.1 (middle).

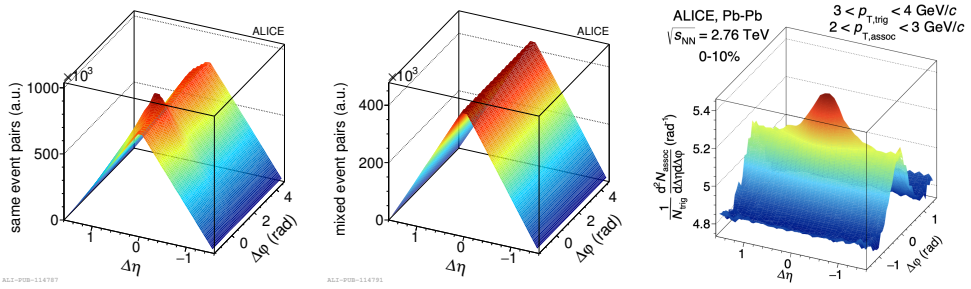

Figure 2.1: Example of the di-hadron correlation yield per trigger particle as a function of $\Delta\varphi$ and $\Delta\varphi$ measured in 0–10% most central Pb–Pb collisions at $\sqrt{s_{\rm NN}}$ = 2.76 TeV, for same (left) and mixed (middle) events. Right: the di-hadron correlation yield per trigger particle after the event mixing correction. Figure taken from [116].

Finally, the "real" associated yield per trigger particle can be obtained by dividing $S(\Delta\varphi, \Delta\eta)$ by $B(\Delta\varphi, \Delta\eta)$:

$$Y = \frac{1}{N_{\rm trig}} \frac{\mathrm{d}^2 N_{\rm assoc}}{\mathrm{d}\Delta\eta \mathrm{d}\Delta\varphi} = \frac{S(\Delta\varphi, \Delta\eta)}{B(\Delta\varphi, \Delta\eta)} \tag{2.58}$$

The corrected distribution is shown in Fig. 2.1 (right), where the trivial distortions shown in Fig. 2.1 (left) are removed.

So far, the pair-wise azimuthal correlation provides an alternative way to get directly the flow coefficients. However, as described above, it is dependent on the factorization assumption, which usually breaks in heavy-ion collisions. In small collision systems, this method is still widely used due its good ability to remove the nonflow contributions. These aspects will be discussed in the chapter 5 dedicated to the measurement of azimuthal anisotropies of inclusive muons.

CHAPTER 3

Experimental Setup

ALICE (A Large Ion Collider Experiment) is one of the four experiments operating at the largest particle collider in the world, the Large Hadron Collider (LHC). The main purpose of ALICE is to investigate the properties of strongly-interacting matter (the quark–gluon plasma) at extreme energy density and temperature in ultra-relativistic heavy-ion collisions. In this chapter, we introduce the current ALICE experimental setup and its upgrade for the upcoming data taking period.

3.1 The Large Hadron Collider (LHC)

The Large Hadron Collider (LHC) with its circumference of 26.7 kilometers is the world's largest and most powerful particle accelerator and collider. It is made of two rings of superconducting magnets installed at the European Organization for Nuclear Research (CERN), which is located in the France-Switzerland border [117]. The LHC is situated in the 3.8-meter-wide tunnel located 50 to 175 meters underground, that was built for, now decommissioned, the Large Electron-Positron (LEP) collider [118]. Inside the accelerator, two high-energy particle beams, which contain protons or ions, are set traveling at a velocity close to the speed of light around a circular tunnel in opposite directions. Then, they collide and the products from the collisions are studied for various physics motivations. Since 2009, the LHC already delivered two round of data taking, and are called "Run 1" (2009–2013) and "Run 2" (2015–2018). During these collision periods, the protons and lead ions were accelerated to center-of-mass energies of up to $\sqrt{s}$ = 13 TeV and (per nucleon) $\sqrt{s_{\rm NN}}$ = 5.02 TeV respectively, which are the highest energies reached by high-energy experiments in the world. In addition, the LHC also accelerated Xe ions at a beam energy of $\sqrt{s_{\rm NN}}$ = 5.44 TeV in 2017 to extend its scientific research to different system size [119].

Up to now (2021), the LHC collected the data from pp collisions at $\sqrt{s}$ = 0.9, 2.76, 5.02, 7, 8, 13 TeV, Pb–Pb collisions at $\sqrt{s_{\rm NN}}$ = 2.76 and 5.02 TeV, p–Pb collisions at $\sqrt{s_{\rm NN}}$ = 5.02 and 8.16 TeV, and Xe–Xe collisions at $\sqrt{s_{\rm NN}}$ = 5.44 TeV, which were collected by the four CERN experiments placed on four LHC beam intersections, as illustrated in Fig. 3.1. The two general-purpose detectors ATLAS (A Toroidal LHC Apparatus) at IP (interaction point) 1 and CMS (Compact Muon Solenoid) at IP5 are designed for studying new and rare processes in proton-proton (pp) collisions, especially the observation of the Higgs boson (which was discovered in 2012 [2, 3]) and the physics beyond the Standard Model. The LHCb (Large Hadron Collider beauty) experiment at IP8 focuses on the study of B mesons to investigate the violation of CP symmetry. Finally, ALICE (A Large Ion Collider

Experiment) is a detector dedicated to the study of heavy-ion collisions with the aim to figure out the properties of the quark–gluon plasma created in such collisions.

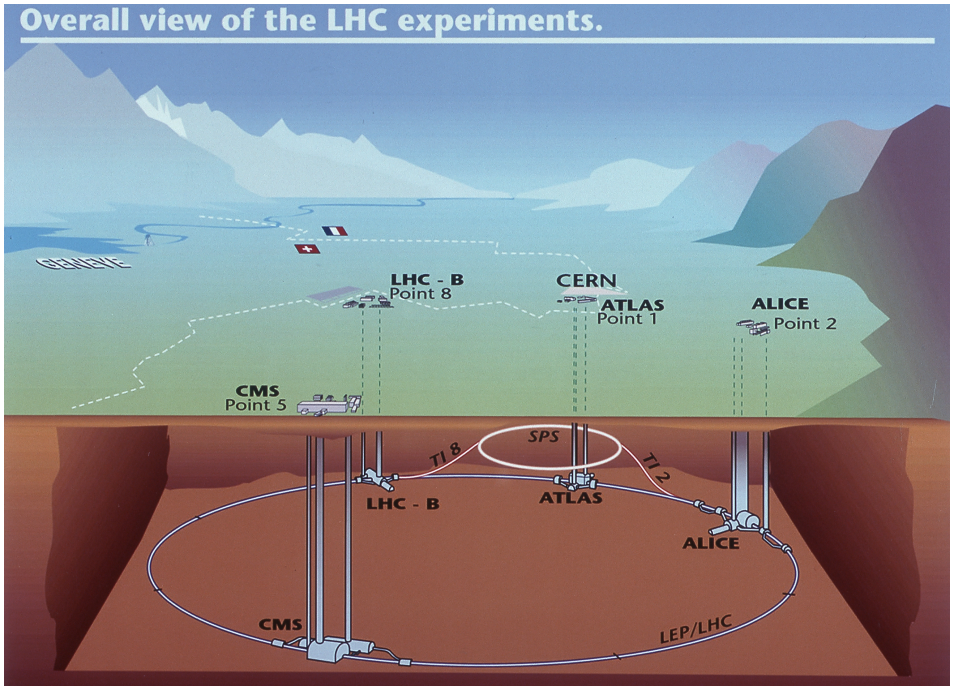

Figure 3.1: Schematic view of the LHC and the main four experiments underground. Figure taken from [120].

3.2 A Large Ion Collider Experiment (ALICE)

As the only LHC experiment which is dedicated to the study of heavy-ion physics, the main aim of ALICE is not to find rare particles as other three experiments, but instead to address the physics of the QGP and to investigate the phase diagram of the QCD phase. It requires ALICE to have powerful sub-detectors to collect and analyse as much data as possible in heavy-ion collisions, which usually generate an environment with a large charged-particle multiplicity. For instance, a Pb–Pb collision generally produces around 500–1000 charged particles per pseudorapidity unit ($\mathrm{d}N_{\mathrm{ch}}/\mathrm{d}\eta$), and it even reaches $\mathrm{d}N_{\mathrm{ch}}/\mathrm{d}\eta \sim 8000$ at midrapidity in the most central collisions [121]. Within such high-multiplicity density environment, ALICE has excellent particle identification (PID) capabilities for charged hadrons at the LHC and especially at low p_{T} (down to 80 MeV/c for pions [122]) where the bulk of the particles is produced, which is particularly relevant for studying the QGP. In addition to heavy-ion collisions, ALICE also records pp, p–Pb and Xe–Xe data for the measurements in small collision systems, aiming to provide a baseline for Pb–Pb measurements and to quantify the effects of cold nuclear matter, and to study the system size dependence of various observables.

The ALICE detector occupies a space of 26 m long, 16 m high, and 16 m wide with a weight of around 10000 tons, and sits in a cavern underground nearby the village of St Genis-Pouilly in France. The layout of the ALICE detector is shown in Fig. 3.2. The ALICE coordinate system is a right-handed Cartesian system. The z axis is along the beam direction and the y axis which always points up, together with x axis identify the transverse plane. Tab. 3.1 shows the summary of the acceptances, positions and dimensions of the sub-detectors. The ALICE apparatus is composed by three main parts: the central barrel, the global detectors and the forward muon spectrometer. The central barrel consists of all the detectors located in the pseudorapidity region $|\eta| < 0.9$. From inside out, these detectors are the Inner Tracking System (ITS), which is made of two silicon pixel detector layers (SPD), two silicon drift detector layers (SDD) and two silicon strip detector layers (SSD), the Time Projection Chamber (TPC), the Transition Radiation Detector (TRD), the Time Of Flight (TOF) detector, the Ring Imaging Cherenkov (HMPID) detector, and two electromagnetic calorimeters (PHOS and EMCal). They are contained within the L3 magnet, which generates a maximum magnetic field of $B = 0.5$ T parallel to the beam direction. Hence charged particles following the curved path in such a magnetic field are separated into positive and negative particles. More information is given in Sec. 3.2.1. The global detectors are the Zero Degree Calorimeter (ZDC), the Photon Multiplicity Detector (PMD), the Forward Multiplicity Detector (FMD), the T0 and the V0 detectors, which are located in the forward and backward pseudorapidity regions. They are mainly used for global event characterization (e.g. centrality determination, multiplicity measurement, and event plane reconstruction), as described in Sec. 3.2.2. The forward muon spectrometer is located in the pseudorapidity region $-4 < \eta < -2.5$, and is mainly designed for the measurements of muons. It is composed of a front absorber, a dipole magnet, five tracking stations for muon reconstruction and two trigger stations for muon identification and triggering. A more detailed description about the layout of the muon spectrometer is given in Sec. 3.2.3.

3.2.1 Central Barrel Detectors

Inner Tracking System (ITS)

The Inner Tracking System is located in close proximity of the interaction point. As shown in Fig. 3.3, three distinct types of cylindrical silicon detectors surround the beam pipe and cover the whole azimuth. The two innermost layers are the silicon pixel detectors (SPD), the third and the fourth ones are the silicon drift detectors (SDD) and the outer two layers form the Silicon Strip Detectors (SSD). The details about the dimensions and spatial resolution for each layer of the ITS are reported in Tab. 3.2. The main task of the SPD is to reconstruct the primary vertex of a collision (i.e. an approximate point where the collision occurs) and, decay vertices (the vertices of heavy flavour and strange particle decays). The number of primary charged particles produced in the collisions can also be estimated with SPD, from the SPD tracklets [123]. In addition, thanks to the fast response of the SPD, it

Detector	Acceptance		Position (m)	Main purpose
	Polar η	Azimuthal ϕ		
Central barrel				
ITS layer 1,2 (SPD)	$\lvert\eta\rvert$ <2, η <$\lvert$1.4$\rvert$	full	$r = 0.039$, $r = 0.076$	tracking, vertex
ITS layer 3,4 (SDD)	$\lvert\eta\rvert$ <0.9, η <$\lvert$0.9$\rvert$	full	$r = 0.150$, $r = 0.239$	tracking, PID
ITS layer 5,6 (SSD)	$\lvert\eta\rvert$ <1.0, η <$\lvert$1.0$\rvert$	full	$r = 0.380$, $r = 0.430$	tracking, PID
TPC	$\lvert\eta\rvert$ <0.9	full	0.085< r <0.247	tracking, PID
TRD	$\lvert\eta\rvert$ <0.8	full	0.290< r <0.368	tracking, $e^{\pm}$ID
TOF	$\lvert\eta\rvert$ <0.9	full	0.370< r <0.399	PID
PHOS	$\lvert\eta\rvert$ <0.12	220° < ϕ < 320°	0.460< r <0.478	photons
EMCal	$\lvert\eta\rvert$ <0.7	80° < ϕ < 187°	0.430< r <0.455	photons and jets
DCal	0.22< $\lvert\eta\rvert$ <0.7 $\lvert\eta\rvert$ <0.7	260° < ϕ < 320° 320° < ϕ < 327°	0.430< r <0.455	photons, jets
HMPID	η <$\lvert$0.6$\rvert$	1° < ϕ < 59°	r = 0.490	PID
ACORDE	η <$\lvert$1.3$\rvert$	30° < ϕ < 150°	r = 0.850	cosmic rays, calibration
Global detectors				
ZDC: ZN	$\lvert\eta\rvert$ >8.8	full	r = ±113	forward neutrons
ZDC: ZP	6.5< $\lvert\eta\rvert$ <7.5	$\lvert\phi\rvert$ < 10°	r = ±113	forward protons
ZDC: ZEM	4.8< $\lvert\eta\rvert$ <5.7	$\lvert 2\phi\rvert$ < 32°	r = 7.3	photons
V0A	2.8 < $\lvert\eta\rvert$ <5.1	full	r = 0.329	charged particles
V0C	-3.7< $\lvert\eta\rvert$ <-1.7	full	r = -0.088	charged particles
T0A	4.6 < $\lvert\eta\rvert$ <4.9	full	r = 0.370	time, vertex
T0C	-3.3< $\lvert\eta\rvert$ <-3.0	full	r = -0.070	time, vertex
FMD disc 1	3.6< $\lvert\eta\rvert$ <5.0	full	r = 0.320	charged particles
FMD disc 2	1.7< $\lvert\eta\rvert$ <3.7	full	r = 0.080	charged particles
FMD disc 3	-3.4< $\lvert\eta\rvert$ <-1.7	full	r = -0.070	charged particles
Muon spectrometer				
Tracking station 1	-4.0<η<-2.5	full	r = -5.36	muon tracking
Tracking station 2			r = -6.86	
Tracking station 3			r = -9.83	
Tracking station 4			r = -12.92	
Tracking station 5			r = -14.22	
Trigger station 1	-4.0<η<-2.5	full	r = -16.12	muon triggering
Trigger station 2			r = -17.12	

Table 3.1: Summary of the ALICE detector subsystems. Extracted from [122].

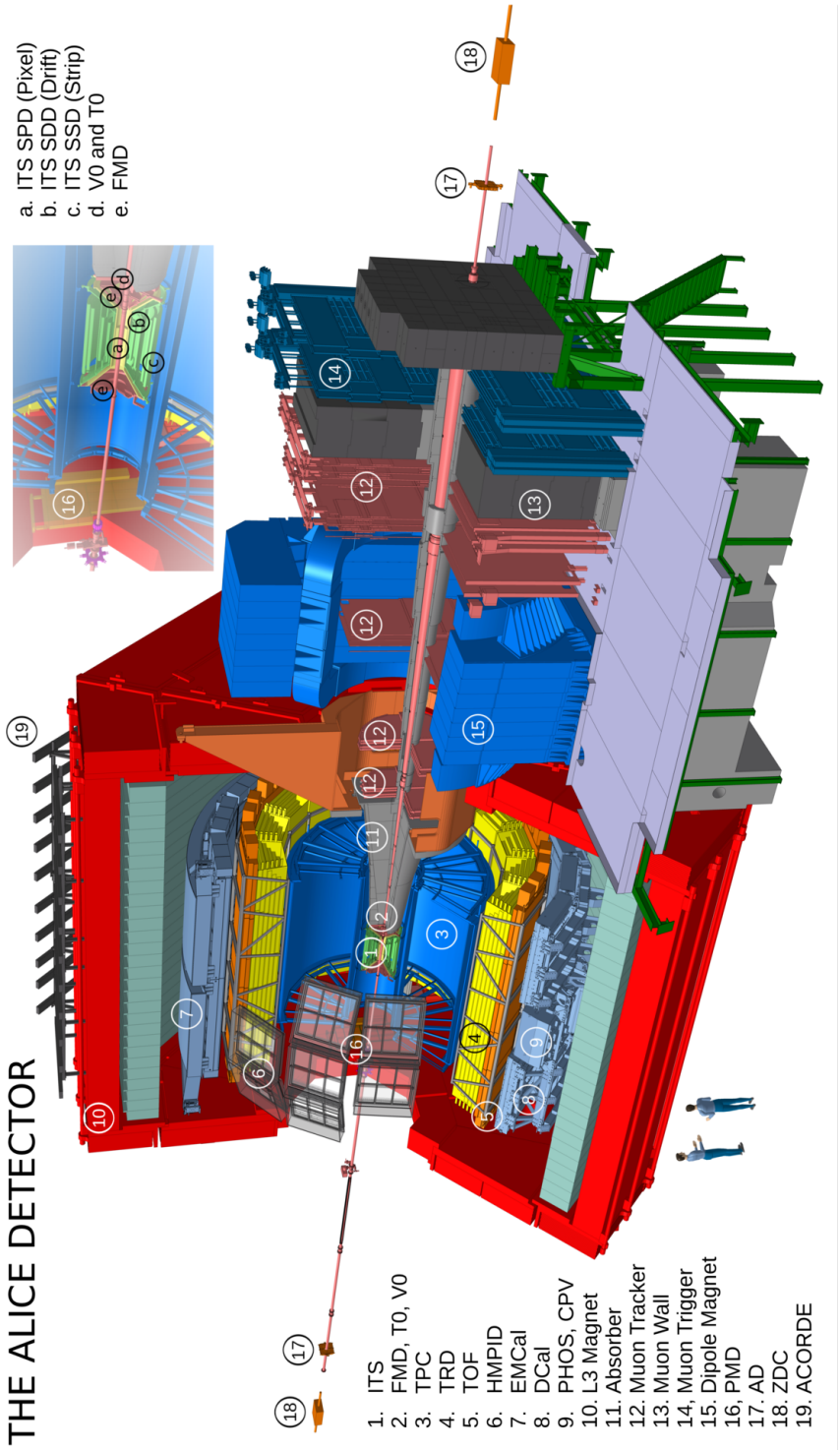

Figure 3.2: The ALICE experimental apparatus with the names of the sub-detectors. Figure taken from ALICE figure repository.

can also provide a fast trigger signal. The SDD and SSD provide the determination of energy loss that is used for the particle identification (PID) of low-momentum particles, and SSD is crucial for the prolongation of tracks from the TPC to the ITS during the track reconstruction.

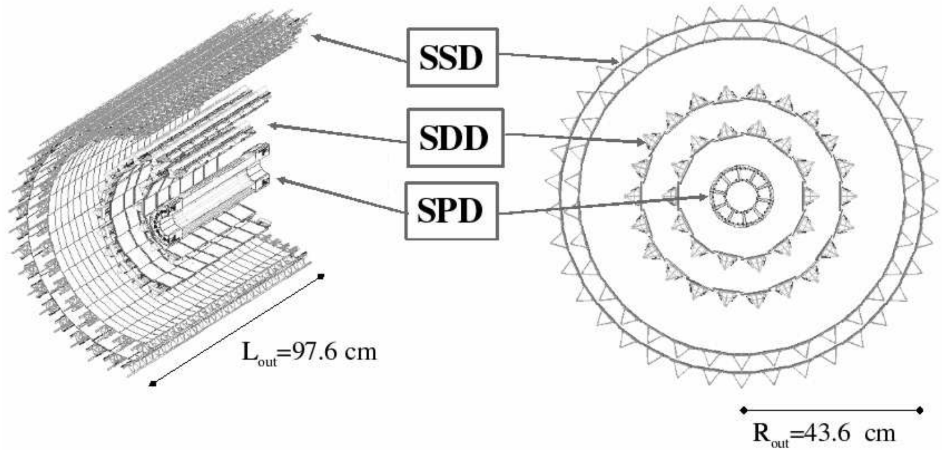

Figure 3.3: The Schematic layout of the ALICE Inner Tracking System. Figure taken from [124].

Detector	Layer	radius (cm)	$\pm z$(cm)	Area (m^2)	spatial resolution (μm)		two-track resolution	
					$r\varphi$	z	$r\varphi$	z
SPD	L1	3.9	14.1	0.07	12	100	100	850
	L2	7.6	14.1	0.14				
SDD	L3	15.0	22.2	0.42	35	25	200	600
	L4	23.9	29.7	0.89				
SSD	L5	38.0	43.1	2.20	20	830	300	2400
	L6	43.0	48.9	2.80				

Table 3.2: Details about the dimensions and spacial resolution of the ITS detector. Extracted from [124].

Time Projection Chamber (TPC)

The TPC is the main and biggest tracking detector in ALICE, whose main purpose is to provide track finding, momentum measurement and particle identification via dE/dx measurements. The TPC is a large cylindrical chamber surrounding the ITS, as shown in Fig. 3.4. The TPC is 500 cm long with inner radius of about 85 cm, outer radius 250 cm. It covers the whole azimuth and the pseudorapidity range $|\eta| < 0.9$. The endplates consists of 36 Multi-Wire Proportional Chambers (MWPC) with almost 560000 readout pads. The TPC is a gaseous detector which

is filled with a mixture of Ne, CO_2, and N_2[1]. When a charged particle travels in the sensitive volume of the TPC, it ionises the gas molecules in the chamber and creates free electrons and ions, which will drift towards the electrodes (electrons drift towards the anode and ions towards the cathode) owing to the presence of a electric field. When electrons arrive in the vicinity of the anode, because the electric field is inversely proportional to the distance to the anode, a very strong electric field is created. Therefore electrons in the field will gain enough energy to cause secondary ionisations, giving rise to a reaction chain, which is called "avalanche multiplication". Finally, a substantial voltage pulse is detected by the system, which reflects the deposited energy at the electrodes. If the voltage is not too high, the deposited energy at the electrodes is proportional to the energy deposited in the gas, giving the $\mathrm{d}E/\mathrm{d}x$ information of the ionizing particles. Thanks to this design, the TPC provides more than 90% efficiency in track finding, with a momentum resolution up to about 2% at p_{T} ~10 GeV/c for charged particles. The relative $\mathrm{d}E/\mathrm{d}x$ resolution in pp (Pb–Pb) collisions was measured to be 5% (6%) for particles crossing the entire detector.

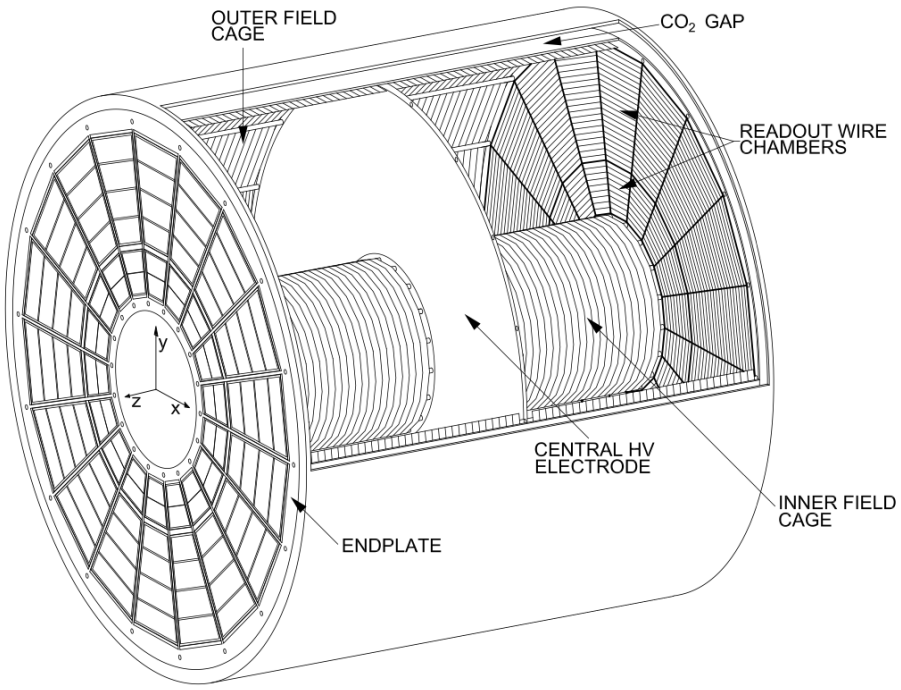

Figure 3.4: The Schematic layout of the ALICE Time Projection Chamber. Figure taken from [125].

[1]At the beginning of Run 2, the Ne was replaced with the Ar. However in 2017, the mixture was changed again to the Ne mixture, due to the larger space-charge distortions observed when using the Ar mixture.

Transition Radiation Detector (TRD)

The TRD is located outside of the TPC. Its main task is to identify electrons especially with momenta larger than 1 GeV/c according to the transition radiation of the charged particles crossing the detector [126]. The TRD consists of 522 chambers arranged in 18 sectors of 6 layers at a radial distance from 2.90 m to 3.68 m from the beam direction. It covers the full azimuth and the pseudorapidity range $-0.84 < \eta < 0.84$. When charged particles pass through the boundary of the radiator and the chamber, photons are emitted by the charged particles due to transition radiation, then the energy loss of the charged particles can be measured in the drift chamber. In addition, the TRD has also been successfully used to trigger on electrons with high transverse momenta and jets, thanks to is fast read out and online reconstruction of its signals.

Time of Flight (TOF)

The TOF detector is arranged around the TRD. It also covers the pseudorapidity range $|\eta| < 0.9$. Its main purpose is to identify the particles in the intermediate momentum range from 0.2 to 2.5 GeV/c [127]. The TOF shape is cylindrical with the inner and outer radius of 370 and 399 cm, and has a length of 745 cm. This is a gaseous detector made of Multigap Resistive Plate Chamber (MRPC), to generate a very high electrostatic field uniform over the whole sensitive volume. Consequently, when particles pass through this field, the subsequent ionisation will immediately start a gas avalanche process which will eventually generate the observed signals on the pick-up electrodes. There is no time jitter associated with the drift of the electrons to a region of high electric field. The time resolution is below 40 ps.

High Momentum Particle Identification Detector (HMPID)

The HMPID is used to identify charged particles at transverse momenta of $1 < p_{\mathrm{T}} < 3$ GeV/c for charged pions and kaons, and $1 < p_{\mathrm{T}} < 5$ GeV/c for protons. The HMPID is a Ring imaging Cherenkov detector consisting of two main parts: a radiator medium, where the Cherenkov light is produced, and a photon detector providing patterns for particle identification [128, 129].

The PHOton Spectrometer (PHOS)

PHOS is an electromagnetic calorimeter positioned on the bottom of the ALICE set up. It covers approximately a quarter of a unit in pseudorapidity, $|\eta| < 0.12$, and 100° in azimuthal angle. The main task of PHOS is to measure the photons as well as neutral mesons in the di-photon decay channel [130].

The ElectroMagnetic Calorimeter (EMCal)

EMCal is a sampling calorimeter based on lead/scintillator layers used for the measurement of electrons, isolated direct photons and neutral mesons to study jet

quenching. It covers the azimuthal angle up to 110° and its pseudorapidity acceptance is $|\eta| < 0.7$. In addition, an extension of EMCal, denominated DCAL (Di-jet Calorimeter), was installed to expand the physics capabilities of the EMCAL by enabling back-to-back correlation measurements [131].

The ALICE cosmic ray detector (ACORDE)

ACORDE consists of an array of plastic scintillator counters placed on the three upper faces of the magnet. It is usually used as the cosmic ray trigger for ALICE. In addition, it can also detect the single atmospheric muons and multi-muon events, together with some of other tracking detectors.

3.2.2 Global Detectors

As shown in Tab. 3.1, there are several smaller detectors (ZDC, PMD, FMD, V0, T0) located at forward and backward rapidities, which are used for event characterization and triggering. They are described in the following.

Zero Degree Calorimete (ZDC)

The ZDC is placed on the beam axis and both sides of the interaction point, to intercept the spectator nucleons in collisions which fly away in the forward direction [132]. The main purpose of the ZDC is to suppress the beam-gas background interactions and to determine the centrality (multiplicity) of the nucleus-nucleus (pp, p–Pb) collisions. The ZDC consists of two electromagnetic calorimeters (ZEM), two tungsten-quartz neutron calorimeters (ZN) and two brass-quartz proton calorimeters (ZP). The ZN and ZP calorimeters are both placed at a distance of 112.5 m from the interaction point, which are used for the detection of neutrons and protons respectively. The ZEM calorimeters are located at 7.25 m away from the interaction point and is used to differentiate the most central and most peripheral collisions by detecting the energy carried by photons in the forward direction.

Photon Multiplicity Detector (PMD)

The PMD is mainly used to measure the multiplicity and the spatial distribution of photons, aiming to study event shapes and fluctuations in the forward rapidity region [133]. The PMD is placed at the distance of 367 cm from the interaction point. It has a fine granularity, full azimuthal coverage and a pseudorapidity acceptance $2.3 < \eta < 3.9$. It consists of a preshower detector and a veto detector. Both of them are based on a honeycomb proportional chamber design. When charged particles and photons arrive in this field, the charged particles are rejected by a veto detector and photons pass through a converter then initiate an electromagnetic shower and produce large signals on several cells, which are recorded by the detector.

Forward Multiplicity Detector (FMD)

The FMD is a segmented silicon strip detector, which consists of 3 sub-detectors: FMD1, FMD2, and FMD3 [134]. FMD1 consists of one ring, FMD1i, while FMD2 and 3 are composed of two rings each, FMD2i, FMD2o, FMD3i, and FMD3o. The FMD has a broad coverage in pseudorapidity and full azimuth coverage with a modest segmentation. The overall placement and parameters of the FMD sub detectors are shown in Tab. 3.3. The main task of FMD is to provide a high resolution charged-particle multiplicity determination at very forward rapidity, which allows ALICE to give a more complete picture of the bulk properties of the interactions in heavy-ion collisions. For instance, the long-range correlations between the particles measured in the central barrel and FMD can be constructed to obtain the anisotropic flow, while the nonflow contributions can be obviously suppressed.

Ring	Azimuthal sectors	Radial strips	z[cm]	r range [cm]	η coverage
FMD1i	20	512	320	4.2 – 17.2	3.68 – 5.03
FMD2i	20	512	83.4	4.2 – 17.2	2.28 – 3.68
FMD2o	40	256	75.2	15.4 – 28.4	1.70 – 3.68
FMD3i	20	512	-75.2	4.2 – 17.2	-2.29 – -1.70
FMD3o	40	256	-83.4	15.4 – 28.4	-3.40 – -2.01

Table 3.3: Overview of parameters of the FMD sub detectors. Extracted from [135].

V0

The V0 is a small-angle detector consisting of two circular arrays of 32 scintillator counters each, called V0A and V0C, which are installed on the two sides of the interaction point. As shown in Tab. 3.1, the V0A detector is located 329 cm from the interaction point in the pseudorapidity range $2.8 < \eta < 5.1$, while the V0C is placed in $-3.7 < \eta < -1.7$ at 88 cm from the interaction point. The main purpose of the V0 is to provide the online L0 trigger, background rejection and centrality determination [134].

T0

The T0 detector is composed of two arrays of Cherenkov radiators, called T0A and T0C. They cover the pseudorapidity range $-3.3 < \eta < -2.9$ and $4.5 < \eta < 5$, respectively. The main tasks of T0 are to provide fast timing signals which will be used in the L0 trigger of ALICE, and a wake-up call for the TRD, and to deliver the collision time reference for the TOF detector [134].

3.2.3 Forward Muon Spectrometer

The main role of the ALICE muon spectrometer is to study the production of quarkonia, low-mass resonances, $W^{\pm}/Z^{0}$ bosons and heavy quarks at forward rapidity via their (di-)muonic decays. The muons can be identified and reconstructed

in the polar angle range from 171° to 178°, which corresponds to an interval of pseudorapidity $-4 < \eta < -2.5$. As shown in Fig. 3.5, the muon spectrometer consists of an absorber system, a dipole magnet, a set of high resolution tracking chambers and a trigger system. Each of them is described in the following.

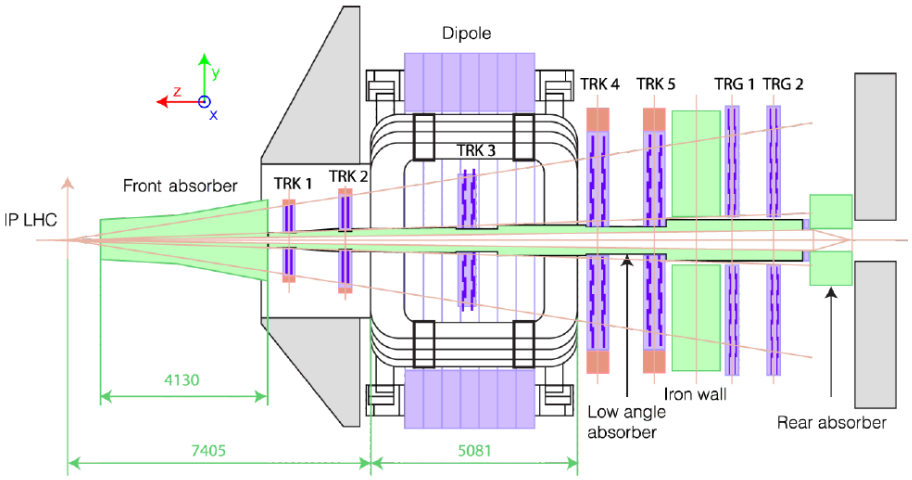

Figure 3.5: The Schematic layout of the ALICE Muon Spectrometer. Figure taken from [136].

3.2.3.1 The Absorber System

The absorber system is composed of four absorbers: the front absorber, the beam shield, the muon filter and the rear absorber. The front absorber is a 4.1 m long cone made of carbon, concrete and steel, as shown in Fig. 3.6. The main two tasks of the front absorber are to suppress the forward flux of charged particles by at least two orders of magnitude and decrease the background of muons from the decay of pions and kaons. In order to protect the following tracking and trigger chambers from secondary particles generated in the beam pipe, a beam shielding, which is made of W, Pb and stainless steel, covers the beam pipe along the length of the muon spectrometer. An additional absorber, called muon filter, is located between the last tracking chamber and the first muon trigger station. It consists of a 1.2 m thick iron wall, which aims to stop almost all hadrons punching through the front absorber (or produced in this absorber). Finally, there is a rear absorber located at the end of the muon spectrometer. It is used to protect the trigger chambers from particles produced in beam-gas interactions.

3.2.3.2 Dipole Magnet

The dipole magnet, as shown in Fig. 3.7, is placed 7.4 m from the interaction point with an overall length of 5 m. It can provide an horizontal magnetic field perpendicular to the beam axis with the magnetic flux density ($B_{\text{norm}} = 0.67$ T, 3

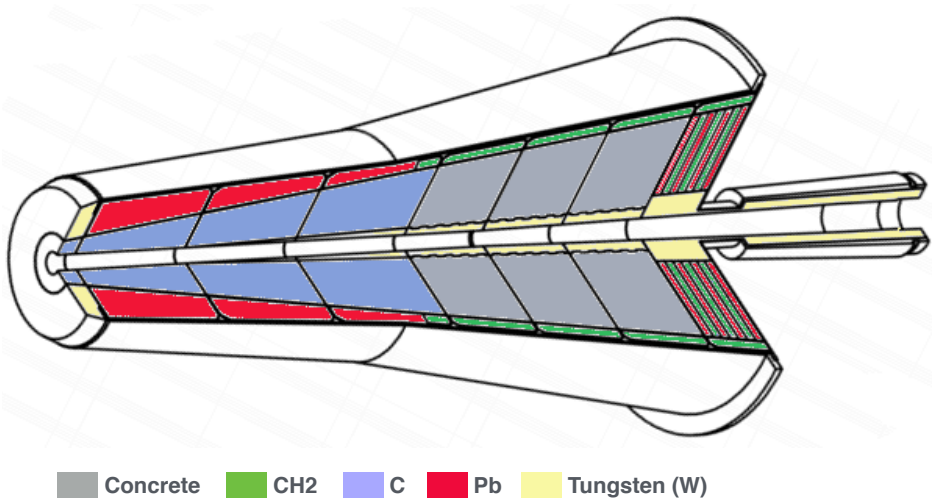

Figure 3.6: The Schematic layout of the absorber. Figure taken from [137].

Tm field integral between IP and muon filter) defined by the requirements on the mass resolution. It can bent the tracks reconstructed in the tracking chambers in order to determine the particle momentum and electric charge.

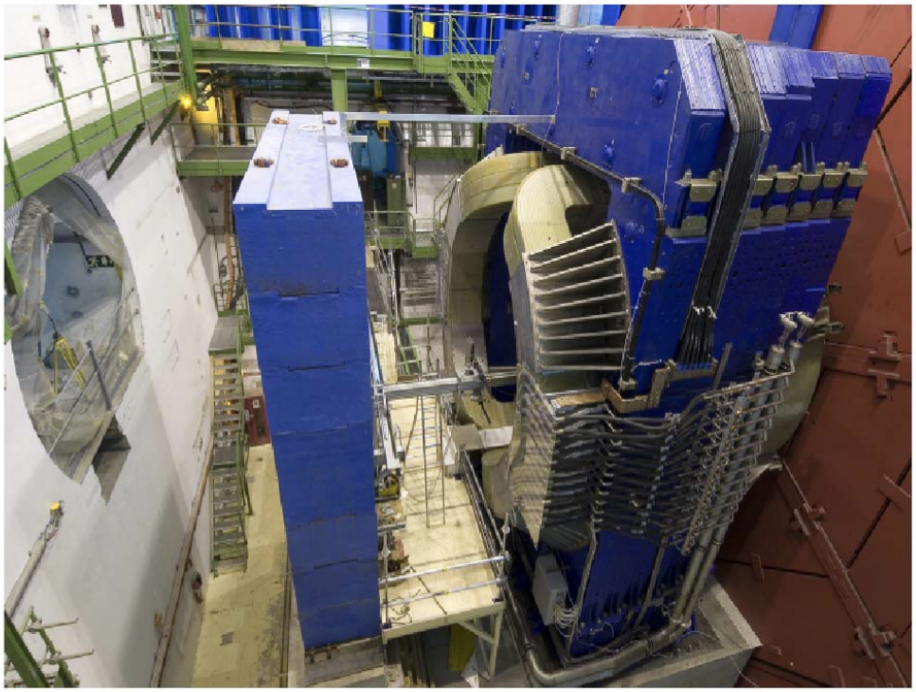

Figure 3.7: The Schematic layout of the dipole magnet. Figure taken from [138].

3.2.3.3 Muon Tracking Chambers (MCH)

The tracking system is designed to reconstruct the three-dimensional information of particles. It consists of five tracking stations. The first two stations, called Station 1 and 2 are placed before the dipole magnet, while the third tracking station, called Station 3 is inside the dipole magnet. The last two tracking stations, called Station 4 and 5 are placed between the dipole magnet and the muon filter, as shown in Fig. 3.5. Each tracking station has two planes of Multi-Wire Proportional Chambers (MWPC) with two cathode planes readout. Those two cathode planes are segmented into many pads as shown in Fig. 3.8. The magnetic field follows the x-axis. The plane called the non-bending cathode has finer segmentations in the x-direction. The plane with finer segmentations in the y-direction corresponds to the bending plane. The wires are supplied by a high voltage of 1600–1650 V and the cathode planes are grounded. Hence, the electric field is formed with a strongest field near the wires. The space between the two cathode planes is filled with a gas mixture of Argon (80%) and CO_2 (20%). The segmentation of the cathode pads is designed to keep the occupancy at a 5% level. Since the hit density decreases with the distance from the beam pipe, larger pads are used at larger radii. This enables to keep the total number of channels at about one million.

Multiple scatterings of the muons measured in the chambers are minimized by using composite material, such as carbon fibers. Although based on standard MWPC design, the individual chambers have been adapted to meet the particular constraints on the different tracking stations. The chambers of the first two stations are based on a quadrant structure, with the readout electronics distributed on their surface, as shown in Fig. 3.9. The other three chambers have a slat structure and their electronics are implemented on the side of the slats, as shown in Fig. 3.10.

For all tracking stations, the front-end electronics is based on a 16-channel chip called Multiplexed ANAlogic Signal (MANAS) processor including the following functionalities: charge amplifier, filter, shaper and track. The channels of four of these chips are fed into a 12-bit ADC, read out by the Muon Arm Readout Chip (MARC) which includes zero suppression. This chain is mounted on a front-end board, the MAnas NUmerique (MANU): the 1.08 milion channels of the tracking system are treated by about 17000 MANU cards. Up to 26 MANUs are connected to the translator board which allows the data transfer to the Concentrator ReadOut Cluster Unit System (CROCUS, for a total number of 20 CROCUS). The main tasks of the CROCUS are to concentrate data from the chambers, to ship them to the Data AcQuisition (DAQ), to perform the calibration of the front-end electronics and to dispatch the signals to the Central Trigger Processor (CTP).

3.2.3.4 Muon Trigger System

The muon trigger system is designed to reduce the collision events without muon tracks or low p_{T} muons tracks, since the low p_{T} muons contain a large fraction of $\pi^{\pm}$ and $\mathrm{K}^{\pm}$ decays, instead of heavy-flavour hadrons, electroweak bosons or quarkonium. The system has two trigger stations (MT1 and MT2) located after the muon filter,

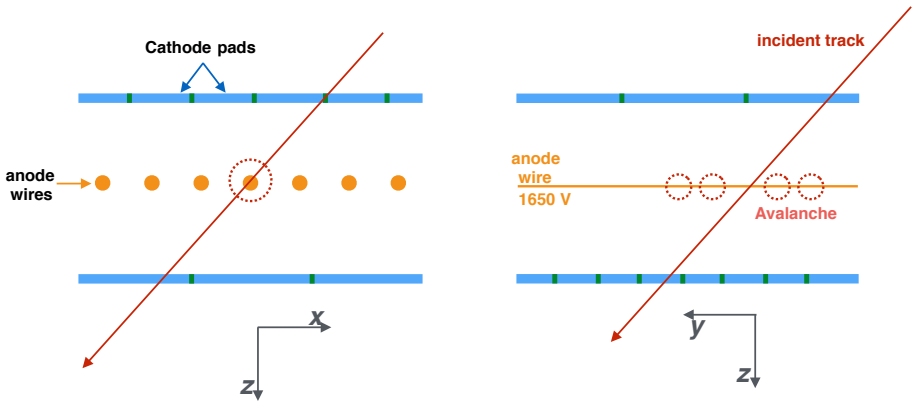

Figure 3.8: The layout and working principle of a MWPC viewed in two planes. Figure taken from [137].

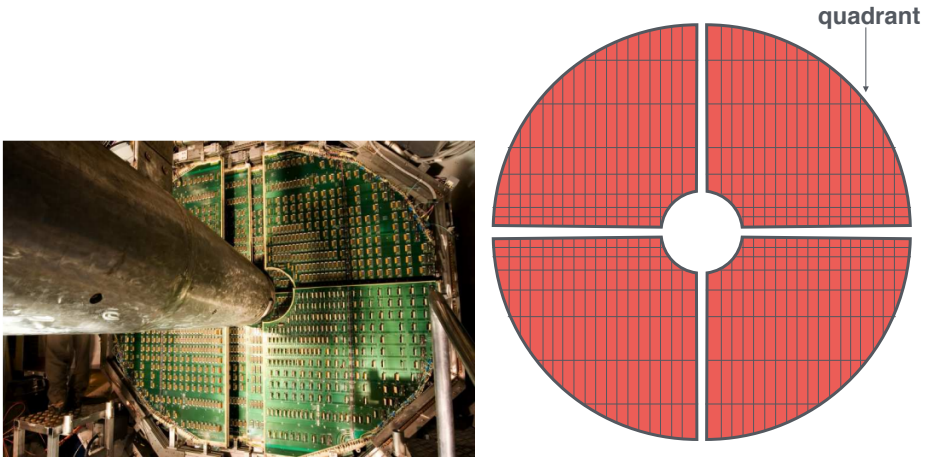

Figure 3.9: A picture of a chamber in station 2 (left) and a schematic view of the quadrant structure (right). Figure taken from [137].

16 meters away from the interaction point, as shown in Fig. 3.11. Each station consists of two planes of 18 Resistive Plate Chambers (RPCs). RPCs are large area detectors, made up of high resistivity ($\sim 3 - 9 \times 10^9 \Omega$m) bakelite electrodes separated by a 2 mm wide gas gap. The surface of the bakelite foils on the gap side is painted with linseed oil, while the external surface is painted with graphite, with one layer connected to the high voltage and the other to the ground, as shown in

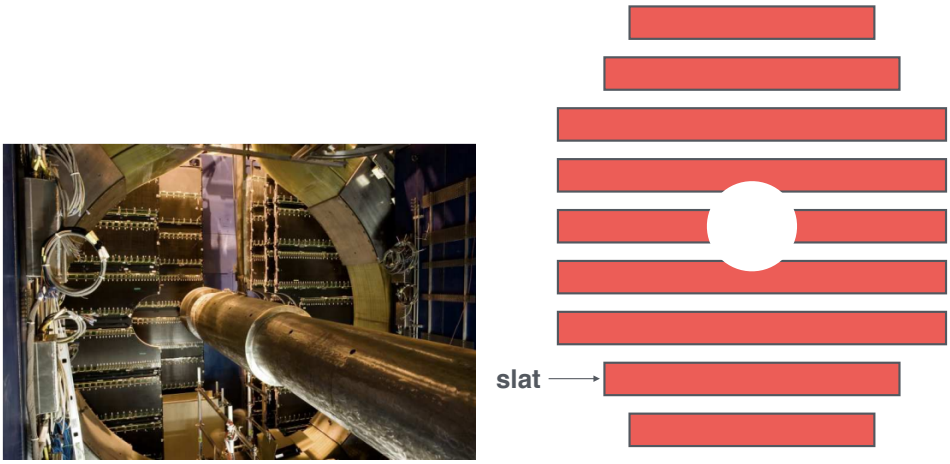

Figure 3.10: A picture of a chamber in station 4 (left) and a schematic view of the slat structure (right). Figure taken from [137].

Fig. 3.12. The signal is picked up by read-out strips connected with the Front-End Electronics (FEE), which basically consists of a leading-edge discriminator stage followed by a shaper. The strips are placed on both sides of the chambers, in order to provide a bi-dimensional information [139]. The horizontal strips measure the bending deviation due to the dipole magnetic field, while vertical strips measure the non-bending direction. The two layers of read-out pads are therefore called "bending" and "non-bending" plane, respectively.

The space inside the two plates is filled with a gas mixture Ar $+C_2H_2F_2+$ i-butane $+SF_6$ (50.5/41.3/7.2/1). When charged particles pass through the gas, an avalanche of secondary electrons is produced and causes the signals. The signals, transmitted by the strips, give the spatial information of the traveling particles. From the position of the track in the two trigger stations, different p_T cuts can be applied on the muon track according to the following algorithm, as shown in Fig. 3.13. A muon detected in tracking chambers is bent by the dipole magnetic field and crosses the trigger stations MT1 and MT2 in Y_2 and Y_2 respectively. Assuming that a muon with infinite p_T passes through the dipole magnet following a straight line trajectory, it is located in Y_1 at MT1. Then it arrives in MT2 at coordinate $Y_{2,\infty}$. The p_T cut can be applied through a cut on the deviation $\delta Y_2 = Y_2 - Y_{2,\infty}$ which is inversely proportional to the muon p_T. The sign of δY_2 can also identify the sign of the muon. Usually ALICE delivers the four following trigger signals to the muon trigger system:

- at least one single muon satisfying a low p_T cut, called "single muon low p_T (0MSL)"
- at least one single muon satisfying a high p_T cut, called "single muon high p_T (0MSH)"

- at least one unlike-sign muon pair, each muon satisfying low (high) p_{T} cut, called "unlike-sign dimuon low (high) p_{T}" (0MUL(0MUH));
- at least one like-sign muon pair, each muon satisfying low (high) p_{T} cut, called "like-sign dimuon low (high) p_{T}" (0MLL(0MLH));

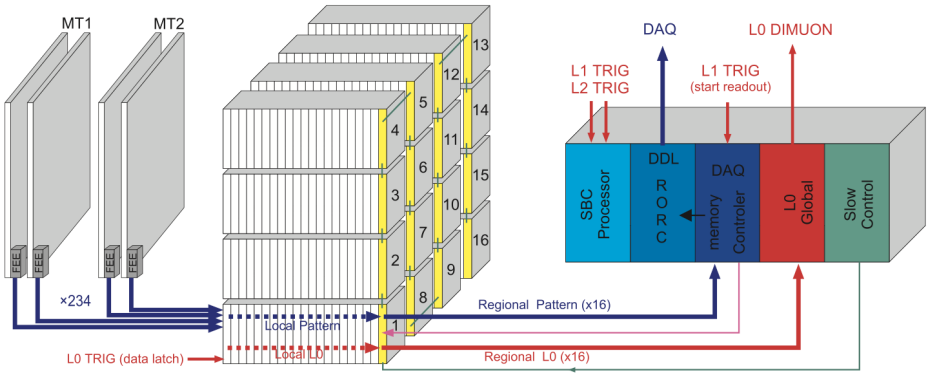

Figure 3.11: Overview of ALICE muon trigger system. Figure taken from [140].

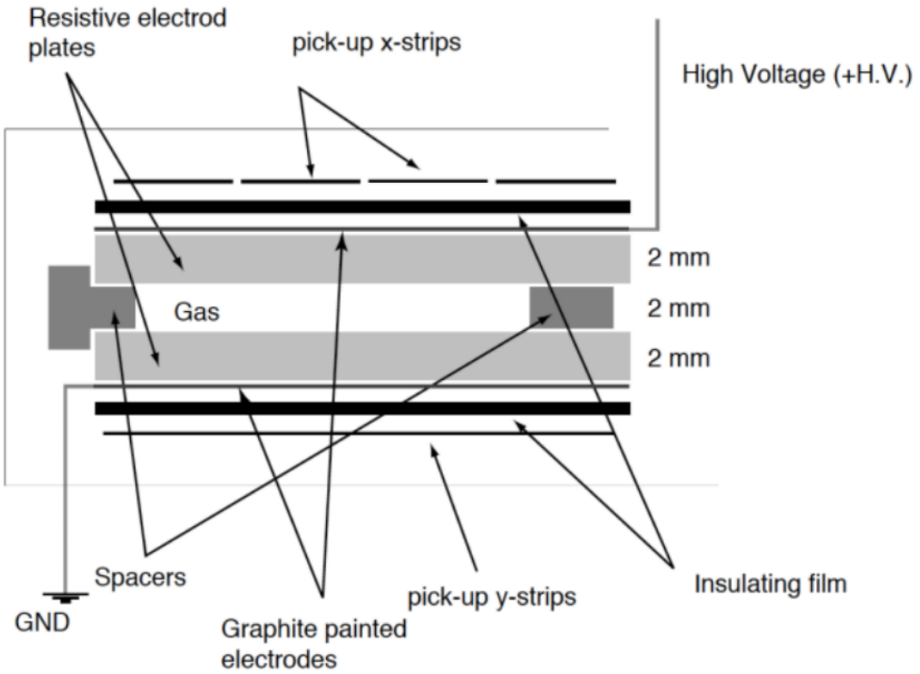

Figure 3.12: The structure of the RPC of the muon trigger system. Figure taken from [141].

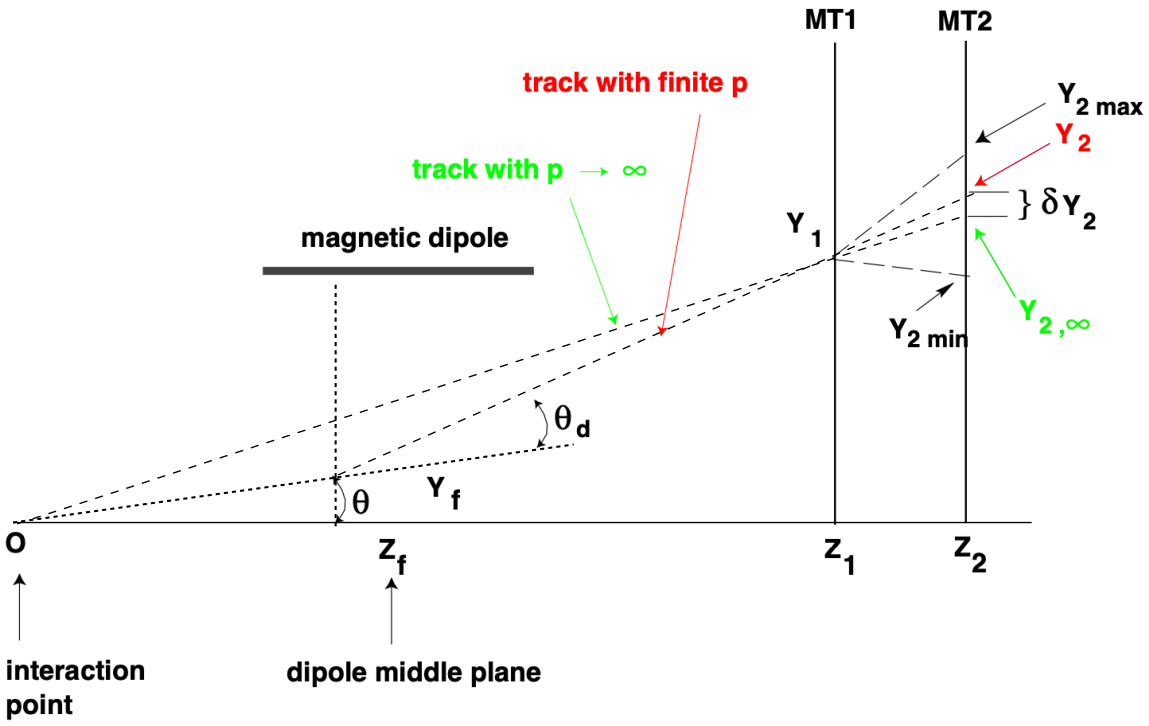

Figure 3.13: A sketch of the working principle of the muon trigger algorithm. Figure taken from [140].

3.3 Data processing and reconstruction

From data collected with the detectors in data analysis, a treatment chain of data processing and reconstruction is employed by the ALICE online and offline systems. It includes three parts which are described in this section. In the first part, the data is processed in the ALICE online system, which includes the Trigger System (TRG) and Data Acquisition System (DAQ), the High-Level Trigger (HLT) and Detector and Experiment Control systems(DCS, ECS). Some of the contents of this part are taken from [142]. In the second part, the events are reconstructed and can be analyzed directly, including - but not limited to - primary vertex reconstruction, track reconstruction and centrality determination. In the third part, analyzers develop their own analysis framework to extract the desired physics information.

3.3.1 ALICE Online System

Due to the various technical limitations in the form of read-out rates and response time of different detectors, processing speed, and even overall file storage capacity, not all collisions need to be processed and recorded. The TRG system can select events having a variety of different features at rates which can be scaled down to suit physics requirements and the restrictions imposed by the bandwidth of the DAQ system and the HLT. In addition, the DCS ensures safe and correct operation of ALICE detectors during the data taking, and the ECS coordinates the operations controlled by all online systems (DCS, DAQ, TRG, HLT).

3.3.1.1 Trigger System

The trigger system is developed based on an electronic system. The input to the trigger is represented by triggering detectors which send the electronic signal to the trigger when a collision occurs. The output from the trigger is represented by the readout detectors which detect the collision[2]. The signals from triggering detectors to the trigger system are called "trigger inputs", and the signals from trigger to readout detectors are called "signals" or simply "triggers". In the trigger system, the Central Trigger Processor (CTP) is the decision maker. The CTP consists of seven different types of 6U Versa Module Eurocard (VME) boards housed in a single VME crate. The signals are distributed to the readout detectors using the Local Trigger Unit (LTU). The transmission of trigger signals to each detector is mediated by one of these boards [124].

The challenge for the ALICE trigger is to make optimum use of the component detectors, which are busy for widely different periods following a valid trigger, and to perform trigger selections in a way which is optimised for several different running modes: ion (Pb-Pb and several lighter species), pA, and pp, varying by almost two orders of magnitude in counting rate. The ALICE trigger system is designed as a 3-level trigger system. It can have three consecutive trigger inputs - L0, L1 and L2 and three consecutive signals (or triggers) - also called L0, L1 and L2. The L0 signal reaches detectors at 1.2 ms, but it is too fast to receive all the trigger inputs. The L1 signal arrives at 6.5 ms, which picks up all remaining fast inputs. Note that the CTP decisions are made in 100 ns, with the rest of the L0 latency coming from the generation time for the trigger input signals and from the cable delays. The L2 trigger waits for the end of the past-future protection[3] interval (88 ms) to verify that the event can be detected. This interval can also be used for running trigger algorithms.

To be more efficient, many triggering detectors are grouped together (they form the so-called **make class**) to give more than 1 trigger input. Meanwhile, several readout detectors are also grouped together (the so-called **make cluster**) to measure the events. Detectors are read in and out in groups, known as classes and clusters.

[2]Note that triggering detectors can be also readout detectors.

[3]The past-future protection is kind of procedure to ensure that the events selected for readout are not spoilt by pile-up [124].

The advantage is that while the slow detectors are processing some event, during that time other fast detectors can process other events. Classes are not represented only by trigger inputs. There are more settings associated with the class like for instance the past-future protection. In general, class defines all trigger input settings. For instance, in the trigger class **CMSL7-B-NOPF-MUFAST**, the string **CMSL7** represents the combination of trigger inputs 0MSL (single muon low p_{T} trigger), V0-A and V0-C; the string **B** means that the current bunch crossing is open for physics analysis; **NOPF** means that no past-future protection is implemented; **MUFAST** means two clusters **MUON** and **FAST** are read out.

When several trigger classes are running concurrently, it becomes necessary to adjust the rates at which they are read out to reflect the physics requirements and the overall DAQ bandwidth. These factors may dictate rates quite different from the natural interaction rates. There are two main mechanisms for controlling readout rates. Downscaling factors may be applied to each trigger class. This mechanism allows gross adjustments to be made, but is inflexible because the downscaling factors remain in place throughout a physics run. In addition to downscaling factors, a second method is used. According to the features of physical process, all trigger classes are classified into two groups: those corresponding to rare processes and those corresponding to common processes. For a signal from the DAQ, if the occupied temporary storage exceeds some preset high mark [124], the common classes are temporarily disabled, thus ensuring that enough bandwidth is assigned for rare processes. When the available temporary storage has gone below some corresponding low mark, the common classes are again enabled. In this case, timing is not critical, and software signals are adequate for toggling the suppression of common classes, due to the long relaxation time [124].

3.3.1.2 Data Acquisition System

The function of the DAQ system is to realize the dataflow from the detector up to the data storage, including the dataflow to and from the High-Level Trigger (HLT) farm as well as sub-event and complete event building. The DAQ system also includes software packages for raw data integrity and system performance monitoring and overall control of the DAQ system. The trigger and DAQ systems were designed to give different observables a fair share of the trigger and DAQ resources with respect to DAQ bandwidth for frequent triggers and detector livetime for rare triggers. The trigger and DAQ systems must balance the capacity to record central collisions which generate large events with the ability to acquire the largest possible fraction of rare events [124].

3.3.1.3 High-Level Trigger

The High-Level Trigger combines and processes the full information from all major detectors in a large computer cluster. Its task is to select the most relevant data from the large input stream and to reduce the data volume by well over an order of magnitude in order to fit the available storage bandwidth while preserving

the physics information of interest. This is achieved by a combination of techniques:

- reducing the event rate by selecting interesting events (software trigger);
- reducing the event size by selecting sub-events;
- reducing the event size by advanced data compression.

All three tasks require at least partial event reconstruction. In order to meet the high computing demands, the HLT consists of a PC farm of up to 1000 multi-processor computers. The data processing is carried out by individual software components running in parallel on the nodes of the computing cluster. In order to keep inter-node network traffic to a minimum and for the means of parallelisation, the HLT data processing follows the natural hierarchical structure. Local data processing of raw data is performed directly on the Front-End Processors (FEPs). Global data processing, with already reduced data, is done on the computing nodes. The trigger decision, Event Summary Data (ESD) of reconstructed events and compressed data are transferred back to the DAQ via the HLT output DDLs [124].

3.3.1.4 Detector Control System and Experiment Control System

It is worth to mention that, condition data[4] are monitored continuously and archived by the Detector Control System (DCS). Some of these data (e.g. temperatures and pressures) affect the detector response and thus are relevant for event reconstruction, which will be processed offline. Those calibration parameters that can be derived from raw data are extracted during data taking, from interaction events and/or dedicated calibration events. At the end of each run the condition data and the online calibration parameters are collected by the Shuttle system [143] and transported to the Offline Conditions DataBase (OCDB). The Experiment Control System (ECS) provides a unified view of the experiment and a central point from where all operations are initiated and controlled. It also has to allow independent concurrent activities on parts of the experiment (at the detector level) by different operators. Finally, it has to coordinate the operations of the specific control system active on a lower level: the detector control, the trigger control, the DAQ run control and the High-Level Trigger control.

3.3.2 ALICE Offline Project

The data after the processing in several online systems described above, is called "raw data". It needs to be reconstructed step by step, which starts with a local reconstruction of clusters in each sub-detector, then, the vertex reconstruction, track reconstruction, particle identification and event characterization as well. During the reconstruction, the calibration parameters stored in OCDB are extracted to improve reconstructed data quality (e.g. resolution, minimisation of biases, particle identification etc.). After that, the raw data is transformed to Event Summary Data

[4]The conditions data includes the information about the detector status and environmental variables.

(ESD), which contains all accessible information at both event and particle level for data analysis. Furthermore, to reduce the size of the files and the computational time needed for the analysis, the ESD data is refiltered and finally transformed to Analysis Object Data (AOD) data, which contains only the information needed for the physics analysis.

3.3.2.1 Calibration Chain

The reconstructed data quality critically depends on the quality of the calibrations used in the reconstruction. The first two reconstruction passes are performed on a sample of events from each run and serve for calibration and monitoring purposes. The first pass is called "CPass0", which starts promptly after the data taking. It provides input for the calibration of TPC, TRD, TOF, T0, and centrality. The second pass is the so-called "cPass1", it applies the calibration obtained from CPass0, and then the reconstructed events are used as input for data Quality Assurance (QA) and for improved calibration of SDD, TPC, and EMCal. After CPass0/1 is done for all runs of a period, a around 4-day window is opened for quality assurance checks and manual calibration. The complete calibration is then verified by a validation pass (vpass) performed on a sample of events from all runs in the period. The subsequent physics reconstruction pass (ppass) is performed on all events and provides the input for physics analysis [122]. Figure 3.14 shows the working flow of ALICE calibration and reconstruction. It is worth mentioning that some fast reconstruction for detectors do not need the automatic calibration of CPass0/1, for example the "muon_calo" reconstruction. It involves the detectors: MUON, EMCAL, PHOS, T0, ITS, V0, ZDC, AD. It starts promptly after the data taking and in parallel with CPass0/1, and its QA is performed in parallel with QA of CPass1.

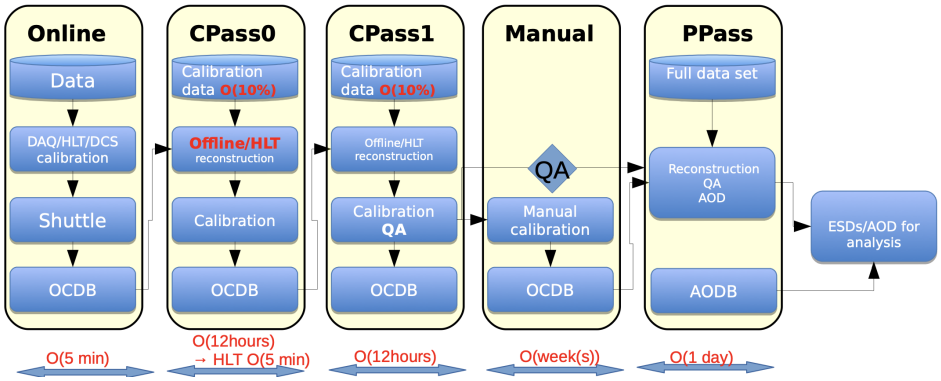

Figure 3.14: The working flow of ALICE calibration and reconstruction. Figure taken from [144].

3.3.2.2 Track and Vertex Reconstruction

Track reconstruction (tracking) is a complex and crucial process during the offline reconstruction, in which the raw signals measured by individual detectors are transformed into complete trajectories representing the path left by physical particles passing through the ALICE apparatus. The main ALICE tracking detectors include ITS, TPC, TRD and muon spectrometer. The first step of the tracking procedure is to digitize the raw signals from individual detectors to obtain digits. Then a set of digits that were presumably generated by the same particle crossing the sensitive element of a detector are converted into a cluster. Generally the center of gravity of the cluster is estimated as the position where a particle crossed the detector, it is called space point. The errors on the space point positions are parameterized as a function of the cluster size and of the deposited charge. For example, the space points reconstructed in the SPD layers of the ITS are then used for a first estimation of primary vertex, which is an essential step in track reconstruction.

The estimation of the primary vertex is actually to figure out where the collision happens. In this step, two algorithms for the determination of the primary vertex coordinates are implemented, they are called **VertexerSPDz** and **VertexerSPD3D**. They are both based on the reconstruction of **SPD tracklets**, which are track segments built by associating pairs of reconstructed points in the two SPD layers within an azimuthal acceptance window [123]. The VertexerSPD3D provides a three-dimensional measurement of the primary vertex by means of the SPD tracklets. The algorithm is used in pp and pA collisions by default. The VertexerSPDz provides the measurement of the $z-$coordinate of the primary vertex assuming that the beam position in the transverse plane is known with an acceptable accuracy. It is usually used when VertexerSPD3D method fails in low-multiplicity events. In addition, the primary vertex estimated by the SPD will be further determined with the so-called **VertexerTracks** algorithm by means of the constructed tracks, as described below[5].

After the primary vertex is estimated, everything is ready for the track reconstruction process, as illustrated in Fig. 3.15. The whole procedure contains five steps along in three paths:

- 1^{st} path, inward from TPC to ITS
  - The initial approximations for the track parameters (so-called seeds) of primary particles are constructed at two outer TPC pad rows by using pairs of space points on it. Then, the seed is regarded as the starting point for a track propagation towards the primary vertex, which is estimated by the two innermost layers of ITS. Such propagation is performed by means of a Kalman filter algorithm [145]. During this step, the track seeds are extended from one pad row to another in the TPC towards the primary vertex, whenever a new space point is found within a prolongation path.

[5]For events triggered by the forward muon spectrometer, there is no need to read and reconstruct the events in the central barrel detectors, so only the SPD is used to provide the primary vertex position.

The track parameters are updated using the Kalman filter, until the inner radius of the TPC is reached. Meanwhile, the energy loss information $\mathrm{d}E/\mathrm{d}x$ given by the TPC is also recorded to provide a preliminary particle identification, which will be used for energy loss correction in the next steps.

- The tracks reconstructed in the TPC are matched to the outermost ITS layer and then become the new seeds for the track finding in the ITS. Following the same procedure with the TPC, the current track is further to be extrapolated inward down to the innermost pixel layer. In addition, the hits in the ITS which are not attached to tracks propagated from the TPC, will be used to reconstruct the ITS standalone track, in order to increase the efficiency for tracks with low p_{T}. The ITS standalone track will not participate in the following steps.

- 2^{nd} path, outward from ITS

  - Similarly, the last point reconstructed in the previous step (labeled as ITSin in Fig. 3.15) is used as the new seed, the tracks reconstructed in the ITS are back-propagated to the outermost layer of the ITS and then to the outermost radius of the TPC, with again the Kalman filter algorithm. Afterwards, the extrapolation is performed to match the clusters in outer TRD and TOF detectors, and even the signals in EMCal, PHOS and HMPID. The information of particle identification $\mathrm{d}E/\mathrm{d}x$ is updated during this stage.

- 3^{rd} path, inward to ITS

  - Finally, the tracks are re-fitted inward in all the previously used clusters and propagated back to the point of distance of closest approach (DCA) to the primary vertex applying the Kalman filter to the space points already attached. At this stage, a set of reconstructed tracks is used to re-evaluate the primary vertex position with the optimal resolution.

The above-mentioned procedure is illustrated in the case of reconstructing primary particles, i.e. the particles with a mean proper lifetime τ larger than 1 cm/c [146]. While for the reconstruction of particles originating from the weak decays of strange, charm and beauty particles, such as K^0_{S} and $\Lambda(\bar{\Lambda})$, the track is considered as secondary and does not contribute to the primary vertex re-evaluation. In this case, the so-called **secondary vertices** are reconstructed by all secondary tracks. The secondary vertex finding is performed by combining all pairs of reconstructed secondary tracks with opposite charges. If the impact parameter (defined as the distance of closest approach between the track trajectory and the primary vertex) between the two secondary tracks is small enough, the corresponding secondary vertices found on the line of their closest approach is recorded as a potential candidate for a weak decay vertex.

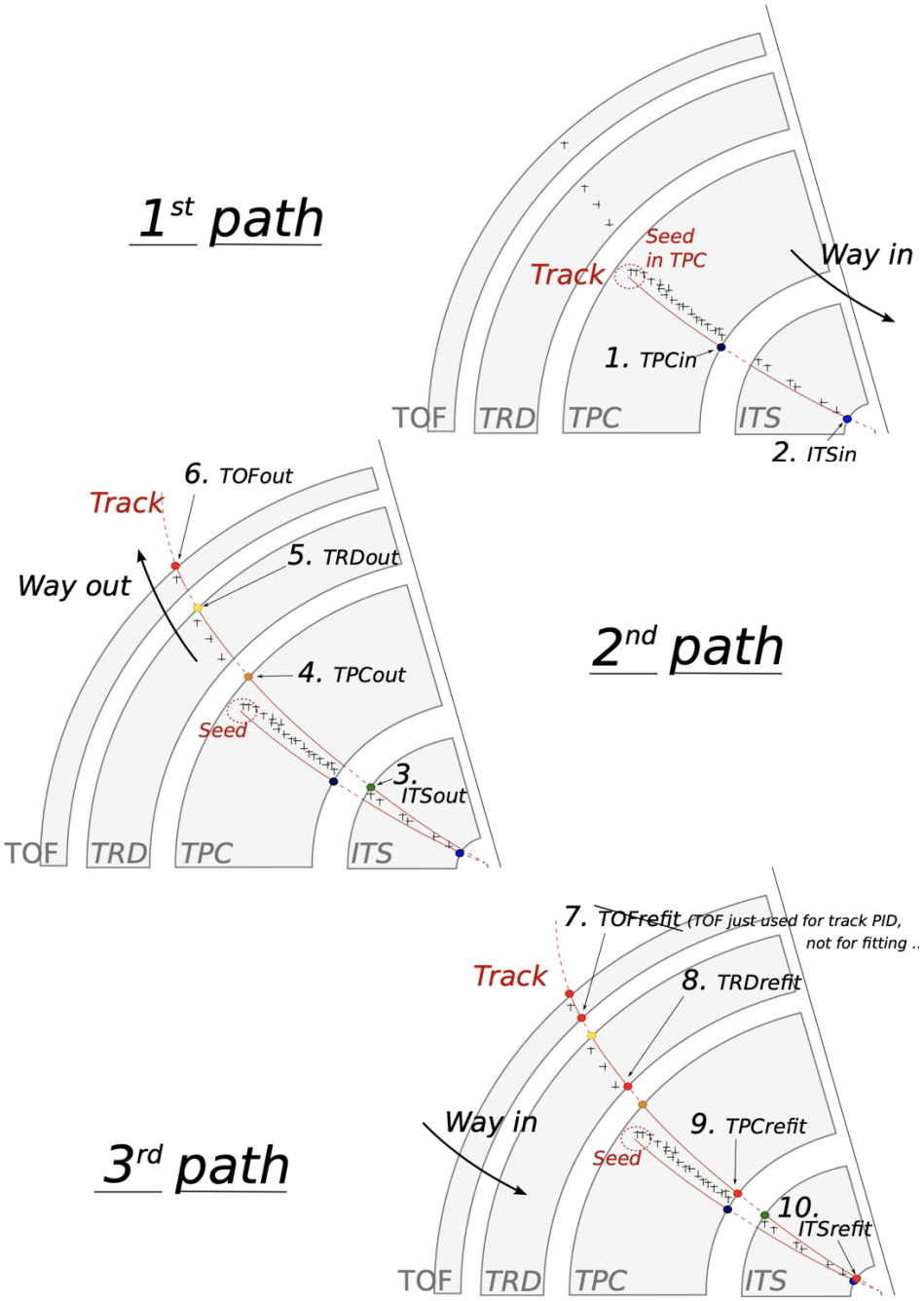

Figure 3.15: The working flow of TPC track reconstruction. Figure taken from [147].

3.3.2.3 Centrality Determination

As described in Sec. 1.2.1, the impact parameter is an important observable to characterize a heavy-ion collision. However, this quantity can not be measured experimentally. Two measurable quantities that are related monotonically to the

impact parameter, are the charged-particle multiplicity and the energy deposited in the ZDC by the spectator nucleons. The centrality of nuclear collisions, which is usually expressed in percentiles of the total inelastic hadronic cross section σ_{AA}, is introduced to express the geometry of heavy-ion collisions. The centrality percentile c of a A–A collision with impact parameter b is defined [148]:

$$c(b) = \frac{\int_0^b \frac{\mathrm{d}\sigma}{\mathrm{d}b'}\mathrm{d}b'}{\int_0^\infty \frac{\mathrm{d}\sigma}{\mathrm{d}b'}\mathrm{d}b'} = \frac{1}{\sigma_{\mathrm{AA}}}\int_0^b \frac{\mathrm{d}\sigma}{\mathrm{d}b'}\mathrm{d}b'. \tag{3.1}$$

Furthermore, the centrality can be experimentally computed with the charged-particle multiplicity (N_{ch}) or energy deposited in the ZDC (E_{ZDC}) according to:

$$c \approx \frac{1}{\sigma_{\mathrm{AA}}}\int_{N_{\mathrm{ch}}}^\infty \frac{\mathrm{d}\sigma}{\mathrm{d}N'_{\mathrm{ch}}}\mathrm{d}N'_{\mathrm{ch}} \approx \frac{1}{\sigma_{\mathrm{AA}}}\int_0^{E_{\mathrm{ZDC}}} \frac{\mathrm{d}\sigma}{\mathrm{d}E'_{\mathrm{ZDC}}}\mathrm{d}E'_{\mathrm{ZDC}}. \tag{3.2}$$

The cross section can be replaced with the number of reconstructed events (N_{ev}):

$$c \approx \frac{1}{N_{\mathrm{ev}}}\int_{N_{\mathrm{ch}}}^\infty \frac{\mathrm{d}n}{\mathrm{d}N'_{\mathrm{ch}}}\mathrm{d}N'_{\mathrm{ch}} \approx \frac{1}{N_{\mathrm{ev}}}\int_0^{E_{\mathrm{ZDC}}} \frac{\mathrm{d}n}{\mathrm{d}E'_{\mathrm{ZDC}}}\mathrm{d}E'_{\mathrm{ZDC}}. \tag{3.3}$$

Eq. 3.2–Eq. 3.3 are based on the assumption that the centrality increases (or decreases) monotonically with the particle multiplicity (or the zero-degree energy). It is worth to mention that for peripheral collisions (i.e. centrality $> 50\%$), the assumption is no longer valid, because nuclear fragments emitted in peripheral collisions may be deflected out of the ZDC, which breaks the monotonicity of the energy deposited in ZDC. This ambiguity can be solved by correlating the ZDC energy deposit with the energy deposit in the ZEM [149].

In Pb–Pb collisions, the centrality is usually determined by the particle multiplicity measured in the V0, as shown in Fig. 3.16. The V0 amplitude is the sum of V0A and V0C amplitudes, requiring a coincidence of V0 and the SPD, and using the ZDC to reduce the electromagnetic dissociation background. The distribution is restricted to events with a primary vertex position within $|Z_{\mathrm{vertex}}| < 10$ cm, and fitted with the Glauber Monte Carlo based on a negative binomial distribution (NBD). The centrality bins are defined by integrating from right to left following Eq. 3.3. As described in Sec. 1.2.1, for an event with a given impact parameter b, the corresponding N_{part} and N_{coll} can be defined from Glauber model. To apply this model to any collision with a given N_{part} and N_{coll} value, we introduce the concept of "ancestors", which represent the independent emitting sources of particles. Considering the two-component models [21], the number of ancestors $N_{\mathrm{ancestors}}$ is assumed to be parameterized as

$$N_{\mathrm{ancestors}} = f \cdot N_{\mathrm{part}} + (1-f) \cdot N_{\mathrm{coll}}, \tag{3.4}$$

where f is a free parameter. In this case, the NBD, which is used to generate the number of particles produced per interaction, can be defined as

$$P_{\mu,k}(n) = \frac{\Gamma(n+k)}{\Gamma(n+1)+\Gamma(k)} \cdot \frac{(\mu/k)^n}{(\mu/k+1)^{n+k}}, \tag{3.5}$$

where μ is the mean multiplicity per ancestor and k controls the width. Therefore, from the fit of V0 amplitude shown in Fig. 3.16, $N_{\rm part}$ and $N_{\rm coll}$ can be also extracted following Eq. 3.4 and Eq. 3.5.

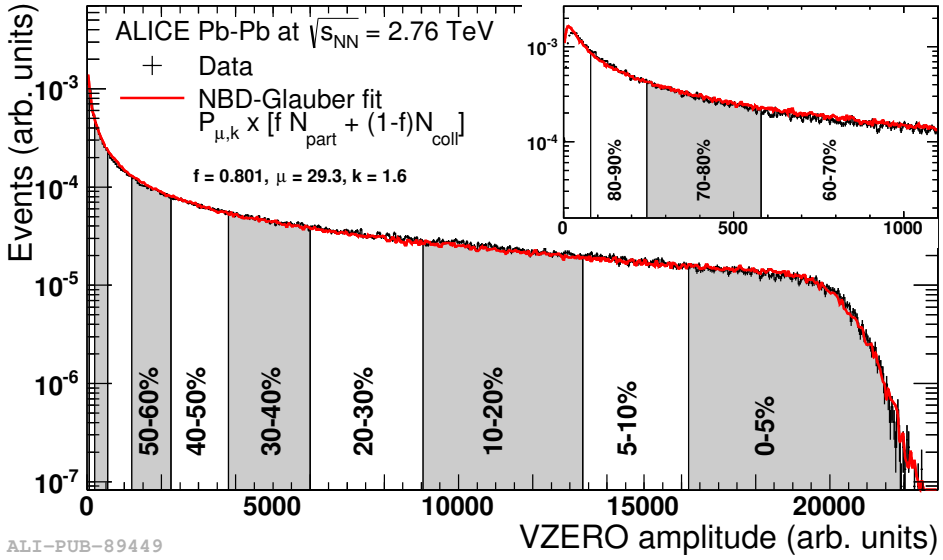

Figure 3.16: Distribution of the V0 amplitude. The distribution is fitted with the NBD-Glauber function, shown as a red curve. The inset shows a zoom of the most peripheral region. Figure taken from [149].

In p–Pb collisions, the centrality determination procedure applied is as that described above. Figure 3.17 (top) shows the distribution of amplitudes in the V0A, as well as the NBD-Glauber fit for p–Pb collisions at $\sqrt{s_{\rm NN}}$ = 5.02 TeV. The $N_{\rm part}$ and $N_{\rm coll}$ quantities in a given centrality class can also be calculated [150]. Similar fits are also performed when using V0M and CL1[6] estimators. However the centrality estimation is biased by three additional effects in p–Pb collisions compared to the Pb–Pb case:

- **Multiplicity bias** Sizeable multiplicity fluctuations are observed in p–Pb collisions compared to Pb–Pb collisions, which results in the centrality selection based on multiplicity different from that using impact parameter b intervals, especially for most central and peripheral collisions. To reduce this bias, the estimator located in the Pb fragmentation region is usually chosen to characterize the centrality for p–Pb or Pb–p data sample;

- **Jet-veto bias** For very peripheral collisions, the multiplicity range that governs the centrality for the bulk of soft collisions can represent an effective veto on hard processes, which shifts events to higher centralities. The CL1 estimator is biased strongly by this effect since it has full overlap with tracking region;

[6]The number of clusters in the outer layer of the Silicon Pixel Detector, $|\eta|$ <1.4.

- **Geometrical bias** The mean impact parameter between two nucleons is almost constant for central collisions, but rises significantly for low-multiplicity collisions ($N_{\text{part}} < 6$). It results in a purely geometrical, centrality estimator independent bias for peripheral p–Pb collisions.

In addition to the V0 and CL1 estimator, the ZNA (ZNC) is also used for centrality determination in p–Pb (Pb–p) collisions. As shown in Fig. 3.17 (bottom), the experimental distribution of the ZDC energy is fitted using a Glauber Monte Carlo based on the slow nucleon emission (SNM) model [150], to extract the centrality classes and N_{coll}. Compared to CL1 and V0, ZN is expected to be an unbiased centrality estimator in p–Pb collisions.

3.3.2.4 Analysis Framework

Two separated frameworks are developed, AliRoot and AliPhysics. AliRoot is mainly used for data processing and offline reconstruction steps, which are described in Sec. 3.3.2.2. It also contains common classes used for general analyses. Most of individual analysis codes are stored in AliPhysics, which are implemented as C++ class objects. In addition, the Offline Analysis DataBase (OADB) stored in AliPhysics contains the calibrations needed at the analysis level, e.g. the centrality percentiles information from estimators[7]. The AliPhysics is updated daily for needs of the running tasks for ALICE users, while updates of AliRoot happen less frequently.

3.4 Upgrade of ALICE in Run 3

As mentioned in Sec. 3.2, ALICE is the only experiment dedicated to the heavy-ion physics at the LHC. During the Run 1 and Run 2, plenty of comprehensive measurements were performed with ALICE, confirming the creation of QGP at unprecedented values of temperature, density and volume, as described in Sec. 1.3. They also exceed the precision and kinematic range of all significant probes of the QGP that had been measured over the past decade. However, due to limitations of detectors, some high precision measurements of rare probes over a broad range of transverse momenta can not be accessed. After the second LHC Long Shutdown (LS2) in 2019–2021, the ALICE collaboration upgraded the detectors. Combined with a significant increase of luminosity, that will greatly improves the measurements of observables such as the heavy-flavour hadrons and decay leptons (down to very low p_{T}), charmonium and bottomonia states, jets, low-mass dileptons and heavy nuclear state [151]. In order to achieve these physics goal, three new detectors have been installed. The Inner Tracking System (ITS), which has been completely replaced at midrapidity, aims to provide a precision improvement by a factor more than three for the reconstruction of heavy-flavour decay vertices [152]. A Muon Forward Tracker (MFT) has been added in front of the muon spectrometer, which

[7] The centrality selection can be processed easily according to running task "AliMultSelectionTask" in AliPhysics.

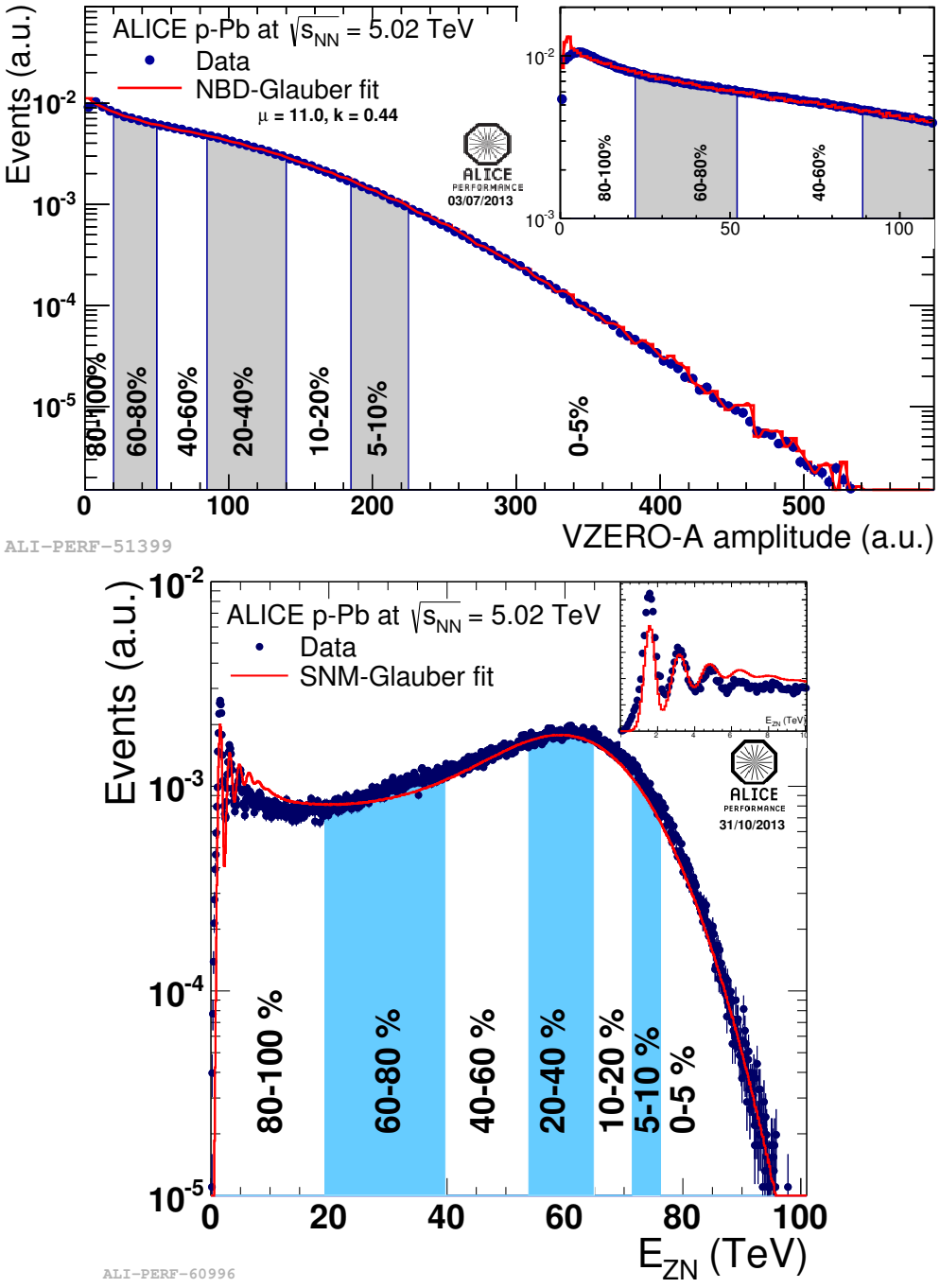

Figure 3.17: Top: distribution of the V0A amplitude, fitted with the NBD-Glauber function, shown as a red curve. Bottom: distribution of the neutron energy spectrum measured in the Pb-remnant side ZN calorimeter, compared with the corresponding distribution from the SNM-Glauber model [150], shown as a red curve. The inset shows a zoom of the most peripheral region. Figure taken from [150].

improve the reconstruction capability for muon-based measurements at forward rapidity. Moreover, a new Fast Interaction Trigger (FIT) detector system has been constructed and placed on both sides of the interaction point. In addition, more of detectors have been upgraded in order to allow for a continuous readout in the upcoming Run 3.

3.4.1 Upgrade of the Central Barrel and Global Detectors

Inner Tracking System 2

The new Inner Tracking System is called "Inner Tracking System 2" (ITS2), which is made of 7 cylindrical layers of silicon pixel detectors, arranged coaxially to the beam line and centered on the interaction point, as shown in Fig. 3.18. The detector can be divided into two parts: the innermost three layers form the Inner Barrel (IB); the middle two and the outermost two layers form the Outer Barrel (OB). Since the ITS2 is designed to improve both vertex and tracking precision, the innermost layer radius is 22 mm, which is much smaller than that in the ITS (39 mm). The ITS 2 is the first large-area silicon tracker based on the CMOS Monolithic Active Pixel Sensor (MAPS) technology operating at a collider [153]. The ALPIDE, the pixel chip developed for the ITS 2, has been designed to perform in-pixel amplification, shaping, discrimination and multi-event buffering while absorbing less than 40 mW/cm^2 of specific power [154]. The pixel pitch is of 27×29 μm^2 and the detection efficiency is $> 99\%$. The ITS 2 can withstand a particle rate of 100 MHz/cm^2 without pile-up. In addition, the high accuracy on secondary vertex determination can be provided by the ITS 2 due to the exceedingly low material budget. It enhances the resolution of impact parameter by a factor of three, therefore the measurement of charm and beauty mesons can be accessible down to zero p_{T} with high precision.

Time Projection Chamber

As mentioned in Sec. 3.2, the readout of the electrons generated inside the TPC active volume was performed by Multi-Wire Proportional Chambers (MWPC) in the Run 2. However, the readout rate is limited to few kHz since there is a wire gating grid which is used to minimize ion backflow into the TPC [154]. In Run 3, the TPC will be operated continuously with new readout chambers that have intrinsic ion-blocking capabilities [151]. Therefore the Gas Electron Multiplier (GEM) technology is applied, and the gated MWPC is replaced with quadruple GEM stack. This new readout chamber consists of inner- and outer-readout chambers with a 4 stage GEM cascade in order to reduce back-drifting ion space charges. In addition, these quadruple stacks can provide ion blocking capabilities [155].

Fast Interaction Trigger Detector

The new FIT [155] is a detector system placed along the beam line, which is composed of three sub-systems, the FV0, FT0 and FDD. The FV0 is the upgrade

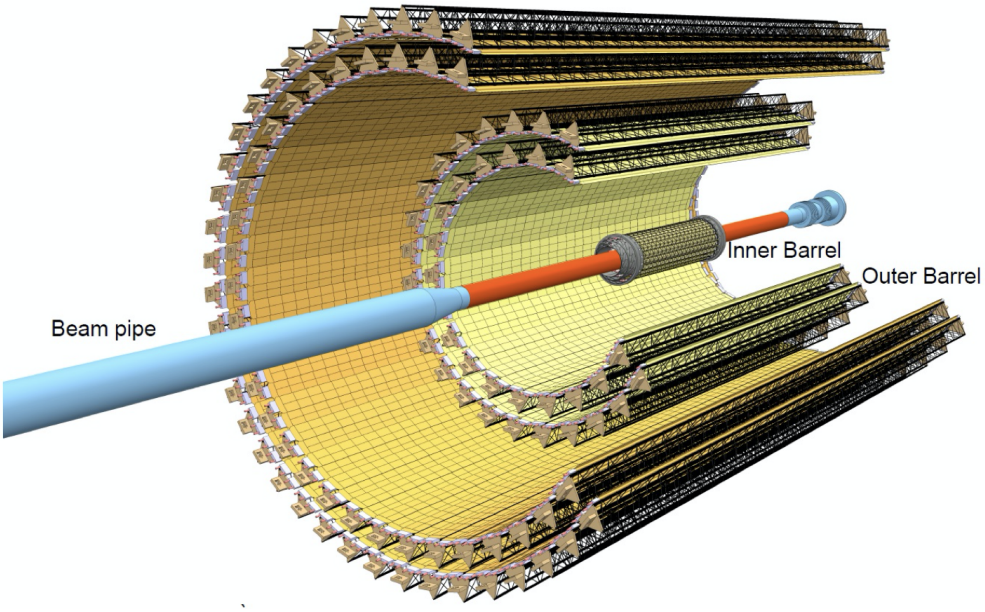

Figure 3.18: The layout of the ITS2 detector. Figure taken from [154].

of the V0. It is placed 3.5 m from the interaction point on the opposite side of the Muon Spectrometer, covering the rapidity interval 2.2< η <5.0. The FT0 consists of two quartz Cherenkov radiators, FT0-A and FT0-C, placed on opposite sides with respect to the interaction point. The main task of FT0 is to measure the collision time, which is subsequently used in TOF-based particle identification. The FDD is formed from two nearly identical scintillators arrays, FDD-A and FDD-C, which are placed on both sides of the interaction point at 17 m and 19.5 m distance, covering the rapidity acceptance up to $\eta = 6.9$. They are used to distinguish the diffractive events, to measure the diffractive production cross section and ultra-peripheral collisions products.

3.4.2 Upgrade of the Forward Muon Spectrometer

For the muon spectrometer, the main limitation comes from the multiple scattering effects induced on the muon tracks by the front absorber, which results in the inability to determine precisely the muon production vertex. The open charm and open beauty production can not be disentangled, as well as the prompt and displaced J/Ψ mesons [156]. In addition, the high background muons coming from the semi-muonic decays of pions and kaons and limited mass resolution for the light neutral resonances, both give difficulties to open the possibility of new measurements. Based on this, a comprehensive upgrade strategy of the muon spectrometer has been raised, which includes the upgrade of current muon tracking and the trigger chambers, and the installation of a new silicon pixel tracker called the Muon Forward Tracker (MFT).

The upgrade of the muon tracking chambers (MCH) mainly focus on the improvement of front-end electronics (FEE) and readout chain to cope with the higher rates in Run 3 and 4 [157]. In order to support the interaction rate of 50 kHz (Pb–Pb collisions), the design read-out rate has been set to 100 kHz as safety margin. Thus, a new read-out ASIC, called the SAMPA ASIC, was developed to provide continuous read-out. The present front-end (FE) boards have been replaced by new Dual SAMPA (DS) boards, each hosting two SAMPA chips providing a total of 64 readout channels. The data from the DS boards has been shipped out through FE links implemented on printed circuit boards. New concentrator boards (SOLAR) accumulate data from several DS boards through the FE links and send them to the new Common Readout Units (CRU) of the ALICE central Data Acquisition System. The muon trigger chambers has been upgraded to become the muon identifier (MID) which also works in continuous readout mode. The present FE chip, called ADULT [158], has been replaced by a new front-end chip, the so-called FEERIC. Unlike ADULT, FEERIC performs amplification of the analog signals from the Resistive Plate Chambers (RPCs). The RPCs will be operated in "genuine" avalanche mode with a significant reduction of the charge produced in the gas, hence limiting ageing effects [156]. Fig. 3.19 shows the efficiency of the RPC equipped with FERRIC as a function of time. The efficiency is very high (>97%) in both the bending and non-bending planes across different collision systems.

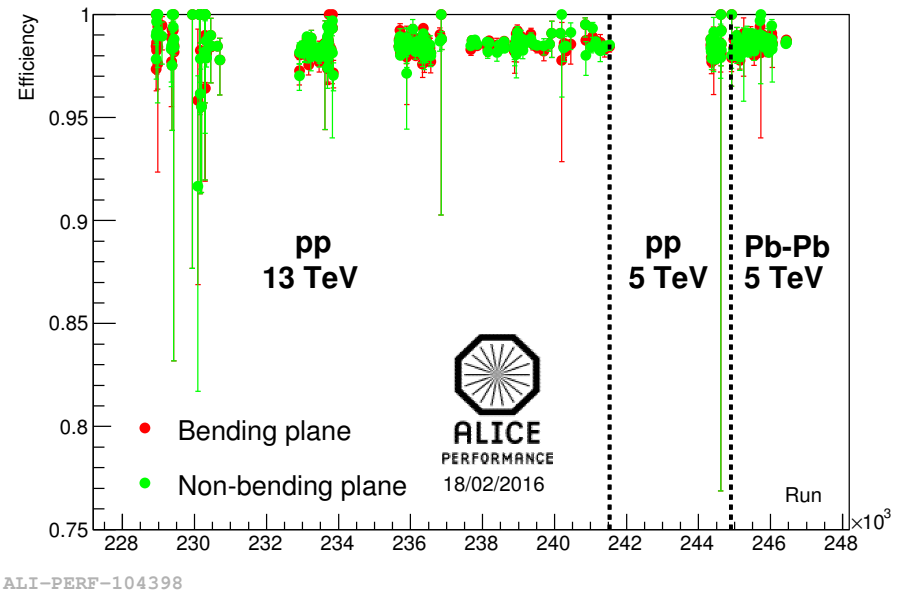

Figure 3.19: The efficiency of a Muon Trigger Chamber RPC equipped with FEERIC, measured in ALICE in 2015. Figure taken from [156].

The MFT is designed to add vertexing capabilities to the muon spectrometer. It surrounds the vacuum beam-pipe, and is positioned inside the ITS outer barrel

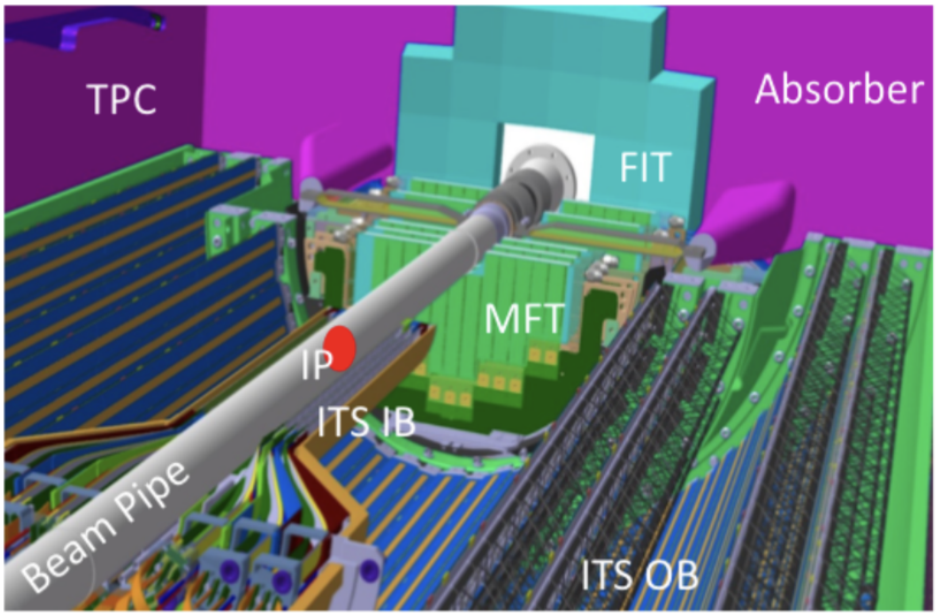

Figure 3.20: A sketch of the MFT in ALICE. Figure taken from [156].

and along the beam axis between the ITS inner barrel and the front absorber of the MUON spectrometer, as shown in Fig. 3.20. The MFT consists of two half-MFT cones, each of them consists of 5 half-disks placed along the beam axis, in the direction of the MUON spectrometer (C-side) at $z = -460, -493, -531, -687, -768$ mm from the interaction point [159]. The first two half-disks are identical (called Half-Disk-0 and 1), while the remaining three half-disks are all different and are called Half-Disk-2, Half-Disk-3 and Half-Disk-4, respectively. Figure 3.21 shows the x-y distributions of tracks measured in two sides of first two half-disks in pp collisions at 900 GeV, obtained from the first Run 3 pilot run in October 2021. The MFT covers the pseudo-rapidity range $-3.6 < \eta < -2.45$, which is almost overlapped by the acceptance of current muon tracking chambers. Thus in the future, the muon tracks reconstructed from the muon tracking chambers after the absorber will be matched to the MFT tracks before the absorber. It can result in high pointing accuracy, allowing a reliable measurement of their offset with respect to the primary interaction vertex. Thanks to the high-precision vertexing capabilities added by the MFT to the current muon spectrometer, a lot of new measurements will be accessible to ALICE, as summarised in Tab. 3.4.

3.4.3 The O^2 Project

During the ALICE data taking in Run 1 and Run 2, the online and offline systems have performed particularly well, allowing the experiment to collect and process data with a delivered performance surpassing the design specifications. After the second Long Shutdown (started in the end of 2018), the LHC has been upgraded, and will

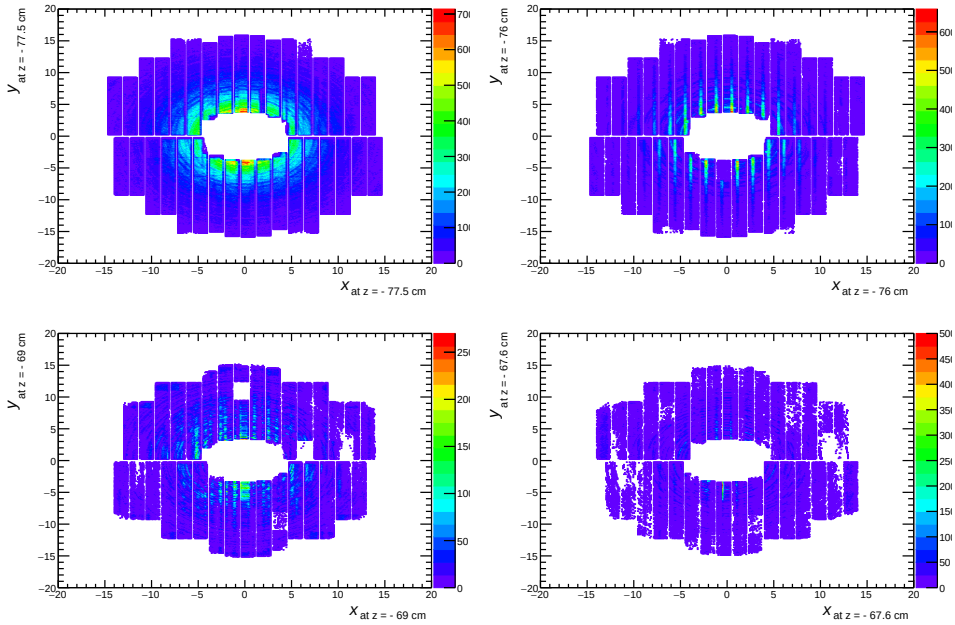

Figure 3.21: The x-y distribution of tracks measured at z = -77.5 (upper left), -76 (upper right), -69 (lower left), -67.5 (lower right) cm with MFT in pp collisions at 900 GeV. The data is collected from the pilot run 505548. Figure taken from [160].

Observable	p_{T}-coverage (GeV/c)
Charm	
Prompt J/ψ - R_{AA}, v_2	$p_{\mathrm{T}}(J/\psi)$>0
ψ(2S) - R_{AA}	$p_{\mathrm{T}}(\psi')$>0
μ from c-hadron decays - R_{AA}, v_2	$p_{\mathrm{T}}(\mu)$>1
Beauty	
Non-prompt J/ψ - R_{AA}, v_2	$p_{\mathrm{T}}(J/\psi)$>0
μ from b-hadron decays - R_{AA}, v_2	$p_{\mathrm{T}}(\mu)$>3
Chiral symmetry and QGP temperature	
Light vector mesons spectral functions and QGP thermal radiation	$p_{\mathrm{T}}(\mu\mu)$>1

Table 3.4: New physics measurements made possible by the MFT addition. Extracted from [159].

provide a higher collision rate. Therefore, the ALICE collaboration has consolidated many of the ALICE detectors, for example the main tracking detector TPC and new ITS (ITS 2) [161], the muon spectrometer, and a new forward tracker (MFT) has been installed. The trigger driven readout of Run 1 and Run 2 of up to 1kHz of Pb–Pb events is replaced by a continuous readout of all Pb–Pb events at 50 kHz in Run 3. Due to the extremely large data readout rate by the detectors, data

reduction techniques need to be adopted during data taking, synchronously. Not only the data format optimization techniques need to be improved and adapted, but it also concerns the output of the online reconstruction and calibration [162]. Therefore the ALICE Online-Offline (O^2) computation system was developed for the analysis in Run 3 and Run 4, which aims to construct the synergy of online and offline processing that existed as separated entities in Run 1 and Run 2.

In the new ALICE O^2 system, the ESD files are replaced by Compressed Time Frame (CTF) data, which are used for creating AOD files. The AOD files are in a compressed format, and named "AO2D" files in Run 3 and Run 4. They still contain the full event information, which can be used in all analyses. In addition, the current analysis framework, AliPhysics is also replaced in the ALICE O^2 system. It is not only because the data file with new format need new requirements, but also the computing resources need to be used more efficiently by means of multi-core and GPU computing. The development of the O^2 framework in each Physics Working Group (PWG) is still on-going at present, including the implementation of the muon analysis framework in Run 3. Figure 3.22 shows an example of performance plots for the MFT-track η and φ distributions obtained from the analysis of the pilot run (pp collisions at 900 GeV) within the O^2 framework.

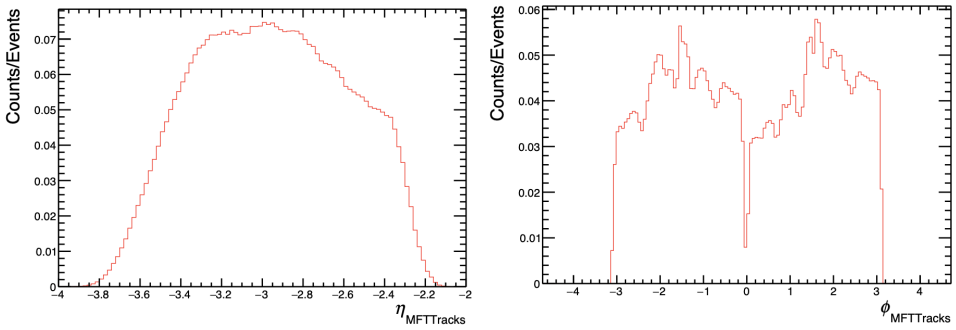

Figure 3.22: The pseudorapidity and azimuthal distribution of tracks measured in the MFT in pp collisions at 900 GeV. Figure taken from [160].

CHAPTER 4

Measurements of the Nuclear Modification Factor of Muons from Heavy-flavour Hadron Decays in Pb–Pb Collisions at $\sqrt{s_{\rm NN}} = 2.76$ and 5.02 TeV

As described in Sec. 1.3.2, heavy quarks (charm and beauty) are key probes of the QGP properties in heavy-ion collisions, since they are predominantly created in the early stage of the collision and experience the full evolution of the QGP medium. The measurements of the nuclear modification factor $R_{\rm AA}$ of heavy-flavour hadrons show a significant suppression of prompt and non-prompt D-meson yields measured at midrapidity in central Pb–Pb collisions with respect to the binary scaled pp reference cross section [163], which results from large in-medium energy loss of heavy quarks. Besides, the measurement of the nuclear modification factor $R_{\rm AA}$ of muons from heavy-flavour hadron decays at forward rapidity allows us to access a smaller Bjorken-x region. With the Pb–Pb data sample collected during the 2010 run, the first measurement of the $R_{\rm AA}$ of muons from heavy-flavour hadron decays with the ALICE detector at the LHC in Pb–Pb collisions at $\sqrt{s_{\rm NN}} = 2.76$ TeV was performed, as shown in Fig. 4.1 (left). It clearly shows a suppression of a factor of about 3−4 in $4 < p_{\rm T} < 10$ GeV/c in the most central collisions. In addition, the $R_{\rm AA}$ of muons from heavy-flavour hadron decays as a function of $\langle N_{\rm part} \rangle$ was also measured in Fig. 4.1 (right). These results show a larger suppression in central collisions than in peripheral collisions.

During the data taking in 2011, the muon triggers (as described in Sec. 3.2.3.4) are implemented. They enhance the statistics of muons in Pb–Pb collisions at $\sqrt{s_{\rm NN}}$ = 2.76 TeV. After the first long LHC shutdown in 2013, a new data sample at a higher centre-of-mass energy $\sqrt{s_{\rm NN}} = 5.02$ TeV was recorded during the Run 2. These new data samples with much higher luminosity compared to the 2010 data allow us to perform a more precise measurement of the $R_{\rm AA}$ of heavy-flavour decay muons and extend it to higher transverse momentum, where the contribution of muons originating from B-hadron decays is dominant. On the other hand, most advanced techniques are also employed, for example for the muon background subtraction, in the new analysis. In this chapter, we present the measurements of the $R_{\rm AA}$ of muons from heavy-flavour hadron decays in Pb–Pb collisions at $\sqrt{s_{\rm NN}} = 2.76$ and 5.02 TeV.

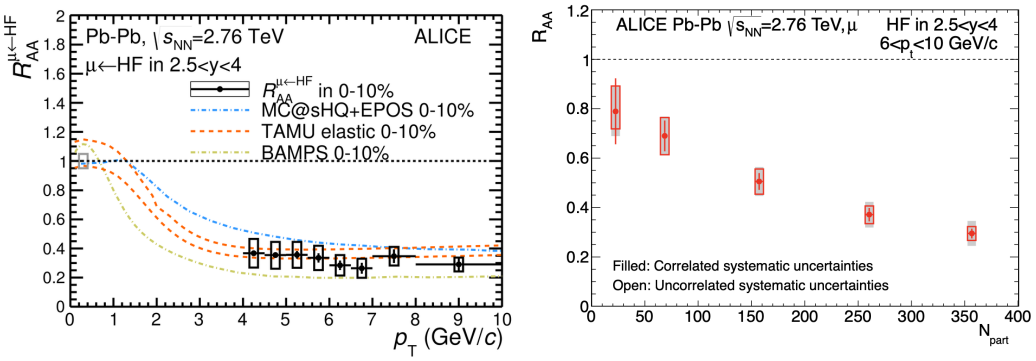

Figure 4.1: Left: p_{T}-differential R_{AA} of muons from heavy-flavour hadron decays for the centrality class 0–10%. Right: R_{AA} of muons from heavy flavour decays as a function of the mean number of participating nucleons, in $2.5 < y < 4$ and $6 < p_{\mathrm{T}} < 10$ GeV/c. Figures are taken from [56].

This analysis is published in *Phys. Lett. B 820 (2021) 136558*. In the following, the main steps of the procedure are summarized and the results are discussed[1].

4.1 Measurement of muons from heavy-flavour hadron decays

Based on the definition of R_{AA} in Eq. 1.13, the R_{AA} of muons from heavy-flavour hadron decays can be expressed as:

$$R_{\mathrm{AA}}(p_{\mathrm{T}}) = \frac{\left(\frac{\mathrm{d}^2 N^{\mathrm{c,b}\to\mu^{\pm}}}{\mathrm{d}p_{\mathrm{T}}\mathrm{d}y}\right)_{\mathrm{Pb-Pb}}}{\langle T_{\mathrm{AA}}\rangle \times \left(\frac{\mathrm{d}\sigma^{\mathrm{c,b}\to\mu^{\pm}}}{\mathrm{d}p_{\mathrm{T}}\mathrm{d}y}\right)_{\mathrm{pp}}}, \tag{4.1}$$

where $\left(\mathrm{d}\sigma^{\mathrm{c,b}\to\mu^{\pm}}/\mathrm{d}p_{\mathrm{T}}\mathrm{d}y\right)_{\mathrm{pp}}$ is the pp differential production cross section of muons from heavy-flavour hadron decays in pp collisions at the same centre-of-mass energy and in the same kinematic region as in Pb–Pb collisions, obtained from [42, 56]. In the numerator, $\left(\mathrm{d}^2 N^{\mathrm{c,b}\to\mu^{\pm}}/\mathrm{d}p_{\mathrm{T}}\mathrm{d}y\right)_{\mathrm{Pb-Pb}}$ is the differential yield of muons from heavy-flavour hadron decays in Pb–Pb collisions. As described in Sec. 3.2.3, the muons from primary kaons and pions decays are suppressed by the front absorber. However, there is a amount of remaining muons from non heavy-flavour sources measured by the spectrometer, called **background muons**. The main contributions to background muons consist of muons from primary charged-pion and kaon decays for $p_{\mathrm{T}} \lesssim 6$ GeV/c, and muons from W-boson, Z-boson and γ^* decays for $p_{\mathrm{T}} \gtrsim 13$ GeV/c. The muons from the interaction of light hadron with the material of the front absorber in $3 < p_{\mathrm{T}} < 5$ GeV/c, which are called **secondary muons**, are also

[1] This analysis work was finished in cooperation with Doctor Zuman Zhang, some details of this measurement are also shown in [164].

regarded as the background muons. In addition, the muons from J/ψ decays over the entire p_{T} range are also considered as the background muons. Therefore, the differential yield of muons from heavy-flavour hadron decays in Pb–Pb collisions is obtained after the subtraction of the background muons to the inclusive muon yield, and the $\mathrm{d}^2N^{\mathrm{c,b}\to\mu^\pm}/\mathrm{d}p_{\mathrm{T}}\mathrm{d}y$ term in eq. 4.1 can be written as:

$$\frac{\mathrm{d}^2N^{\mathrm{c,b}\to\mu^\pm}}{\mathrm{d}p_{\mathrm{T}}\mathrm{d}y} = \frac{\mathrm{d}^2N^{\mu^\pm}}{\mathrm{d}p_{\mathrm{T}}\mathrm{d}y} - \frac{\mathrm{d}^2N^{\mathrm{K}^\pm/\pi^\pm\to\mu^\pm}}{\mathrm{d}p_{\mathrm{T}}\mathrm{d}y} - \frac{\mathrm{d}^2N^{\mathrm{sec.K}^\pm/\pi^\pm\to\mu^\pm}}{\mathrm{d}p_{\mathrm{T}}\mathrm{d}y} - \frac{\mathrm{d}^2N^{\mathrm{W/Z}/\gamma^*\to\mu^\pm}}{\mathrm{d}p_{\mathrm{T}}\mathrm{d}y} - \frac{\mathrm{d}^2N^{\mathrm{J}/\psi\to\mu^\pm}}{\mathrm{d}p_{\mathrm{T}}\mathrm{d}y}, \tag{4.2}$$

where $\mathrm{d}^2N^{\mu^\pm}/\mathrm{d}p_{\mathrm{T}}\mathrm{d}y$ is the differential yield of inclusive muons. The terms $\mathrm{d}^2N^{\mathrm{K}^\pm/\pi^\pm\to\mu^\pm}/\mathrm{d}p_{\mathrm{T}}\mathrm{d}y$, $\mathrm{d}^2N^{\mathrm{sec.K}^\pm/\pi^\pm\to\mu^\pm}/\mathrm{d}p_{\mathrm{T}}\mathrm{d}y$, $\mathrm{d}^2N^{\mathrm{W/Z}/\gamma^*\to\mu^\pm}/\mathrm{d}p_{\mathrm{T}}\mathrm{d}y$ and $\mathrm{d}^2N^{\mathrm{J}/\psi\to\mu^\pm}/\mathrm{d}p_{\mathrm{T}}\mathrm{d}y$ are muons from primary $\pi^\pm/\mathrm{K}^\pm$ decays, secondary muons, muons from W/Z/γ^* decays and muons from J/ψ decays, respectively. The calculation of each term in Eq. 4.2 is discussed in the following sections.

4.1.1 Measurement of Inclusive Muons

In this analysis, data from Pb–Pb collisions at $\sqrt{s_{\mathrm{NN}}}$ = 2.76 TeV and 5.02 TeV, collected during the LHC Run 1 and Run 2, respectively, are used. The detailed information of run periods and numbers are summarized below:

- **2.76 TeV**, LHC11h, muon_pass2, AOD119, 132 runs:
  167706 167713 167806 167807 167808 167813 167814 167818 167915 167920 167921 167985 167986 167987 167988 168066 168069 168076 168107 168108 168115 168172 168173 168175 168181 168203 168205 168206 168207 168208 168212 168213 168310 168311 168318 168322 168325 168341 168342 168356 168361 168362 168458 168460 168461 168464 168467 168511 168512 168514 168777 168826 168992 169035 169040 169044 169045 169091 169094 169099 169138 169144 169145 169148 169156 169160 169167 169236 169238 169411 169415 169417 169418 169419 169420 169475 169498 169504 169506 169512 169515 169550 169553 169554 169555 169557 169586 169587 169588 169590 169835 169837 169838 169846 169855 169858 169859 169965 169969 170027 170036 170040 170081 170083 170084 170085 170088 170089 170091 170155 170159 170163 170193 170203 170204 170207 170228 170230 170268 170269 170270 170306 170308 170309 170311 170312 170313 170315 170387 170388 170572 170593

- **5.02 TeV**, LHC15o, muon_pass1, AOD175, 137 runs:
  - Negative Polarity (−−) 246994 246991 246989 246984 246982 246980 246949 246948 246945 246942 246937 246930 246871 246867 246865 246864 246859 246855 246851 246847 246846 246845 246844 246809 246808 246807 246806 246805 246804 246765 246763 246760 246759 246758 246757 246755 246751 246750 246676 246675 246495 246493 246488 246487 246434 246433 246431 246428 246424 246392 246391

– Positive Polarity (++) 246390 246276 246275 246272 246225 246222 246220 246217 246182 246181 246178 246153 246152 246151 246148 246115 246113 246089 246087 246053 246049 246048 246042 246037 246036 246012 246003 246001 245996 245963 245954 245952 245949 245833 245831 245829 245793 245785 245775 245766 245759 245752 245738 245731 245729 245705 245700 245692 245683 245554 245543 245542 245540 245535 245507 245505 245504 245501 245496 245450 245446 245410 245409 245407 245401 245353 245347 245346 245345 245343 245259 245253 245233 245232 245231 245152 245151 245146 245145 245068 245066 245064 244983 244982 244980 244918

All runs shown above have been selected after the muon Quality Assurance (QA) checks [165, 166].

Event and Track Selection

In order to enhance the statistics of muons, the muon-triggered events requiring a minimum-bias (MB) trigger and at least one track measured in the muon trigger system with a p_{T} larger than a predefined threshold [124], are selected. The two p_{T}-trigger thresholds applied in Pb–Pb collisions at $\sqrt{s_{\mathrm{NN}}} = 5.02$ (2.76) TeV are 1 (0.5) and 4.2 (4.2) GeV/c, whose corresponding trigger-threshold samples are called MSL and MSH, respectively (as described in Sec. 3.2.3.4). An offline event selection is applied to remove beam-induced background (i.e. beam-gas events) by utilizing the V0 and ZDC timing information and requiring a minimum energy deposited in the ZDC [167, 168]. Only events with a primary vertex position within ±10 cm from the interaction point along the beam direction are used in the analysis. Finally, the measurements are performed in the three representative centrality classes 0–10%, 20–40% and 60–80%, which are characterized by the V0M estimator.

As described in Sec. 3.2.3, thanks to the absorber system, the hadrons produced in the collisions and background muons are suppressed a lot at forward rapidity. Even so, some of them still escape and are detected in the acceptance of the muon spectrometer. In order to improve the purity of the analyzed events, the following muon track selections are applied:

- Muon tracks are required to be reconstructed within the acceptance of the muon spectrometer ($-4 < \eta_{\mathrm{lab}} < -2.5$);
- Polar angle at the end of the front absorber (θ_{abs}) of muon tracks should satisfy the condition: $170^{\circ} < \theta_{\mathrm{abs}} < 178^{\circ}$;
- The track candidate in the tracking system matches the track segment reconstructed in the trigger system;
- The $p\times$DCA cut within 6σ is applied in order to remove remaining beam-induced background and particles produced in the absorber.

Figure. 4.2 shows the p_{T} distribution of inclusive muons with different event and track selections in Pb–Pb collisions at $\sqrt{s_{\mathrm{NN}}} = 5.02$ TeV and 2.76 TeV for MSL and MSH triggers, in the 0–90% centrality class.

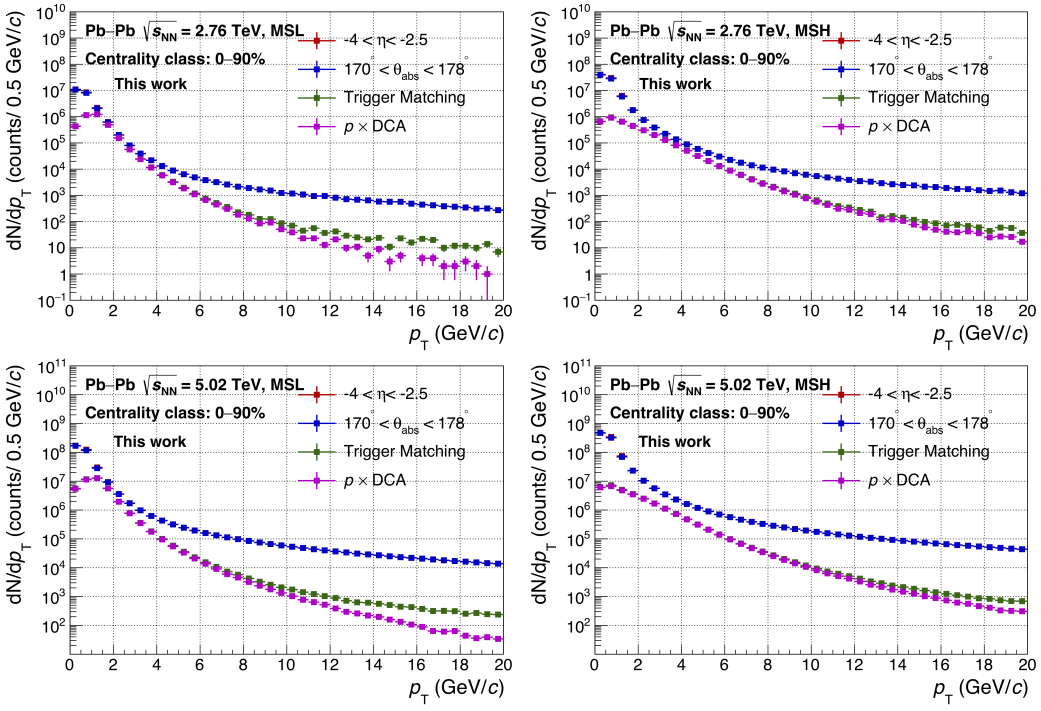

Figure 4.2: Transverse momentum distributions of inclusive muons with different track selections in Pb–Pb collisions at $\sqrt{s_{\rm NN}} = 5.02$ TeV (top) and 2.76 TeV (bottom) for MSL (left) and MSH (right) triggers in 0–90% centrality class.

Normalization

As described in Sec. 3.2.3.4, the requirement that at least one single muon satisfying low (high) $p_{\rm T}$ cut in each event is applied in MSL- (MSH-) triggered data sample, aiming to enhance the statistics of heavy-flavour decay muons. In this case, one needs to get the equivalent number of MB events for MSL- and MSH-triggered data samples. The normalization factor ($F_{\rm norm}^{\rm MSL/MSH}$) needs to be obtained. There are two methods, **offline method** and **online method**, implemented in the calculation of the normalization factors [164]. In the offline method, the normalization factor MSL ($F_{\rm norm}^{\rm MSL}$) and MSH ($F_{\rm norm}^{\rm MSH}$) triggers are determined by the fraction of the events which contains 0MSL and 0MSH inputs (see Sec. 3.2.3.4) in MB events[2], as shown in:

$$F_{\rm norm}({\rm MSL}) = \frac{N_{\rm MB} \times F_{\rm pile-up}}{N_{\rm (MB\&\&0MSL)}}, \tag{4.3}$$

$$F_{\rm norm}({\rm MSH}) = F_{\rm pile-up} \times \frac{N_{\rm MB}}{N_{\rm (MB\&\&0MSL)}} \times \frac{N_{\rm MSL}}{N_{\rm (MSL\&\&0MSH)}}, \tag{4.4}$$

where $N_{\rm MB}$ and $N_{\rm MSL}$ are the number of events triggered by MB and MSL after the event selections. $N_{\rm (MB\&\&0MSL)}$ and $N_{\rm (MSL\&\&0MSH)}$ are the number of MB events

[2]In practice, due to a lack of statistics in MB events containing 0MSH inputs, the MSL triggers are also usually used in the calculations of $F_{\rm norm}^{\rm MSH}$, as shown in Eq. 4.4

containing a 0MSL input and the number of MSL events containing a 0MSH input, respectively. The pile-up factor $F_{\rm pile-up}$ is set to unity since the pile-up effect is negligible in the Pb–Pb collisions. The online method is based on the *L0b* counting rates (scalers) taken from the OCDB, as shown in:

$$F_{\rm norm-onl}({\rm MSL(MSH)}) = \frac{L0b_{\rm C0V0M} \times F_{\rm purity}^{\rm C0V0M} \times F_{\rm pile-up}}{L0b_{\rm MSL(MSH)} \times F_{\rm purity}^{\rm MSL(MSH)}}, \tag{4.5}$$

where $L0b_{\rm C0V0M}$, $L0b_{\rm MSL}$ and $L0b_{\rm MSH}$ are the scalers recorded for C0V0M, MSL and MSH triggers, respectively. $F_{\rm purity}^{\rm i,C0V0M}$, $F_{\rm purity}^{\rm MSL(MSH)}$ are the purity factors, which are defined as the ratio of the number of physics selected events to the total number of events recorded with C0V0M, MSL (MSH) trigger, respectively. The $F_{\rm purity}^{\rm C0V0M}$ and $F_{\rm pile-up}$ are set to unity [169]. Usually the normalization factor is obtained in each run and then the weighted average value of them is calculated where the weight is number of events in each run. Once this factor is determined in each centrality, the equivalent number of minimum bias events ($N_{\rm MB}^{\rm eq}$) is calculated as $N_{\rm MB}^{\rm eq} = F_{\rm norm}^{\rm MSL/MSH} \times N_{\rm MSL(MSH)}$. Finally, the data samples correspond to integrated luminosities of about 21.9 (224.8) μb^{-1} and 4.0 (71.0) μb^{-1} for MSL- (MSH-) triggered events at $\sqrt{s_{\rm NN}}$ = 5.02 and 2.76 TeV, respectively.

Acceptance × efficiency correction

The muon detection is affected by the acceptance and efficiency ($A \times \varepsilon$) of the detector during the data taking, which needs to be evaluated by means of realistic Monte Carlo simulations. The correction procedures are the same as in previous measurements in [42, 56]. Firstly, the $p_{\rm T}$ and rapidity distribution of muons from heavy flavours (charm and beauty) decays are obtained from FONLL calculations [37], which are further parameterized by:

$$\frac{dN}{dp_{\rm T}} = x_1 \cdot (e^{x_2(1-e^{p_{\rm T}\cdot x_3})} + x_4) \cdot \frac{1}{p_{\rm T}^{x_5}} \cdot (x_6 + p_{\rm T} \cdot x_7 + p_{\rm T}^2 \cdot x_8), \tag{4.6}$$

$$\frac{dN}{dy} = y^8 \cdot p_1 + y^6 \cdot p_2 + y^4 \cdot p_3 + y^2 \cdot p_4 + y \cdot p_5 + p_6, \tag{4.7}$$

where x_1–x_8 and p_1–p_6 are free parameters. Then, the detector description and its response are modeled using the GEANT3 transport package. In addition, the simulated statistics is proportional to the number of MSL- and MSH-triggered events in each run to account for the time evolution of $A \times \varepsilon$. Finally, the dependence of $A \times \varepsilon$ on the collision centrality related to the occupancy of tracking chambers is taken into account [170]. The ratio of the number of muons obtained in generated and reconstructed events is the $A \times \varepsilon$, as shown:

$$A \times \varepsilon(p_{\rm T}^{\rm rec}, y^{\rm rec}) = \frac{N_{\rm rec}(p_{\rm T}^{\rm rec}, y^{\rm rec})}{N_{\rm gen}(p_{\rm T}^{\rm gen}, y^{\rm gen})}, \tag{4.8}$$

where $N_{\rm gen}$ is the number of generated muons and $N_{\rm rec}$ is the number of reconstructed muons. $p_{\rm T}^{\rm rec}$ and $y^{\rm rec}$ ($p_{\rm T}^{\rm gen}$ and $y^{\rm gen}$) are the transverse momentum and rapidity of reconstructed (generated) muons.

The $A \times \varepsilon$ obtained in peripheral Pb–Pb collisions at $\sqrt{s_{\rm NN}} = 5.02$ TeV has almost no dependence on $p_{\rm T}$ ($p_{\rm T}$ >3 GeV/c), and amounts to about 90% for MSL-triggered events. While for MSH-triggered events, the $A \times \varepsilon$ increases with $p_{\rm T}$ from 75% at $p_{\rm T} = 7$ GeV/c towards a plateau at a value close to 90% for $p_{\rm T} > 14$ GeV/c. From peripheral (60–80%) to central (0–10%) collisions, the $A \times \varepsilon$ decreases of 6%, due to the detector occupancy. The trend of $A \times \varepsilon$ as a function of $p_{\rm T}$ in peripheral Pb–Pb collisions at $\sqrt{s_{\rm NN}} = 2.76$ TeV is similar as that at $\sqrt{s_{\rm NN}} = 5.02$ TeV, while the values of the former are smaller, around 80% in the high-$p_{\rm T}$ region. Similarly, a decrease of the efficiency of 4% from peripheral collisions to the 0–10% most central collisions is observed at $\sqrt{s_{\rm NN}} = 2.76$ TeV.

4.1.2 Estimation of the Background Muons

Estimation of the background muons from primary $\rm K^{\pm}$, $\pi^{\pm}$ decays

The strategy to estimate the background muons from primary $\rm K^{\pm}$, $\pi^{\pm}$ decays is based on a data-driven Monte Carlo cocktail method, which uses the midrapidity $\rm K^{\pm}$, $\pi^{\pm}$ spectra in pp [63] and Pb–Pb collisions [171] as inputs. In order to get the estimation of the decay muons up to $p_{\rm T} = 20$ GeV/c, the $\rm K^{\pm}$ and $\pi^{\pm}$ spectra need to be further extended to higher $p_{\rm T}$, up to 40 GeV/c. The extrapolation is performed by means of fitting the primary $\rm K^{\pm}$, $\pi^{\pm}$ $p_{\rm T}$ distributions with a power-law function:

$$\mathrm{f}(p_{\rm T}) = p_0 \frac{p_{\rm T}}{(1 + (p_{\rm T}/p_1)^2)^{p_2}}, \tag{4.9}$$

where p_0, p_1 and p_2 are free parameters. The procedure can be summarized as follows:

- For a given $p_{\rm T}$ bin of primary $\rm K^{\pm}$, $\pi^{\pm}$ distribution, one generates 1000 sample values randomly from a Gaussian function, Gaus(μ, σ), where the mean value μ is the central value of the data points and the standard deviation σ is the quadrature sum of statistical and systematic uncertainties of the input data points;
- Previous step in each $p_{\rm T}$ bin is repeated, therefore 1000 $p_{\rm T}$ spectra are obtained;
- These 1000 $p_{\rm T}$ spectra are fitted with Eq. 4.9 and extrapolated them to higher-$p_{\rm T}$ region;
- In each extrapolated $p_{\rm T}$ bin, the mean and standard deviation of the 1000 values are regarded as the central value and the uncertainty of the extrapolated data point, respectively.

Then, the $p_{\rm T}$ extrapolated midrapidity $\rm K^{\pm}$, $\pi^{\pm}$ spectra are further extrapolated to forward rapidities according to:

$$\begin{aligned}\left[\frac{\mathrm{d}^2N^{\pi^{\pm}(\mathrm{K}^{\pm})}}{\mathrm{d}p_T\mathrm{d}y}\right]_{\rm AA}^{\rm forward-y} &= n_{\rm y}\times\langle N_{\rm coll}\rangle\times\left[R_{\rm AA}^{\pi^{\pm}(\mathrm{K}^{\pm})}\right]^{\rm mid-y}\times\left[F_{\rm extrap}^{\pi^{\pm}(\mathrm{K}^{\pm})}(p_{\rm T},y)\right]_{\rm pp}\times\left[\frac{\mathrm{d}^2N^{\pi^{\pm}(\mathrm{K}^{\pm})}}{\mathrm{d}p_T\mathrm{d}y}\right]_{\rm pp}^{\rm mid-y}\\ &= n_{\rm y}\times\left[F_{\rm extrap}^{\pi^{\pm}(\mathrm{K}^{\pm})}(p_{\rm T},y)\right]_{\rm pp}\times\left[\frac{\mathrm{d}^2N^{\pi^{\pm}(\mathrm{K}^{\pm})}}{\mathrm{d}p_T\mathrm{d}y}\right]_{\rm AA}^{\rm mid-y},\end{aligned} \tag{4.10}$$

where $\left[\frac{\mathrm{d}^2N^{\pi^{\pm}(\mathrm{K}^{\pm})}}{\mathrm{d}p_T\mathrm{d}y}\right]_{\rm pp}$ and $\left[\frac{\mathrm{d}^2N^{\pi^{\pm}(\mathrm{K}^{\pm})}}{\mathrm{d}p_T\mathrm{d}y}\right]_{\rm AA}$ are the $p_{\rm T}$-extrapolated primary $\pi^{\pm}$ ($\rm K^{\pm}$) spectra in pp and Pb–Pb collisions. The suppression of $\pi^{\pm}$ and $\rm K^{\pm}$ in Pb–Pb collisions is considered to be independent of rapidity [172], therefore the factor $n_{\rm y}$ is considered as unity. The factor $F_{\rm extrap}^{\pi^{\pm}(\mathrm{K}^{\pm})}(p_{\rm T},y)]_{\rm pp}$ is the $p_{\rm T}$- and y-dependent extrapolation factor in pp collisions, which is obtained from Monte Carlo simulations, as discussed in [42]. Both PYTHIA 6 [173] and PHOJET [174] event generators are used for the rapidity extrapolation, and the rapidity dependence of the $p_{\rm T}$ extrapolation is considered by means of PYTHIA 8 simulations [175] with various colour reconnection (CR) options. Regarding the extrapolated $\pi^{\pm}$ and $\rm K^{\pm}$ spectra at forward rapidity obtained from Eq. 4.10 as inputs, a fast detector simulation of the decay kinematics with the effect of the front absorber is performed to generate the $p_{\rm T}$ and rapidity distributions of muons from primary $\pi^{\pm}$ and $\rm K^{\pm}$ decays in Pb–Pb collisions for each centrality class. Figure 4.3 shows the fraction of muons from primary $\pi^{\pm}$ and $\rm K^{\pm}$ decays relative to inclusive muons. In Pb–Pb collisions at 5.02 TeV, the total contribution of muons from primary $\pi^{\pm}$ and $\rm K^{\pm}$ decays decreases with increasing $p_{\rm T}$ from ∼21% (13%) at $p_{\rm T}$ = 3 GeV/c down to ∼7% (4%) at $p_{\rm T}$ = 20 GeV/c in the 60–80% (0–10%) centrality class. For $p_{\rm T}$ > 10 GeV/c, a weak $p_{\rm T}$ dependence is observed. At 2.76 TeV, the ratio between muons from primary $\pi^{\pm}$ and $\rm K^{\pm}$ decays and inclusive muons varies between about 3% (3%) and 14% (22%) in the 0–10% (60–80%) most central collisions, and the largest value is obtained at $p_{\rm T}$ = 3 GeV/c.

Estimation of the background muons from J/Ψ decays

The strategy to estimate the background muons from J/Ψ decays is the same as that for the estimation of muons from primary $\pi^{\pm}$ and $\rm K^{\pm}$ decays, as described above. The $p_{\rm T}$ and y distributions of J/Ψ are extrapolated up to $p_{\rm T}$ ∼ 50 GeV/c and $|y|$ = 6.5 by means of a power-law and Gaussian function, respectively. Then, a fast simulation of the decay kinematics of J/Ψ is performed to get the decay muon distributions. In the 0–10% most central Pb–Pb collisions at 5.02 TeV, the relative contribution of muons from J/Ψ decays to the inclusive muon distribution varies between 0.5 and 4%, and the maximum fraction is observed at 4 < $p_{\rm T}$ < 6 GeV/c, as shown in Fig. 4.4 (left). For 2.76 TeV, the fraction of muons from J/Ψ decays to inclusive muons reaches a maximum of ∼ 3% at intermediate $p_{\rm T}$ (∼6 GeV/c) in central collisions.

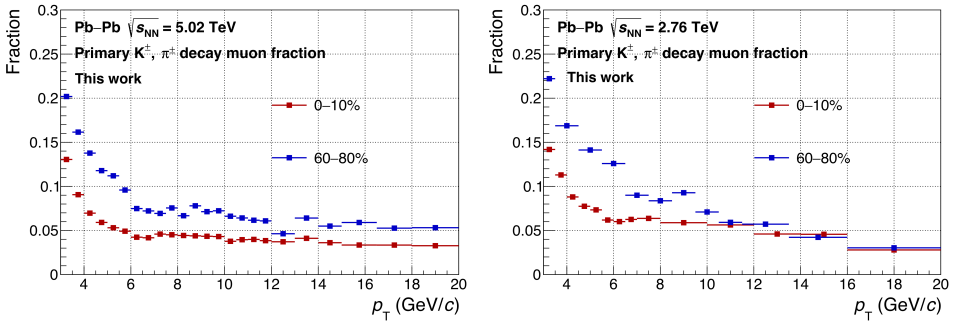

Figure 4.3: The fraction of muons from primary $\pi^{\pm}$ and $K^{\pm}$ decays relative to inclusive muons as a function of p_T in Pb–Pb collisions at $\sqrt{s_{NN}}$ = 5.02 (left) and 2.76 (right) TeV.

Estimation of the background muons from secondary $K^{\pm}$, $\pi^{\pm}$ decays

The contribution of muons from secondary $K^{\pm}$ and $\pi^{\pm}$ decays is estimated by means of Monte Carlo simulations using the HIJING event generator [176] and the GEANT3 transport package [177]. Figure 4.4 (right) shows the ratio of secondary muons with respect to the muons from primary charged pion and kaon decays for different multiplicity ranges. It indicates that the ratio has no dependence on both p_T and collision centrality in p_T >2 GeV/c and amounts to about 9% within uncertainties. Given the estimated contribution of muons from charged kaon and pion decays described as above, the contribution of these secondary muons relative to the inclusive muons decreases with increasing p_T from about 2% (1%) at p_T = 3 GeV/c in the 60–80% (0–10%) centrality class to less than 1% at p_T = 5 GeV/c for all centrality classes in Pb–Pb collisions at $\sqrt{s_{NN}}$ = 5.02 TeV. With a similar strategy, the estimated fraction of muons from secondary $\pi^{\pm}$ and $K^{\pm}$ decays reaches about 1% at p_T = 3 GeV/c in Pb–Pb collisions at $\sqrt{s_{NN}}$ = 2.76 TeV.

Estimation of the background muons from W and Z/γ^* decays

The estimation of the contribution of muons from W boson decays and dimuons from Z/γ^*-boson decays is based on the simulations of pp, nn, np, pn collisions with the POWHEG NLO [178] event generator. In addition, the PYTHIA 6 [173] is used for the parton shower. The p_T-differential cross section per nucleon-nucleon collision for Pb–Pb collisions, is expressed as a weighted sum of the production cross sections in the four systems

$$\frac{d\sigma_{NN}}{dp_T} \approx \frac{Z^2}{A^2} \times \frac{d\sigma_{pp}}{dp_T} + \frac{(A-Z)^2}{A^2} \times \frac{d\sigma_{nn}}{dp_T} + \frac{Z(A-Z)}{A^2} \times (\frac{d\sigma_{pn}}{dp_T} + \frac{d\sigma_{np}}{dp_T}), \quad (4.11)$$

where A and Z are the mass and atomic number of the Pb nucleus. In order to estimate the W, Z/γ^* decay muons in different centrality classes, $\frac{d\sigma_{NN}}{dp_T}$ in Eq. 4.11 is further scaled by $\langle T_{AA} \rangle$. Figure 4.5 (left) shows the relative contribution of muons from W and Z/γ^* decays with respect to inclusive muons for various centrality

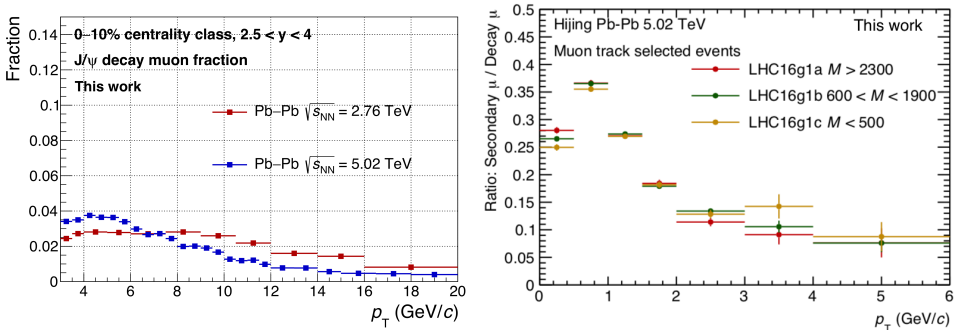

Figure 4.4: Left: the relative contribution of muons from J/Ψ decays with respect to inclusive muons in the 0–10% most central Pb–Pb collisions at $\sqrt{s_{\rm NN}}$ = 2.76 and 5.02 TeV. Right: the relative contribution of secondary muons with respect to muons from primary $\pi^{\pm}$ and $\rm K^{\pm}$ decays in Pb–Pb collisions at $\sqrt{s_{\rm NN}}$ = 5.02 TeV with the HIJING event generator.

classes in Pb–Pb collisions at $\sqrt{s_{\rm NN}}$ = 5.02 TeV. At low $p_{\rm T}$ ($p_{\rm T} \lesssim 13$ GeV/c), the fraction of muons from W and Z/γ^* with respect to inclusive muons is negligible. It increases with increasing $p_{\rm T}$ from about 3% (6%) at $p_{\rm T}$ = 14 GeV/c up to 18% (35%) at $p_{\rm T}$ = 20 GeV/c in the 60–80% (0–10%) centrality class. With the same strategy, the production of muons from W and Z/γ^* decays in Pb–Pb collisions at 2.76 TeV is estimated. As shown in Fig. 4.5 (right), the relative contribution of muons from electroweak-boson decays dominates at high $p_{\rm T}$, where it reaches around 31% (12%) in the interval 15 < $p_{\rm T}$ < 20 GeV/c for 0–10% (60–80%) collisions.

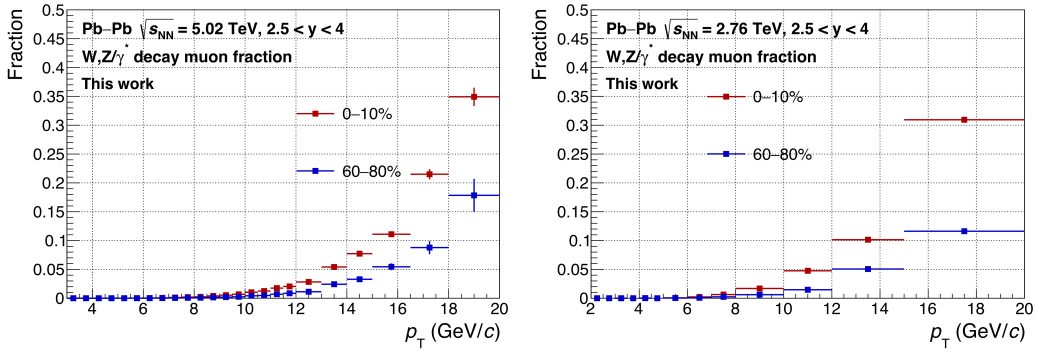

Figure 4.5: The fraction of muons from W and Z/γ^* decays with respect to inclusive muons for 0–10% and 60–80% centrality classes in Pb–Pb collisions at $\sqrt{s_{\rm NN}}$ = 5.02 (left) and 2.76 (right) TeV.

4.2 Systematic Uncertainty

The estimation of systematic uncertainties on the $R_{\rm AA}$ of muons from heavy-flavour hadron decays, as defined in Eq. 4.1, in Pb–Pb collisions at $\sqrt{s_{\rm NN}}$ = 5.02 TeV and 2.76 TeV is based on four contributions, as described below.

The Systematic Uncertainty on the Inclusive Muon Yields

The strategy to estimate the systematic uncertainties of inclusive muon yields is the same as that described in [42], for Pb–Pb collisions at $\sqrt{s_{\rm NN}}$ = 5.02 and 2.76 TeV. The measurement in Pb–Pb collisions at $\sqrt{s_{\rm NN}}$ = 5.02 TeV is taken as an example. The uncertainty on the muon tracking efficiency is obtained by comparing the single-muon tracking efficiency in data and simulation, as discussed in ref. [170], which amounts to 1.5%. The uncertainties on the muon trigger efficiency include the intrinsic efficiency of the muon trigger chambers and the response of the trigger algorithm, which are 1.4% and 3% for MSL- and MSH-triggered samples. The uncertainty on the muon tracking-trigger matching is generally considered to be 0.5%, which is related to the choice of χ^2 cut applied in the matching between the reconstructed tracks in the tracking chambers and the trigger tracklets [179]. The systematic uncertainty arising from the dependence of $A \times \varepsilon$ on the centrality classes is obtained from a constant fit of $p_{\rm T}$-differential ratio of the efficiency in a given centrality class to that in peripheral collisions. It varies up to 0.5% from 0–10% most central collisions to peripheral collisions. The systematic uncertainty due to the tracking chamber resolution and alignment is obtained from a Monte Carlo simulation, as described in [42], and it varies from 0 to 12%. The systematic uncertainties on the inclusive muon yields in Pb–Pb collisions at $\sqrt{s_{\rm NN}}$ = 2.76 TeV summarized in Tab. 4.1 are obtained following the same procedure.

The Systematic Uncertainty on the Subtraction of Background Muons

The systematic uncertainties on the estimation of muons from primary $\rm K^{\pm}$ and $\pi^{\pm}$ decays arise from the following sources:

- the uncertainties of the measured midrapidity spectra of $\rm K^{\pm}$ and $\pi^{\pm}$ and their $p_{\rm T}$ extrapolation;
- the uncertainty due to the rapidity extrapolation, which is obtained by comparing the results with PYTHIA 6 and PHOJET generators;
- the uncertainty due to the $p_{\rm T}$ dependence of the rapidity extrapolation, which are obtained from the PYTHIA 8 generator with different color reconnection options;
- the uncertainty on the absorber effect driven by the simulation of hadronic interactions, as reported in [42].

The uncertainties coming from above sources are added in quadrature to obtain the total systematic uncertainty affecting muons from primary $\pi^{\pm}$ and $\rm K^{\pm}$ decays,

which ranges from about 9% (10%) to 13% (15%) as a function of the p_{T} of muons from primary $\pi^{\pm}$ ($\mathrm{K}^{\pm}$) decays in Pb–Pb collisions at $\sqrt{s_{\mathrm{NN}}} = 5.02$ TeV. Besides, the uncertainty on the suppression factor n_y in Eq. 4.10 is obtained by varying it conservatively from 0.5 to 1.5, and dividing the difference between the upper and lower limits by $\sqrt{12}$. For the estimation of the uncertainty on the subtraction of secondary muons, the effect of the transport code is conservatively evaluated by varying the estimated yield of secondary muons by ±100% and dividing also the difference between lower and upper limits by $\sqrt{12}$. The uncertainties obtained in Pb–Pb collisions at $\sqrt{s_{\mathrm{NN}}} = 2.76$ TeV using the same strategy can be found in Tab. 4.1.

The systematic uncertainty of the estimation of muons from J/ψ decays reflects the uncertainty of the measured J/ψ spectra at forward rapidity and their extrapolation to a wider kinematic region. It varies from about 9% (4%) at $p_{\mathrm{T}} = 3$ GeV/c to 34% (42%) at $p_{\mathrm{T}} = 20$ GeV/c in central Pb–Pb collisions at $\sqrt{s_{\mathrm{NN}}} = 5.02$ (2.76) TeV.

The systematic uncertainty of the extracted muon yields from W and Z/γ^* decays is obtained considering the CT10 PDF uncertainty and a different nuclear modification of the PDF (EPS09NLO and EKS98). It amounts to 14.5% (10.8%) for central Pb–Pb collisions at $\sqrt{s_{\mathrm{NN}}} = 5.02$ (2.76) TeV.

The Systematic Uncertainty on Normalization

The systematic uncertainty on the normalization is composed of two sources: the systematic uncertainty on the normalization factor and the $\langle T_{\mathrm{AA}} \rangle$ values [180]. The systematic uncertainty on the normalization factor is 0.3% (0.7%) for MSL (MSH) Pb–Pb data samples at 5.02 TeV and 0.4% (1.6%) for MSL (MSH) in Pb–Pb data samples at 2.76 TeV reflects the difference between the normalization factor obtained with online and offline methods, described in Sec. 4.1.1.

The Systematic Uncertainty on the pp Reference

The sources of systematic uncertainty affecting the measurement of the pp reference production cross section were evaluated in [42]. For pp collisions at $\sqrt{s} = 5.02$ TeV, the total systematic uncertainty ranges from 2.1% to 15.1%, depending on p_{T}. A global uncertainty on the normalization factor in pp collisions of 2.1%, discussed in [42], is considered as well. For pp collisions at $\sqrt{s} = 2.76$ TeV, the systematic uncertainty varies within 15–18%, while at high p_{T}, it reaches 30–34%, due to the p_{T} extrapolation (the p_{T} range of published results is only up to 10 GeV/c [56]).

All systematic uncertainties discussed above are propagated to the measurement of the yields and nuclear modification factors of muons from heavy-flavour hadron decays and added in quadrature. The systematic uncertainties on the normalization are shown separately. Table 4.1 presents a summary of the relative systematic uncertainties of the p_{T}-differential yields of muons from heavy-flavour

hadron decays in Pb–Pb collisions at $\sqrt{s_{\rm NN}}$ = 5.02 and 2.76 TeV.

4.3 Results and Discussion

Figure 4.6 shows the $p_{\rm T}$-differential yields of muons from heavy-flavour hadron decays at forward rapidity ($2.5 < y < 4$) in central (0–10%), semi-central (20–40%), and peripheral (60–80%) Pb–Pb collisions at $\sqrt{s_{\rm NN}}$ = 5.02 TeV (left), and in central (0–10%) Pb–Pb collisions at $\sqrt{s_{\rm NN}}$ = 2.76 TeV (right). The statistical and systematic uncertainties are shown as vertical bars and open boxes, while the systematic uncertainties on normalization are not included in the uncertainty boxes (shown in Tab. 4.1). The latter are shown as filled boxes at $R_{\rm AA} = 1$. The yield of muons from heavy-flavour hadron decays increases with increasing centrality and collision energy as expected from the enhancement of hard scattering rates.

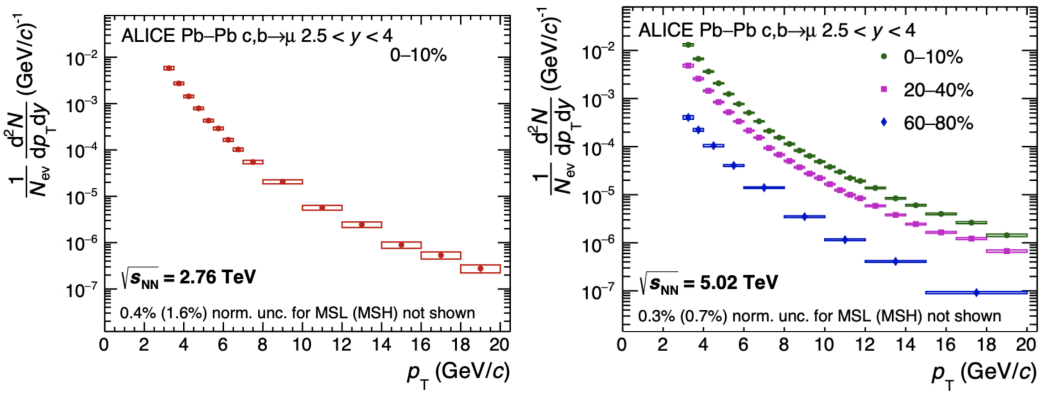

Figure 4.6: The $p_{\rm T}$-differential distribution of muons from heavy-flavour hadron decays normalized to the equivalent number of MB events at forward rapidity ($2.5 < y < 4$) in central (0–10%), semi-central (20–40%), and peripheral (60–80%) Pb–Pb collisions at $\sqrt{s_{\rm NN}}$ = 5.02 TeV (left), and in central (0–10%) Pb–Pb collisions at $\sqrt{s_{\rm NN}}$ = 2.76 TeV (right). Figure taken from [181].

The $R_{\rm AA}$ of muons from heavy-flavour hadron decays as a function of $p_{\rm T}$ at forward rapidity ($2.5 < y < 4$) for various centrality classes in Pb–Pb collisions at $\sqrt{s_{\rm NN}}$ = 5.02 TeV is presented in Fig. 4.7. A reduction of the yield of muons from heavy-flavour hadron decays with respect to the pp reference scaled by the average nuclear overlap function, which depends on the collision centrality, is clearly observed (i.e. $R_{\rm AA} < 1$). The suppression is stronger in the 0–10% most central collisions, and reaches up to a factor of about three at intermediate $p_{\rm T}$ ($6 < p_{\rm T} < 10$ GeV/c) in the 10% most central collisions. In addition, a clear $p_{\rm T}$ dependence of $R_{\rm AA}$ is observed in central and semi-central collisions, while it is not obvious in peripheral collisions. Since the $R_{\rm pPb}$ of muons from heavy-flavour hadron decays was observed to be compatible with unity in minimum bias p–Pb collisions at 5.02 TeV [182], where the QGP is not expected to form, the measured $R_{\rm AA} < 1$ is believed to be due to the energy loss of charm and beauty quarks when they interact with

Table 4.1: Summary of the relative systematic uncertainties of the p_{T}-differential yields of muons from heavy-flavour hadron decays at forward rapidity ($2.5 < y < 4$) in Pb–Pb collisions at $\sqrt{s_{\mathrm{NN}}} = 5.02$ and 2.76 TeV. Extracted from [181].

Source	$\sqrt{s_{\mathrm{NN}}} = 5.02$ TeV		$\sqrt{s_{\mathrm{NN}}} = 2.76$ TeV
	0-10% centrality class	60-80% centrality class	0-10% centrality class
Tracking efficiency	1.5%	1.5%	2.5%
Trigger efficiency	1.4% (MSL), 3% (MSH)	1.4% (MSL), 3% (MSH)	1.4% (MSL), 2.3% (MSH)
Matching efficiency	0.5%	0.5%	0.5%
$A \times \varepsilon$	0.5%	0	1%
Resolution and alignment	$0 - 12\%$ (0-4.1% on R_{AA})	0-12% (0-4.1% on R_{AA})	$1\% \times p_{\mathrm{T}}$ (p_{T} in GeV/c)
Background subtraction $\mu \leftarrow \pi$	$< 1.6\%$	$< 2.5\%$	$< 1.8\%$
Background subtraction $\mu \leftarrow \mathrm{K}$	$< 1.6\%$	$< 2.5\%$	$< 4\%$
$R_{\mathrm{AA}}^{\pi^{\pm}(\mathrm{K}^{\pm})}(y)$ assumption	1.3-4.8%	1.5-7.8%	1.8-5.2%
Background subtraction $\mu \leftarrow$ sec.π/K	0-0.8%	0-1.4%	0-0.9%
Background subtraction $\mu \leftarrow \mathrm{W/Z}/\gamma^{\star}$	0-1.6%	0-0.7%	0-3.1%
Background subtraction $\mu \leftarrow \mathrm{J}/\psi$	$< 0.4\%$	$< 0.4\%$	$< 0.3\%$
Normalisation factor	0.3% (MSL), 0.7% (MSH)	0.3% (MSL), 0.7% (MSH)	0.4% (MSL), 1.6% (MSH)
$\langle T_{\mathrm{AA}} \rangle$	0.7%	2.5%	0.9%
pp reference for R_{AA}	2.1-4.2%	2.1-4.2%	15-18% ($3 < p_{\mathrm{t}} < 10$ GeV/c data) 30-34% ($10 < p_{\mathrm{t}} < 20$ GeV/c extrapolation)
pp reference (global) for R_{AA}	2.1%	2.1%	1.9%

the QGP medium. Besides, a larger R_{AA} is observed in peripheral collisions than that in central collisions, as shown in Fig. 4.7. It indicates that the heavy-quark energy loss and average path length in QGP are larger in central collisions than in peripheral collisions.

Several model comparisons are also included in Fig. 4.7, such as TAMU [183], SCET [184] and MC@sHQ+EPOS2 [185]. The main characteristics of these three models are summarized in Tab. 4.2. In TAMU model, only collisional energy loss is included in the description of heavy-quark interactions, which could be a possible explanation for its underestimation of R_{AA} at $p_{\mathrm{T}} > 6$ GeV/c where radiative energy loss dominates in central and semi-central collisions. The SCET calculations not only include the collisional energy loss but also introduce the medium-induced gluon radiation for describing interactions, while the hadronization is only driven by the independent fragmentation, and the hydrodynamic description of the medium is excluded. A fair description of the R_{AA} of muons from heavy-flavour hadron decays in central collisions is provided by SCET model, but a large deviation is observed in the comparison between the SCET calculations and the data in non-central collisions. The MC@sHQ+EPOS2 model contains two different options: energy loss from medium-induced gluon radiation (i.e. radiative energy loss) and collisional energy loss. One can see that, no matter combining the radiative energy loss and collisional energy loss or including pure collisional energy loss in MC@sHQ+EPOS2 model, a fair description of the measurement can be provided, for all centrality classes in the whole p_{T} range within uncertainties. In addition, the nuclear modification of the PDF (EPS09) is considered in all these models.

Model Calculations	Heavy quark interactions	hadronization	hydrodynamic	nPDF
TAMU	Collisional energy loss	Fragmentation Recombination	Yes	EPS09
SCET	Collisional energy loss In-medium meson dissociation	Fragmentation	No	EPS09
MC@sHQ+EPOS2	Collisional energy loss (or) Radiative energy loss	Fragmentation Recombination	Yes	EPS09

Table 4.2: Summary of the characteristics of TAMU, SCET and MC@sHQ+EPOS2 model calculations, which are used to describe the R_{AA} of muons from heavy-flavour hadron decays in Pb–Pb collisions at $\sqrt{s_{\mathrm{NN}}} = 5.02$ TeV, as shown in Fig. 4.7.

A comparison of the R_{AA} of muons from heavy-flavour hadron decays in the 10% most central Pb–Pb collisions at $\sqrt{s_{\mathrm{NN}}} = 2.76$ TeV and 5.02 TeV is shown in Fig. 4.8. One can observe that the total systematic uncertainty on the R_{AA} in Pb–Pb collisions at $\sqrt{s_{\mathrm{NN}}} = 2.76$ TeV is significantly larger than that in Pb–Pb collisions at $\sqrt{s_{\mathrm{NN}}} = 5.02$ TeV, because the detector conditions for Pb–Pb and pp runs are more comparable and stable during the Run 2 data taking. The R_{AA} measured at the two centre-of-mass energies are consistent within uncertainties, which indicates a similar suppression of heavy quarks in the QGP medium. Such trend was also observed in the measurement of the R_{AA} of electrons from heavy-flavour hadron

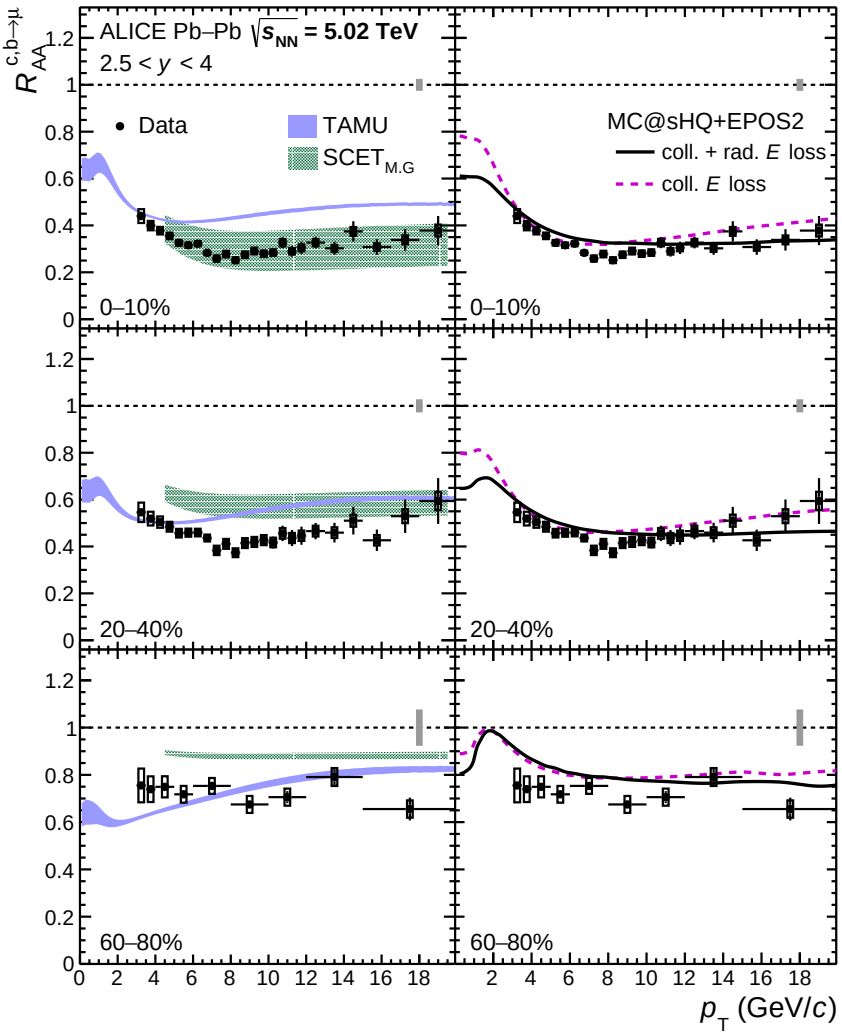

Figure 4.7: The p_{T}-differential nuclear modification factor R_{AA} of muons from heavy-flavour hadron decays at forward rapidity ($2.5 < y < 4$) in central (0–10%, top), semi-central (20–40%, middle), and peripheral (60–80%, bottom) Pb–Pb collisions at $\sqrt{s_{\mathrm{NN}}} = 5.02$ TeV. Left: the comparison between the measured R_{AA} and TAMU and SCET model predictions. Right: the comparison between the measured R_{AA} and MC@sHQ+EPOS2 model calculations with pure collisional energy loss (full lines) and a combination of collisional and radiative energy loss (dashed lines). Figure taken from [181].

decays at midrapidity in Pb–Pb collisions at $\sqrt{s_{\mathrm{NN}}} = 5.02$ and 2.76 TeV [55, 186]. As discussed in [48], such a similar R_{AA} observed at two energies is caused by the interplay of two effects: a) a flattening of the p_{T} spectra of charm and beauty quarks with increasing collision energy, which will increase the R_{AA} by about 5%; b) a higher temperature of about 7% in Pb–Pb collisions at 5.02 TeV than that at 2.76 TeV, which would decrease the R_{AA} by about 10% (5%) for charm (beauty)

quarks.

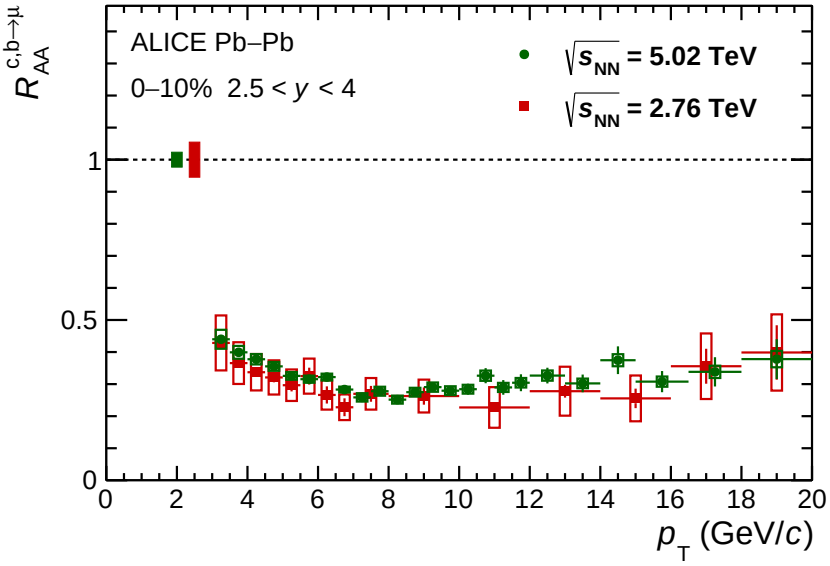

Figure 4.8: Comparison of the p_{T}-differential R_{AA} of muons from heavy-flavour hadron decays at forward rapidity ($2.5 < y < 4$) in the 0–10% most central Pb–Pb collisions at $\sqrt{s_{\mathrm{NN}}} = 5.02$ TeV and 2.76 TeV. Figure taken from [181].

As mentioned at the beginning of this chapter, one of the greatest improvement of this analysis is to extend the measurement to the high-p_{T} region ($p_{\mathrm{T}} > 10$ GeV/c), where more than 70% of muons from heavy-flavour hadron decays originate from beauty quarks as predicted in FONLL calculations [37]. This contribution can even reach 75% in the interval $18 < p_{\mathrm{T}} < 20$ GeV/c. It indicates that the in-medium energy loss of beauty quarks can be reflected in the observed strong suppression of muons from heavy-flavour hadron decays at high p_{T}. In order to further describe the beauty-quark energy loss mechanism in this measurement, a comparison with MC@sHQ+EPOS2 predictions for muons from charm-hadron, beauty-hadron and heavy-flavour hadron decays, in the most 10% central Pb–Pb collisions at $\sqrt{s_{\mathrm{NN}}} =$ 5.02 (top) and 2.76 TeV (bottom), is shown in Fig. 4.9. In addition, two versions of MC@sHQ+EPOS2 predictions are provided: one includes a combination of collisional and radiative energy loss and the other one includes a pure collisional energy loss, as shown in Fig. 4.9. Both versions of the MC@sHQ+EPOS2 model calculations provide a fair description of the R_{AA} of muons from heavy-flavour hadron decays in the most central (0–10%) Pb–Pb collisions at $\sqrt{s_{\mathrm{NN}}} = 5.02$ TeV within uncertainties. For what concerns the comparison at $\sqrt{s_{\mathrm{NN}}} = 2.76$ TeV, the model with the combination of collisional and radiative energy loss overestimates the R_{AA} slightly at low/intermediate p_{T}. In the high-p_{T} region, the data is always closer to the model calculations for muons from beauty-hadron decays than for muons from charm-hadron decays, no matter which energy loss mechanism is included. For the scenario involving only collisional energy loss, the difference between the predicted

$R_{\rm AA}$ of muons from charm and beauty-hadron decays is less pronounced.

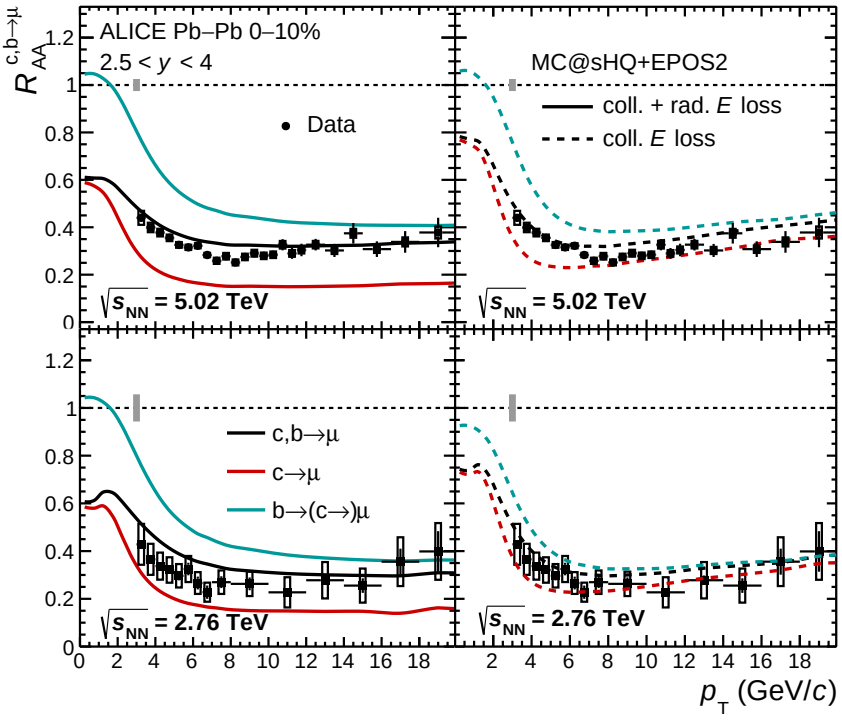

Figure 4.9: Comparison of the $p_{\rm T}$-differential $R_{\rm AA}$ of muons from heavy-flavour hadron decays at forward rapidity ($2.5 < y < 4$) in the most central (0–10%) Pb–Pb collisions at $\sqrt{s_{\rm NN}} = 5.02$ TeV (top) and 2.76 TeV (bottom) with MC@sHQ+EPOS2 calculations with different scenarios considering either a combination of collisional and radiative energy loss (left) or a pure collisional energy loss (right). The calculations are shown for muons from heavy-flavour hadron decays, muons from only charm-hadron or beauty-hadron decays. Figure taken from [181].

4.4 Summary and Outlook

In this chapter, we presented the measurement of the $p_{\rm T}$-differential normalized yield and the nuclear modification factor $R_{\rm AA}$ of muons from charm- and beauty-hadron decays at forward rapidity ($2.5 < y < 4$) in central, semi-central, and peripheral Pb–Pb collisions at $\sqrt{s_{\rm NN}} = 5.02$ TeV, and in central Pb–Pb collisions at $\sqrt{s_{\rm NN}} = 2.76$ TeV. Compared to previous measurements, a wider $p_{\rm T}$ range ($3 < p_{\rm T} < 20$ GeV/c) is accessible for the first time and the systematic uncertainties are reduced in this analysis. A large suppression, up to a factor of three, is observed in the 10% most central collisions with respect to the binary-scaled pp reference, which is compatible with a large heavy-quark in-medium energy loss. The measured $R_{\rm AA}$ is smaller than unity at high $p_{\rm T}$, which indicates that beauty quarks lose a prominent fraction of their energy in the QGP medium. The comparison between different

model calculations and data provide new constraints on the relative in-medium energy loss of charm and beauty quarks.

A new detector, the Muon Forward Tracker (MFT) has been installed during the second Long Shutdown (LS2). It will add new vertexing capabilities to the muon spectrometer. Therefore muons from charm-hadron and beauty-hadron decays will be separated down to low p_{T} [126]. The nuclear modification factor R_{AA} of muons from charm-hadron decays and beauty-hadron decays will become accessible in the upcoming Run 3. The ratio of the two R_{AA} at forward rapidity will be a new observable, which can provide further insights on the parton energy loss mechanisms of heavy quarks in the QGP medium.

CHAPTER 5

Measurements of Azimuthal Anisotropies of Muons in p–Pb Collisions at $\sqrt{s_{\rm NN}} = 8.16$ TeV

In the previous chapter, the nuclear modification factor $R_{\rm AA}$ of muons from heavy flavour hadron decays in Pb–Pb collisions has been presented, and the observed clear suppression indicates large in-medium energy loss effects for heavy quarks. On the other hand, the anisotropic flow is an other key observable to investigate the transport properties of the QGP created in heavy-ion collisions. Based on this, the heavy-flavour decay muon v_2 is measured in Pb–Pb collisions at 2.76 TeV [187], as shown in Fig. 5.1 (upper left). The positive elliptic flow observed in $3 < p_{\rm T} < 7.5$ GeV/c, together with the $R_{\rm AA}$ measurement [56] shown in Fig. 5.1(upper right), provides further important constraints to transport model calculations for high $p_{\rm T}$ muons. However in p–Pb collisions, the $R_{\rm pPb}$ of heavy-flavour decay muons [182] is found equal to unity within uncertainty in the whole $p_{\rm T}$ range, and is well described by Next-to-Leading Order (NLO) perturbative QCD calculations [188]. Naturally, the measurement of muon v_2 at forward rapidity in p–Pb collisions will bring new inspirations and insights for the interpretation of the QGP-like effects observed in small collision systems, as described in this chapter.

In this chapter, we present the azimuthal anisotropy of inclusive muons as a function of $p_{\rm T}$ in p–Pb and Pb–p collisions at $\sqrt{s_{\rm NN}} = 8.16$ TeV with the ALICE detector. Two methods are implemented in this analysis: two-particle cumulant and two-particle correlation methods, which have been introduced in Chap. 2. Besides, various strategies of nonflow suppression are studied, especially for the subtraction of the remaining recoil jet contribution. Finally, the results concerning the inclusive muon v_2 measured with different multiplicity estimators are discussed. Additionally, comparisons to model calculations are considered and the results are also compared to existing measurements at $\sqrt{s_{\rm NN}} = 5.02$ TeV.

5.1 Data Sample and Selection

The data samples used in this analysis were collected in 2016 during the LHC Run 2 data taking. These data are recorded with two different beam configurations, by inverting the direction of colliding particles (proton and lead). For the first case, the proton is moving towards the muon spectrometer. The corresponding measurement of muons covers the forward rapidity interval $2.03 < y_{\rm CMS} < 3.53$, it

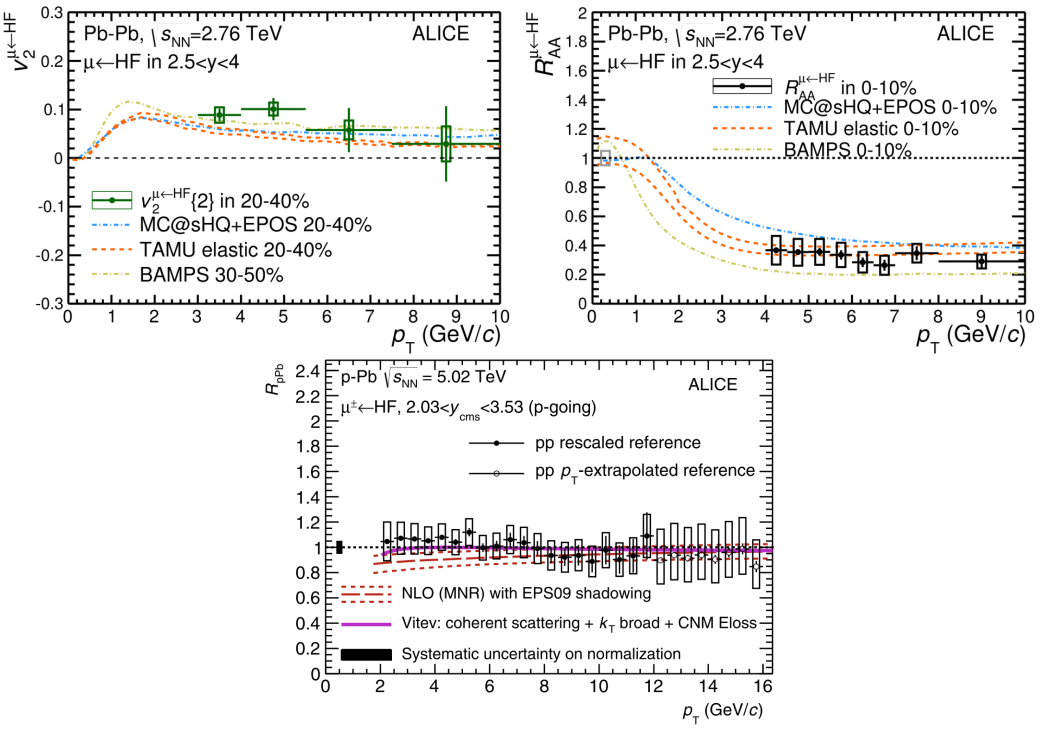

Figure 5.1: Upper left: the p_{T}-differential elliptic flow of muons from heavy-flavour hadron decays in Pb–Pb collisions at $\sqrt{s_{\mathrm{NN}}} = 2.76$ TeV for the multiplicity class 20–40% [187]. Upper right: the p_{T}-differential R_{AA} of muons from heavy-flavour hadron decays for the multiplicity class 0–10% [56]. Bottom: nuclear modification factor of muons from heavy-flavour hadron decays as a function of p_{T} in p–Pb collisions at $\sqrt{s_{\mathrm{NN}}} = 5.02$ TeV at forward rapidity compared to model predictions [182].

is called p–Pb collisions. For the second case of beam configuration, the Pb nucleus is moving towards the muon spectrometer, the resulting measurement is performed at backward rapidity -4.46 < y_{CMS} < -2.96, it is called Pb–p collisions.

Detailed information of run periods and numbers are summarized below:

- p–Pb: LHC16r, muon_calo_pass2, AOD 191, 57 runs
  266318, 266316, 266312, 266305, 266304, 266300, 266299, 266296, 266235, 266234, 266208, 266197, 266196, 266193, 266190, 266189, 266187, 266117, 266086, 266085, 266084, 266081, 266076, 266074, 266034, 266025, 266023, 266022, 265841, 265840, 265797, 265795, 265792, 265789, 265788, 265787, 265785, 265756, 265754, 265746, 265744, 265742, 265741, 265740, 265714, 265713, 265709, 265701, 265700, 265698, 265697, 265696, 265694, 265691, 265607, 265596, 265594;

- Pb–p: LHC16s, muon_calo_pass3, AOD 191, 75 runs
  267131, 267110, 267109, 267077, 267072, 267070, 267067, 267063, 267062, 267022, 267020, 266997, 266994, 266993, 266988, 266944, 266943, 266942,

266940, 266915, 266912, 266886, 266885, 266883, 266882, 266880, 266878, 266857, 266807, 266805, 266800, 266776, 266775, 266708, 266706, 266703, 266702, 266676, 266674, 266669, 266668, 266665, 266659, 266658, 266657, 266630, 266621, 266618, 266614, 266613, 266595, 266593, 266591, 266588, 266587, 266549, 266543, 266539, 266534, 266533, 266525, 266523, 266522, 266520, 266518, 266516, 266514, 266487, 266480, 266472, 266470, 266441, 266439, 266438, 266437.

All runs have been selected after the muon Quality Assurance (QA) checks. The AliPhysics version used for this analysis is 20190808-1.

5.1.1 Event Selection

As mentioned in section 3.3.1.1, not all collisions produced at the LHC will be stored. Only a part of events requiring some non-negligible activity in detectors can pass the trigger system, then they are stored in categories according to the relevant trigger classes that they fired. We can choose offline the events which suit the purpose of specific analysis, this is called **trigger selection**[1]. Furthermore, the events that are not suitable for data analysis (e.g. the beam-gas and pile-up events) also need to be removed offline, such selection together with trigger selection are called **physics selection**. The selection criteria can be easily implemented in the common analysis tasks, though the physics selection framework `AliPhysicsSelectionTask` widely used with ALICE in the Run 2. [189]

5.1.1.1 Trigger Classes

In this analysis, three types of trigger events are selected, the corresponding information is summarized hereafter:

Table 5.1: The trigger alias and trigger classes in p–Pb collisions at $\sqrt{s_{\rm NN}} = 8.16$ TeV

Triggers	Trigger alias	Trigger Class
MB	kINT7inMUON	CINT7-B-NOPF-MUFAST
MSL	kMUS7	CMSL7-B-NOPF-MUFAST
MSH	kMUSH7	CMSH7-B-NOPF-MUFAST

All these three triggers select events are based on at least one hit in both arrays of the V0 detector (V0A and V0C). Besides, the MSL trigger requires that the events have single muons with a $p_{\rm T}$ trigger threshold of 0.5 GeV/c in coincidence with the MB trigger, and the MSH trigger requires at least a single muon with a $p_{\rm T}$ threshold of 4.2 GeV/c.

[1] Note that the trigger selection here is the trivial offline selection, i.e. to choose the events which fired the trigger classes of interest. It should be distinguished from the online trigger selection as described in Sec. 3.3.1.1

5.1.1.2 Physics Selection

After the appropriated triggered events are selected, we also need to reject the remaining background and pile-up events[2].

Background

The background, which is also called beam background, is composited of the products from the interactions of the beam with the remaining beam gas (BG) in the beam pipe. The strategy to remove these events depends on the collision system. Here we take the data collected in p–Pb collisions as an example. Since the products from beam background usually cross the ITS pixel layers in a direction at a small angle (almost parallel) with respect to the beam axis, the reconstruction of such a track pointing to the vertex just requires much more number of clusters compared to that in a physical event. Therefore, the events contaminated by beam background can be rejected by applying a selection on the number of SPD tracklets and clusters, as shown in Fig. 5.2 (upper left). Similarly, the events with a small number of SPD tracklets but with a large number hits in the V0 detector are considered to be removed by applying cuts in the correlation between the multiplicity of V0C012 (i.e. the signals in the rings 0, 1, 2 of the V0C) and the number of tracklets, as shown in Fig. 5.2 (upper right). The events with an asymmetry multiplicity in V0C012 and V0C3 (i.e. the signals in the ring 3 of the V0) also need to be discarded, as shown in Fig. 5.2 (bottom). Furthermore, some selections on the timing information delivered by the V0 and ZDC are also considered.

Pileup

Due to the high interaction rate in the LHC, when the ALICE experiment records the collisions, a fraction of extra collisions are found piled together in the same event. These events are the so-called pileup, they should be removed by an offline event selection, especially in pp and p–Pb collisions. There are two main categories of pileup events:

- **same bunch-crossing pileup:** two or more collisions occurring in the same bunch crossing;
- **out-of-bunch pileup:** one or more collisions occurring in bunch crossings different from the ones which triggered the acquisition.

The same bunch-crossing pileup events are seen in all detectors, they can be removed based on multiple reconstructed vertices[3]. After finding the first vertex in an event, if there is another vertex reconstructed by the tracks which are not from the first vertex and satisfies some selections based on the number of contributors (i.e. the

[2] In fact, these two selections are processed together in ALICE physics selection task without any order.

[3] Multiple reconstructed vertices are also used for pileup events in different bunch crossings within the SPD readout time.

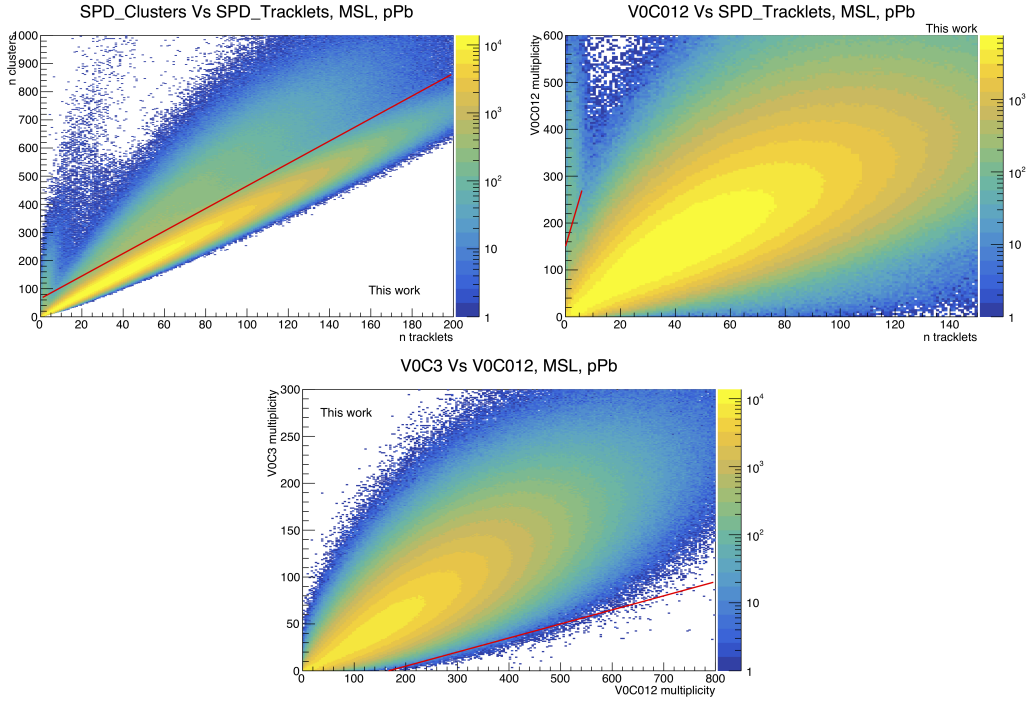

Figure 5.2: Upper left: the correlation between the number of SPD tracklets and clusters. Upper right: the correlation between the number of SPD tracklets and the multiplicity in rings 0, 1, 2 of V0C. Bottom: the correlation between the multiplicity in rings 0, 1, 2 and ring 3 of V0C.

number of tracklets used to calculate the vertex position), the distance from the first vertex [123], this event should be tagged as pileup event. The out-of-bunch pileup events, influence detectors differently depending on their readout time. Usually, the slower detectors (e.g. SPD with a 300ns readout time) has larger probability to catch the out-of-bunch pileup events compared to faster detectors (V0 with 25ns read out time). Therefore, the out-of-bunch pileup events can be removed by rejecting the events accompanied by an additional V0 activity in the SPD readout window, based on the information of $+/-$ 10 bunch crossings around the trigger crossing recorded by the V0, this is the so-called **past future protection**. On the other hand, even for the same detector (e.g V0), the online signal integrated time is much smaller than that offline, due to the fast L0 trigger decision, as described in Sec. 3.3.1.1. So, applying cuts on the correlation of signals at online and offline levels can also reject the out-of-bunch pileup, as shown in Fig. 5.3 (left). Similarly, the selection applied on the correlation between the offline and online SPD Fast-OR is shown in Fig. 5.3 (right).

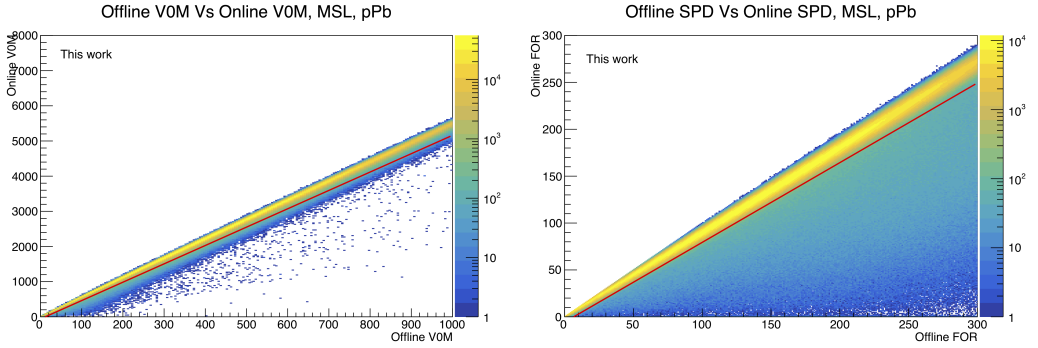

Figure 5.3: Left: the correlation between the offline and online V0M amplitudes. Right: the correlation between the offline and online SPD tracklets.

5.1.2 Collision vertex selection

As described in Sec. 3.3.2.2, the primary vertex can be reconstructed with the ALICE Inner Tracking System with three algorithms: SPD vertex-Z reconstruction (VertexerSPDz), SPD 3-dimension of reconstruction (VertexerSPD3D) and track reconstruction (VertexerTracks). Since this analysis is performed with the muon triggered events, only the SPD is used for the vertex reconstruction. In this case, the number of contributors to the vertex should be larger than unity. If the primary vertex is reconstructed from SPD vertex-Z, the spacial resolution along the beam axis has to be better than 0.25 cm. The last but not least, only events with a primary vertex along the beam axis within ± 10 cm are considered.

5.1.3 Centrality selection

Different estimators can reflect different multiplicity distributions. Figure 5.4 shows the multiplicity distribution for MB, MSL, MSH triggered events with V0, CL1, ZN estimators[4] in both p–Pb and Pb–p collisions. As expected, the centrality distribution in the MB sample is uniform due to the centrality definition described in Sec. 3.3.2.3, but in the MSL and the MSH samples, less events are measured in peripheral collisions because high-multiplicity events are more likely to produce hard probes (i.e. heavy-flavour decay muons). Considering the large fluctuations observed in the 90–100% multiplicity class, only the 0–90% multiplicity class is considered in this analysis.

After all event selections described above are applied, the integrated luminosity of the p–Pb and Pb–p data samples in LHC16r and LHC16s periods corresponds to about 0.25 (6.85) nb^{-1} and 0.26 (9.68) nb^{-1} for MSL- (MSH-) triggered events, respectively.

[4]Due to the asymmetric p–Pb and Pb–p collisions, the fragmentation regions are A side and C side, respectively. Therefore, V0A and ZNA are used in p–Pb collisions, and V0C and ZNC are used for Pb–p colllisions.

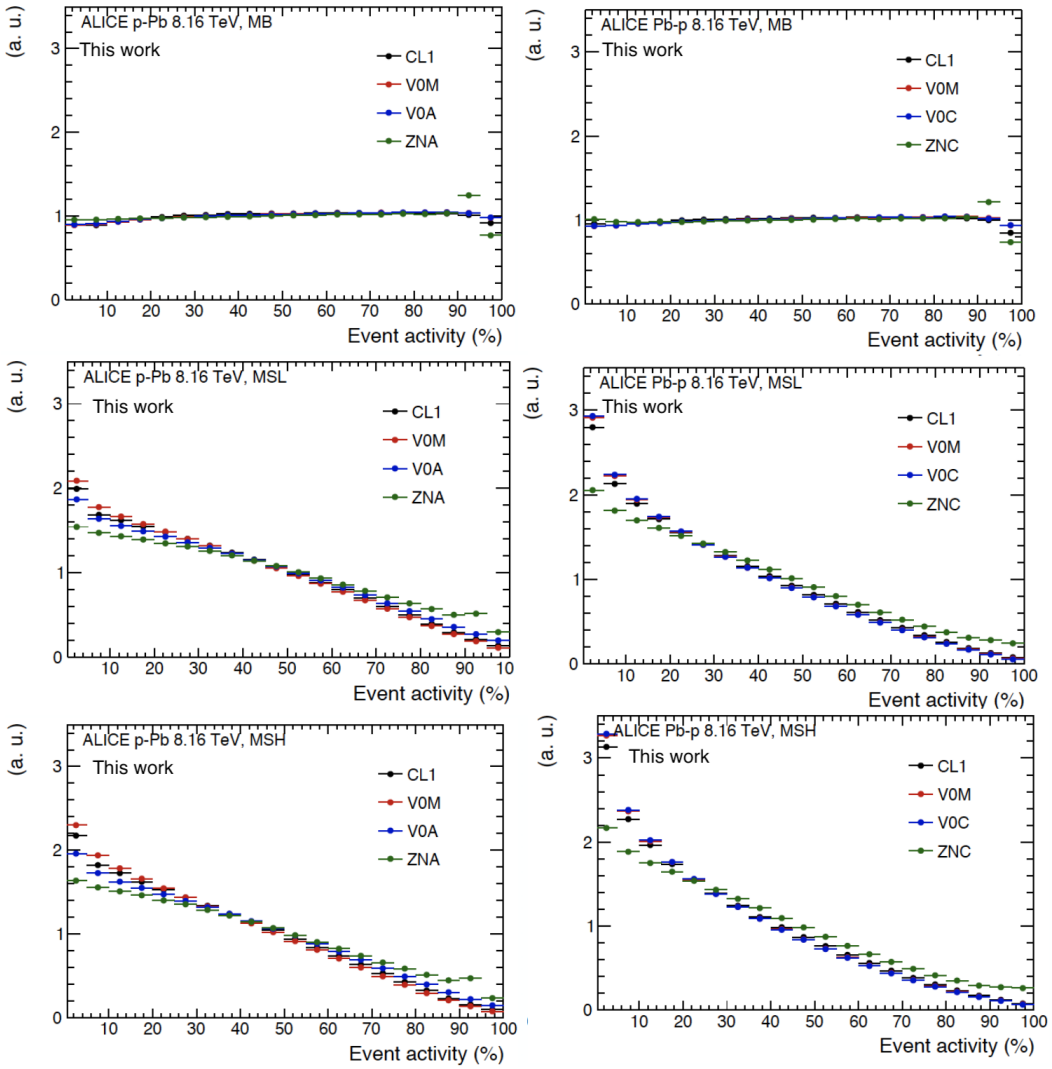

Figure 5.4: The multiplicity distribution in p–Pb (left) and Pb–p (right) collisions with different multiplicity estimators for MB (top), MSL (middle), MSH triggers (bottom).

5.1.4 Track selection

In this analysis, the SPD tracklets at central rapidities and muon tracks at forward rapidities are regarded as the reference particles (RPs) and particles of interest (POIs), respectively. The following cuts are applied.

SPD tracklets

As described in Sec. 3.2.1, the first two layers of the Inner Tracking System (ITS) are the Silicon Pixel Detectors (SPD). Considering the geometry of the SPD, in this analysis, additional cuts need to be applied on the pseudorapidity and the azimuthal

angle of the SPD tracklets. Figure 5.5 shows the z-y plane (left) and the transverse plane (right) of the SPD, where R_1 (3.9 cm) and R_2 (7.6 cm) are the radius of first and second layer of the ITS, L_1(14.1 cm) is the half of the longitudinal size of the second layer, Z_{vertex} is z coordinate of the reconstructed primary vertex and $\Delta\varphi$ is the difference between the azimuthal angles of tracklets in first and second layers.

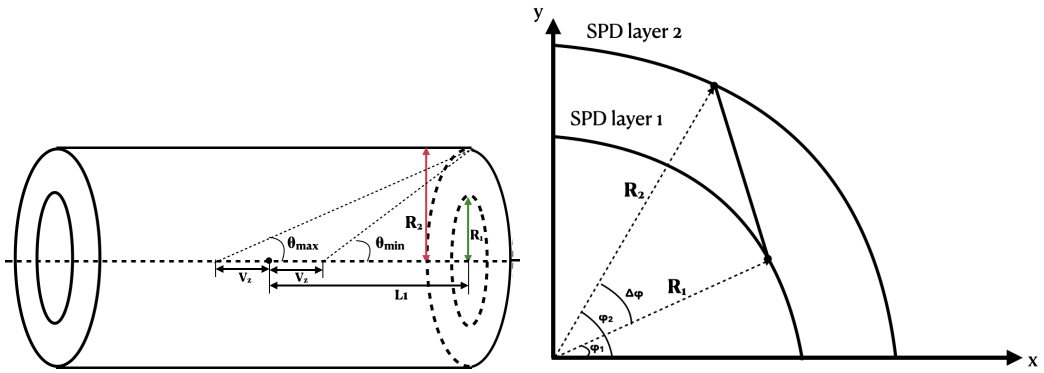

Figure 5.5: The sketch of the SPD detector. Left: the z-y plane of the SPD. Right: the transverse plane of the SPD.

It is easy to observe that the pseudorapidity range of SPD tracklets depends on the Z_{vertex} from Fig. 5.5 (left). The pseudorapidity range $\eta_{\text{min}} < \eta_{\text{tracklets}} < \eta_{\text{max}}$ is defined via the following functions:

$$\begin{aligned} \eta_{min} &= \log(\tan(\frac{1}{2}\arctan(\frac{7.6}{14.1 + Z_{\text{vertex}}})) + 0.1, \\ \eta_{max} &= \log(\tan(\frac{1}{2}\arctan(\frac{7.6}{14.1 - Z_{\text{vertex}}})) - 0.05, \end{aligned} \tag{5.1}$$

where the values 0.1 and 0.05 have been chosen in order to avoid edge effects of the detector where the acceptance drops rather steeply. Figure 5.6 shows the selections on η as a function of Z_{vertex} of SPD tracklets in p–Pb and Pb–p collisions. Furthermore, in order to have a uniform coverage in the SPD, only events with $|Z_{\text{vertex}}| < 7$ cm are considered. The corresponding η selection is $|\eta| < 1$.

Due to the fact that the azimuthal angle (φ) of the SPD tracklets stored in the AOD files only corresponds to the reconstructed space points in the first SPD layer, as shown in Fig. 5.5 (right), it should be corrected to the true azimuthal angle of φ_{corr} value by using the $\Delta\varphi$ value defined as:

$$\varphi_{corr} = \varphi_1 + \frac{R_2 - R_1}{R_1}\Delta\varphi, \quad \Delta\varphi = |\varphi_2 - \varphi_1|, \tag{5.2}$$

where φ_{corr} is the corrected azimuthal angle. Figure 5.7 shows the corrected azimuthal angle distribution in p–Pb (left) and Pb–p (right) collisions for muon-triggered events.

On the other hand, following a previous analysis for p–Pb collisions at $\sqrt{s_{\text{NN}}} =$ 5.02 TeV [190], a tighter cut on $\Delta\varphi$ is applied ($\Delta\varphi < 5$ mrad) to select particles with larger p_{T} and to reduce the contributions of fake and secondary tracks.

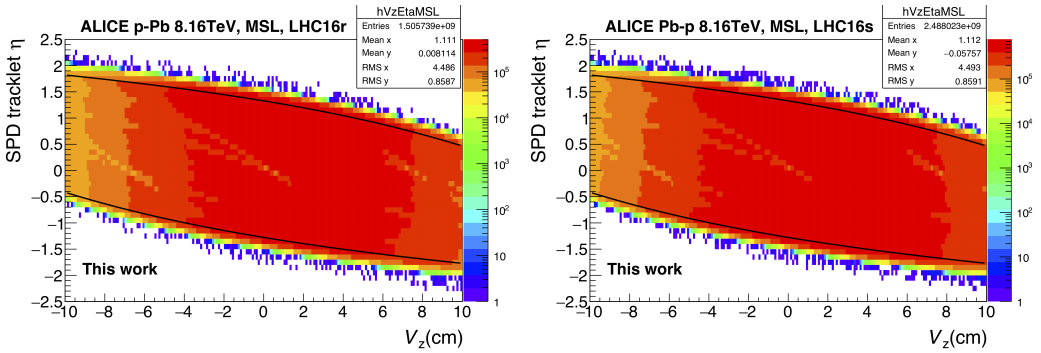

Figure 5.6: Variation of the SPD tracklet η distribution along the Z_{vertex} position for MSL-triggered events in p–Pb (left) and Pb–p (right) collisions. The two black lines show the two outer boundary acceptance cuts, as described in Sec. 5.1.

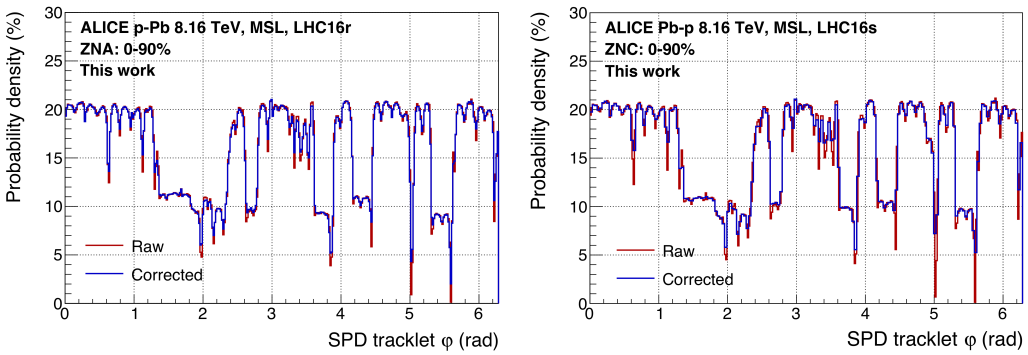

Figure 5.7: Probability density for the raw and corrected SPD tracklet azimuthal angle, for MSL triggered events for p–Pb (left) and Pb–p (right) collisions.

Muon tracks

As in Chap. 4, the standard muon track cuts are applied, and they are implemented via AliMuonTrackCuts with default parameters:

- Muon tracks are required to be reconstructed within the acceptance of the muon spectrometer ($-4 < \eta_{\text{lab}} < -2.5$);
- Polar angle at the end of the front absorber (θ_{abs}) of muon tracks should satisfy the condition: $170^\circ < \theta_{\text{abs}} < 178^\circ$;
- The track candidate in the tracking system matches the track segment reconstructed in the trigger system;
- The $p\times$ DCA cut within 6σ is applied in order to remove remaining beam-induced background tracks and fake tracks.

Figure 5.8 shows the number of muons as a function of p_{T} after the different muon

selections are applied for MSL-(left) and MSH-(right) triggered events in p–Pb collisions at $\sqrt{s_{\rm NN}} = 8.16$ TeV.

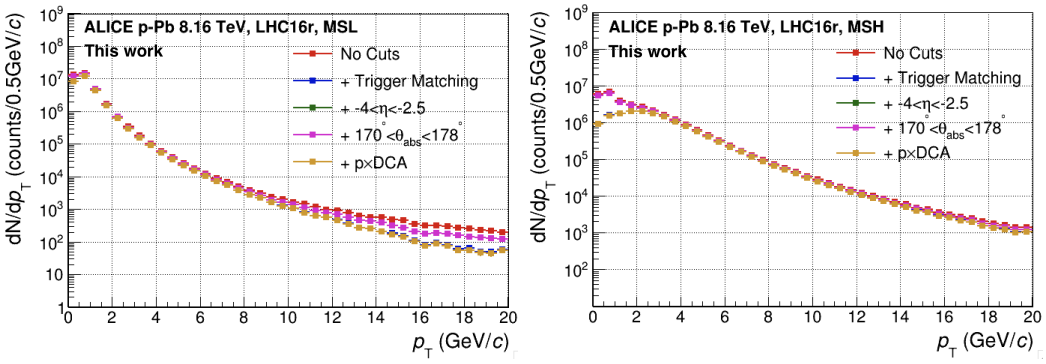

Figure 5.8: The number of muons as a function of $p_{\rm T}$ after different muon selections for MSL-(left) and MSH-(right) triggered events in p–Pb collisions at $\sqrt{s_{\rm NN}} = 8.16$ TeV.

5.2 Two-particle Correlation Method

The two-particle correlation method is a standard method used in the flow analyses. However in heavy-ion collisions, due to the bias from the break of factorization [114], we usually use the scalar product, multi-particle cumulants, Lee-Yang zeros. However in small collision systems, the two-particle correlation method is still widely used [93, 190, 191] since it has a larger power to suppress the nonflow contribution, which is always the largest challenge in the flow measurements in small collision systems.

5.2.1 Correlation Function

As described in Sec. 2.4, the two-particle correlation is defined as the distribution of the associated-particle yield per trigger particle, the so-called **per-trigger yield**. In this analysis, the muon tracks and SPD tracklets are selected as the trigger and associated particles, to construct the muon(μ)-tracklet correlation as a function of their azimuthal angle difference ($\Delta\varphi$) and pseudorapidity difference ($\Delta\eta$), defined as:

$$Y(\Delta\varphi, \Delta\eta) = \frac{1}{N_{\rm trig}} \frac{{\rm d}^2 N_{\rm assoc}^{\mu-{\rm tracklet}}}{{\rm d}\Delta\eta {\rm d}\Delta\varphi} = \frac{S(\Delta\eta, \Delta\varphi)}{B(\Delta\eta, \Delta\varphi)}, \tag{5.3}$$

where $N_{\rm trig}$ is the total number of trigger particles i.e. the number of inclusive muons in a given multiplicity class, $Z_{\rm vertex}$ interval and $p_{\rm T}$ interval. The signal distribution $S(\Delta\eta, \Delta\varphi)$ given by $\frac{1}{N_{\rm trig}} \frac{{\rm d}^2 N_{\rm same}}{{\rm d}\Delta\eta {\rm d}\Delta\varphi}$ corresponds to the per-trigger yield from the same event. The background distribution $B(\Delta\eta, \Delta\varphi) = \alpha \frac{{\rm d}^2 N_{\rm mix}}{{\rm d}\Delta\eta {\rm d}\Delta\varphi}$ is obtained by correlating trigger particles in an event with associated particles from other events in the same multiplicity class and $Z_{\rm vertex}$ interval. The parameter α is introduced

to normalize the background distribution to unity in the $\Delta\eta$ region of maximal pair acceptance. Both the signal and background distributions are calculated in the same centrality class and same $Z_{\rm vertex}$ interval of 1 cm width. The final associated yield per trigger particle is obtained from an average over the $Z_{\rm vertex}$ intervals weighted by $N_{\rm trig}$.

The correlation distribution (Eq. 5.3) is usually composed of correlations arising from collective effects and nonflow effects, the latter consisting of the contribution from both near-side ($|\Delta\varphi| < \pi/2$) and away-side ($\pi/2 < |\Delta\varphi| < 3\pi/2$) regions. Figure 5.9 (upper left) shows an example of the distribution of the associated yield per trigger particle for muon-tracklet correlations as a function of $\Delta\eta$ and $\Delta\varphi$ for high-multiplicity (0–20%) p–Pb collisions at $\sqrt{s_{\rm NN}} = 8.16$ TeV. Since there is a natural large η gap $-5.0 < \Delta\eta < -1.5$ between trigger (muons) and associated (tracklets) particles, the nonflow contribution from near-side is negligible, while the nonflow effects from the away-side are estimated with the correlations calculated from low-multiplicity (60–90%) events [93, 191], as shown in Fig. 5.9 (upper left). This is based on the assumption that the jet contribution is expected to be unchanged with the event multiplicity[5]. Figure 5.9 (lower left) shows the associated yield per trigger particle for muon-tracklet correlations for high-multiplicity events after the subtraction of the per-trigger yield measured in low-multiplicity events. A double-ridge structure is observed with a near-side ridge and a away-side ridge centered at $\Delta\varphi = 0$ and $\Delta\varphi = \pi$, respectively. This double-ridge structure is a clear signature of the presence of collective effects in p–Pb collisions.

In order to quantify the collective effects in the remaining correlations, the two dimensional correlation function (Eq. 5.3) is projected on the $\Delta\varphi$ axis, as shown in Fig. 5.9 (lower right). The Fourier moments can be extracted by fitting the correlation function with:

$$\frac{1}{N_{\rm trig}}\frac{{\rm d}^2 N_{\rm assoc}^{\mu-{\rm tracklet}}}{{\rm d}\Delta\varphi} = a_0 + 2a_1\cos(\Delta\varphi) + 2a_2\cos(2\Delta\varphi) + 2a_3\cos(3\Delta\varphi), \tag{5.4}$$

The fit parameter a_2 is the measurement of the absolute modulation in the subtracted per-trigger yield and characterizes a modulation relative to the baseline b in the high-multiplicity class assuming that such a modulation is not present in the low-multiplicity class below the baseline. Usually, the baseline is estimated at the minimum of the $\Delta\varphi$ distribution in low-multiplicity events[6]. Therefore, the second order flow coefficients $V_{2\Delta}^{\mu-{\rm tracklet}}$ are calculated according to:

$$V_{2\Delta}^{\mu-{\rm tracklet}} = \sqrt{a_2/(a_0+b)} \tag{5.5}$$

[5]The assumption is not fully correct, so an improved nonflow subtraction way will be introduced in section 5.2.2.

[6]It is also called **zero yield at minimum** (ZYAM) hypothesis, which is still debated in the community. Some ATLAS measurements [112] prefer to suppress the nonflow with the so-called **default template fit** method, which remove the baseline b in Eq. 5.5. But in ALICE, we still keep the ZYAM hypothesis in p–Pb collisions, and we will test the subtraction in different multiplicity classes of peripheral collisions, the deviation between them will be considered as the systematic uncertainty.

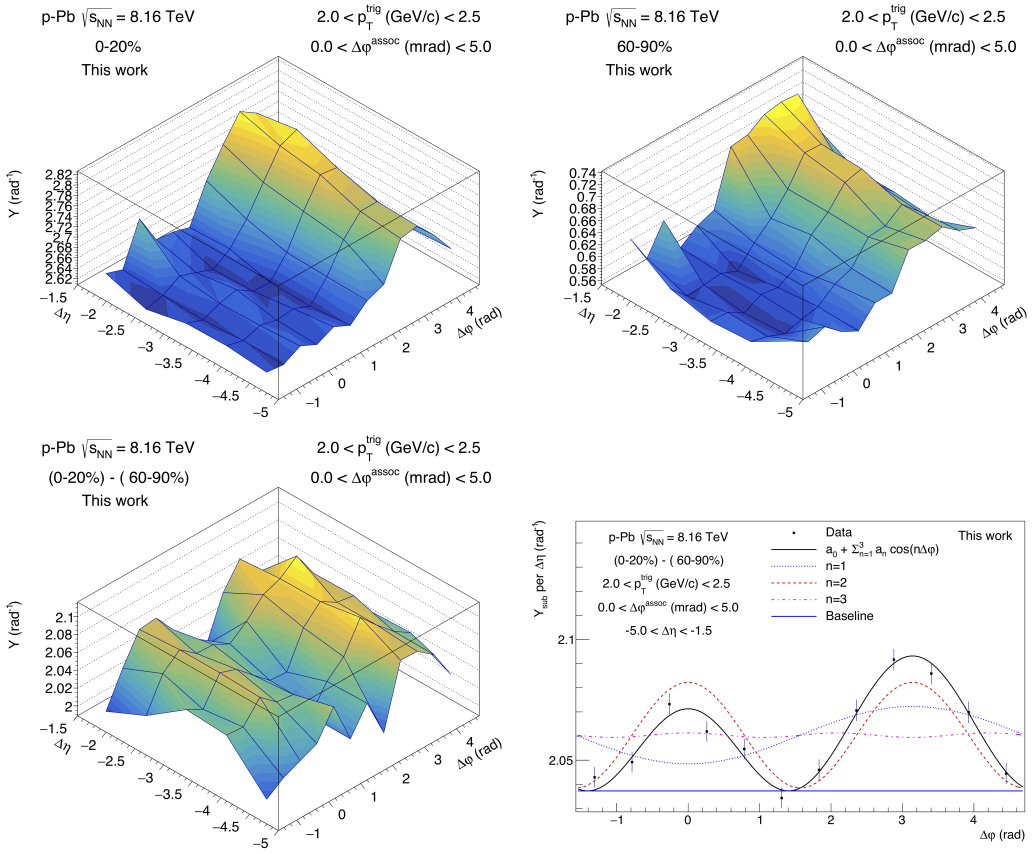

Figure 5.9: Upper left: the per-trigger yield of muon-tracklet correlations in high-multiplicity events. Upper right: the per-trigger yield of muon-tracklet correlations in low-multiplicity events. Lower left: the per-trigger yield after subtraction. Lower right: the $\Delta\varphi$ projection of the two-dimensional correlation function.

As described in Sec. 2.4, the $V_{2\Delta}$ can be factorized into the product of the v_2 of trigger and associated particle, via the factorization relation commonly used for heavy-ion collisions [93, 111, 191]:

$$v_2^{\mu} = V_{2\Delta}^{\mu-\text{tracklet}} / v_2^{\text{tracklet}}, \tag{5.6}$$

where $V_{2\Delta}^{\mu-\text{tracklet}}$ is defined in Eq. 5.5. The v_2^{tracklet} is the v_2 of associated particles (SPD tracklets), which is calculated by constructing the tracklet-tracklet correlation.

In tracklet-tracklet correlations, a similar procedure is implemented, replacing the "μ-tracklet" with "tracklet-tracklet" in Eq. 5.3, Eq. 5.4 and Eq. 5.5. Figure 5.10 shows the distribution of the associated yield per trigger particle for tracklet-tracklet correlations as a function of $\Delta\eta$ and $\Delta\varphi$ for high-multiplicity (upper left) and low-multiplicity (upper right) p–Pb collisions at $\sqrt{s_{\text{NN}}} = 8.16$ TeV. Following the same nonflow subtraction technique as in muon-tracklet correlations, the associated yield per trigger particle in high-multiplicity events after the subtraction of that in low-multiplicity events is shown in Fig. 5.10 (lower left). Since both the trigger and

associated particles are selected at central rapidity, a significant jet-peak is still observed in the near-side after the nonflow subtraction. In order to remove the remaining jet peak at $(\Delta\eta \sim 0, \Delta\varphi \sim 0)$, the region $|\Delta\eta| < 1.2$ is excluded when projecting the distribution of associated yield per trigger particle in tracklet-tracklet correlations into $\Delta\varphi$ direction, as shown in Fig. 5.10 (lower right). The factorization of tracklet-tracklet correlations is implemented via:

$$v_2^{\text{tracklet}} = \sqrt{V_{2\Delta}^{\text{tracklet}-\text{tracklet}}}. \tag{5.7}$$

The stability of the factorization in tracklet-tracklet and muon-tracklet correlations will be further discussed in App. A.

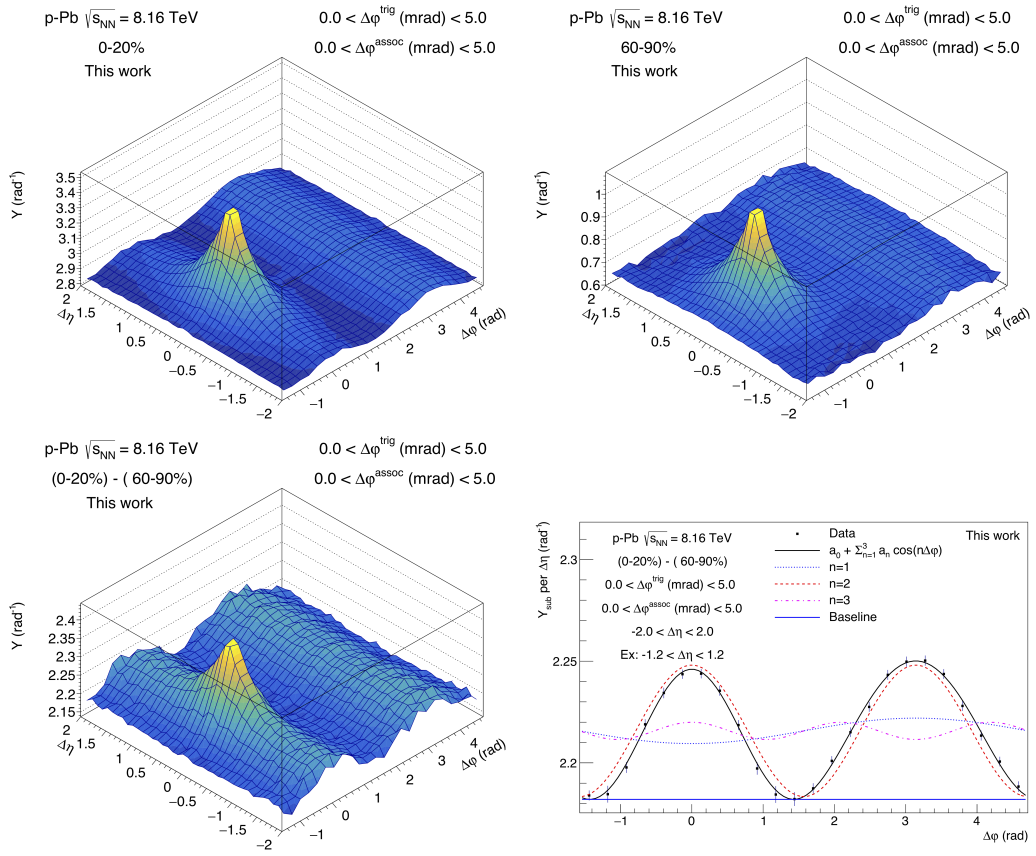

Figure 5.10: Upper left: the per-trigger yield of tracklet-tracklet correlation distribution in high-multiplicity p–Pb collisions. Upper right: the per-trigger yield of tracklet-tracklet correlation distribution in low-multiplicity p–Pb collisions. Lower left: the per-trigger yield after subtraction. Lower right: the $\Delta\varphi$ projection of two-dimensional correlation function.

After the v_2 of the SPD tracklets is calculated, the v_2 of inclusive muons as a function of p_{T} can obtained via the reconstruction of the muon-tracklet correlations in different muon p_{T} intervals. Figure 5.11 shows the v_2 of inclusive muons as a function of p_{T} in the 0–20% high-multiplicity p–Pb collisions with different multiplicity

estimators for both MSL- and MSH-triggered events. It is observed that the muon v_2 for MSL and MSH triggers are consistent within uncertainty. Considering the different p_{T} threshold in muon triggers and the statistics collected with each trigger, we use the MSL and MSH for $p_{\mathrm{T}} < 2$ GeV/c and $p_{\mathrm{T}} > 2$ GeV/c, respectively.

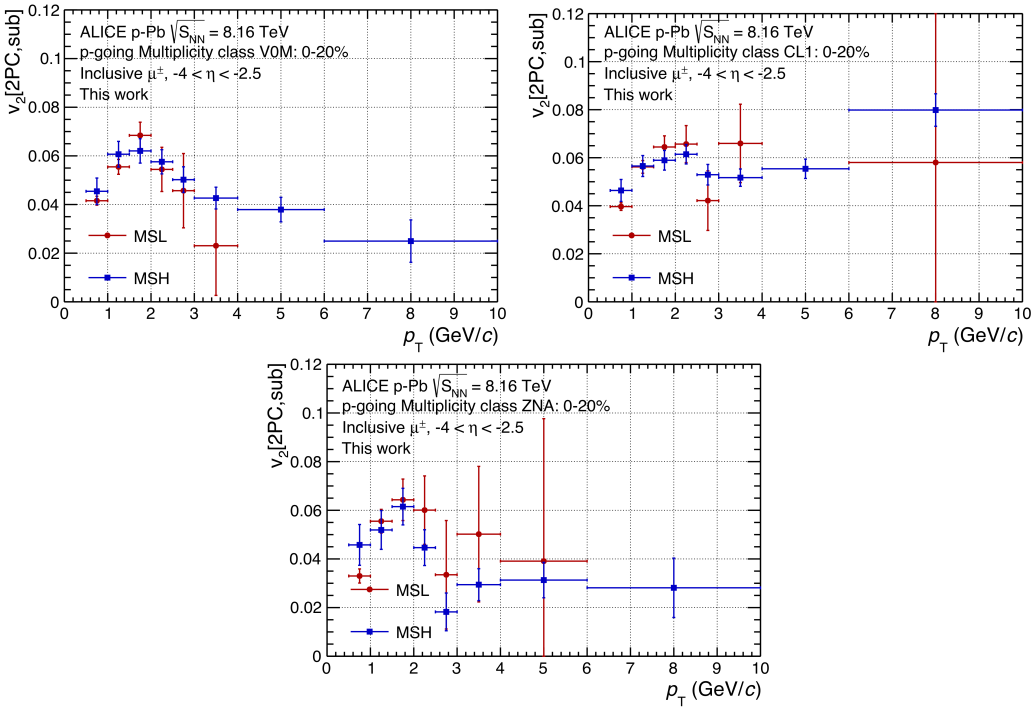

Figure 5.11: The comparison between the muon v_2 in MSL- and MSH-triggered events in high-multiplicity p–Pb collisions at $\sqrt{s_{\mathrm{NN}}} = 8.16$ TeV with V0M (upper left), CL1 (upper right) and ZN (bottom) multiplicity estimators in p–Pb collisions.

5.2.2 Improved Strategy to Subtract Nonflow Effects

The nonflow subtraction is always the most arduous task in the flow analyses in small collision systems. In two-particle correlations, the jet-like correlations represent the main nonflow contribution, which can be divided into two groups: the near-side jet and away-side jet (also called **recoil jet**). The former one is easy to be removed by applying a large η gap between trigger and associated particles or choosing central and forward rapidity particles to obtain a natural η gap. The away-side jet is impossible to be perfectly removed due to its annoying elongated $\Delta\eta$. The traditional way to suppress it, as described above, is to subtract the per-trigger yield in low-multiplicity events from that in high-multiplicity events. The method is based on the strong assumption that the jet-associated yields have no dependence on the event multiplicity. However, some studies [192] show that both near-side and away-side jet-like correlations have a weak dependence on multiplicity, especially in the very low-multiplicity region. The dependence is much stronger when CL1 is

regarded as the multiplicity estimator, since its pseudorapidity range overlaps with the acceptance of the SPD tracklets, which are the associated particles in this analysis. On the other hand, Fig. 5.9 shows that even after the nonflow subtraction, there is still a large remaining away-side jet contribution, and Fig. 5.11 shows the increasing trend of v_2 at high p_{T} which may indicate that the recoil-jet is not well subtracted.

In this case, an improved nonflow subtraction method is introduced, the so-called **low-multiplicity scale**. It was proposed for the first time in the muon-track (tracklet) analysis with p–Pb collisions at $\sqrt{s_{\mathrm{NN}}} = 5.02$ TeV [190], but at that time it was just regarded as the systematic check of remaining nonflow contribution. The general idea is to scale the correlation function in low-multiplicity events before the subtraction. The calculation of the scaling factor is the key point, and the following steps are implemented:

1) To reduce the statistical fluctuations, one symmetrizes the $\Delta\varphi$ distribution from low-multiplicity and high-multiplicity from $(-0.5\pi, 1.5\pi)$ to $(0, \pi)$ region.

2) The $\Delta\varphi$ distribution from low-multiplicity events is fitted with the second order harmonic plus a Gaussian function: $\frac{\mathrm{d}N}{\mathrm{d}\Delta\varphi} = a_0 + 2a_1\cos(2\Delta\varphi) + a_2 e^{-\frac{(x-\pi)^2}{2a_3^2}}$, where the a_1 coefficient is fixed as 0, as shown in Fig. 5.12 (left). Then we can get the fit parameter a_3 as the σ of the Gaussian distribution, and a_2 as the normalization value;

3) The $\Delta\varphi$ distribution from the high-multiplicity events is fitted with same function (i.e. second-order harmonic plus a Gaussian function), but the σ parameter of the Gaussian distribution (a_3) is fixed to that obtained from the fit of the $\Delta\varphi$ distribution in low-multiplicity events in the previous step, as shown in Fig. 5.12 (right);

4) The ratio of the area of the Gaussian between high- and low-multiplicity events is regarded as the scaling factor, which is used to scale the per-trigger yield in low-multiplicity events before its subtraction.

Figure 5.13 shows an example of the scaling factor as a function of p_{T} in p–Pb and Pb–p collisions for the CL1 multiplicity estimator, which indicates that the relative jet contribution has no dependence on the p_{T} of trigger particles within uncertainties. Figure 5.14 shows the per-trigger yield before and after subtraction in tracklet-tracklet (left) and muon-tracklet (right) correlations, where we can see the obvious suppression on the away-side jet contribution. On the other hand, Fig. 5.15 shows the inclusive muon v_2 using the improved nonflow subtraction procedure with different multiplicity estimators. We can see that the v_2 is suppressed a lot at high p_{T}, that is what we expect since the jet contribution dominates at high p_{T}.

A similar improved subtraction strategy to deal with the remaining recoil jet contribution has been investigated, that is the so-called **Fit Subtraction** method, which is firstly studied in the J/ψ v_2 analysis with ALICE [193]. The first two

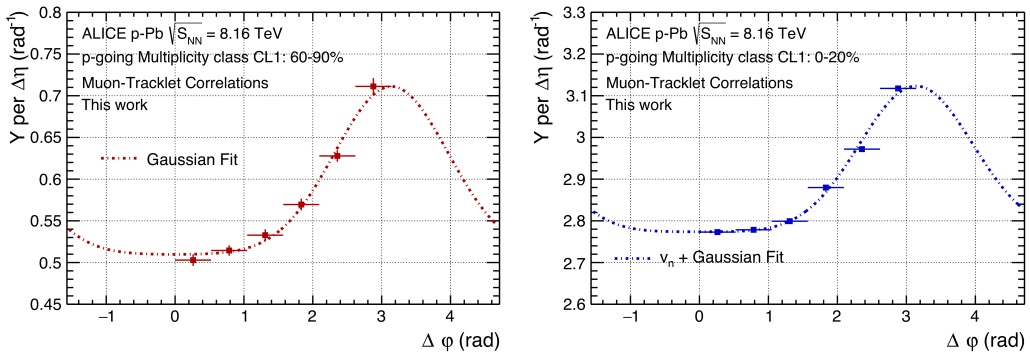

Figure 5.12: Left: the fit of the correlation in low-multiplicity events. Right: the fit of correlation in high-multiplicity events.

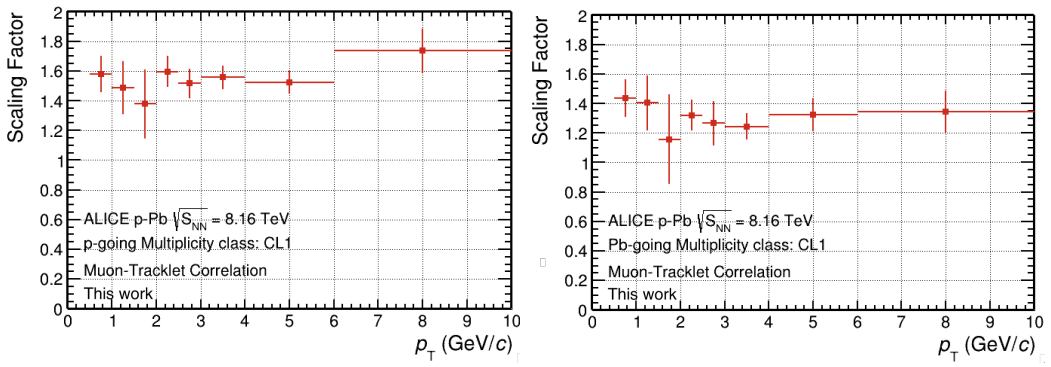

Figure 5.13: The scaling factor as a function of p_{T} in p–Pb (left) and Pb–p (right) collisions with CL1 estimator.

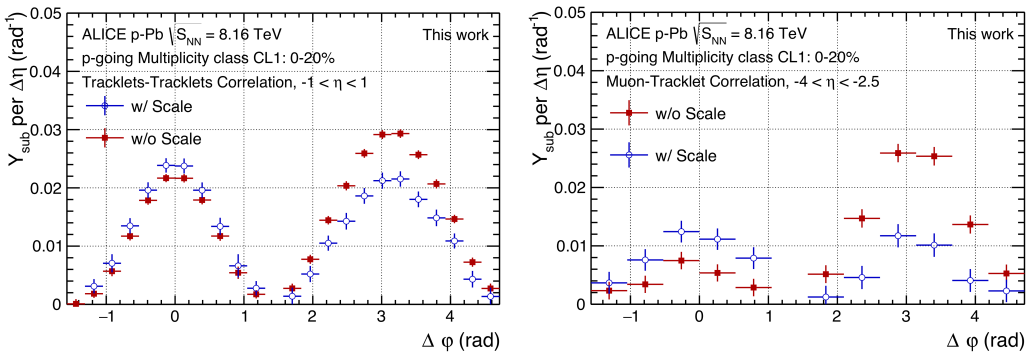

Figure 5.14: The per-trigger yield correlation distribution before and after the improved subtraction procedure in tracklet-tracklet correlations (left) and muon-tracklet correlations (right).

steps of this method are the same as the calculation of the scaling factor in the

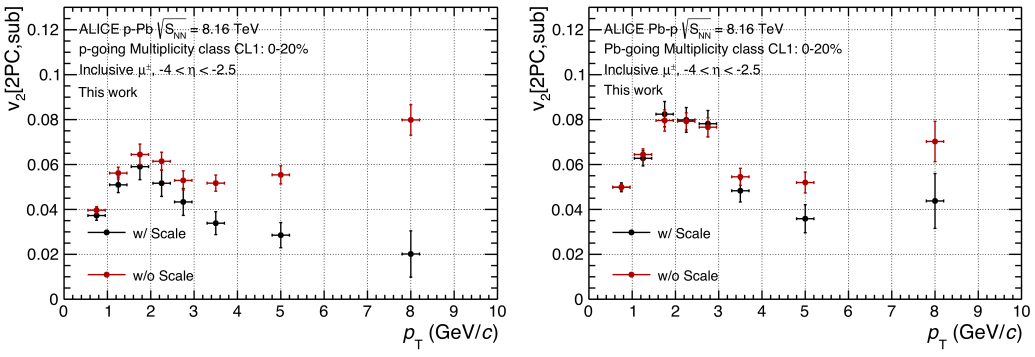

Figure 5.15: The muon v_2 before and after the improved subtraction procedure in p–Pb collisions (left) and Pb–p (right) collisions.

low-multiplicity scale method, i.e. it is based on the subtraction of the σ of the Gaussian fit of the correlation function in low-multiplicity events. Then, following the traditional subtraction strategy, the subtracted $\Delta\varphi$ distribution is obtained, as shown in the bottom plots in Fig. 5.9 and Fig. 5.10. The difference is the fit of the $\Delta\varphi$ distribution, where the fit function shown in Eq. 5.4, is replaced with the Fourier series plus a Gaussian function:

$$\frac{1}{N_{\text{trig}}}\frac{\mathrm{d}^2 N_{\text{assoc}}^{\mu-\text{tracklet}}(N_{\text{assoc}}^{\text{tracklet}-\text{tracklet}})}{\mathrm{d}\Delta\varphi} = a_0 + 2a_1\cos(\Delta\varphi) + 2a_2\cos(2\Delta\varphi) + 2a_3\cos(3\Delta\varphi) + a_4 e^{-\frac{(x-\pi)^2}{2a_5^2}}, \tag{5.8}$$

where the parameter a_1 is fixed to 0, since the contribution from first-order flow coefficient is considered in the gaussian peak, and the parameter a_5 is fixed at the σ obtained in the last step, i.e. the σ of the Gaussian fit of the correlation function in low-multiplicity events. The muon v_2 obtained with the fit subtraction method will be considered as a systematic uncertainty, as shown in Sec. 5.2.3.

5.2.3 Systematic Uncertainties

Various systematic uncertainties are evaluated, which take into account the deviations caused by the related analysis procedures. They will affect both the tracklet-tracklet correlations and muon-tracklet correlations, but we only focus on the effect of the final muon v_2, to see how large it will change when we vary the selections. Based on this purpose, only one selection from the overall set is varied every time, while the rest is kept as the default.

Most of systematic uncertainties are estimated following the previous muon-track (tracklet) analysis for p–Pb collisions at $\sqrt{s_{\text{NN}}} = 5.02$ TeV [190]. Five systematic uncertainty sources are investigated in the following:

- **Correlation function calculation**

  - **Vertex05** The Z_{vertex} cut is restricted to $|Z_{\text{vertex}}| < 5$ cm

- **Remaining jet contribution after nonflow subtraction**
  - **exclusion08** The η gap in the calculation of $v_{2,\text{tracklet}}$ is reduced to $|\Delta\eta| < 0.8$;
  - **Fit Subtraction** The fit subtraction method is used to suppress the remaining jet, as described in section 5.2.2.

- **Remaining ridge in the low multiplicitiy class**
  - **70 to 90%** The multiplicity class 70–90% is used instead of 60–90% for the nonflow subtraction[7].

- v_2 **extraction**
  - **baseline estimation**
    - **baselineGausFit** The baseline is evaluated from a fit of the correlation function using a Gaussian with v_2 and the baseline;
    - **baselineHighMult** The v_2 is calculated using the baseline estimated in the high-multiplicity class directly;
    - **baselineHighMultParab** The baseline in the high-multiplicity class is estimated using a parabolic fit around $\pi/2$ ($\pi/2 \pm 0.2$).
  - **constant fit** Instead of a first order polynomial function, a constant fit is used to reduce the statistical fluctuations in the projection procedure.
  - **no** v_3 The v_2 is calculated only using the first and second Fourier harmonics in the fit.

- **Resolution** The effect of the muon track resolution[8] is evaluated by means of a dedicated Monte Carlo simulation based on the DPMJET event generator [195] which uses the GEANT4 transport code [177] and the afterburner flow technique [196]. More details are given in App. B.

The deviation between the muon v_2 obtained in each systematic check and the default muon v_2 is regarded as the systematic uncertainty. Besides, the following principles need to be considered:

- All systematic checks should pass the barlow test [197] bin by bin, i.e. the significance σ should be larger than 1:

$$\frac{|x_1 - x_2|}{\sqrt{|\sigma_1^2 \pm \sigma_2^2|}} > 1. \tag{5.9}$$

[7] In order to reduce the bias from the remaining ridge in low-multiplicity events, a improved template fit method was proposed in [194]. However, due to the limit of the data statistics, it is not employed in this analysis.

[8] The resolution of SPD tracklets is not considered in this analysis, since a previous analysis [190] shows that the discrepancy of $\Delta\varphi$ distribution between reconstructed and generated SPD tracklets is uniform. Therefore it does not introduce a modulation.

Table 5.2: Summary of absolute systematic uncertainties with the centrality estimator V0M. The intervals of the uncertainties correspond to the measured inclusive muon p_{T} range.

Source	V0M	
	p-going ($\times 10^3$)	Pb-going ($\times 10^3$)
SPD acceptance	$0.2 - 8.0$	$0.9 - 6.5$
Residual jet	$0.6 - 6.7$	$0.3 - 7.1$
Remaining ridge in $60 - 90\%$	$0.3 - 6.2$	$0.05 - 13.7$
$v_2^{\mu}\{2\mathrm{PC}\}$ calculation	$0.2 - 1.7$	$0.4 - 3.4$
Resolution effects	$0 - 0.7$	$0.2 - 0.7$
Total	$1.5 - 10.7$	$1.4 - 17.1$

In case of correlated variables, the denominator will have a - sign, otherwise the denominator will have a + sign.

- For each systematic uncertainty source, only the largest contribution is considered.
- If the systematic checks are believed to be "typical", then the variation is divided by $\sqrt{2}$ to get the uncertainty [198]

Finally, the systematic uncertainties are shown in Fig. 5.16. They are added in quadrature to obtain the overall systematic uncertainty on $v_2^{\mu}\{2\mathrm{PC}\}$ which varies from about 0.001 at low p_{T} to 0.011-0.017 at high p_{T}, depending on the beam configuration. The summary of these uncertainties is also shown in Tab. 5.2 for the V0M multiplicity estimator. The uncertainties exhibit the similar trend with other multiplicity estimators.

5.3 Two-particle Cumulants

Cumulants methods are widely used in flow analyses, due to an important advantage that the flow coefficients can be obtained analytically order by order. In this analysis, due to the limits of statistics, we only use the two-particle cumulants to get the v_2, i.e. $v_2\{2\}$. The SPD tracklets, under the same selection criteria as with two-particle correlations, are chosen as the reference particles, the muon tracks after standard selections are the particles of interest. As described in Sec. 2.3.2, thanks to the development of the generic framework, the two-particle second-order reference and p_{T}-differential cumulants, $c_2\{2\}$ and $d_2^{\mu}\{2\}$ can be easily calculated after constructing the weighted $\vec{Q}$ vector. The calculation of the p_{T}-differential inclusive muon $v_2^{\mu}\{2\}$ in a given multiplicity is performed as

$$v_2^{\mu}\{2\}(p_{\mathrm{T}}) = \frac{d_2^{\mu}\{2\}(p_{\mathrm{T}})}{V_2\{2\}}, \tag{5.10}$$

where $V_2\{2\}$, the reference elliptic flow, is expressed as

$$V_2\{2\} = \sqrt{c_2\{2\}}. \tag{5.11}$$

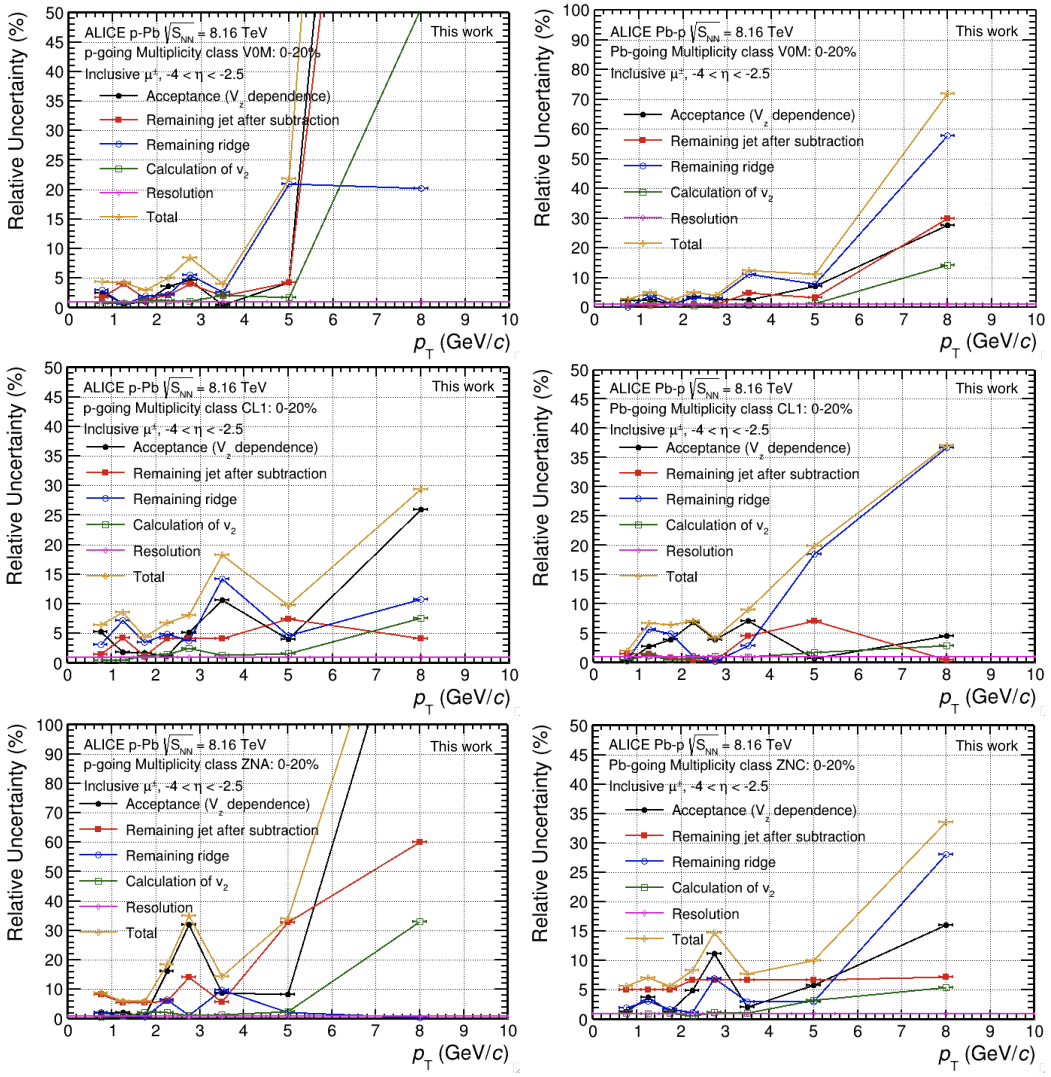

Figure 5.16: The systematic uncertainty as a function of p_{T} in p–Pb (left) and Pb–p (right) collisions with V0M (top), CL1 (middle) and ZN (bottom) multiplicity estimators.

5.3.1 Non-Uniform Acceptance

Measurements of two-particle cumulants are sensitive to detector inefficiencies in their azimuthal acceptance, which can bias the final results [108]. This is the so-called **Non-Uniform Acceptance (NUA)** effect. In an ideal case of a fully efficient detector, the event-averaged φ distribution of particles will be uniform. However, as an example shown in Fig. 5.17, non-uniform azimuthal distributions are observed for SPD tracklets (left) and muon tracks (right) in MSH-triggered events for p–Pb collisions in the 0–20% multiplicity class, which need to be further corrected before the calculation of cumulants. The correction for the NUA is implemented in the Generic Framework in the form of per-particle weight, as introduced in Eq. 2.39

and Eq. 2.45 of Sec. 2.3.2. The weights are calculated from the event-averaged φ distribution as $w_i = 1/N_i$, where N_i is the number of entries in the i^{th} bin of the φ distribution. The final event-averaged φ distribution is unity after applying the weight w_i in each φ bin, as shown in Fig. 5.18. In addition, the results of the NUA correction are applied in other multiplicity classes, $Z_{\rm vertex}$ bins and transverse momentum ranges (for muon track case) are shown in App. C.

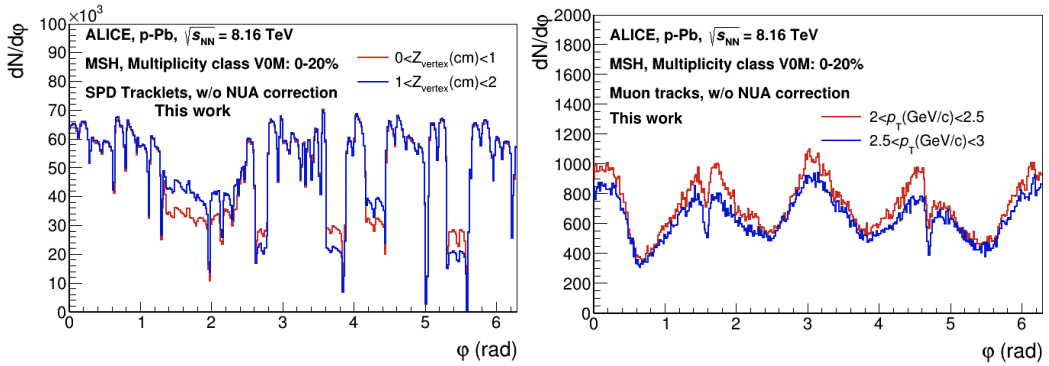

Figure 5.17: The φ distribution of SPD tracklets (left) and muon tracks (right) before the NUA correction in MSH-triggered events for high-multiplicity (0–20%) p–Pb collisions at $\sqrt{s_{\rm NN}} = 8.16$ TeV.

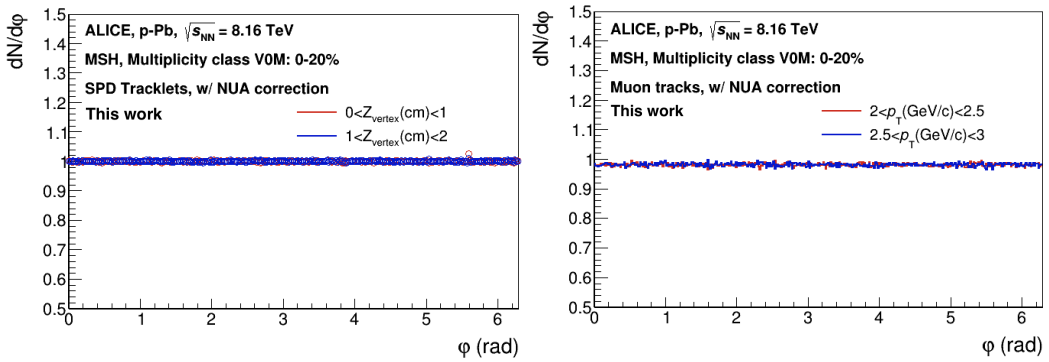

Figure 5.18: The φ distribution of SPD tracklets (left) and muon tracks (right) after the NUA correction in MSH-triggered events for high multiplicity (0–20%) p–Pb collisions at $\sqrt{s_{\rm NN}} = 8.16$ TeV.

5.3.2 Reference Cumulants and Differential Cumulants

After the appropriate NUA correction of SPD tracklets, the reference cumulants c_2 and reference flow V_2 can be obtained, where $V_2 = \sqrt{c_2}$. Figure 5.19 shows the V_2 as a function of event multiplicity with two different estimators. The increasing trend indicates the existence of a nonflow contribution, which also includes the

near-side jet and recoil jet contributions. Their subtraction will be discussed in Sec. 5.3.3. Besides, no dependence on the trigger selection is observed, which shows that the muon triggers do not introduce a bias in the measurement of the azimuthal anisotropy of particles located at midrapidity.

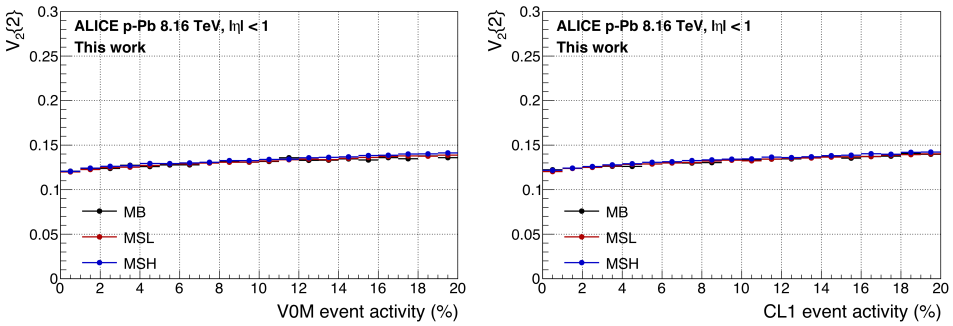

Figure 5.19: Reference flow V_2 as a function of the event activity with the V0M (left) and the CL1 estimator (right).

After the NUA correction of muon tracks, the differential cumulants d_2 can be obtained, as shown in Fig. 5.20 (upper left and upper right). The d_2 coefficient measured in MSL- and MSH-triggered events are consistent within uncertainties, but obvious larger fluctuations are observed for MSL trigger with $p_{\mathrm{T}} > 2$ GeV/c. Therefore, we will use MSL data for $p_{\mathrm{T}} < 2$ GeV/c, while MSH-triggered data is used for $p_{\mathrm{T}} > 2$ GeV/c. Together with the reference V_2, the differential v_2 is calculated as $v_2 = d_2/V_2$, as shown in Fig. 5.20 (lower left and lower right). One can observe that v_2 increases with increasing p_{T} due to the nonflow contribution, which is not yet subtracted (see Sec. 5.3.3).

5.3.3 Nonflow Subtraction

As in the two-particle correlation analysis, the nonflow contribution includes both short-range and long-range jet contribution. For the long-range jet component, we still estimate it in the low-multiplicity events (60–90%) and subtract it from the high-multiplicity events (0–20%) for both differential and reference cumulants, as shown in:

$$v_2\{2\}^{\mathrm{pPb,sub}}(p_{\mathrm{T}}) = \frac{d_2^{\mathrm{high}} - k \cdot d_2^{\mathrm{low}}}{\sqrt{c_2^{\mathrm{high}} - k \cdot c_2^{\mathrm{low}}}}, \tag{5.12}$$

where k is the ratio of the number of SPD tracklets in low-multiplicity events to that in high-multiplicity events. It is regarded as the factor to scale the cumulants of nonflow in low-multiplicity events to match that in high-multiplicity events.

However, as we discussed in Sec. 5.2.2, the subtraction method with low-multiplicity events can not deal with the remaining away-side nonflow contributions, since the assumption that the recoil jet has no dependence on the multiplicity is not fully correct. So for differential cumulants, i.e. the numerator in Eq. 5.12, we introduce an additional scaling factor to the cumulants in peripheral collisions when

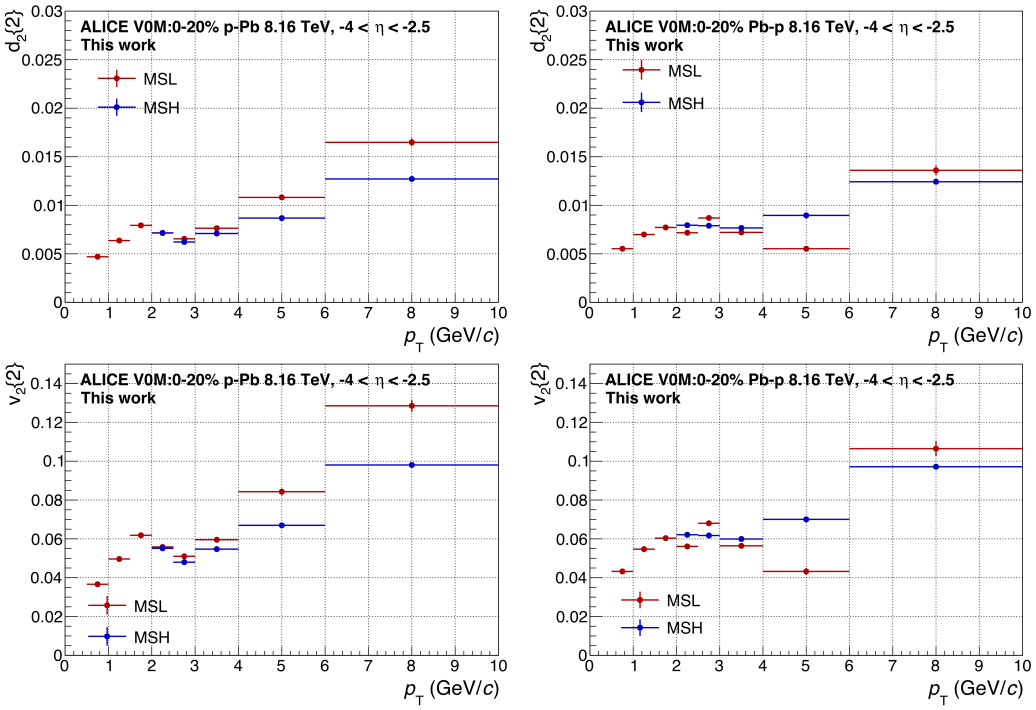

Figure 5.20: Differential cumulants and v_2 as a function of p_{T} for MSL- and MSH-triggered sample in the 0–20% multiplicity class with the V0M estimator. Upper left: differential cumulants in p–Pb collisions. Upper right: differential cumulants in Pb–p collisions. Lower left: differential v_2 in p–Pb collisions. Lower right: differential v_2 in Pb–p collisions.

doing the subtraction. Thus the Eq. 5.12 is written as:

$$v_2\{2\}^{\mathrm{pPb,sub}}(p_{\mathrm{T}}) = \frac{d_2^{\mathrm{high}} - k \cdot k^{'} \cdot d_2^{\mathrm{low}}}{\sqrt{c_2^{\mathrm{high}} - k \cdot c_2^{\mathrm{low}}}}, \tag{5.13}$$

where the $k^{'}$ is the ratio of the away-side jet contribution between high- and low-multiplicity events, obtained via the two-particle correlation method, as discussed in Sec. 5.2.2 and shown in Fig. 5.13. Figure 5.21 shows the differential cumulants as a function of p_{T} with and without the long-range jet subtraction in p–Pb and Pb–p collisions with different centrality estimators. We can clearly observe that the cumulants can be well suppressed after the subtraction, especially at high p_{T}. For the reference cumulants, i.e. the denominator of Eq. 5.13, the remaining non-flow contribution includes near-side and away-side jet contribution, which are both suppressed by introducing an additional factor. The away-side jet contribution is suppressed by applying the factor f_{RP} to the reference flow V_2. The factor f_{RP} is obtained from the tracklet-tracklet correlation function, and is the ratio of the reference flow coefficient obtained from tracklet-tracklet correlations with the scaling of the remaining jet contribution to that obtained without any scaling procedure, as shown in Fig. 5.14 (left). Therefore the Eq. 5.13 is further transformed into:

$$v_2\{2\}^{\mathrm{pPb,sub}}(p_{\mathrm{T}}) = \frac{d_2^{\mathrm{high}} - k \cdot k^{'} \cdot d_2^{\mathrm{low}}}{f_{\mathrm{RP}} \cdot \sqrt{c_2^{\mathrm{high}} - k \cdot c_2^{\mathrm{low}}}}. \tag{5.14}$$

The near-side jet contribution is suppressed via the scaling of the muon second-order coefficient by an other factor, $f_{\Delta\eta}$, estimated by means of AMPT simulations. We choose the AMPT fast simulation production LHC15d4a, LHC15d4b (p–Pb, 5.02 TeV) and LHC15d4c (Pb–p, 5.02 TeV), with the string melting option activated. The event activity is estimated from the charged-particle multiplicity in the V0A and V0C acceptance. The particles located in the acceptance of SPD ($|\eta| < 1$) and muon spectrometer (-4 $< \eta <$ -2.5) are used as the reference particles (RPs) and particles of interest (POIs). Then, the η gap is applied in both RPs and POIs, and varied with different values, as shown in Fig. 5.22. We can find that the larger η gap refers to the larger differential v_2, which is due to the fact that the η gap decreases the reference flow. To quantify this effect, the ratio between v_2 with different η gap and v_2 with no η gap is calculated, as shown in Fig. 5.23 (left). As expected, the ratio has no dependence on p_{T} since the near-side jet contribution only dominates for the reference particles. In order to add a cross check about such η gap effect, we also did same estimations in data, but employed the raw NUA correction without considering the Z_{vertex} dependence. Here we assume that the η gap effect should have no dependence on the NUA correction strategy which is only driven by the detector issues. Figure 5.23 (right) shows the ratio from data, which is consistent with the results in AMPT within large uncertainties. The deviation between the data and AMPT will be regarded as the systematic uncertainty. In this case, we would like to choose the ratio obtained from AMPT as the factor $f_{\Delta\eta}$ to describe

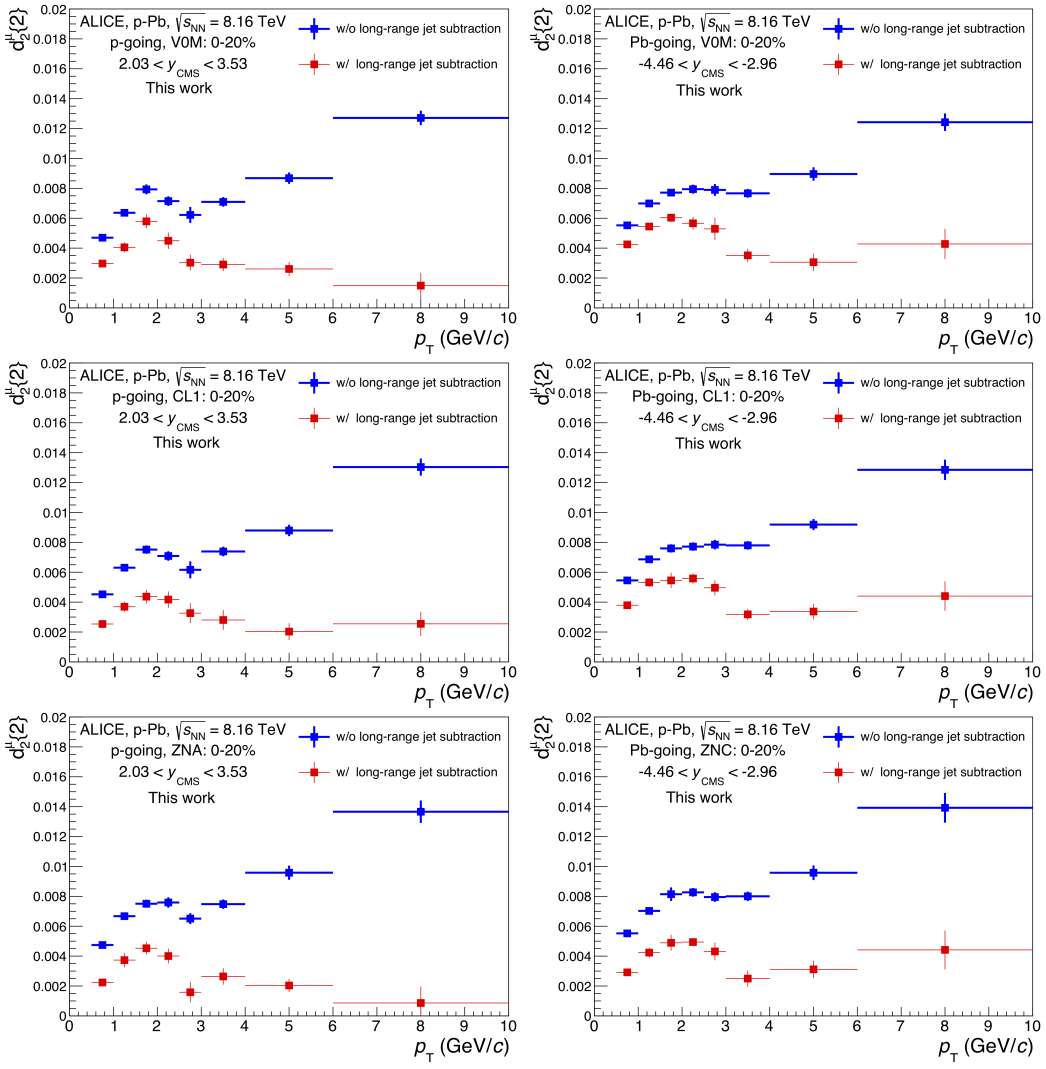

Figure 5.21: The differential cumulants as a function of p_{T} with and without long-range jet subtraction in p–Pb (left) and Pb–p (right) collisions with V0M (top), CL1 (middle), ZN (bottom) multiplicity estimators.

the contribution from short-range jet contribution in Eq. 5.15, and 0.4 is set as the default η gap. Finally, the Eq. 5.14 can be transformed into

$$v_2\{2\}^{\mathrm{pPb,sub}}(p_{\mathrm{T}}) = \frac{d_2^{\mathrm{high}} - k \cdot k' \cdot d_2^{\mathrm{low}}}{f_{\mathrm{RP}} \cdot \sqrt{c_2^{\mathrm{high}} - k \cdot c_2^{\mathrm{low}}}} \cdot f_{\Delta\eta}. \tag{5.15}$$

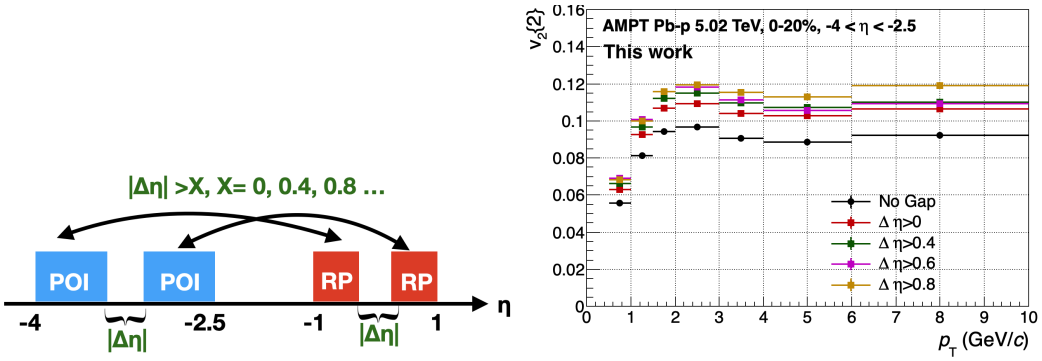

Figure 5.22: Left: the illustration of the application of η gap. Right: the comparison between v_2 extracted applying different η gaps.

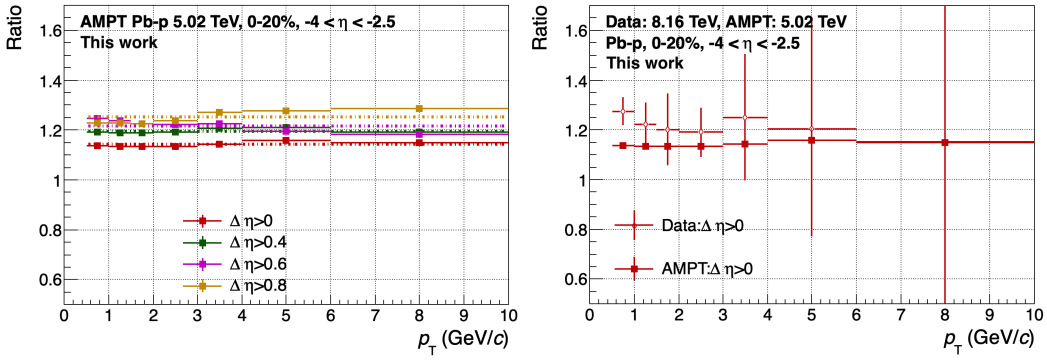

Figure 5.23: The ratio between the muon v_2 with different $\Delta\eta$ intervals and the muon v_2 with no η gap in AMPT (left) and data (right).

So far, the whole nonflow subtraction in cumulant method is finished. Figure 5.24 shows the comparison of the final muon v_2 before and after the nonflow subtraction. It shows the combined effect from the long-range and short-range nonflow contributions.

5.3.4 Systematic Uncertainties

The strategy to estimate the systematic uncertainties is the same as that with the two-particle correlation method. The deviation between the default v_2 measurement and the v_2 value obtained varying selections and strategies is considered as the systematic uncertainty if it can pass the barlow test which allows us to check if

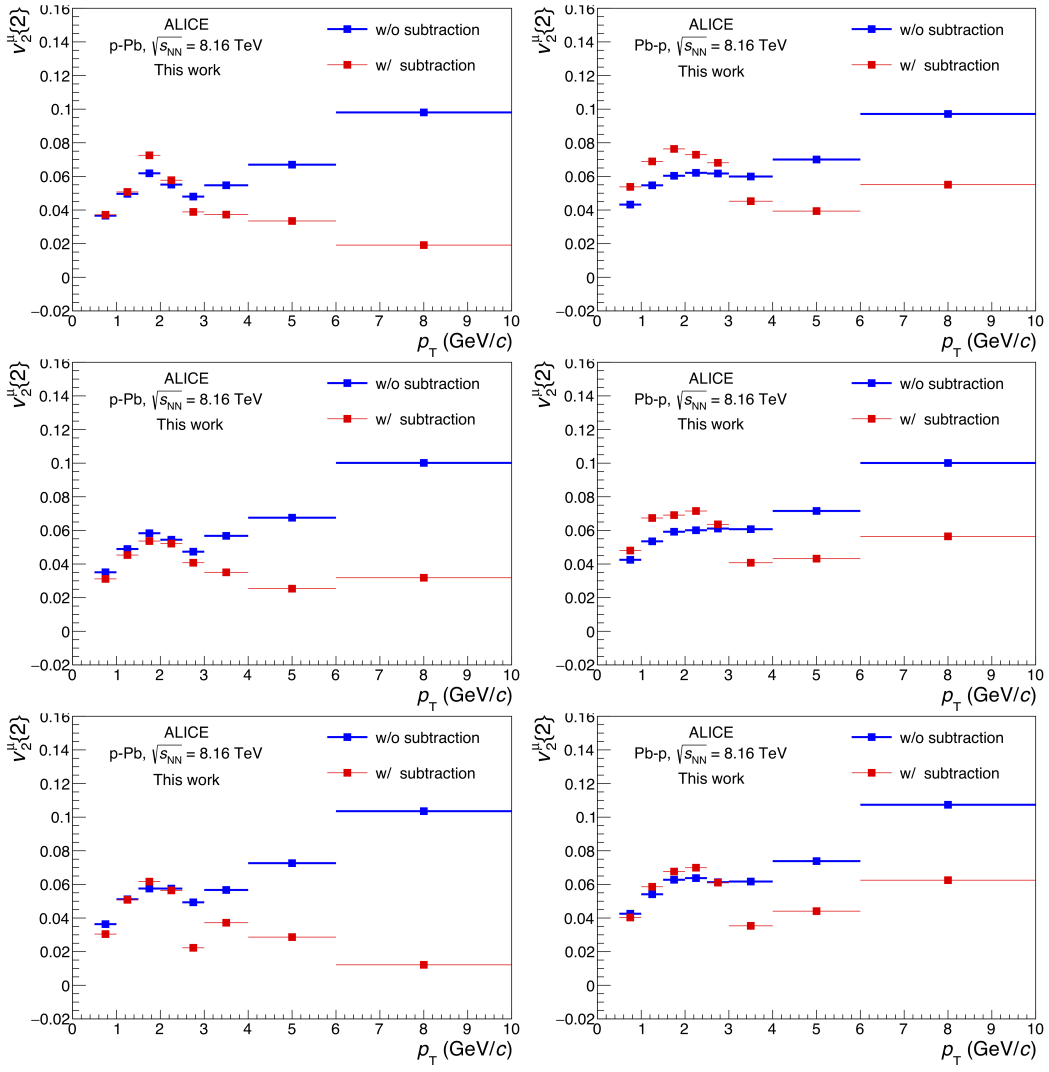

Figure 5.24: The differential v_2 as a function of p_{T} with and without nonflow subtraction in p–Pb (left) and Pb–p (right) collisions with V0M (top), CL1 (middle) and ZN (bottom) multiplicity estimators.

the deviation is due to statistical fluctuations. The determination of statistical uncertainties is firstly discussed.

Statistical Uncertainty

Differently from the two-particle correlation method, the statistical uncertainties in two-particle cumulants can not be directly obtained from the calculation. A more appropriate way is to analyze part of events sampled from the whole dataset, and to choose the variance of these results to describe the statistical fluctuations, this is so-called **sub-sample** method. To make the estimation more stable, we use the **delete-*d* jackknife** [199] to do the re-sampling. The detailed procedure is:

- Divide the full sample into 12 sub-samples, choose six of them randomly as a new sample, thus we have up to 924 different combinations (new samples);
- For each new sample, we do the whole analysis as one trail and we can get the final muon v_2. The v_2 distribution can be obtained in each p_{T} interval, as shown in Fig. 5.25. The distribution gradually converges into a gaussian distribution;
- The RMS of the v_2 distribution becomes more stable with the increasing number of combinations, as an example shown in Fig. 5.26, so we fit the data points at the plateau to extract the uncertainty.

Systematic Uncertainties

In the two-particle cumulants method, the systematic uncertainty sources are divided into following parts:

- **Trigger Bias** Muon-trigger bias for the NUA correction of SPD Tracklets: the NUA correction template obtained from MB trigger is used to correct MSL and MSH samples;
- $\boldsymbol{|\eta_{\mathrm{tracklets}}| < 1.2}$ The pseudorapidity η range of reference particles varied from $|\eta| < 1$ to $|\eta| < 1.2$;
- **$\Delta\eta$ gap MC/Data** The difference between the simulation and data when estimating the η gap;
- **$\Delta\eta$ gap variation** The η gap in reference particles varied from $|\Delta\eta| < 0.4$ to $|\Delta\eta| < 0.8$;
- **Resolution** Resolution effect, same with the two-particle correlation method;
- **70_90 subtraction** The multiplicity range 70–90% is used instead of 60–90% for the subtraction of nonflow effects;

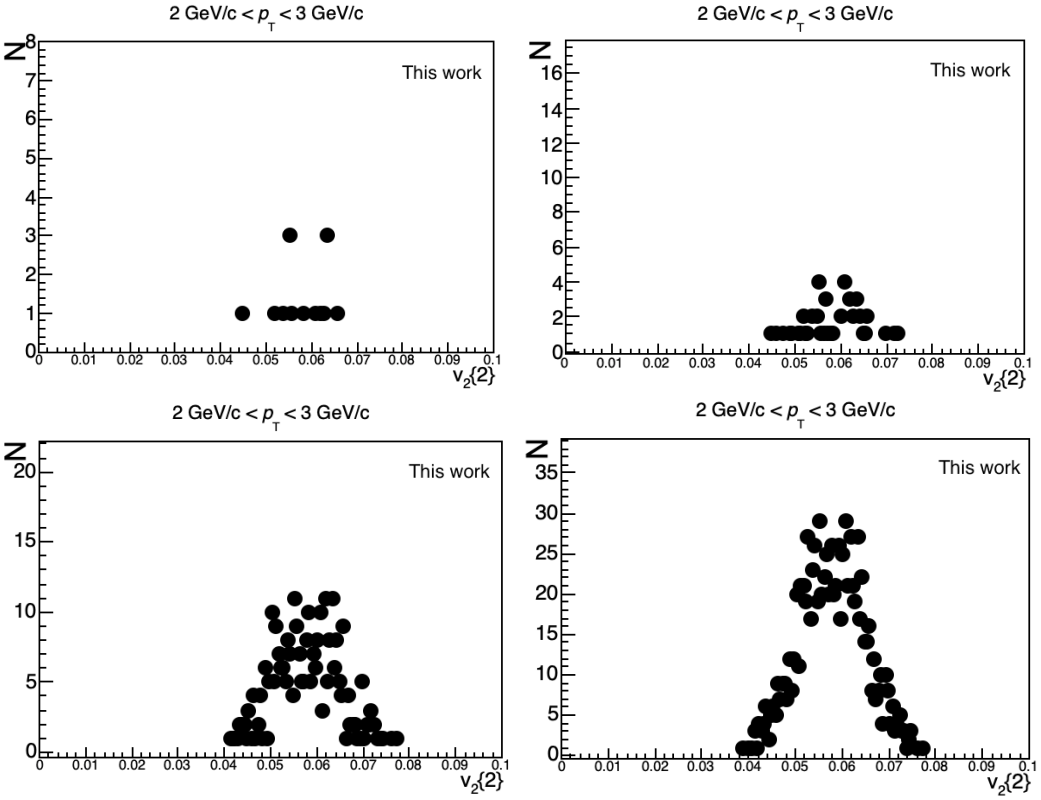

Figure 5.25: The v_2 distribution in $2 < p_{\mathrm{T}} < 3$ GeV/c interval with 15 trials (upper left), 50 trials (upper right), 300 trials (lower left) and 900 trials (lower right).

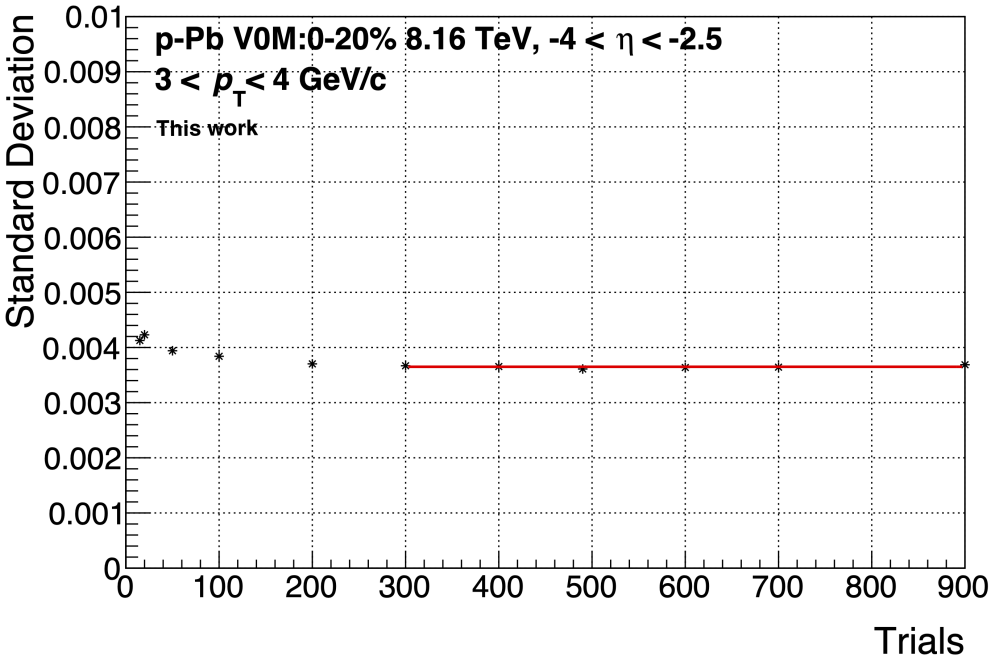

Figure 5.26: The RMS of the muon v_2 distribution as a function of the number of trails for $3 < p_{\mathrm{T}} < 4$ GeV/c intervals.

- **Remaining nonflow** Replace the numerator of Eq. 5.15 with $k'' \cdot [d_2^{\mathrm{high}} - k' \cdot d_2^{\mathrm{low}}]$, where the k'' is the ratio between the $V_{2\Delta}^{\mu-\mathrm{tracklet}}$ with and without remaining nonflow subtraction. It is estimated from two-particle correlation with the fit subtraction method.

The relative uncertainty sources with different multiplicity estimators in p–Pb and Pb–p collisions are shown in Fig. 5.27, where some p_{T} intervals are combined to smooth the trend of the uncertainties. These absolute values of uncertainties are also shown in Tab. 5.3. Similar trends are obtained with other multiplicity estimators.

Comparison with the Systematic Uncertainty in Two-particle Correlation Method

One can see that the systematic uncertainties obtained in two-particle cumulants are different from those obtained in the two-particle correlation as shown in Sec. 5.2.3. In general, the uncertainties related to the nonflow subtraction are smaller in two-particle correlations, while the uncertainties related to the v_2 calculation are smaller in two-particle cumulants. Such behaviour reflects the advantages and disadvantages of these two methods. The two-particle correlation method has a larger power to suppress the contribution from nonflow effect since the recoil jets can be characterized in correlation function straightforwardly, but it is difficult to be quantified in the cumulant method. On the other hand, without considering the nonflow contributions, the two-particle cumulant method can provide more precise results

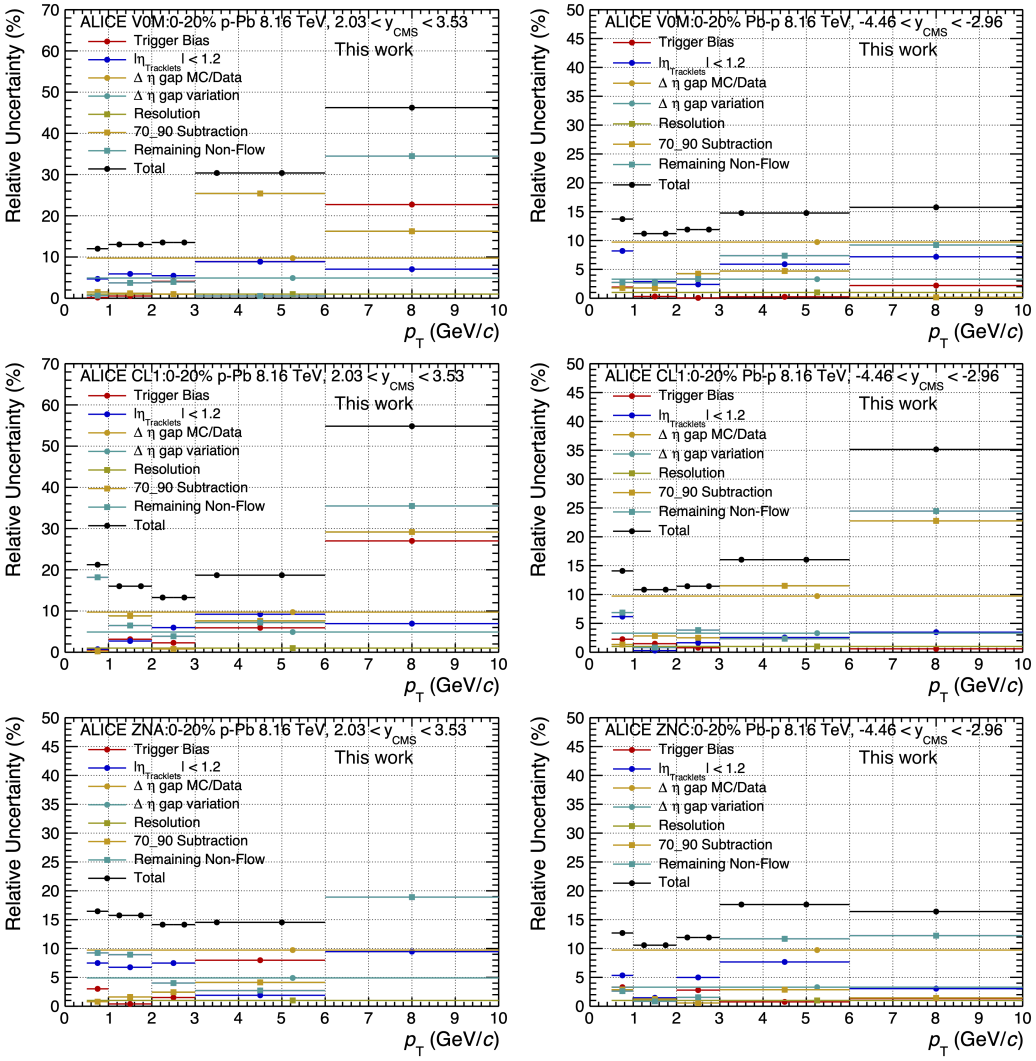

Figure 5.27: The relative systematic uncertainty in p–Pb (left) and Pb–p (right) collisions with V0M (top), CL1 (middle) and ZN (bottom) multiplicity estimators.

Table 5.3: Summary of absolute systematic uncertainties affecting the $v_2^{\mu}\{2\}$ coefficients measured in high-multiplicity (0–20%) p–Pb collisions at 8.16 TeV at forward and backward rapidities. The values are reported for the event class selected with V0M. The intervals of the uncertainties correspond to the measured inclusive muon p_{T} range.

Source	V0M	
	p–Pb ($\times 10^3$)	Pb–p ($\times 10^3$)
Trigger bias	$0.06 - 4.3$	$0.04 - 1.2$
SPD acceptance	$1.3 - 4.3$	$1.6 - 4.4$
Short-range jet correlations: $\lvert\Delta\eta\rvert$ gap	$0.9 - 3.6$	$1.3 - 2.5$
Short-range jet correlations: $\lvert\Delta\eta\rvert$ data vs. AMPT	$1.8 - 7.1$	$3.8 - 7.4$
Remaining ridge in $60 - 90\%$	$0.4 - 9.5$	$0.1 - 3.1$
Residual jet	$0.2 - 6.6$	$1.5 - 5.1$
Resolution effects	$0.2 - 0.7$	$0.4 - 0.8$
Total	$4.5 - 11.3$	$5.8 - 8.7$

since the flow coefficients can be calculated analytically order by order, while the two-particle correlation method is always affected by the break of factorization, as discussed in Sec. 5.2.

5.4 Results and Discussion

In this analysis, the inclusive muon v_2 is measured for the first time with different multiplicity estimators in p–Pb and Pb–p at $\sqrt{s_{\mathrm{NN}}} = 8.16$ TeV collisions with the ALICE detector. Figure 5.28 (left) shows the comparison of the inclusive muon v_2 obtained with the two-particle correlation method in p–Pb and Pb–p collisions. Figure 5.28 (right) shows the significance of a positive muon v_2 as a function of p_{T}[9]. The results show that a positive inclusive muon v_2 is observed in high-multiplicity p–Pb and Pb–p collisions, especially in the region $p_{\mathrm{T}} > 2$ GeV/c where heavy-flavour hadron decay muons dominate. The measured muon v_2 is positive with a significance which reaches values between 4.7σ–12σ (7.6σ–11.9σ) at intermediate p_{T} ($2 < p_{\mathrm{T}} < 6$ GeV/c) for Pb–p (p–Pb) collisions. Besides, the p_{T} dependence of v_2 is similar in p–Pb and Pb–p collisions. We also calculate the p_{T}-differential ratio of the measured muon v_2 with two-particle correlations in p–Pb collisions to that in Pb–p collisions, and this ratio indicates a uniform behaviour within uncertainties which can be adjusted with a zero-order polynomial function. It amounts to 1.28 ± 0.07, where the uncertainty is obtained from the fit. The 4σ of the ratio away from unity shows a evidence for a higher elliptic flow signal at backward rapidity than at forward rapidity as observed in a previous analysis [190]. This asymmetry may result from decorrelations of event planes at different rapidities [115].

[9]For a given observable P, the significance of positive P is $\sigma = \frac{\mathrm{P}-0}{\sqrt{\sigma^2_{\mathrm{syst.}}+\sigma^2_{\mathrm{stat.}}}}$, $\sigma > 3$ allows us to conclude that the observable is positive.

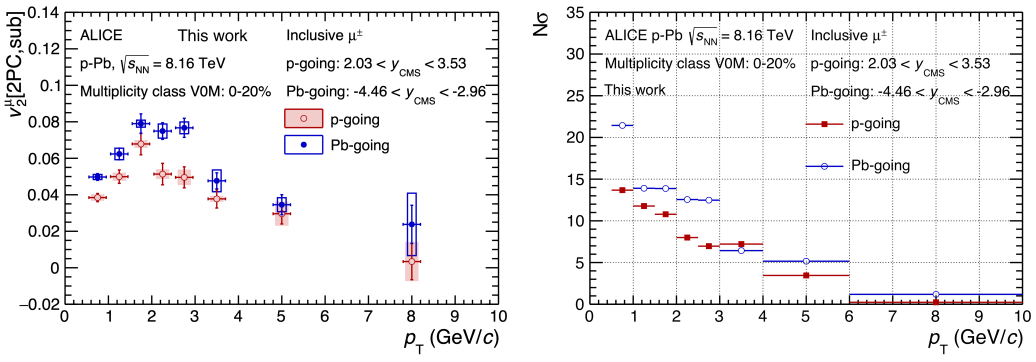

Figure 5.28: Left: comparison between the inclusive muon v_2 with the two-particle correlation method in high-multiplicity p–Pb and Pb–p collisions at $\sqrt{s_{\rm NN}}$ = 8.16 TeV. Right: the significance of a positive muon v_2 as a function of $p_{\rm T}$ in high-multiplicity p–Pb and Pb–p collisions at $\sqrt{s_{\rm NN}}$ = 8.16 TeV.

Figure 5.29 shows the comparison of the two methods used for p–Pb (left) and Pb–p (right) collisions. The results obtained with the two methods after their respective nonflow subtraction give consistent results within the uncertainties.

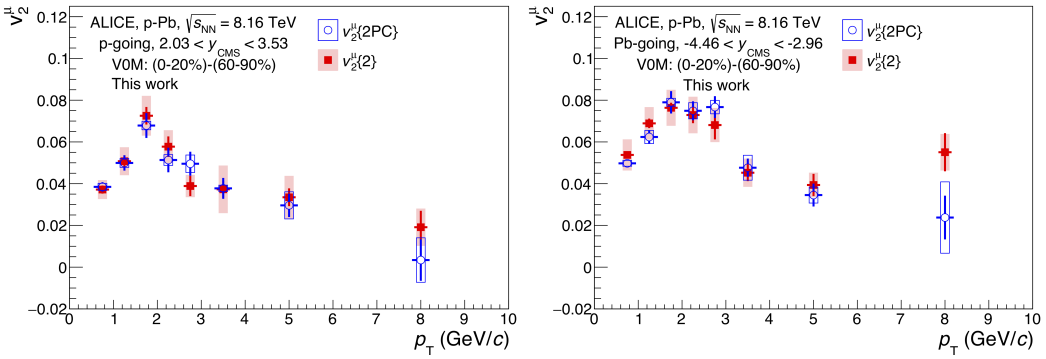

Figure 5.29: Inclusive muon v_2 coefficient as a function of $p_{\rm T}$ at forward (left) and backward (right) rapidity in high-multiplicity p–Pb collisions at $\sqrt{s_{\rm NN}}$ = 8.16 TeV. The event activity is estimated with V0M. Open and full symbols refer to the measurements with two-particle correlations and two-particle cumulants, respectively.

Different multiplicity estimators (V0M, CL1, ZN) are also tested in this analysis, as shown in Fig. 5.30. It has been demonstrated that these multiplicity estimators select events with different mean charged-particle multiplicity [150], so it is expected to observe differences between the results obtained from these estimators. On the other hand, the ZN estimator selects events with smaller charged-particle multiplicity density in the high-multiplicity class than V0M and CL1 estimators, while the opposite trend is observed for the low-multiplicity class [200]. Consequently, a smaller muon v_2 is expected after the nonflow subtraction from low-multiplicity events with ZN estimator, which is consistent with the behaviour shown in Fig. 5.30.

Figure 5.31 (left) shows the comparison between the inclusive muon v_2 in p–Pb

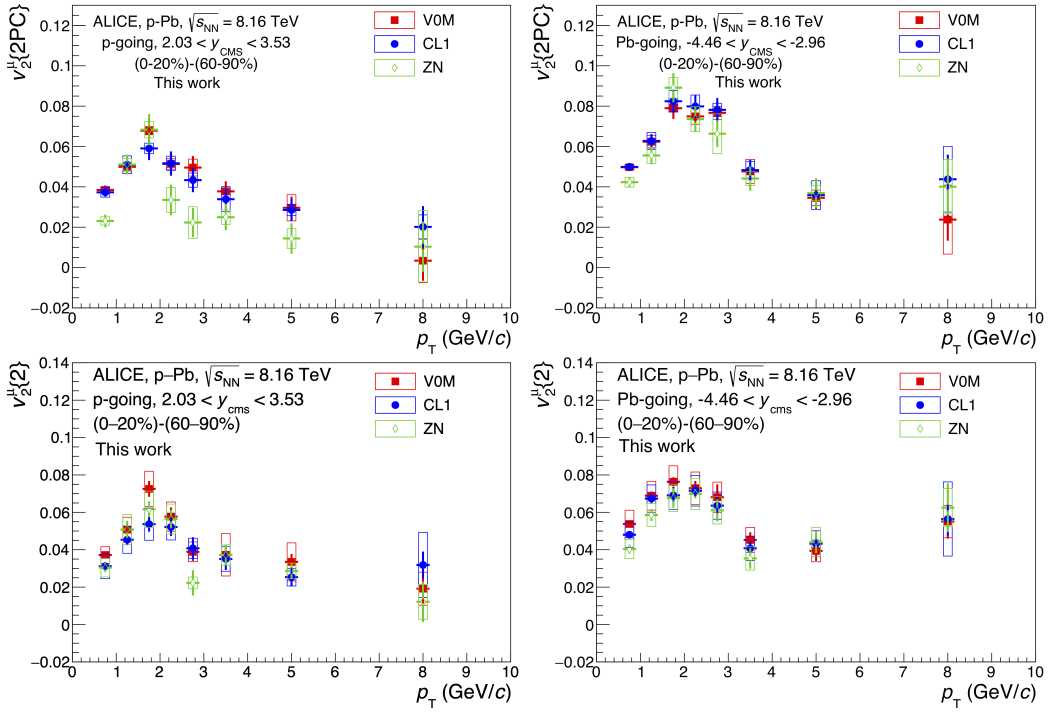

Figure 5.30: Inclusive muon v_2 as a function of p_{T} at forward (left) and backward (right) rapidity in high-multiplicity p–Pb collisions at $\sqrt{s_{\mathrm{NN}}} = 8.16$ TeV, extracted with two-particle cumulants (top) and two-particle correlations (bottom). The results are obtained with different estimators of the event activity: V0M, CL1, and ZN.

8.16 TeV and published results about the measurements of inclusive muon v_2 and heavy-flavour decay electron v_2 [190, 201] in p–Pb collisions at $\sqrt{s_{\rm NN}} = 5.02$ TeV. The muon v_2 measured in this analysis is consistent with the published results within the uncertainty, but has much smaller uncertainties. This comparison indicates that there is no significant dependence on the collision energy in the muon v_2 measured at $\sqrt{s_{\rm NN}} = 5.02$ TeV and 8.16 TeV. In order to explain the origin of such collective behaviour of heavy flavour decay muons, we compare the results with the color glass condensate (CGC) model calculations. The CGC framework uses the dilute-dense formalism [202, 203], where interactions between partons from the proton projectile and dense gluons inside the target Pb nucleus at the early stage of the collision generate azimuthal anisotropies. The elliptic flow has been calculated for $\rm D^0$ and B mesons, separately with the CGC framework, then according to a fast simulation of the decay kinematics which uses the $p_{\rm T}$ and v_2 distribution of $\rm D^0$ mesons and B-mesons as inputs, the v_2 of $\rm D^0$ and B meson decay muons is obtained separately. Then, assuming that the all D-meson species have the same elliptic flow as $\rm D^0$ mesons[10], the v_2 of muons from heavy-flavour hadron decays is further computed by means of the fraction of muons from charm (beauty) decays with respect to the total yield of muons from heavy-flavour hadron decays obtained from the fixed-order plus next-to-leading logarithms (FONLL) approach [37, 38]. As shown in Fig. 5.31 (right), the CGC-based calculations for muons from both charm- and beauty-hadron decays provide a fair description with the measured inclusive muon v_2 for $p_{\rm T} > 2$ GeV/c, where the fraction of muons originating from charm and beauty decays represents about 60% in p–Pb collisions. At low $p_{\rm T}$ region ($p_{\rm T} < 2$ GeV/c), the main contribution of muons is from pion and kaon decays [190], which indicates the CGC-based calculations overestimate the data. Such an overestimation is already observed before in the studies of charm and beauty hadron long-range correlations in small collision systems by the CMS collaboration [113].

Furthermore, this measurement of muon v_2 is compared with the AMPT model calculations, based on the v2-26t7b string-melting version [205]. The v_2 of heavy-flavour hadrons ($\rm D_0$ and B mesons) and primary charged pions and kaons are calculated with the two-particle correlation method, and the event selection is performed by counting the charged particles in the acceptance of the V0 detector. After that, a fast simulation based on the PYTHIA 6.4 [173] is performed to obtain the muons from charm-hadron, beauty-hadron, charged-pion and charged-kaon decays, separately. The inclusive muon v_2 can be calculated as a weighted sum of the v_2 coefficient of muons from heavy-flavour hadron decays, $v_2^{\mu\leftarrow\rm b,c}$, and the v_2 of muons from charged pion and kaon decays, $v_2^{\pi,\rm K}$, i.e. $v_2^{\mu} = (1-f)\cdot v_2^{\mu\leftarrow\rm b,c} + f\cdot v_2^{\mu\leftarrow\pi,\rm K}$, where the f is the relative production of muons from decay of charged pions and kaons estimated from Monte Carlo simulations with DPMJET event generator [195]. Similarly, the $v_2^{\mu\leftarrow\rm b,c}$ is computed as a weighted sum of the v_2 of muons from charm-hadron and beauty-hadron decays, $v_2^{\mu\leftarrow\rm b}$ and $v_2^{\mu\leftarrow\rm c}$, i.e. $f^c \cdot v_2^{\mu\leftarrow\rm c} + f^b \cdot v_2^{\mu\leftarrow\rm b}$, where f^c and f^b are obtained from the fixed-order plus next-to-leading logarithms (FONLL) cal-

[10] The elliptic flow of prompt $\rm D^0$, $\rm D^+$, $\rm D^{*+}$ and $\rm D_s^+$ measured by ALICE in Pb–Pb collisions at $\sqrt{s_{\rm NN}} = 5.02$ TeV is found compatible within uncertainties [204].

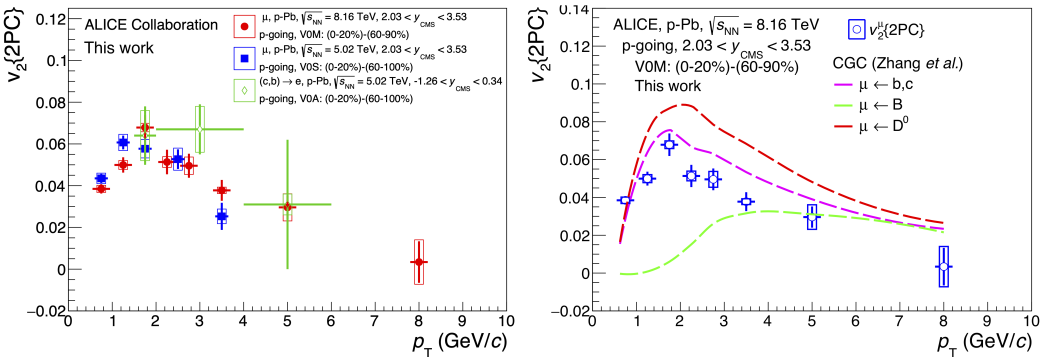

Figure 5.31: Left: comparison of the p_T-differential inclusive muon v_2 at forward rapidity in high-multiplicity p–Pb collisions at $\sqrt{s_{NN}} = 8.16$ TeV extracted with two-particle correlations with previous measurements performed in p–Pb collisions at $\sqrt{s_{NN}} = 5.02$ TeV for inclusive muons [190] and electrons from heavy-flavour hadron decays [201]. Right: comparison of the p_T-differential inclusive muon elliptic flow coefficient at forward rapidity in high-multiplicity p–Pb collisions at $\sqrt{s_{NN}} = 8.16$ TeV with CGC-based calculations [202, 203]. The predictions are shown for muons from D^0-hadron decays and B-hadron decays, separately, and from the combination of the two.

culations [37]. Figure 5.32 shows the comparison of inclusive muon $v_2^\mu\{2PC\}$ and the v_2 of muons from charm- and beauty-hadron, and charged light-flavour hadron decays separately in p–Pb (left) and Pb–p (right) collisions. The inclusive muon v_2 calculated in AMPT is also presented. A positive v_2 for all particle species is reproduced by AMPT, and its magnitude increases significantly up to about 2–3.5 GeV/c, then saturates or decreases smoothly with increasing p_T. As observed with the data, a larger v_2^μ is obtained in the backward rapidity region compared to the forward rapidity region, which may be a consequence of rapidity-dependent flow-vector fluctuations [115]. In general, a fair agreement with the measured inclusive muon v_2 is proved by the AMPT model calculations, although the model tends to slightly overestimate the data in the backward rapidity region. These comparisons suggest that the azimuthal anisotropies are driven by the hydrodynamic evolution of the medium and the anisotropic parton escape mechanism where partons have a higher probability to escape along the shorter axis of the interaction zone [206].

5.5 Summary and Outlook

In this chapter, we discussed the measurement of the inclusive muon v_2 in high-multiplicity p–Pb 8.16 TeV collisions with the ALICE detector. The cumulants method with generic framework is implemented in the heavy-flavour sector for the first time and the nonflow subtraction strategy is improved in both correlation and cumulant methods. On the other hand, the comparison between the observed positive v_2 of muons from heavy-flavour hadron decays and theoretical models provide us new insights on the interpretation of the origin of the "collective" behaviour in

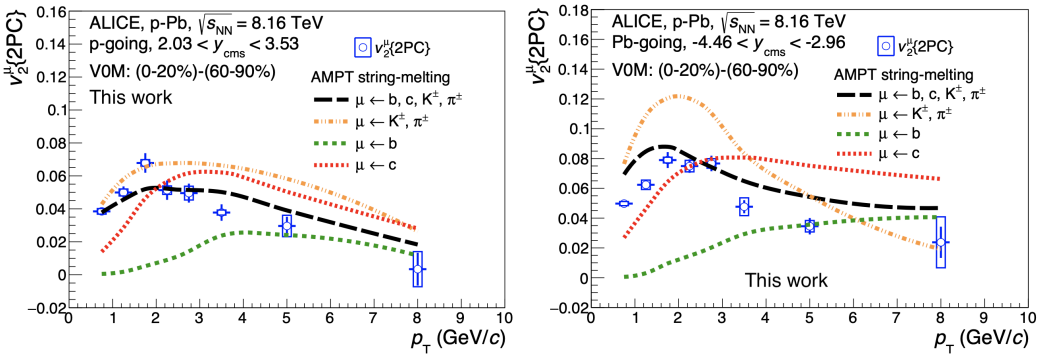

Figure 5.32: Comparison of the p_{T}-differential $v_2^{\mu}\{2\mathrm{PC}\}$ of inclusive muons at forward (left) and backward (right) rapidities in high-multiplicity p–Pb collisions at $\sqrt{s_{NN}}$ = 8.16 TeV with AMPT calculations.

small collision systems.

However, the discussions in small systems are far from over. Even many theoretical predictions are proposed, none of them can describe the full picture perfectly. On the other hand, if we extend our horizon from heavy flavours to other hard probes, e.g. high-p_{T} particles or jets, which kind of collective behaviour can be expected? Will be they consistent with the current heavy-ion physics results? Thanks to our improved flow analysis method, this will be investigated in next chapter!

CHAPTER 6

Measurements of the Azimuthal Anisotropy of Particles Associated with Jets in p–Pb and Pb–Pb Collisions at $\sqrt{s_{\mathrm{NN}}} = 5.02$ TeV

As mentioned in Sec. 1.3, hard probes play an important role in investigating the properties of the quark-gluon plasma (QGP) formed in ultra-relativistic heavy-ion collisions. In the previous two chapters we discussed one hard probe, the muons from open heavy-flavour hadron decays. In this chapter we would like to extend the study to the high-p_{T} charged particles and charged particles associated with jets. The measured R_{AA} and v_2 of high-p_{T} particles and jets in heavy-ion collisions are both well interpreted by the path-length dependent energy loss mechanism, which is named jet quenching. However, a non-zero v_2 for both minimum-bias triggered events and jet events[1] in p–Pb collisions at high-p_{T} (up to 20∼50 GeV/c) is observed by ATLAS [98], as shown in Fig. 1.29 (left), while no jet quenching effect is observed from the nuclear modification factor R_{pPb} [31] and hadron-jet correlations [207]. Furthermore, after a proper scaling, the v_2 measured in p–Pb collisions is found comparable to the v_2 measured in Pb–Pb collisions at high p_{T}, as shown in Fig. 1.29 (right), but the Pb–Pb results indicate a slow decrease of v_2 values with increasing p_{T} and the p–Pb results tend to exhibit a plateau. These experimental results trigger a puzzle. How to explain the origin of the non-zero high-p_{T} particle v_2 in p–Pb collisions? These results also suggest that there might be additional contribution to v_2 at high p_{T} in Pb–Pb collisions.

In order to further understand such "collective" behaviour (QGP-like effect) of high-p_{T} particles in small collision systems, we present the measurement of the v_2 of particles associated with jets (the so-called jet particles) in both p–Pb and Pb–Pb collisions at $\sqrt{s_{\mathrm{NN}}} = 5.02$ TeV, with a novel three-particle correlation method. Compared to the measurement in ATLAS described in [98], the particles that originate from the soft processes are fully separated in this analysis, which provides straightforward insights on the study of hard partons. The Sec. 6.1 and Sec. 6.2 focus on the analysis strategy in Pb–Pb and p–Pb collisions, respectively. The Sec. 6.3 shows the analysis results and related discussions, and a final summary is given in Sec. 6.4.

[1] The events which require a jet with a p_{T} larger than a specific value.

6.1 Measurement of the Jet-particle v_2 in Pb–Pb Collisions

6.1.1 Data Sample and Selection

The data used in this analysis was collected in 2015 during the LHC Run 2 data taking. The runs which passed the quality assurance checks are listed below:

- LHC15o pass1, AOD 194, 77 runs
  246994, 246991, 246989, 246984, 246982, 246948, 246945, 246928, 246851, 246847, 246846, 246845, 246844, 246810, 246809, 246808, 246807, 246805, 246804, 246766, 246765, 246763, 246760, 246759, 246758, 246757, 246751, 246750, 246495, 246493, 246488, 246487, 246434, 246431, 246424, 246276, 246275, 246272, 246271, 246225, 246222, 246217, 246185, 246182, 246181, 246180, 246178, 246153, 246152, 246151, 246148, 246115, 246113, 246089, 246087, 246053, 246052, 246049, 246048, 246042, 246037, 246036, 246012, 246003, 246001, 245963, 245954, 245952, 245949, 245923, 245833, 245831, 245829, 245705, 245702, 245692, 245683.

The AliPhysics version used in this analysis is vAN-20200525-1.

Event Selection

The events used in this analysis all pass the trigger selection and related physics selections. The data samples collected with the MB trigger (`AliEvent::kINT7`) are analysed, and the physics selection is processed via the `AliPhysicsSelection` task while the parameter `applyPileupCuts` is set to `kFALSE`. This is because the default pileup cuts in the physics selection task are too tight for the analysis in Pb–Pb collisions, hence a small fraction of good events is removed, resulting in a biased centrality distribution. In this case, the pileup cuts are applied manually to:

- the correlation between the sum of the signal amplitude collected in the V0 within the trigger bunch crossing (i.e. V0M online) and the total charge deposited in the V0 counters (i.e. V0M offline);
- the correlation between the number of SPD clusters and the number of tracklets;
- the correlation between the centrality determined using the V0 multiplicity and the hits in the first SPD layer (labeled as CL0)

Besides, we require a reconstructed primary vertex in the SPD with a longitudinal coordinate Z_{vertex} within $\pm$ 10 cm and the resolution along the z axis is required to be smaller than 0.25 cm if the vertex is reconstructed with VertexerSPDz algorithm. The collision centrality is characterized by the centrality estimator V0M. In order to obtain a significant elliptic flow v_2 signal [208] and collect more statistics, this analysis is performed in 20–60% semi-central Pb–Pb collisions. Finally, about 69.3M events are obtained after all event selections.

Track Selection

Only the tracks passing the specific selection criteria can be used for an analysis. Thanks to the filter-bit scheme of the ALICE reconstruction framework [147], every AOD track has a filter-bit mask, which corresponds to a set of cuts and stores the information about whether the track satisfies such set of cuts or not. The track criteria related to a given filter-bit can be changed from a production to an other production. In this analysis, we select the reconstructed tracks which satisfied the cuts corresponding to the filter-bit 32, which are the standard TPC+ITS cuts with a tight DCA cut. These selected tracks are reconstructed utilizing the response from both ITS and TPC detectors. It requires a given number of SPD hits and rows crossed by the TPC track, and the high-quality Kalman filter fit in terms of χ^2, during the track reconstruction, as described in Sec. 3.3.2.2. Moreover, the successful re-fitting of available ITS and TPC hits is required. Besides, in order to remove the tracks produced in weak decays of long-lived hadrons and interactions in the detector material (i.e. secondary particles), we should also applied cuts on the distance of closest approach (DCA) to the primary vertex. It includes the cuts on the DCA along the beam direction ($\mathrm{DCA_z}$) and in the transverse plane ($\mathrm{DCA_{xy}}$), the latter being p_T dependent. In addition, the kinematic cuts $|\eta| < 0.8$ and $p_\mathrm{T} > 0.2$ GeV/c are applied. The pseudorapidity cut avoids the significant drop of efficiency at the edges of acceptance and the transverse momentum cut removes the low p_T particles with low tracking performance. The full list of all applied track selections discussed above is summarized as follows:

- At least 70 rows TPC track crossed and the number of crossed rows divided by the number of findable clusters is larger than 0.8;
- Kalman filter fit quality per TPC cluster of $\chi^2/N_\mathrm{TPC} < 4$;
- Successful re-fit using TPC space-points and ITS hits;
- Kalman filter fit quality per ITS cluster of $\chi^2/N_\mathrm{ITS} < 36$;
- Kink daughters are not accepted;
- Maximal DCA in the beam direction $|\mathrm{DCA}_z| < 2$ cm;
- Maximal DCA in the transverse plane $|\mathrm{DCA}_{xy}| < 0.0105 + 0.0350 \cdot (p_\mathrm{T})^{-1.1}$;
- At least 70 TPC clusters are included[2];
- Pseudorapidity and transverse momentum selection: $|\eta| < 0.8$, $p_\mathrm{T} > 0.2$ GeV/c.

[2]This cut is a added to the set of cuts stored in filter-bit 32 due to the limited efficiency during the track reconstruction.

6.1.2 Inclusive Charged-particle v_2 in Pb–Pb Collisions

Before starting the analysis of the jet-particle v_2, the measurement of the inclusive charged-particle v_2 should be performed to provide the baseline. The p_{T}-differential v_2 of charged particles was already measured precisely in Pb–Pb collisions at $\sqrt{s_{\mathrm{NN}}} = 5.02$ and 2.76 TeV [208], as shown in Fig. 6.1. Following the same strategy, i.e. using the scalar product method, we would like to measure the inclusive charged-particle v_2 in a wider centrality range 20–60%.

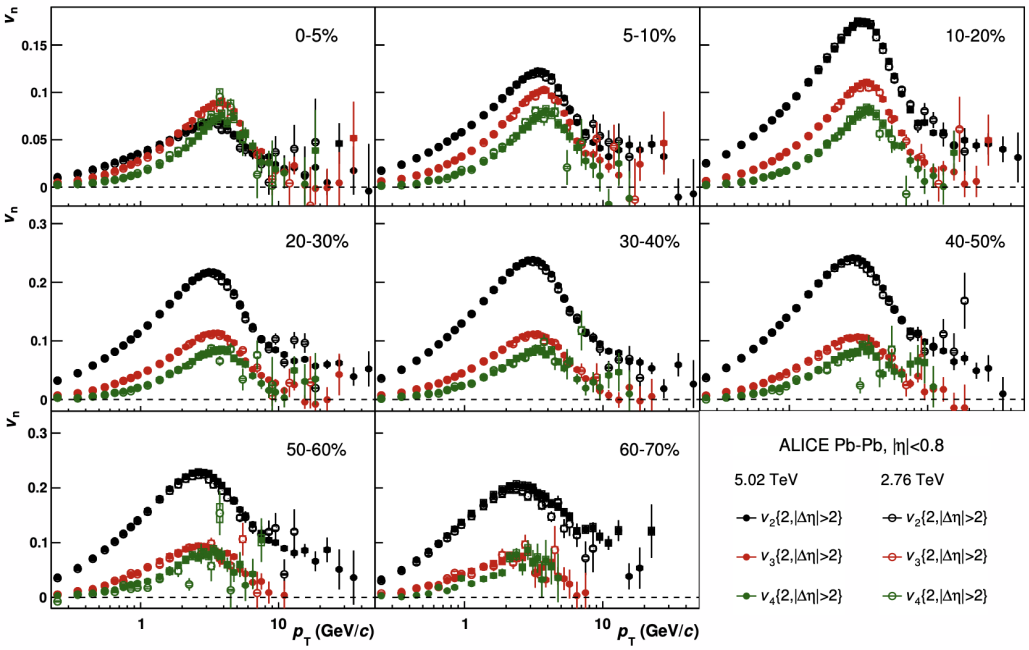

Figure 6.1: Anisotropic flow coefficients $v_{\mathrm{n}}(p_{\mathrm{T}})$ of inclusive charged particles in different centrality classes. The measurements in Pb–Pb collisions at 5.02 (2.76) TeV are shown by solid (open) markers [208].

As introduced in Sec. 2.2, the scalar product method is based on the calculation of the flow vector in sub-events. To suppress the non-flow contribution, the long-range correlation ($\Delta\eta > 2$) is constructed using the TPC tracks (at mid-rapidity with $|\eta| < 0.8$) and the particles measured in the V0A detector (at forward rapidity with $2.8 < \eta < 5.1$) are used to calculate the flow vectors $\vec{u}_{\mathrm{n}}$ and $\vec{Q}_{\mathrm{n}}^{\mathrm{V0A}}$. The anisotropic flow coefficient obtained with the scalar product of the flow vectors, is obtained according to:

$$v_n(\Delta\eta > 2) = \frac{\langle \vec{u}_n \cdot \vec{Q}_n^{\mathrm{V0A}*} \rangle}{\sqrt{\frac{\langle \vec{Q}_n^{\mathrm{V0A}*} \cdot \vec{Q}_n^{\mathrm{V0C}} \rangle \langle \vec{Q}_n^{\mathrm{V0A}} \cdot \vec{Q}_n^{\mathrm{SPD}*} \rangle}{\langle \vec{Q}_n^{\mathrm{V0C}} \cdot \vec{Q}_n^{\mathrm{SPD}*} \rangle}}}, \tag{6.1}$$

where the $\vec{u}_n$ is the unit flow vector obtained from TPC tracks, $\vec{Q}_n^{\mathrm{SPD}}$, $\vec{Q}_n^{\mathrm{V0C}}$ and $\vec{Q}_n^{\mathrm{V0A}}$ are calculated from the particles measured in SPD, V0C and V0A. The symbol * represents the complex conjugate. A recentering procedure is applied to correct

the event flow vectors for the non-uniform azimuthal acceptance [110]. The pseudo-rapidity gaps between the TPC and V0A (two units) and between the V0A, V0C, and SPD suppress nonflow effects and eliminate autocorrelations. Figure 6.2 shows the v_2 of inclusive charged particles as a function of p_{T} in the 20–60% centrality class, compared to the published results measured in 20–30%, 30–40% and 50–60% centrality classes. The consistency between them indicates the usage of the scalar product method in this analysis is validated.

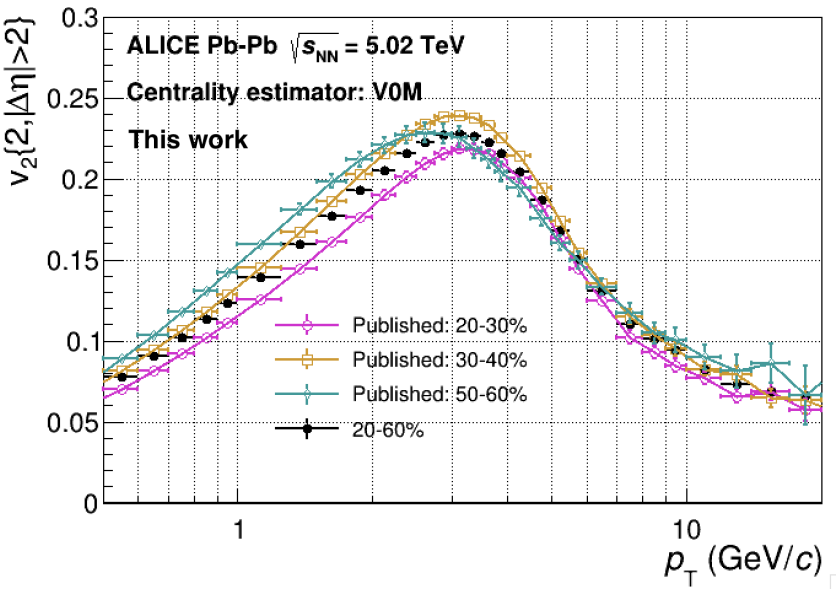

Figure 6.2: The comparison of the $v_2(p_{\mathrm{T}})$ of inclusive charged particles in 20–30%, 30–40%, 50–60% and 20–60% centrality classes. The results measured in 20–30%, 30–40%, 50–60% are from [208].

6.1.3 Jet-particle v_2 in Pb–Pb collisions

Extraction of the Jet Yield

The first step of the measurement of the jet-particle v_2 is to isolate the charged particles from jets. Instead of reconstructing the jet with the jet finder [209], the two-particle correlation method is employed here. The TPC tracks located at mid-rapidity are chosen as the trigger and associated particles, and only the same-sign charged particles are selected to remove the contribution from resonances. The associated yield per trigger particle as a function of the pseudorapidity difference $\Delta\eta$ and azimuthal angle difference $\Delta\varphi$ between the trigger and associated particles is defined, as in the single muon v_2 analysis (see Sec. 5.2.1) as:

$$Y(\Delta\eta,\Delta\varphi)=\frac{1}{N_{\mathrm{trig}}}\frac{\mathrm{d}^2N_{\mathrm{assoc}}}{\mathrm{d}\Delta\eta\mathrm{d}\Delta\varphi}=\frac{S(\Delta\eta,\Delta\varphi)}{B(\Delta\eta,\Delta\varphi)}, \tag{6.2}$$

where $N_{\rm trig}$ is the number of the trigger particles, $S(\Delta\eta,\Delta\varphi) = \frac{1}{N_{\rm trig}}\frac{{\rm d}^2N_{\rm same}}{{\rm d}\Delta\eta{\rm d}\Delta\varphi}$ is the associated yield per trigger in the same event and $B(\Delta\eta,\Delta\varphi) = \alpha\frac{{\rm d}^2N_{\rm mixed}}{{\rm d}\Delta\eta{\rm d}\Delta\varphi}$ is the pair yield in different events obtained with the event-mixing technique and normalized to unity in the region of maximum pair acceptance with the parameter α. Figure 6.3 (upper left) shows the associated yield per trigger particle as a function of $\Delta\varphi$ and $\Delta\eta$, where we clearly observe the jet peak in the near-side region (i.e. $\Delta\varphi < \frac{1}{2}\pi$) and the ridge structure under the jet peak. To extract the jet yield from the associated yield per trigger particle, we fit the TPC-TPC correlation distribution with the following function:

$$\begin{aligned} C(x,y) = {} & \frac{1}{2}a_2(e^{-(\frac{x^2}{2a_3^2}+\frac{y^2}{2a_4^2})} + e^{-(\frac{(2\pi-x)^2}{2a_3^2}+\frac{y^2}{2a_4^2})}) + \frac{1}{2}a_5(e^{-(\frac{x^2}{2a_6^2}+\frac{y^2}{2a_7^2})} + e^{-(\frac{(2\pi-x)^2}{2a_6^2}+\frac{y^2}{2a_7^2})}) \\ & + a_0 + 2a_0a_1{\rm cos}x(2x) + a_0a_8(1-{\rm cos}x) + 2a_0a_9{\rm cos}x(3x) + 2a_0a_{10}{\rm cos}x(4x) \\ & + 2a_0a_{11}{\rm cos}x(5x), \end{aligned} \tag{6.3}$$

where $x = \Delta\varphi$ and $y = \Delta\eta$. The fit function includes two parts. The term $\frac{1}{2}a_2(e^{-(\frac{x^2}{2a_3^2}+\frac{y^2}{2a_4^2})} + e^{-(\frac{(2\pi-x)^2}{2a_3^2}+\frac{y^2}{2a_4^2})}) + \frac{1}{2}a_5(e^{-(\frac{x^2}{2a_6^2}+\frac{y^2}{2a_7^2})} + e^{-(\frac{(2\pi-x)^2}{2a_6^2}+\frac{y^2}{2a_7^2})})$ is the double Gaussian function to fit the jet peak in the near-side, where the $(2\pi - x)$ term is introduced to describe the periodicity of the azimuthal angle. The term $a_0 + 2a_0a_1{\rm cos}(2x) + a_0a_8(1-{\rm cos}x) + 2a_0a_9{\rm cos}(3x) + 2a_0a_{10}{\rm cos}(4x) + 2a_0a_{11}{\rm cos}(5x)$ is the Fourier-series term, to describe the ridge structure as a function of $\Delta\varphi$ and $\Delta\eta$. Figure 6.3 (upper right) shows the fit of the TPC-TPC correlation distribution and Fig. 6.3 (bottom) shows the deviation between the fit and data. The small deviation between the data and the fit indicates that the fit works well. The yield of the jet peak and background[3] as a function of $\Delta\varphi$ and $\Delta\eta$ are shown in Fig. 6.4. They will be used in the next step to extract the jet-particle v_2.

Extraction of the Jet-particle v_2

As shown in Fig. 6.3 (left), the associated yield per trigger particle as a function of $\Delta\varphi$ and $\Delta\eta$ is calculated. If we divide the $\Delta\varphi$-$\Delta\eta$ plane into many regions, there is a lot of particle pairs in each region, as shown in Fig. 6.5, and the v_2 of the trigger particle in the charged-particle pairs of each ($\Delta\varphi$, $\Delta\eta$) region can be calculated according to the so-called **three-particle correlation** technique. In the three-particle correlations, two of them are chosen from the particle pair obtained in TPC-TPC correlation distributions, as shown in Fig. 6.3 (left), and the third particle is selected in the V0A. Hence, the long-range correlations between the trigger particle of the TPC-TPC particle pairs and the forward particles are constructed, and the v_2 is calculated directly by means of the scalar product method, as done for the calculation of the inclusive charged-particle v_2 (Sec. 6.1.2). The flow vectors of the trigger particles in TPC-TPC particle pairs and V0A (V0C, SPD) are calculated,

[3]The background corresponds to the particles which are not from the near-side jet peak.

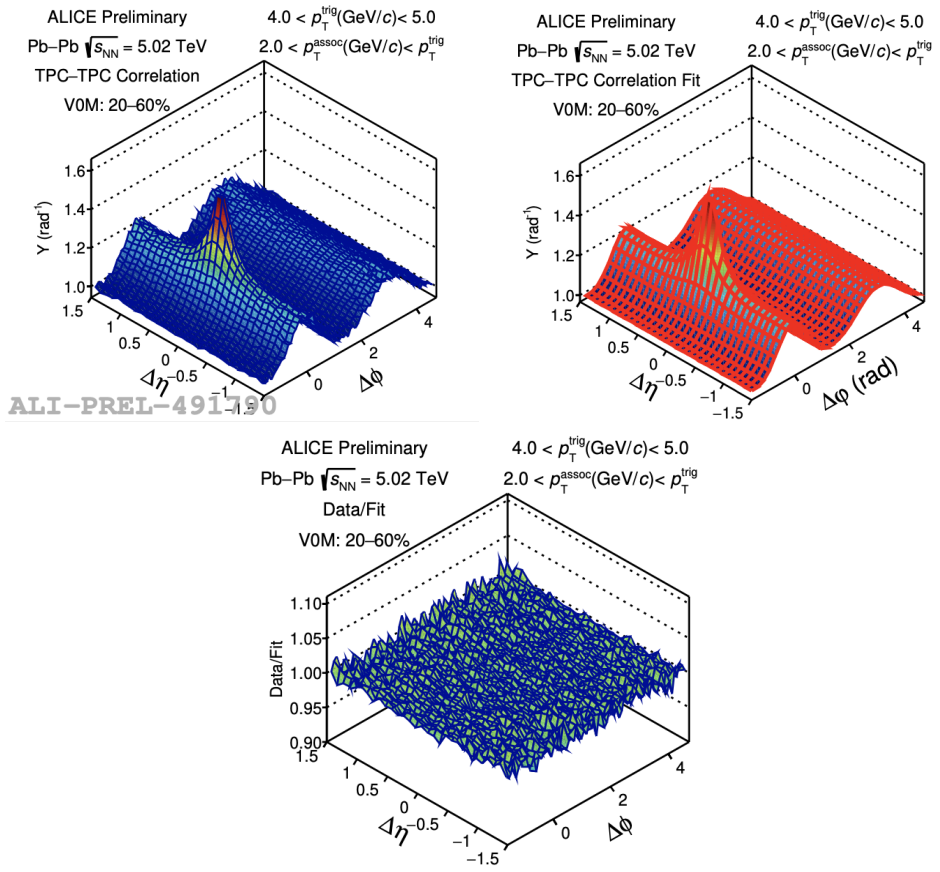

Figure 6.3: Upper left: the associated yield per trigger particle in TPC-TPC correlations for Pb–Pb collisions at $\sqrt{s_{\rm NN}}$ = 5.02 TeV. Upper right: the fit of TPC-TPC correlations. Bottom: the ratio between the data and fit.

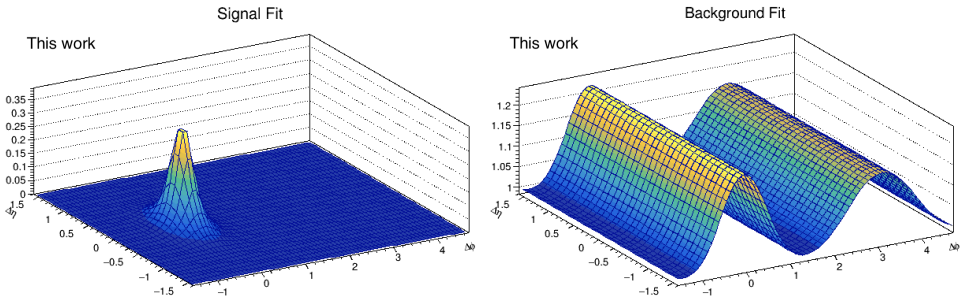

Figure 6.4: The yield of jet peak (left) and background (right) as a function of $\Delta\varphi$ and $\Delta\eta$ from the fit of TPC-TPC correlation distribution in Pb–Pb collisions at $\sqrt{s_{\rm NN}}$ = 5.02 TeV

and the v_n coefficients of the trigger particles in TPC-TPC particle pairs can be obtained via

$$v_{\rm n}(\Delta\varphi,\Delta\eta)=\frac{\langle\vec{u}_{\rm n}(\Delta\varphi,\Delta\eta)\cdot\vec{Q}_{\rm n}^{\rm V0A*}\rangle_{\rm TPC-TPC}}{\sqrt{\frac{\langle\vec{Q}_{\rm n}^{\rm V0A}\cdot\vec{Q}_{\rm n}^{\rm V0C*}\rangle\langle\vec{Q}_{\rm n}^{\rm V0A}\cdot\vec{Q}_{\rm n}^{\rm SPD*}\rangle}{\langle\vec{Q}_{\rm n}^{\rm V0C}\cdot\vec{Q}_{\rm n}^{\rm SPD*}\rangle}}},\tag{6.4}$$

where $\Delta\varphi$, $\Delta\eta$ are the pseudorapidity difference and azimuthal angle difference between the trigger and associated particles in TPC-TPC particle pairs. Compared to Eq. 6.1, the $\vec{u}_n$ and $v_2(\Delta\eta>2)$ are replaced by $\vec{u}_n(\Delta\varphi,\Delta\eta)$ and $v_2(\Delta\varphi,\Delta\eta)$, since the $v_{\rm n}$ is calculated in each $(\Delta\varphi,\Delta\eta)$ region of the TPC-TPC particle pairs. In addition, the bracket $\langle...\rangle_{\rm TPC-TPC}$ denotes the average over pairs of particles in each $(\Delta\varphi,\Delta\eta)$ region of TPC-TPC correlations in a given $p_{\rm T}$ interval for trigger and associated tracks, and centrality interval. The brackets in the denominator indicate the average over all events in a centrality interval containing the particle pair under consideration.

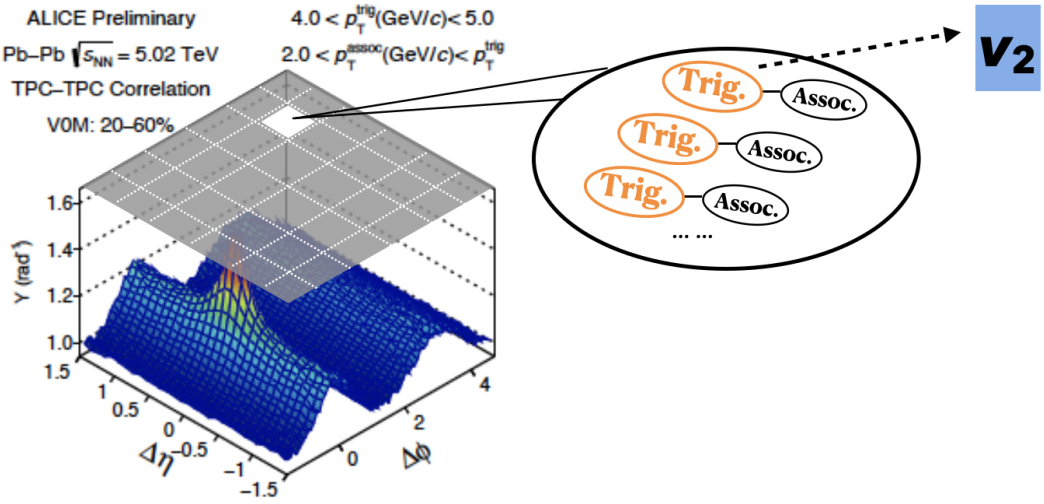

Figure 6.5: The TPC-TPC correlation function is divided into many regions. In each region, particle pairs are found. The v_2 of the trigger particles in TPC-TPC particle pairs is further calculated.

Figure. 6.6 (upper left) shows the v_2 distribution of the trigger particles of TPC-TPC pairs as a function of $\Delta\varphi$ and $\Delta\eta$. Interestingly, the concavity is clearly observed at $(\Delta\varphi\sim0,\Delta\eta\sim0)$ where the jet peak is located. It indicates that the v_2 of particles in jets is different from the v_2 of the background particles. The way to extract the v_2 of jet particles from the v_2 distribution is similar as that employed for the identified-particle v_2 calculation via an invariant mass fit [79, 210]. Considering that $v_2(\Delta\varphi,\Delta\eta)$ is the weighted sum of the v_2 of jet particles ($v_{2,\rm jet}$) and background ($v_{2,\rm bkg}$), where the weight is the ratio of the yield of the jet peak ($Y_{\rm jet}$) to the background ($Y_{\rm bkg}$) obtained when fitting the TPC-TPC correlations[4](see

[4]In the identified particle v_2 extraction, the v_2 as a function of invariant mass is considered as the weighted sum of the v_2 of signal and background, where the weight is the ratio of the invariant

Fig. 6.4), one gets:

$$v_2(\Delta\varphi, \Delta\eta) = \frac{Y_{\rm jet}}{Y_{\rm jet} + Y_{\rm bkg}} \times v_{2,\rm jet} + \frac{Y_{\rm bkg}}{Y_{\rm jet} + Y_{\rm bkg}} \times v_{2,\rm bkg}(\Delta\varphi, \Delta\eta), \tag{6.5}$$

where $v_{2,\rm jet}$ is a constant, and $v_{2,\rm bkg}$, which exhibits a dependence on $\Delta\varphi$ and $\Delta\eta$, is parameterized with a Fourier series up to the fifth order. The fit of the $v_2(\Delta\varphi, \Delta\eta)$ distribution is obtained using Eq. 6.5 in each $p_{\rm T}$ interval of trigger and associated particles, and it is shown in the right panel of Fig. 6.6. The small differences between the fit and the data shown in the bottom panel of Fig. 6.6 demonstrate that the fit strategy is suited to extract $v_{2,\rm jet}$.

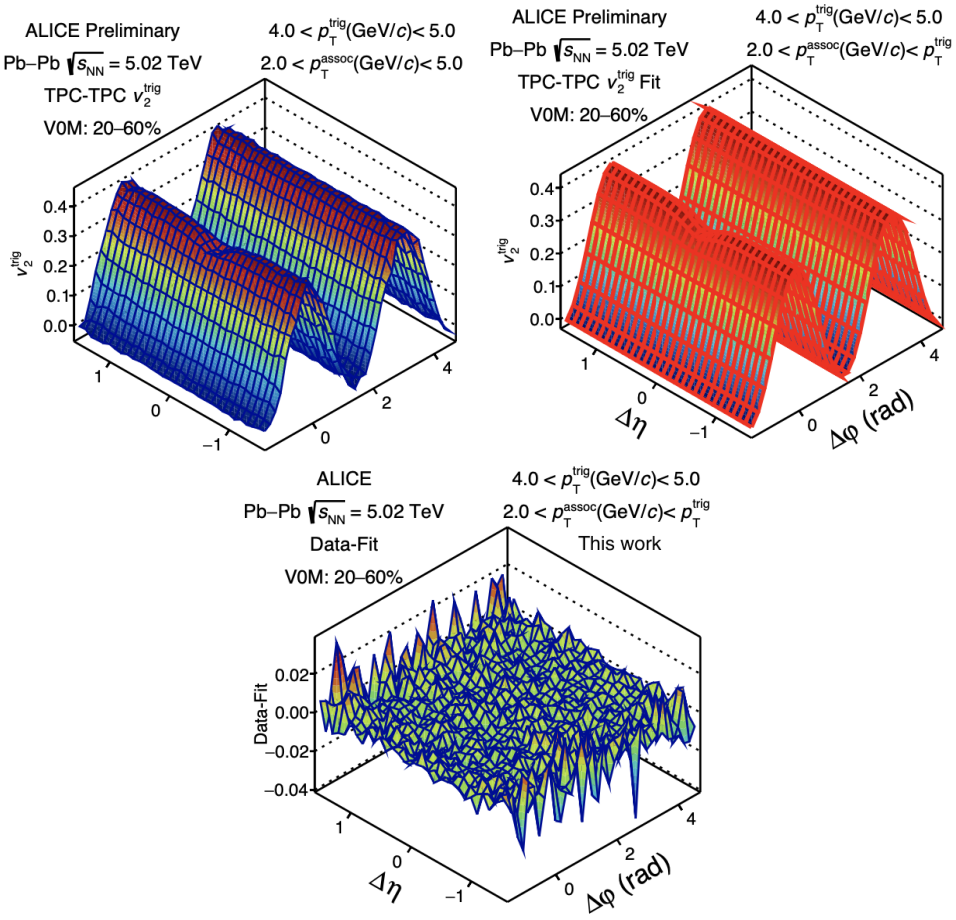

Figure 6.6: Upper left: $v_2(\Delta\varphi, \Delta\eta)$ distribution of trigger particles in TPC-TPC pairs in Pb–Pb collisions at $\sqrt{s_{\rm NN}} = 5.02$ TeV. Upper right: fit of $v_2(\Delta\varphi, \Delta\eta)$ distribution of trigger particles with Eq. 6.5. Bottom: difference between data and fit.

mass distribution of signal and background. As an analogy, the invariant mass distribution is replaced by the TPC-TPC correlation distribution in this analysis.

6.1.4 Systematic Uncertainty on the Inclusive Charged-particle and Jet-particle v_2

The deviation between the default v_2 value and the results obtained with the systematic variation is considered as the systematic uncertainty, if it can pass the barlow test [197]. Same sources of systematic uncertainties in the measurement of the inclusive charged-particle v_2 and jet-particle v_2 in Pb–Pb collisions are considered. They include:

- Variation of the track selection, filter-bit 32 is replaced by filter-bit 96;
- The Z_{vertex} cut $|Z_{\text{vertex}}| < 10$ cm is replaced by $|Z_{\text{vertex}}| < 8$ cm;
- Pileup cuts are not applied;
- V0M centrality estimator is replaced by CL1 centrality estimator;
- The reference flow vector $\vec{Q}_n^{\text{V0A}}$ is replaced by $\vec{Q}_n^{\text{V0C}}$.

Figure 6.7 (upper left) shows the systematic uncertainties of the inclusive charged-particle v_2 as a function of p_{T} and Fig. 6.7 (upper right and bottom) shows the systematic uncertainties of the jet-particle v_2 as a function of the trigger-particle p_{T} with different associated p_{T} selections.

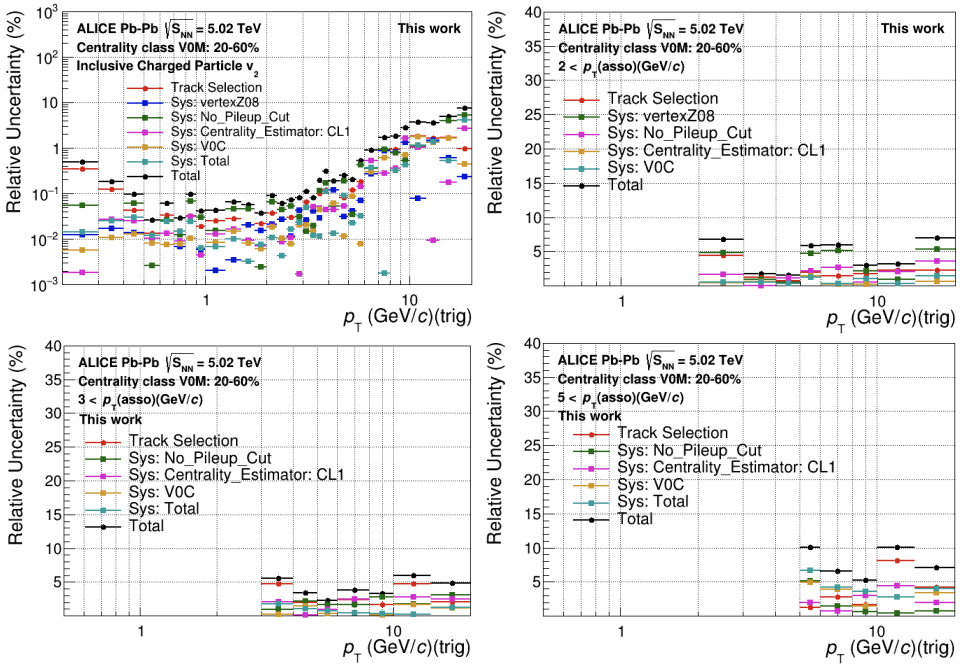

Figure 6.7: Upper left: the systematic uncertainties of inclusive charged-particle v_2 in Pb–Pb collisions at $\sqrt{s_{\text{NN}}} = 5.02$ TeV. Upper right and bottom panels: the systematic uncertainties of the jet-particle v_2 with different associated-particle p_{T} selections in Pb–Pb collisions at $\sqrt{s_{\text{NN}}} = 5.02$ TeV.

6.2 Measurement of the Jet-particle v_2 in p–Pb Collisions

6.2.1 Data Sample and Selection

The p–Pb collisions collected in 2016 are used for this measurement, and the selected runs are:

- LHC16q pass1 FAST, AOD 190, 32 runs
  265309, 265332, 265334, 265335, 265336, 265338, 265339, 265342, 265343, 265344, 265377, 265378, 265381, 265383, 265384, 265385, 265387, 265388, 265419, 265420, 265421, 265422, 265424, 265425, 265426, 265427, 265435, 265499, 265500, 265501, 265521, 265525;

- LHC16q pass1 CENT woSDD, AOD 190, 32 runs
  265309, 265332, 265334, 265335, 265336, 265338, 265339, 265342, 265343, 265344, 265377, 265378, 265381, 265383, 265384, 265385, 265387, 265388, 265419, 265420, 265421, 265422, 265424, 265425, 265426, 265427, 265435, 265499, 265500, 265501, 265521, 265525;

- LHC16t pass1 FAST, AOD 190, 4 runs
  267163, 267164, 267165, 267166;

- LHC16t pass1 CENT woSDD, AOD 190, 4 runs
  267163, 267164, 267165, 267166

These periods correspond to the p-going direction. All runs have been selected after the Quality Assurance (QA) checks. The AliPhysics version used in this analysis is vAN-20200525-1.

Event Selection

In this analysis, only the data samples collected with the MB trigger, are analysed. As in the muon v_2 analysis in p–Pb collisions (see Sec. 5.1), the physics selection is applied by means of the `AliPhysicsSelection` task. It includes both the beam background removal and pileup cuts. The events with longitudinal primary vertex position (i.e. Z_{vertex}) smaller than 10 cm are selected, and if the vertex is reconstructed with VertexerSPDz, the resolution along the Z axis is required to be smaller than 0.25 cm. The data sample is divided into several multiplicity classes based on the charge deposited in the V0A scintillators located in the Pb going direction.

Furthermore, since the FMD detector is used in this analysis, the event selections related to the FMD detector should be considered. Only the events with at least one hit in both FMD1,2 and FMD3 acceptance are selected. Besides, since the read out time of FMD is long ($\sim 2\mu$s) [134], additional pileup cuts using the FMD need to be applied. The acceptances of V0 and FMD overlap while the read out time of the V0 is faster. So, the additional pileup event selection is based on multiplicity

correlations between V0 and FMD for each beam direction. Following the previous analysis of TPC-FMD correlations [211], the combination of conditions: $N_{\mathrm{V0A}} > 1.65 \times N_{\mathrm{FMD1+FMD2}} - 119.60$, $N_{\mathrm{V0C}} > 2.73 \times N_{\mathrm{FMD3}} - 150.31$ are applied here. About 52.6M events are selected after all above event selections.

Track Selection

As for the measurements in Pb–Pb collisions (shown in Sec. 6.1.1), the set of track selections contained in the filter-bit 32 is used. In addition, the pseudorapidity of tracks is limited to $|\eta| < 0.8$, and their transverse momentum should satisfy $p_{\mathrm{T}} > 0.2$ GeV/c.

6.2.2 Inclusive Charged-particle v_2 in p–Pb Collisions

Before the calculation of the jet-particle v_2, the v_2 of inclusive charged particles needs to be obtained. The so-called **three sub-events** technique is employed. The particles in the acceptance of TPC, FMD1,2 and FMD3 are selected to construct two-particle correlations between each other, i.e. TPC-FMD1,2 correlations, TPC-FMD3 correlations and FMD1,2-FMD3 correlations. We take the TPC-FMD1,2 correlation as an example. As Eq. 5.3 (Sec. 5.2.1), the correlation function $Y^{\mathrm{TPC-FMD1,2}}(\Delta\varphi, \Delta\eta) = \frac{1}{N_{\mathrm{trig}}} \frac{\mathrm{d}^2 N_{\mathrm{assoc}}^{\mathrm{TPC-FMD1,2}}}{\mathrm{d}\Delta\eta \mathrm{d}\Delta\varphi}$ can be obtained via the event mixing technique, where N_{trig} is the total number of trigger particles in a given multiplicity class. The non-flow contribution in small collision systems is estimated from the scaled per-trigger associated yield in the low-multiplicity events (the so-called **low-multiplicity scale method**), as the done for measurement of the muon v_2 (see Sec. 5.2.2). Figure. 6.8 shows the per-trigger associated yield in high- and low-multiplicity events for TPC-FMD1,2 correlations in top-left and top-right panels, respectively. The subtracted correlation function $Y^{\mathrm{TPC-FMD1,2}}(\Delta\varphi, \Delta\eta)$ can be projected on $\Delta\varphi$-axis to get $Y^{\mathrm{TPC-FMD1,2}}(\Delta\varphi)$, as shown in Fig. 6.8 (bottom), and the Fourier coefficients can be extracted via:

$$Y^{\mathrm{TPC-FMD1,2}}(\Delta\varphi) = a_0 + 2a_1\cos(\Delta\varphi) + 2a_2\cos(2\Delta\varphi) + 2a_3\cos(3\Delta\varphi). \quad (6.6)$$

The fit parameter a_2 is the measurement of the absolute modulation in the subtracted per-trigger yield and characterizes a modulation relative to the baseline b, which is estimated at the minimum of the $\Delta\varphi$ distribution in low-multiplicity events (see also Sec. 5.2.1). Therefore, the second order flow coefficient $V_{2\Delta}^{\mathrm{TPC-FMD1,2}}$ is calculated according to:

$$V_{2\Delta}^{\mathrm{TPC-FMD1,2}} = \sqrt{a_2/(a_0 + b)}. \quad (6.7)$$

Similarly, the $V_{2\Delta}^{\mathrm{TPC-FMD1,2}}$ and $V_{2\Delta}^{\mathrm{FMD1,2-FMD3}}$ can be obtained by replacing the "TPC-FMD1,2" in Eq. 6.6 and Eq. 6.7 with "TPC-FMD3" and "FMD1,2-FMD3", respectively. Based on the factorization assumption, the v_2 of particles in the ac-

ceptance of TPC, FMD1,2 and FMD3 can be obtained by

$$
\begin{aligned}
v_2^{\mathrm{TPC}} &= \sqrt{\frac{V_{2\Delta}^{\mathrm{TPC-FMD1,2}}\, V_{2\Delta}^{\mathrm{TPC-FMD3}}}{V_{2\Delta}^{\mathrm{FMD1,2-FMD3}}}}, \\
v_2^{\mathrm{FMD3}} &= \sqrt{\frac{V_{2\Delta}^{\mathrm{FMD1,2-FMD3}}\, V_{2\Delta}^{\mathrm{TPC-FMD3}}}{V_{2\Delta}^{\mathrm{TPC-FMD1,2}}}}, \\
v_2^{\mathrm{FMD1,2}} &= \sqrt{\frac{V_{2\Delta}^{\mathrm{FMD1,2-FMD3}}\, V_{2\Delta}^{\mathrm{TPC-FMD1,2}}}{V_{2\Delta}^{\mathrm{TPC-FMD3}}}}.
\end{aligned}
\tag{6.8}
$$

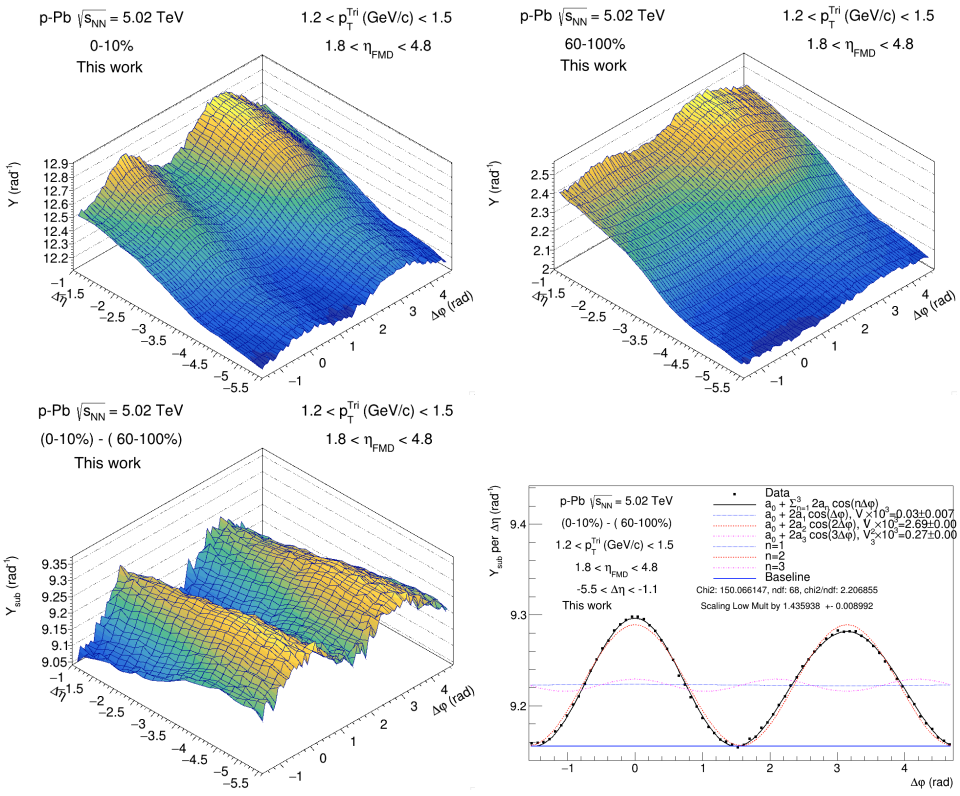

Figure 6.8: Upper left: the per-trigger yield of the TPC-FMD3 correlation distribution in high-multiplicity p–Pb collisions. Upper right: the per-trigger yield of the TPC-FMD3 correlation distribution in low-multiplicity p–Pb collisions. Lower left: the per-trigger yield after subtraction of the scaled low-multiplicity p–Pb collisions. Lower right: the $\Delta\varphi$ projection of the two-dimensional correlation function.

In order to further understand the nonflow effects in small collision systems, the so-called **template fit method** [112] is used in this analysis to suppress the nonflow contribution. In this method, the per-trigger associated yield measured in high-multiplicity events, $Y^{\mathrm{templ}}(\Delta\varphi)$, is assumed to result from a superposition of the per-trigger associated yield measured in low-multiplicity events, $Y^{\mathrm{periph}}(\Delta\varphi)$,

scaled up by a multiplicative factor, and a constant modulated by $\cos(n\Delta\varphi)$ for $n > 1$. The resulting template fit function is

$$Y^{\mathrm{templ}}(\Delta\varphi) = Y^{\mathrm{ridge}}(\Delta\varphi) + FY^{\mathrm{periph}}(\Delta\varphi), \tag{6.9}$$

where

$$Y^{\mathrm{ridge}}(\Delta\varphi) = a_0 + \sum_{n=2}^{3} 2a_n \cos(n\Delta\varphi). \tag{6.10}$$

The parameter F is the multiplicative factor to scale the $Y^{\mathrm{periph}}(\Delta\varphi)$, and the fit parameter a_2 is the absolute modulation, which is equivalent to the a_2 coefficient in Eq. 6.6. Figure. 6.9 shows the template fit to the per-trigger particle yield in high-multiplicity events for TPC-FMD1,2 (left) and TPC-FMD3 (right) correlations. Naturally, the v_2 of TPC tracks and of particles in FMD1,2 and FMD3 can be obtained according to Eq. 6.7 and Eq. 6.8, respectively.

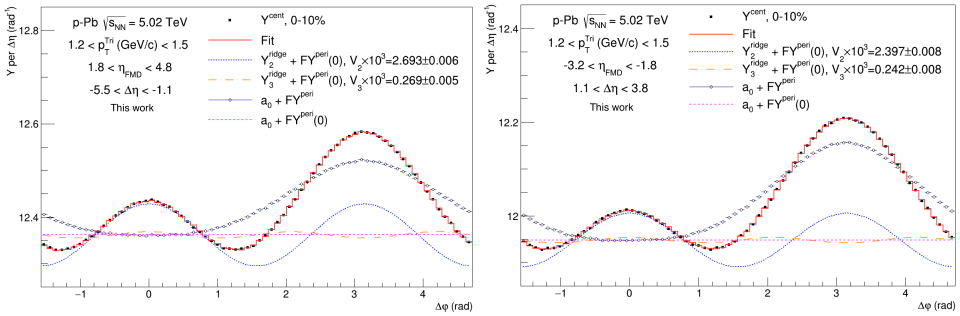

Figure 6.9: The template fit to the per-trigger particle yields $Y^{\mathrm{TPC-FMD3}}(\Delta\varphi)$ in p–Pb collisions at $\sqrt{s_{\mathrm{NN}}} = 5.02$ TeV for TPC-FMD1,2 (left) and TPC-FMD3 (right) particle pairs with $1.2 < p_{\mathrm{T}} < 1.5$ GeV/c.

Figure. 6.10 shows the comparison between the inclusive charged-particle v_2 obtained with the subtraction method and the template fit method in p–Pb collisions at $\sqrt{s_{\mathrm{NN}}} = 5.02$ TeV, and the published inclusive charged-particle v_2 obtained with the subtraction method in the 0–20% multiplicity class [93]. One observes that our measurement is obtained in a wider p_{T} region and with smaller uncertainties compared to the published results [93]. The results obtained with the template fit method are compatible with those obtained with the subtraction method. The non-flow contribution is also evaluated in lower multiplicity (70–100%) collisions with two methods, which still give compatible results, as shown in Fig. 6.10. The deviations between these results obtained using different nonflow subtraction procedures will be considered as the systematic uncertainty, as discussed in Sec. 6.2.4.

On the other hand, the v_2 of charged particles in the acceptance of FMD as a function of the TPC-track p_{T} obtained with the template fit method and the subtraction method are also consistent, as shown in Fig. 6.11. The v_2 has no dependence on the TPC-track p_{T}, which shows that the factorization in Eq. 6.8 is valid in this analysis. The values $v_2^{\mathrm{FMD1,2}} = 0.028$ and $v_2^{\mathrm{FMD3}} = 0.025$ are obtained from

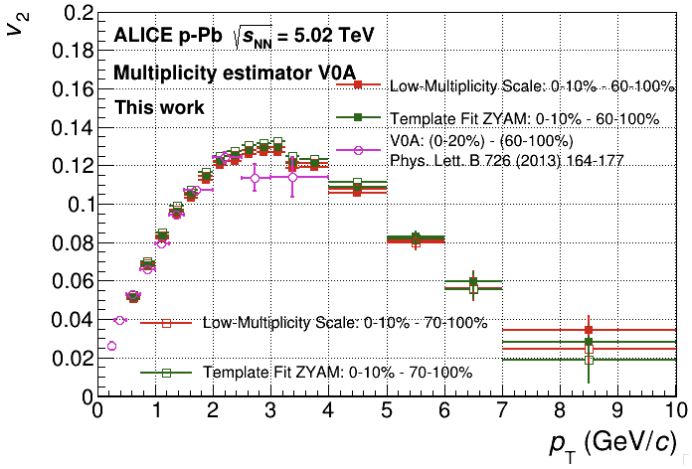

Figure 6.10: Comparison between the inclusive charged-particle v_2 at mid-rapidity obtained with the subtraction method and the template fit[6]method in p–Pb collisions at $\sqrt{s_{\rm NN}} = 5.02$ TeV and the published same measurement obtained with the subtraction method in 0–20% multiplicity class [93]. The results obtained with the nonflow subtration methods performed in lower multiplicity (70–100%) collisions are also shown.

the fit of the v_2 distributions with zero-polynomial functions. They are consistent with the measurements in [212].

6.2.3 Jet-particle v_2 in p–Pb Collisions

As in Sec. 6.1.3, the first step to extract the jet-particle v_2 is to isolate the particles from jets. With the two-particle correlations constructed by TPC tracks at midrapidity, the near-side jet peak is observed in $(\Delta\varphi \sim 0, \Delta\eta \sim 0)$, as shown in Fig. 6.12 (upper left). The associated yield in the near-side jet peak is extracted with a two-dimensional fit method, using a double Gaussian on the near-side superimposed with the sum of harmonics up to fifth order, as shown in Eq. 6.3. Figure. 6.12 shows the fit of the TPC-TPC correlation function (upper right) and the deviation between the fit and data (bottom). Figure 6.13 shows the extracted jet-peak yield (left) and background yield (right).

As described in Sec. 6.1.3, the v_2 of trigger particles in TPC-TPC correlations as a function of $(\Delta\eta, \Delta\varphi)$ can be calculated via the three-particle correlation technique. In the three-particle correlations, two of them are chosen from the particle pairs obtained in TPC-TPC correlations, as shown in Fig. 6.12 (left), and the third particle is selected in the FMD1,2 acceptance. The pseudorapidity and azimuthal angles of the two particles in the TPC-TPC particle pair are labeled as (η_1, φ_1) and (η_2, φ_2), and the pseudorapidity and azimuthal angle of the third particle in FMD1,2 are labeled as (η_3, φ_3), as shown in Fig. 6.14. The trigger particle in the TPC-TPC

[6]As discussed in Sec. 5.2.1, the ZYAM hypothesis is considered in this thesis, therefore the template fit method is labeled as **Template Fit ZYAM** in the figure.

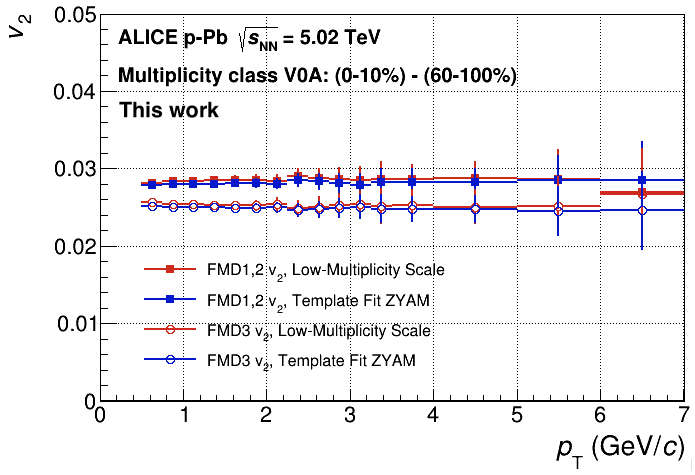

Figure 6.11: Comparison between the v_2 of charged particles in the FMD1,2 and FMD3 as a function of the TPC-track p_T obtained with the subtraction method and the template fit method in p–Pb collisions at $\sqrt{s_{NN}} = 5.02$ TeV.

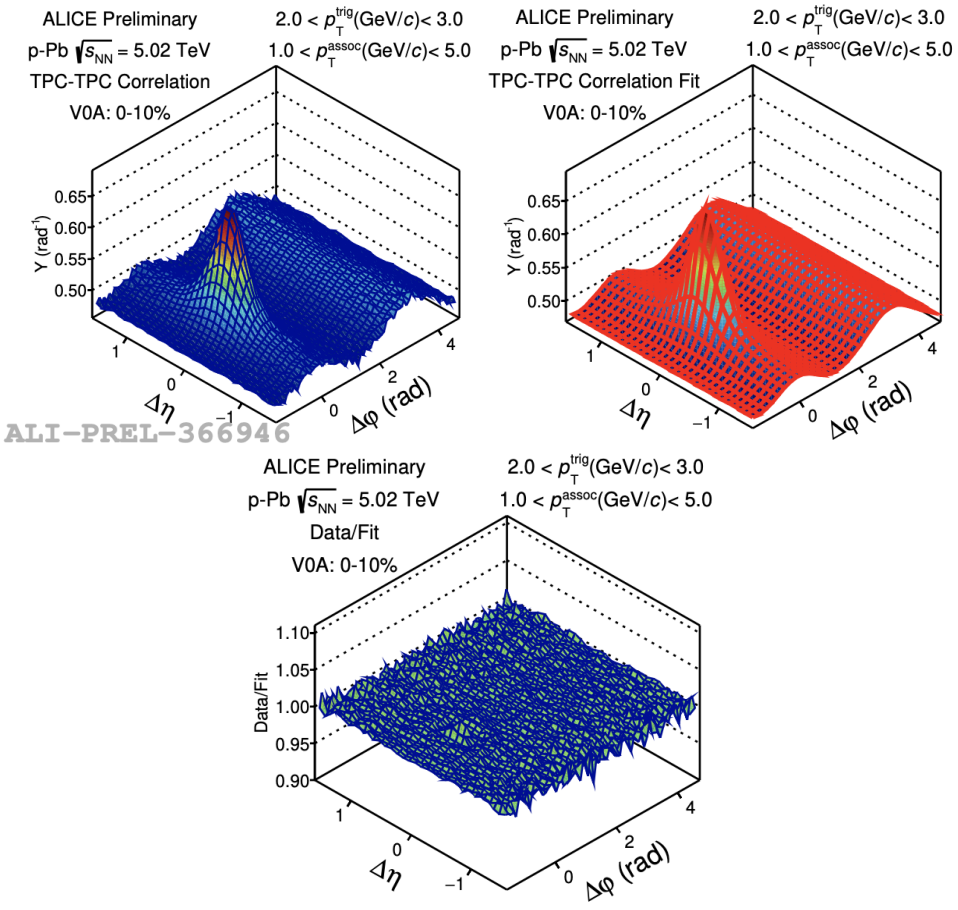

Figure 6.12: Upper left: the associated yield per trigger particle in TPC-TPC correlations for p–Pb collisions at $\sqrt{s_{NN}} = 5.02$ TeV. Upper right: the fit of the TPC-TPC correlation distribution. Bottom: the deviation between the fit and data.

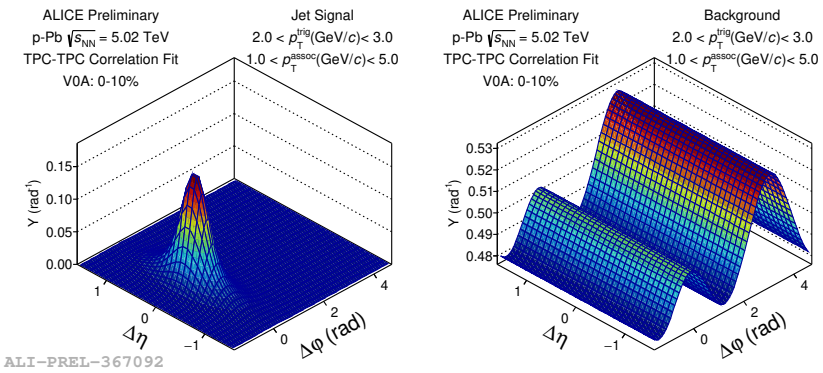

Figure 6.13: The extracted near-side jet (left) and background (right) yields after the fit of the TPC-TPC correlation distribution in p–Pb collisions at $\sqrt{s_{\rm NN}} = 5.02$ TeV.

particle pair is correlated with the particles in FMD1,2 to construct the long-range correlation distribution as a function of the azimuthal angle difference ($\Delta\varphi'$) and pseudorapidity difference ($\Delta\eta'$) in high- and low-multiplicity events, as shown in Fig. 6.15 (upper left and right). The nonflow contributions are suppressed by applying the subtraction of the scaled per-trigger yield measured in low-multiplicity collisions, as shown in Fig. 6.15 (bottom). The correlation distribution is further projected onto $\Delta\varphi'$ axis and fitted with a Fourier series parameterized with the first three harmonics as

$$\frac{{\rm d}N}{{\rm d}\Delta\varphi'} \propto 1 + 2\sum_{n=1}^{3} V_{n\Delta}(\Delta\varphi, \Delta\eta)\cos(n\Delta\varphi'), \tag{6.11}$$

where

$$\begin{aligned} \Delta\varphi &= \varphi_1 - \varphi_2, \;\; \Delta\eta = \eta_1 - \eta_2, \\ \Delta\varphi' &= \varphi_1 - \varphi_3, \;\; \Delta\eta' = \eta_1 - \eta_3. \end{aligned} \tag{6.12}$$

The $\Delta\varphi'$ projection is obtained from a first-order polynomial fit along $\Delta\eta'$ for each $\Delta\varphi'$ interval in order to reduce the statistical fluctuations [190]. Assuming its factorization in single-particle v_2 coefficients, the $V_{2\Delta}(\Delta\varphi, \Delta\eta)$ can be expressed as the product of the v_2 of trigger particles ($v_2(\Delta\varphi, \Delta\eta)$) and the v_2 of particles in FMD1,2 ($v_2^{\rm FMD1,2}$):

$$v_2(\Delta\varphi, \Delta\eta) = \frac{V_{2\Delta}(\Delta\varphi, \Delta\eta)}{v_2^{\rm FMD1,2}}, \tag{6.13}$$

where the $v_2^{\rm FMD1,2}$ was already obtained in Sec. 6.2.2, as shown in Fig. 6.11.

Figure 6.16 (upper left) shows the v_2 distribution of trigger particles in TPC-TPC pairs as a function of $\Delta\varphi$ and $\Delta\eta$. Similar to Fig. 6.6, the concavity is observed at ($\Delta\varphi \sim 0, \Delta\eta \sim 0$) where the jet peak is located. This also indicates that the jet-particle v_2 is different from the v_2 of the background particles in p–Pb collisions. As already shown in Eq. 6.5, the $v_2(\Delta\varphi, \Delta\eta)$ is the weighted sum of the v_2 of jet particles ($v_{2,\rm jet}$) and background ($v_{2,\rm bkg}$), where the weight is the ratio of the yield

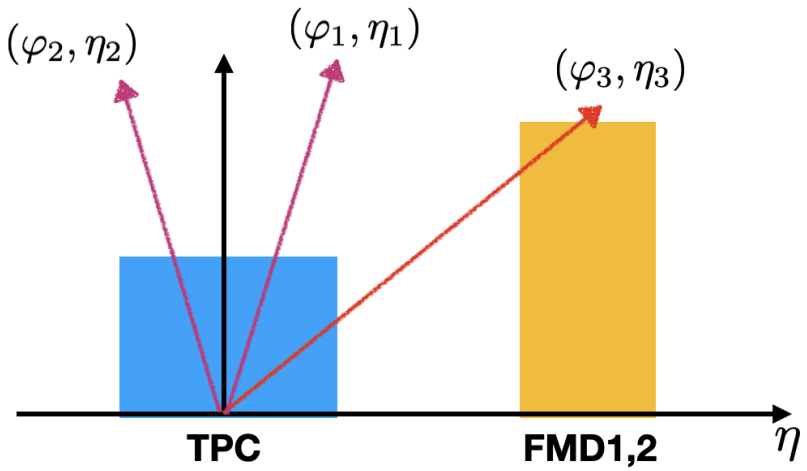

Figure 6.14: The selection of three particles in the jet-particle v_2 measurement in p–Pb collisions at $\sqrt{s_{\rm NN}} = 5.02$ TeV. Two particles are chosen in the TPC acceptance and the third particle is in FMD1,2.

of the jet peak ($Y_{\rm jet}$) to the background yield ($Y_{\rm bkg}$) obtained when fitting the TPC-TPC correlation, as shown in Eq. 6.5. The fit of the $v_2(\Delta\varphi, \Delta\eta)$ distribution with Eq. 6.5 in each $p_{\rm T}$ interval of trigger and associated particles is displayed in the right panel of Fig. 6.16. The agreement between the fit and the data shown in the bottom panel of Fig. 6.16 demonstrates that the fit strategy is suited to extract the v_2 of jet particles.

6.2.4 Systematic Uncertainty

Same sources of systematic uncertainties are considered in the measurement of inclusive charged-particle v_2 and jet-particle v_2 in p–Pb collisions at $\sqrt{s_{\rm NN}} = 5.02$ TeV, as shown in the following:

- **Vertex08** The cut on $Z_{\rm vertex}$ is restricted to $|Z_{\rm vertex}| < 8$ cm;
- **Filter bit** The filter-bit 32 is replaced by 96;
- **Nonflow subtraction** The nonflow subtraction method is replaced by the template fit method;
- **FMD pileup cuts** Looser FMD/V0 selection is used: $N_{\rm V0A} > 1.65 \times N_{\rm FMD1+FMD2} - 159.47$, $N_{\rm V0C} > 2.73 \times N_{\rm FMD3} - 200.41$;
- **Remaining ridge in the low multiplicitiy class**
  - **70 to 90%** The multiplicity class 70–90% is used instead of 60–90% for the non-flow subtraction;
- v_2 **extraction**

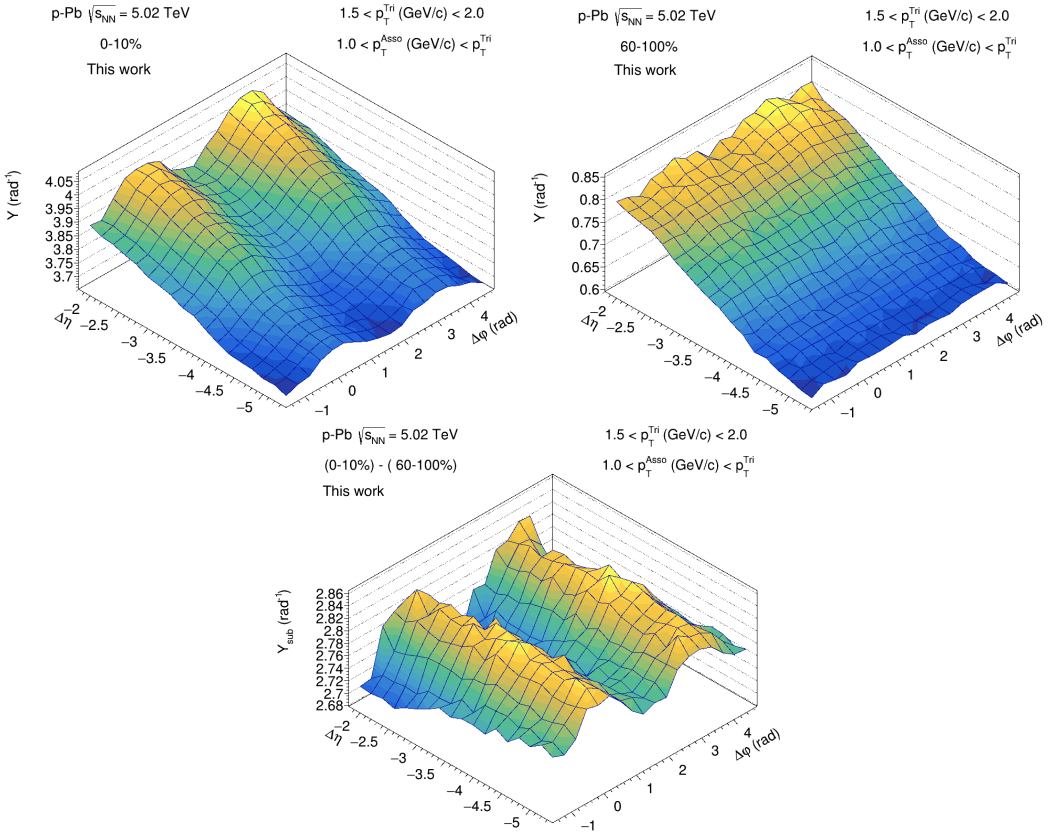

Figure 6.15: Upper left: the per-trigger yield of TPC-FMD1,2 correlations in high-multiplicity events. Upper right: the per-trigger yield of TPC-FMD1,2 correlations in low-multiplicity events. Bottom: the per-trigger yield after subtraction of correlations in low-multiplicity events.

  - **baseline estimation**
    - **baselineHighMult** The v_2 is calculated using the baseline estimated in the high-multiplicity class directly,
    - **baselineHighMultParab** The baseline in the high-multiplicity class is estimated using a parabolic fit around $\pi/2(\pi/2 \pm 0.2)$;
  - **constant fit** Instead of a first order polynomial function, a constant fit is used to reduce the statistical fluctuations in the projection procedure;
  - **no** v_3 The v_2 is calculated only using the first and second Fourier harmonics in the fit;

- **Secondary particles in FMD** The effect of the presence of secondary particles in the FMD detector is evaluated by means of a dedicated Monte Carlo simulation with A Multi-Phase Transport (AMPT) model [213]. The deviation between the v_2 measured with FMD particles at generation level and reconstruction level is regarded as the corresponding systematic uncertainty.

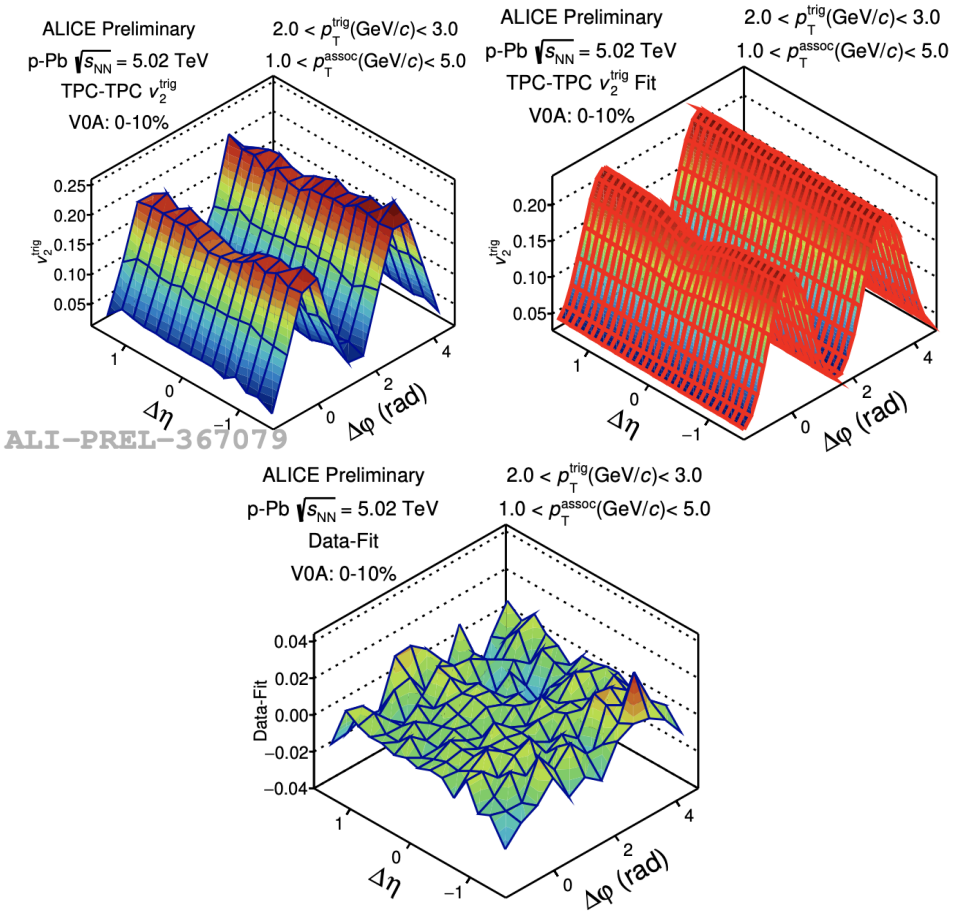

Figure 6.16: Upper left: v_2 distribution of trigger particles in TPC-TPC pairs in p–Pb collisions at $\sqrt{s_{\rm NN}} = 5.02$ TeV. Upper right: fit to the v_2 of the trigger-particle distribution with Eq. 6.5. Bottom: difference between data and fit as a function of $\Delta\varphi$ and $\Delta\eta$.

All systematic checks satisfy the barlow test [197]. Figure. 6.17 (upper left) shows the systematic uncertainty of the inclusive charged-particle v_2 as a function of $p_{\rm T}$. The systematic uncertainty of the jet-particle v_2 as a function of trigger-particle $p_{\rm T}$ for different associated-particle $p_{\rm T}$ selections in p–Pb collisions at $\sqrt{s_{\rm NN}} = 5.02$ TeV are shown in Fig. 6.17 (upper right and bottom panel). The systematic uncertainties discussed above are added in quadrature in each $p_{\rm T}$ interval of trigger and associated particles to obtain the total systematic uncertainty of 11.2–34.3% and 4.4–25.2% for the jet-particle v_2 and inclusive charged-particle v_2, respectively.

6.3 Results and Discussions

Figure. 6.18 (left) presents the v_2 of jet particles as a function of the trigger charged-particle $p_{\rm T}$ at midrapidity ($|\eta| < 0.8$) for different ranges of the associated

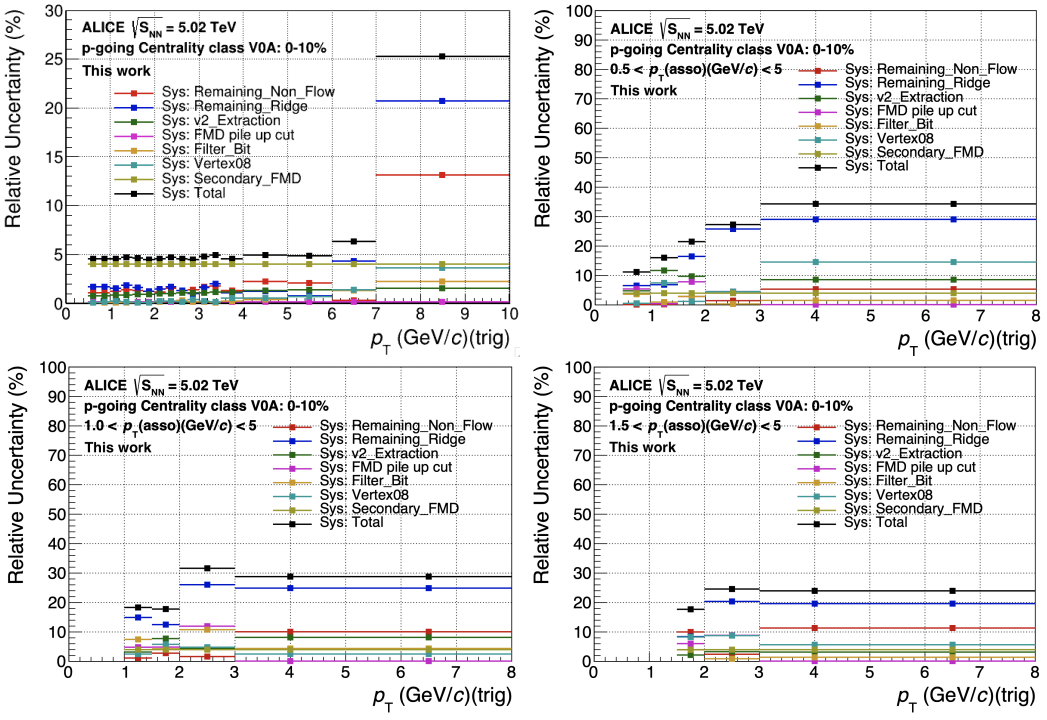

Figure 6.17: Upper left: the systematic uncertainty sources of inclusive charged-particle v_2 in p–Pb collisions at $\sqrt{s_{\rm NN}}$ = 5.02 TeV. Upper right and bottom: the systematic uncertainty sources of the jet-particle v_2 with different associated-particle $p_{\rm T}$ selections in p–Pb collisions at $\sqrt{s_{\rm NN}}$ = 5.02 TeV.

$p_{\rm T}$, in high-multiplicity (0–10%) p–Pb collisions at $\sqrt{s_{\rm NN}}$ = 5.02 TeV. The $p_{\rm T}$-differential inclusive charged-particle v_2 coefficient is also displayed for comparison. A positive v_2 signal is measured with a significance about 2–7σ (3–7σ) in the $p_{\rm T}$ interval $0.5 < p_{\rm T} < 8$ GeV/c ($0.5 < p_{\rm T} < 3$ GeV/c), as shown in Fig. 6.18 (right). The measured v_2 is independent of both the trigger-particle and associated-particle $p_{\rm T}$ within uncertainties. On the other hand, the v_2 of the inclusive charged particles shows a clear dependence on $p_{\rm T}$ and its magnitude is found larger than that of the jet-particle v_2. Indeed, the v_2 signal of inclusive charged particles increases up to $p_{\rm T}$ ~3 GeV/c where it reaches a maximum value of ~ 0.13 and decreases with increasing $p_{\rm T}$.

Furthermore, the jet-particle v_2 measured in this analysis is compared to the v_2 of charged particles measured by ATLAS [98] (see Fig. 1.29 (right)), as shown in Fig. 6.19. In the ATLAS measurement, the charged-particle v_2 is measured separately for MBT events and events requiring a jet with $p_{\rm T}$ larger than 100 GeV/c (the so-called jet-triggered event). In order to make a direct comparison, the v_2 measured in the p–Pb collisions by ALICE and ATLAS is scaled by the factor[7] 1.5,

[7]This multiplicative factor is obtained directly from ATLAS measurements [98], which is empirically determined.

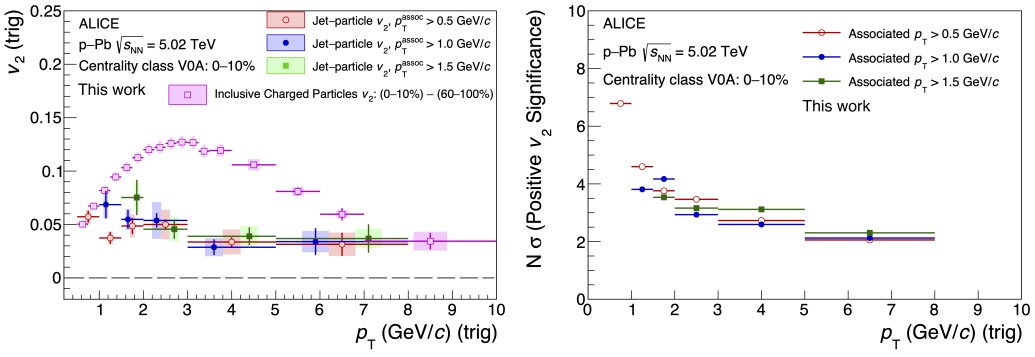

Figure 6.18: Left: jet-particle v_2 as a function of the trigger-particle p_{T} for several p_{T} intervals of associated particles compared with the inclusive charged-particle v_2 in 0–10% p–Pb collisions at $\sqrt{s_{\mathrm{NN}}} = 5.02$ TeV. Right: the significance of the positive jet-particle v_2 as a function of p_{T}.

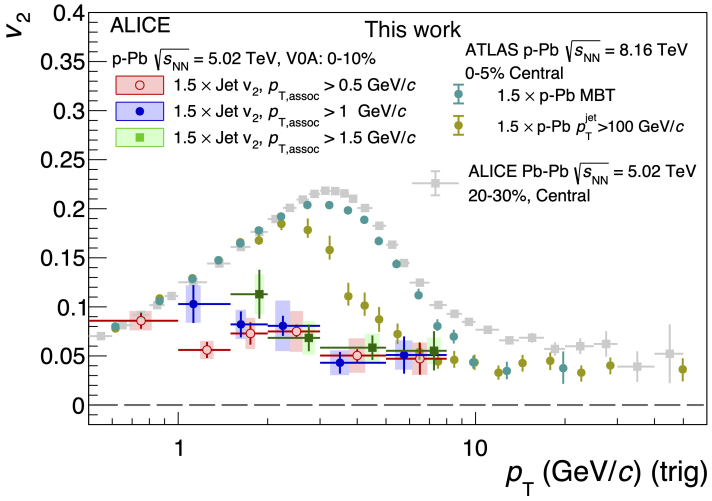

Figure 6.19: The comparison between the jet-particle v_2 as a function of p_{T} measured in this analysis and the charged-particle v_2 in MBT events and events requiring a jet with p_{T} larger than 100 GeV/c measured by ATLAS [98]. The v_2 of charged particles measured by ALICE in 20–30% Pb–Pb collisions is also shown [208]. All the results measured in p–Pb collisions are scaled by the factor 1.5.

and the v_2 of charged particles measured by ALICE [208] in the same centrality as ATLAS is also shown. One can see that the v_2 measured in jet-triggered events is consistent with the results in MBT events at low p_{T}, and decreases faster at intermediate p_{T}, finally to converge again toward the v_2 measured in MBT events at high p_{T}. That indicates that the jet-trigger conditions in the ATLAS measurement indeed enhance the contributions from hard partons, but there are still sizable soft components contained in jet-triggered events. Since the measured jet-particle v_2

is significantly lower than the v_2 measured in jet-triggered events at low p_{T}, that implies that the hard and soft components are fully separated in the measurement of the jet-particle v_2. On the other hand, one can observe that the scaled jet-particle v_2 is comparable to the charged-particle v_2 in Pb–Pb collisions in the high-p_{T} region, where the path-length dependent energy loss dominates in Pb–Pb collisions [208].

Figure. 6.20 (left) shows the jet-particle v_2 as a function of the trigger charged-particle p_{T} at mid-rapidity ($|\eta| < 0.8$) for the different associated p_{T} selections, in Pb–Pb collisions at $\sqrt{s_{\mathrm{NN}}} = 5.02$ TeV for the 20–60% centrality class. A positive jet-particle v_2 is measured for the first time down to 2 GeV/c and does not show any dependence on the associated-p_{T} selections. In addition, the jet-particle v_2 converges towards the v_2 of inclusive charged particles in Pb–Pb collisions for $p_{\mathrm{T}} > 7$ GeV/c. Such a behaviour is consistent with parton energy loss expectations [31]. These energy loss effects are also confirmed from the nuclear modification factor measurement of charged particles in Pb–Pb collisions, as shown in Fig. 6.20 (right).

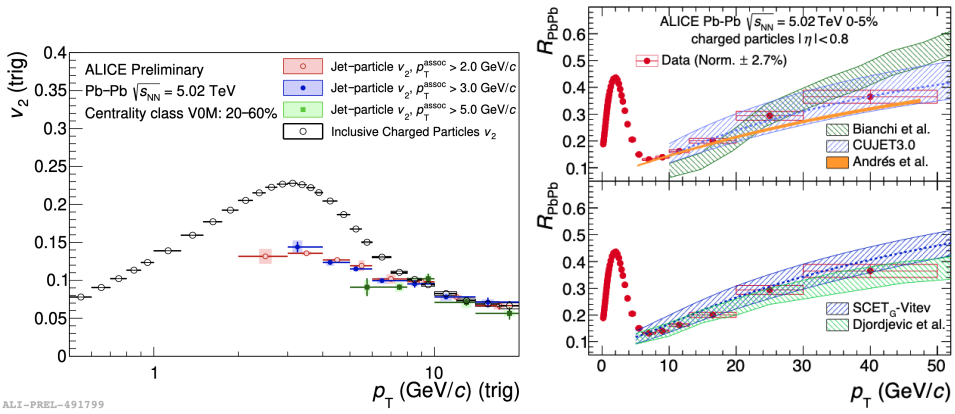

Figure 6.20: Left: jet-particle v_2 as a function of the trigger charged-particle p_{T} for several p_{T} intervals of associated charged particles compared with the inclusive charged-particle v_2 in Pb–Pb collisions at $\sqrt{s_{\mathrm{NN}}} = 5.02$ TeV for the 20–60% centrality class. Right: the charged-particle nuclear modification factor measured in the 0–5% most central Pb–Pb collisions at $\sqrt{s_{\mathrm{NN}}} = 5.02$ TeV [31] in comparison to model predictions [48, 49, 51, 214–218].

Figure 6.21 shows the comparison among the jet-particle v_2, inclusive charged-particle v_2 in p–Pb and Pb–Pb collisions at $\sqrt{s_{\mathrm{NN}}} = 5.02$ TeV. The ALICE published results for reconstructed jets measured in 30–50% Pb–Pb collisions at $\sqrt{s_{\mathrm{NN}}} = 2.76$ TeV [209] which complement the present measurements in Pb–Pb collisions by extending them up to $p_{\mathrm{T}} = 90$ GeV/c, are also displayed. The jet-particle v_2 in Pb–Pb collisions is consistent with the reconstructed-jet v_2 at high p_{T}, which are both interpreted by the path-length dependent energy loss effect. Due to the close eccentricity estimated in semicentral Pb–Pb collisions and high-multiplicity p–Pb collisions [219], the inclusive charged-particle v_2 in Pb–Pb collisions is downscaled by a empirical factor 0.6 in order to match the same measurement at low p_{T} ($p_{\mathrm{T}} \lesssim$

3 GeV/c) in p–Pb collisions. This factor, also applied to the jet-particle v_2 and reconstructed-jet v_2 measured in Pb–Pb collisions, may reflect the slightly different spatial anisotropies and the larger multiplicities in Pb–Pb collisions. After this scaling, the jet-particle v_2 measured in p–Pb collisions has a magnitude comparable to the v_2 of jet particles and reconstructed jets measured in Pb–Pb collisions at high p_{T} ($p_{\mathrm{T}} \gtrsim 10$ GeV/c), which are both attributed to jet-quenching effects. This hints to a similar collective behaviour of hard probes in large and small collision systems, even if no jet quenching effect is observed in p–Pb collisions [31, 207].

In order to shed more light on the origin of such QGP-like effects observed from the measurement of the jet-particle v_2 in high-multiplicity p–Pb collisions, a comparison with a multiphase transport model predictions (AMPT) [205, 220] with the string-melting mechanism enabled is presented in Fig. 6.22 for jet particles and inclusive charged particles. In this model, the v_2 is calculated following the same analysis procedure as that in data analysis. The event characterisation is done by mimicking the V0A criteria at particle level, i.e. by counting charged particles in $2.8 < \eta < 5.1$. The AMPT calculations reproduce the experimental trends, predicting a positive jet-particle v_2 smaller than that of inclusive charged particles, and provide a fair agreement with the inclusive charged-particle v_2. In addition, the calculation of Q_{pPb} is performed in AMPT simulation, as shown in Fig. 6.22. No significant suppression is observed at high p_{T} ($p_{\mathrm{T}} \gtrsim 7$ GeV/c), which is consistent with the data. These comparisons tend to indicate that the azimuthal anisotropies in p–Pb collisions are dominated by a non-equilibrium parton escape mechanism [206], instead of a hydrodynamic expansion of the medium or jet quenching, as in Pb–Pb collisions [221]. On the other hand, the v_2 of u and d quarks predicted by AMPT [220], shows a similar trend as the measured jet-particle v_2 at low p_{T}, while the magnitude and trend of the jet-particle v_2 are not well reproduced by the AMPT. This may reflect the effects of quark coalescence [213] on the azimuthal anisotropies of final-state particles in small collision systems.

6.4 Summary and Outlook

In this chapter, the first measurement of the jet-particle v_2 in high-multiplicity p–Pb collisions and semi-central Pb–Pb collisions at LHC is presented. These measurements are obtained using a novel multi-particle correlation technique. A non-zero and p_{T}-independent v_2 signal of jet particles is observed with a significance reaching 7σ at low p_{T} in high-multiplicity (0–10%) p–Pb collisions at $\sqrt{s_{\mathrm{NN}}} = 5.02$ TeV. Besides, the jet-particle v_2 measured down to low p_{T} in semicentral Pb–Pb collisions at $\sqrt{s_{\mathrm{NN}}} = 5.02$ TeV complements the existing jet v_2 results measured in large collision systems [209]. The AMPT predictions are in qualitative agreement with the measurement of v_2 of inclusive charged particles, and generate a positive v_2 of jet particles. These new results bring significant new insights into the understanding of the observed azimuthal anisotropies of jet particles in p–Pb collisions.

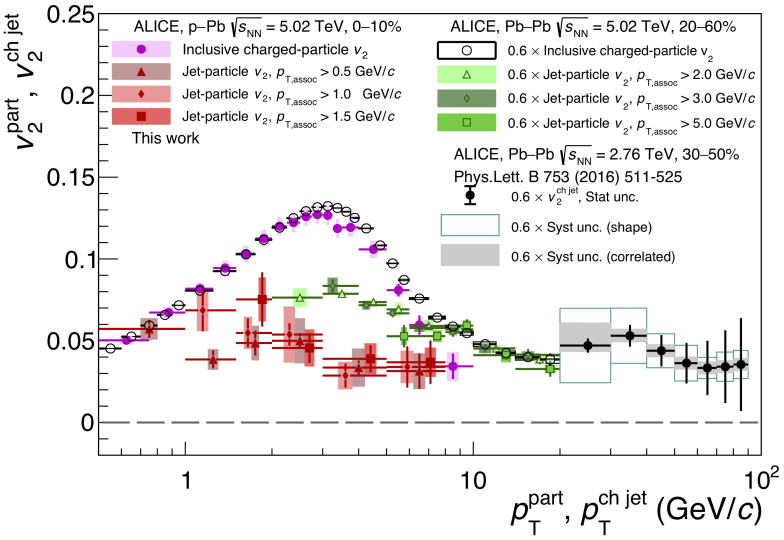

Figure 6.21: p_{T}-differential jet-particle v_2 for several p_{T} intervals of associated charged particles compared with the inclusive charged-particle v_2 in 0–10% p–Pb and 20–60% Pb–Pb collisions at $\sqrt{s_{\mathrm{NN}}} = 5.02$ TeV. The published jet v_2 measured in 30–50% Pb–Pb collisions at $\sqrt{s_{\mathrm{NN}}} = 2.76$ TeV is also shown [209].

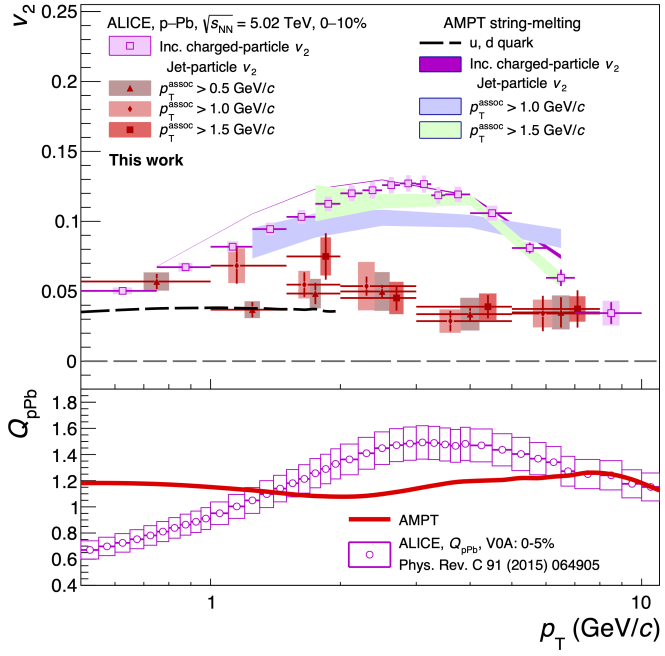

Figure 6.22: Comparisons of the jet-particle and inclusive charged-particle v_2 measured in high-multiplicity (0–10%) p–Pb collisions with AMPT model calculations [205, 220]. The comparison of Q_{pPb} in AMPT and data is also shown.

Chapter 7

Conclusions

In high-energy heavy-ion collisions, hard probes, for example the heavy flavours and jets, are powerful tools to investigate the properties of the quark-gluon plasma (QGP) since they are created at the early stage of collisions and suffer the whole evolution of the system. Compared to many interesting measurements at midrapidity, we focus on the production of muons from heavy-flavour hadron decays at forward rapidity in Pb–Pb collisions, aiming to provide additional insights to the study of energy loss of heavy quarks in QGP, especially at high transverse momentum and in the low Bjorken-x region. On the other hand, pp and p–Pb collisions are commonly regarded as the baseline for the heavy-ion collisions due to the absence of QGP medium. However, recent collective features observed in these small collision systems change our understanding about the collision dynamics, which hint at the existence of the QGP and its fluid-like character. In order to provide significant new insights for the understanding of the origin of possible collectivity in small collision systems, we performed two measurements concerning the v_2 of muons and jet particles in p–Pb collisions.

The first work presented in this thesis is the measurement of the p_{T}-differential nuclear modification factor of heavy-flavour decay muons in Pb–Pb collisions at $\sqrt{s_{\mathrm{NN}}}$ = 5.02 TeV and 2.76 TeV. This analysis is based on the muon-triggered data collected in LHC Run 1 and Run 2, which allow us to measure the R_{AA} of muons from heavy-flavour hadron decays up to 20 GeV/c in several centrality classes with an improved precision compared to published results in a p_{T} interval limited to 10 GeV/c [56]. The results show a strong suppression of the yield of muons from heavy-flavour hadron decays in Pb–Pb collisions with respect to the pp reference scaled by the average nuclear overlap function, which reaches a factor up to about three at intermediate p_{T} ($6 < p_{\mathrm{T}} < 10$ GeV/c) in the 10% most central collisions. Considering the unity of the R_{pPb} of muons from heavy-flavour hadron decays observed in minimum-bias p–Pb collisions at 5.02 TeV [182], where the QGP is not expected to exist, such a strong suppression measured in Pb–Pb collisions is believed to be caused by the energy loss of charm and beauty quarks when they interact with the QGP medium. On the other hand, a smaller R_{AA} is observed in central collisions compared to peripheral collisions. This indicates that the heavy-quark energy loss and average path length in QGP are larger in central collisions than those in peripheral collisions. Furthermore, the measured R_{AA} is compared with different model calculations, which brings new constraints on the relative in-medium energy loss of charm and beauty quarks. This work is published in Physics Letters B 820 (2021) 136558 [181].

The azimuthal anisotropy of inclusive muons was measured in high-multiplicity

(0–20%) p–Pb collisions at $\sqrt{s_{\rm NN}}$ = 8.16 TeV, with the two-particle correlation and two-particle cumulant methods. The second-order Fourier coefficient (v_2) is found to be positive with a significance which reaches values between 4.7σ–12σ (7.6σ–11.9σ) at intermediate $p_{\rm T}$ ($2 < p_{\rm T} < 6$ GeV/c) in p–Pb (Pb–p) collisions, and the results obtained with two methods give consistent results within the uncertainties after their respective non-flow subtraction. Besides, the $p_{\rm T}$ dependence of the v_2 is similar in the p–Pb and Pb–p collisions, with a hint for a higher v_2 signal at backward rapidity than at forward rapidity, as observed in a previous analysis [190]. Various multiplicity estimators (V0M, CL1, ZN) have been investigated in this analysis since they select different mean charged-particle multiplicities [150]. Compared to the published measurements of the inclusive muon v_2 and heavy-flavor decay electron v_2 [190, 201] in p–Pb collisions at $\sqrt{s_{\rm NN}}$ = 5.02 TeV, the results shown in this thesis are extended to higher $p_{\rm T}$ and are affected by much smaller uncertainties due to the higher statistics and improved analysis methods. Finally, the inclusive muon v_2 measured in this analysis is compared to the elliptic flow of muons from $\rm D^0$ and B mesons decays obtained in color glass condensate (CGC) and AMPT model calculations. It shows that both the CGC-based and AMPT calculations for muons from both charm- and beauty-hadron decays provide a fair description of the measured inclusive muon v_2 for $p_{\rm T} > 2$ GeV/c, while in the low-$p_{\rm T}$ region ($p_{\rm T} < 2$ GeV/c) dominated by muons from light-flavour hadron decays, the CGC-based calculations overestimate the data.

The measurement of v_2 of particles associated with jets as a function of $p_{\rm T}$ at midrapidity ($|\eta| < 0.8$) in high-multiplicity (0–10%) p–Pb collisions and semi-central (20–60%) Pb–Pb collisions at $\sqrt{s_{\rm NN}}$ = 5.02 TeV, was performed for the first time at the LHC, based on a novel multi-particle correlation technique. In p–Pb collisions, a positive v_2 signal of jet particles is observed with a significance in the range 3–6.8 σ. The magnitude of the jet-particle v_2 is lower than that of the v_2 of inclusive charged particles. The measured jet-particle v_2 is independent of the trigger- and associated-particle $p_{\rm T}$ within uncertainties, while the inclusive charged-particle v_2 shows a clear dependence on $p_{\rm T}$. On the other hand, a positive jet-particle v_2 measured in Pb–Pb collisions is also observed, which extends, for the first time, the existing measurements of jets reconstructed from charged particles to lower $p_{\rm T}$, down to $p_{\rm T}$ = 2 GeV/c. The jet-particle v_2 is consistent with the v_2 of inclusive charged particles at $p_{\rm T} > 7$ GeV/c in Pb–Pb collisions, where the path-length dependent energy loss is expected to dominate. Furthermore, a comparison between the jet-particle v_2 measured in Pb–Pb collisions and p–Pb collisions, and the v_2 of inclusive charged particles in these two systems is performed. The v_2 of jet particles and inclusive charged particles in p–Pb collisions, is compatible with the same observable scaled by the factor 0.6 in Pb–Pb collisions, which indicates a similar collective behaviour from small to large collision systems. Finally, the comparisons with AMPT calculations in p–Pb collisions are discussed. The AMPT calculations are in qualitative agreement with the measurement of v_2 of inclusive charged particles, and predict a positive v_2 of jet particles. It suggests that the azimuthal anisotropies in p–Pb collisions may be driven by the equilibrium anisotropic parton escape mechanism. These new

results bring significant insights into the understanding of the observed azimuthal anisotropies of jet particles in p–Pb collisions.

Appendix A

Test of the Factorization

The success of the two-particle correlation method largely depends on the validity of the factorization, as described in Sec. 2.4. The break of the factorization is observed to have a dependence on the p_{T} of trigger and associated particles, which may be due to autocorrelations induced by resonance decays, fragmentation of back-to-back jets or initial-state eccentricity fluctuations [114]. As described in Sec. 5.2, the measurement of the muon v_2 with the two-particle correlation method being based on the factorization of muon-tracklet correlations into single factorization, we need to test the stability of the factorization by comparing the v_2 measured with different selections of SPD tracklets.

As mentioned in Sec. 5.1.4, the difference between the azimuthal angle of SPD tracklets in the two layers of SPD, $\Delta\varphi$, reflects the mean p_{T} of the charged particles represented by the SPD tracklets. The selections are applied on the $\Delta\varphi$ of SPD tracklets in both tracklet-tracklet and muon-tracklet correlations. Figure A.1 shows the v_2 of the SPD tracklets as a function of $\Delta\varphi$ selections applied on trigger particles. Different colors represent the different $\Delta\varphi$ selections for associated SPD tracklets. One can observe that the v_2 of SPD tracklets with $\Delta\varphi$ cut $= 1$ mrad ($\Delta\varphi > 1$ mrad) deviate from the values obtained with other selections on $\Delta\varphi$. It indicates that the factorization is broken with the tightest $\Delta\varphi$ selection, while with looser $\Delta\varphi$ selections, the factorization recovers. To keep sufficient statistics, the default selection $\Delta\varphi > 5$ mrad is applied in this analysis [190].

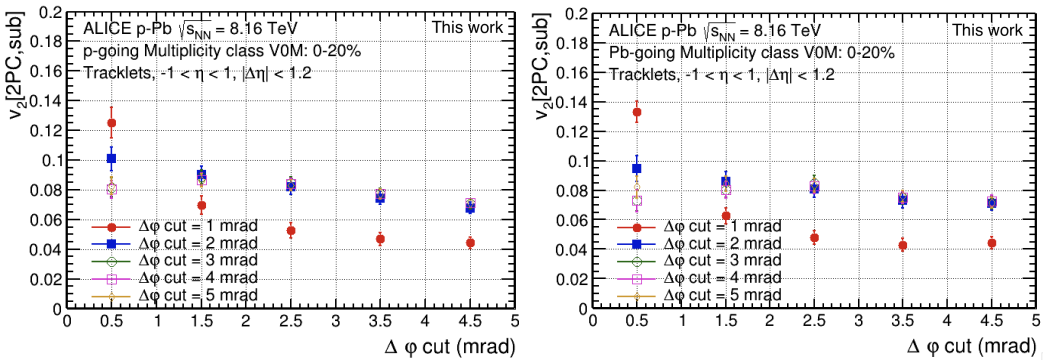

Figure A.1: The v_2 of the SPD tracklets as a function of the $\Delta\varphi$ selections applied on the trigger-particle in p–Pb (left) and Pb–p (right) collisions. Different colors represent the different $\Delta\varphi$ selections for associated SPD tracklets.

Similarly, the test of various $\Delta\varphi$ selections has been also performed in the muon-tracklet correlations. Figure A.2 shows the inclusive muon v_2 as a function of muon

p_{T} with different $\Delta\varphi$ selections applied on SPD tracklets. The results show that the factorization is broken significantly with $\Delta\varphi > 1$ mrad applied on the SPD tracklets, while the muon v_2 values with other $\Delta\varphi$ cuts are consistent within uncertainties. That indicates again that the factorization is valid with the default selection $\Delta\varphi > 5$ mrad.

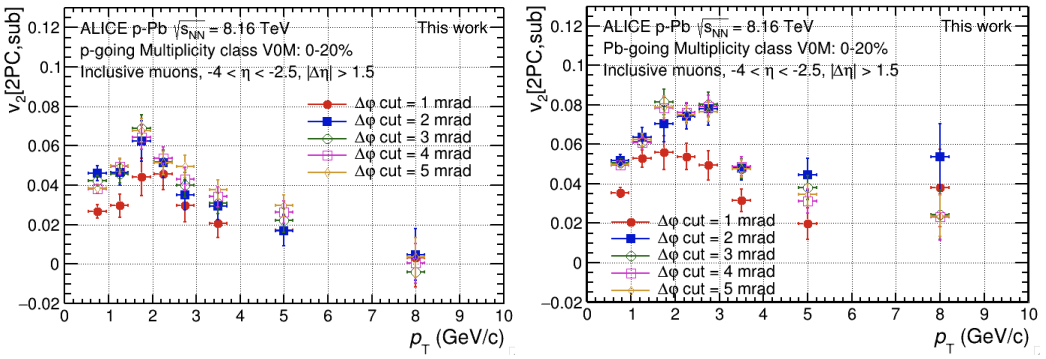

Figure A.2: The inclusive muon v_2 as a function of muon p_{T} in p–Pb (left) and Pb–p (right) collisions. Different colors represent different $\Delta\varphi$ selections applied on associated SPD tracklets.

Appendix B

Afterburner Technique in Flow Analysis

In order to investigate detector effects on the flow observables, one needs to introduce the anisotropic flow into a Monte Carlo (MC) event generator and perform a full simulation based on a transport package. This can be done by modifying the azimuthal angle of each particle, and one can further check that such a change results in the required effects in the anisotropic flow. This is the so-called **afterburner** flow technique.

In the measurement of the muon v_2, the track resolution in the muon spectrometer is estimated with this technique. The p_{T} and φ distribution of simulated muons are labeled as $p_{\mathrm{T,Gen}}$ and φ_{Gen}. The p_{T} and φ of reconstructed muons are labeled as $p_{\mathrm{T,Rec}}$ and φ_{Rec}. The difference between the generated and reconstructed muons can be expressed as:

$$\Delta p_{\mathrm{T}} = p_{\mathrm{T,Rec}} - p_{\mathrm{T,Gen}}, \quad \Delta\varphi = \varphi_{\mathrm{Rec}} - \varphi_{\mathrm{Gen}}. \tag{B.1}$$

Then, we assume that the generated particles experience a collective behaviour with a $v_{2,\mathrm{Gen}}$ coefficient[1], and the reconstructed particles also have their v_2, which is labeled as $v_{2,\mathrm{Rec}}$. Based on the flow definitions given in Sec. 1.3.3, the φ_{Gen} distribution can be approximated as a Fourier series with respect to the common symmetry plane as:

$$\frac{\mathrm{d}N}{\mathrm{d}\varphi_{\mathrm{Gen}}} \sim 1 + 2v_{2,\mathrm{Gen}}(p_{\mathrm{T,Gen}})\cos(2(\varphi_{\mathrm{Gen}} - \Psi_2)). \tag{B.2}$$

Similarly, the φ_{Rec} is obtained:

$$\frac{\mathrm{d}N}{\mathrm{d}\varphi_{\mathrm{Rec}}} \sim 1 + 2v_{2,\mathrm{Rec}}(p_{\mathrm{T,Rec}})\cos(2(\varphi_{\mathrm{Rec}} - \Psi_2)). \tag{B.3}$$

Substituting Eq. B.1 into Eq. B.3, one obtains:

$$\frac{\mathrm{d}N}{\mathrm{d}\varphi_{\mathrm{Rec}}} \sim 1 + 2v_2(p_{\mathrm{T,Gen}} + \Delta p_{\mathrm{T}})\cos(2(\varphi_{\mathrm{Gen}} + \Delta\varphi - \Psi_2)), \tag{B.4}$$

where Ψ_2 is the azimuthal angle of the symmetry plane, which is the sampling from a uniform distribution in $(0, 2\pi)$. One can study $\Delta\varphi$ and Δp_{T} from the full simulation with the DPMJET event generator and GEANT4 transport code [177,

[1] In principle, the $v_{2,\mathrm{Gen}}$ can be set as any value. However, to minimize the possible bias from the deviation between the truth and MC, the v_2 measured in data is used as the $v_{2,\mathrm{Gen}}$ here.

196]. Figure B.1 shows the $\Delta\varphi$ distribution of muon tracks with $0.5 < p_{\mathrm{T}} < 1$ GeV/c, which is fitted with a Gaussian function. The width of the Gaussian function (σ) reflects the effect of the detector resolution on the azimuthal angle φ of measured particles. The p_{T} distribution of generated and reconstructed muons are shown in Figure B.2. Each bin is normalized to make the sum of each row equal to unity.

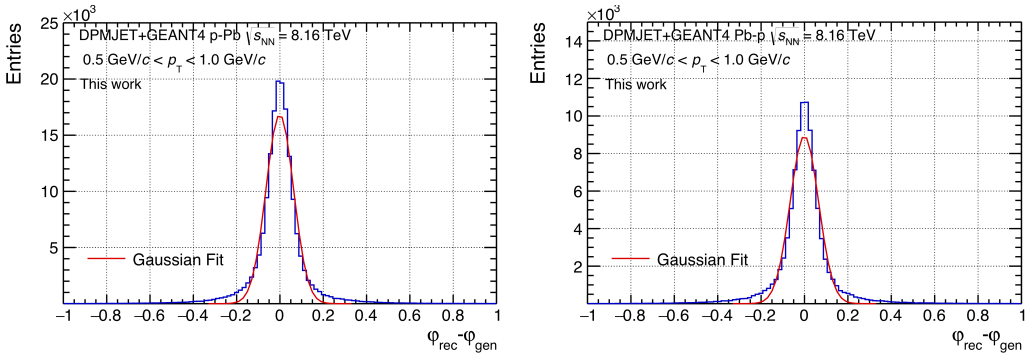

Figure B.1: $\varphi_{\mathrm{Rec}} - \varphi_{\mathrm{Gen}}$ distribution of muon tracks with $0.5 < p_{\mathrm{T}} < 1$ GeV/c estimated from MC simulations with the DPMJET event generator and GEANT4 transport code in p–Pb (left) and Pb–p (right) collisions. The lines correspond to the fit with a Gaussian function.

The φ distribution of reconstructed muon tracks can be sampled from Eq. B.4 and consequently the $v_{2,\mathrm{Rec}}$ is extracted from the φ distribution. The ratio $v_{2,\mathrm{Rec}}/v_{2,\mathrm{Gen}}$ quantifies the muon resolution effect, as shown in Fig. B.3. The results indicate that the deviation of the ratio with respect to unity is smaller than 1% in the whole p_{T} range. Finally, a systematic uncertainty of 1% is conservatively assigned to the whole p_{T} range.

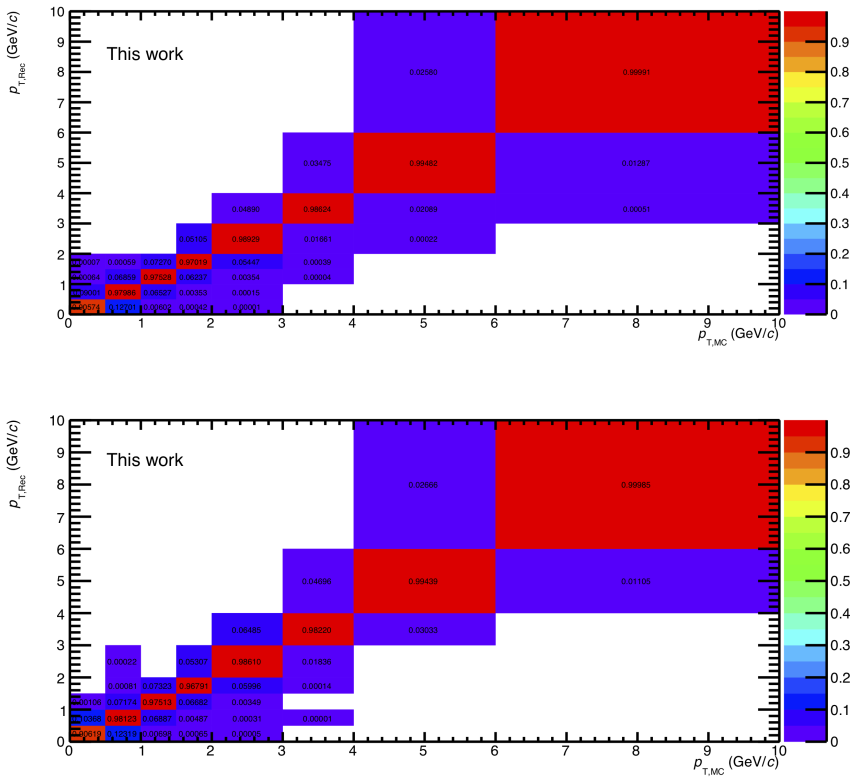

Figure B.2: $p_{\mathrm{T,Gen}}$, $p_{\mathrm{T,Rec}}$ distribution of muon tracks estimated from MC simulations with the DPMJET event generator and GEANT4 transport code in p–Pb (top) and Pb–p (bottom) collisions, each bin is normalized so that the sum of each row is equal to unity.

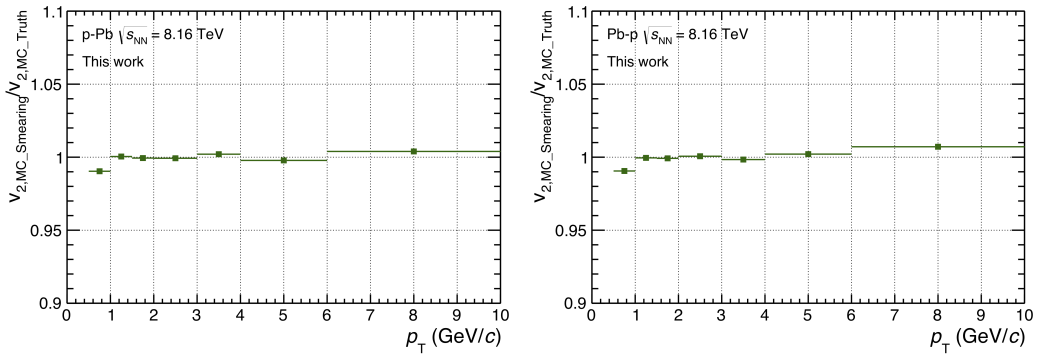

Figure B.3: Resolution effect on the muon v_2 estimated in p–Pb (left) and Pb–p (right) collisions with MC simulations.

Appendix C

Non-uniform Acceptance in the Two-particle Cumulant Method

The procedure to correct the non-uniform acceptance (NUA) is described in Sec. 5.3.1. The correction factor is calculated from the event-averaged φ distribution and a uniform φ distribution can be obtained after the NUA correction is applied. The NUA effects may vary with the trigger selections, multiplicity classes, Z_{vertex} and even the dead zones[1] of the detectors. Similar NUA corrections are applied for all cases and the related checks are summarized hereafter.

Trigger and Multiplicity Dependence of NUA

Figure C.1 shows the ratio of the SPD tracklet φ distribution in MSL (MSH)-triggered events to that in MB-triggered events, for p–Pb and Pb–p collisions. One can see that the effect of different trigger selections on the NUA correction is not negligible. Figure C.2 shows the ratio of the φ distribution of SPD tracklets in different multiplitiy ranges. The deviation from unity indicates that the NUA effects depend slightly on the multiplicity selections. Figure C.3 shows the SPD tracklet φ versus η in $|Z_{\text{vertex}}| < 10$ cm. It indicates that the η dependence of NUA correction should be considered. On the other hand, as shown in Fig. 5.6, a strong correlation is observed between SPD tracklet η and Z_{vertex}, which confirms that NUA effects for SPD tracklets should be also tested in several Z_{vertex} intervals.

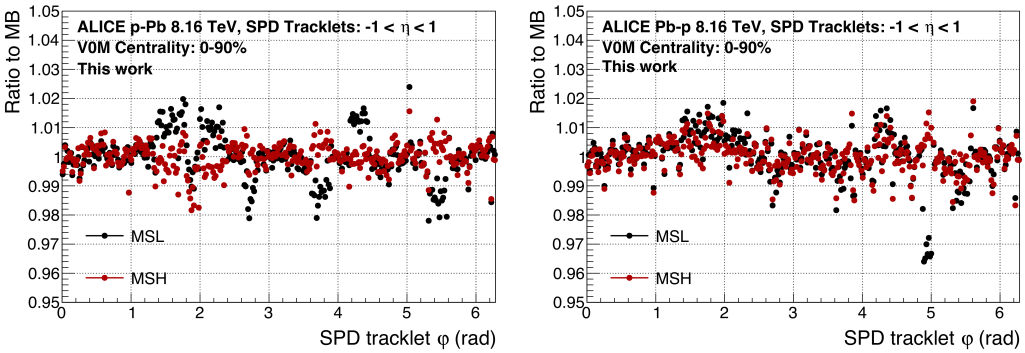

Figure C.1: Ratio of the corrected SPD-tracklet azimuthal angle in MSL and MSH events to that in MB events in p–Pb (left) and Pb–p (right) collisions

[1] If no particle is detected in some regions of the φ acceptance of the detector, these regions are the so-called "dead zones".

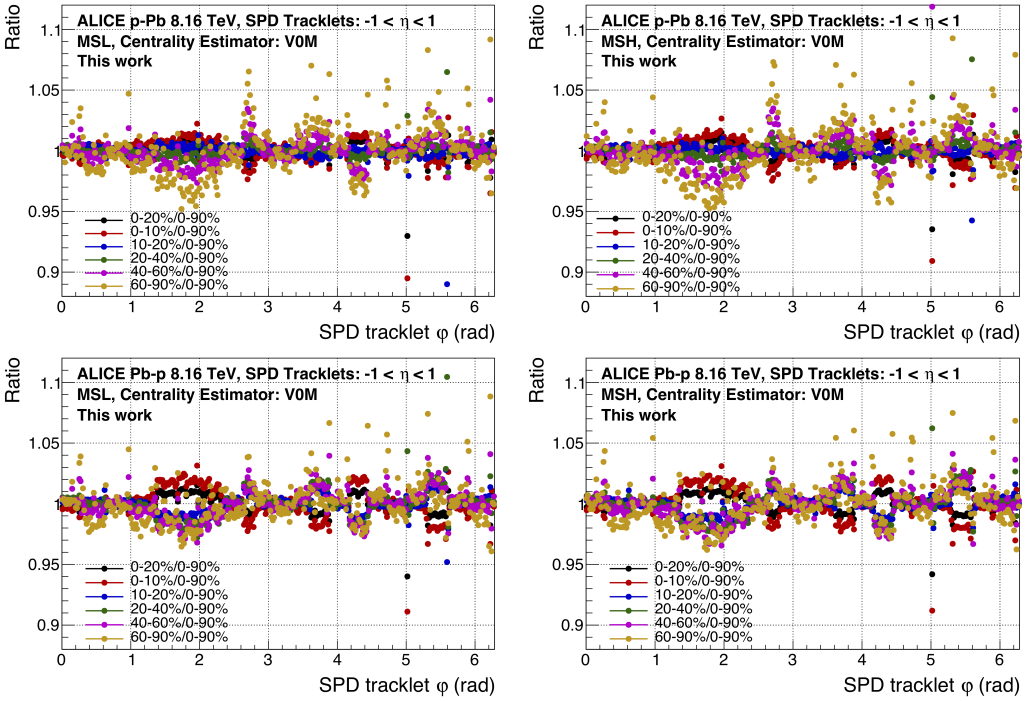

Figure C.2: Ratio between the azimuthal distributions of SPD tracklets in different multiplicity classes with respect to the 0–90% multiplicity class in p–Pb (top) and Pb–p (bottom) collisions for MSL (left) and MSH (right) triggered events.

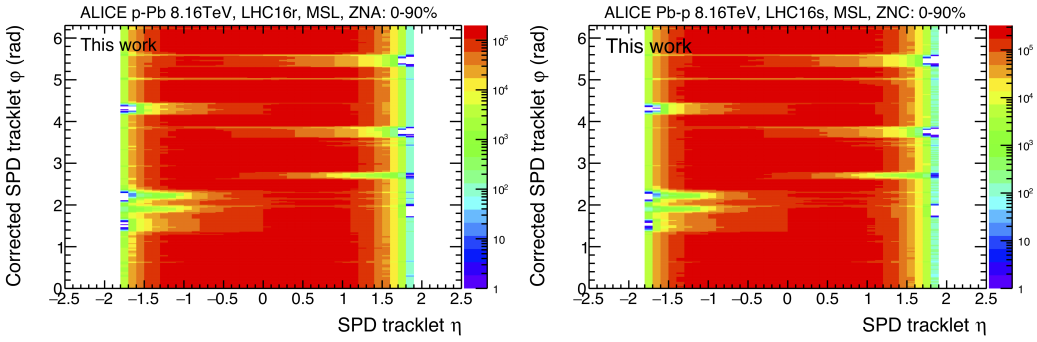

Figure C.3: Variation of the corrected SPD tracklet φ as a function of the SPD tracklet η for MSL-triggered p–Pb (left) and Pb–p (right) collisions with the ZN estimator. The results are shown in the 0–90% multiplicity class.

Dead Zones

Figure C.4 shows the η-φ map of SPD tracklets in each Z_{vertex} interval. It is observed several dead zones in some Z_{vertex} ranges, and some dead zones even exist throughout the whole η range. In this case, it is impossible to correct the φ distribution considering the simultaneous dependence on Z_{vertex} and η. Is it possible if we only applied the φ correction in each Z_{vertex} bin? In order to answer

the question, we have to characterize this effect more precisely by means of a toy MC simulation.

First, we have to find out if the reference flow V_2 has a dependence on Z_{vertex} when the NUA effects are perfectly corrected. As shown in Fig. C.5, with the current SPD tracklet selection strategy, the average η of tracklets slightly depends on Z_{vertex}, and this can be seen mainly in the most central midrapidity region ($|\eta| < 0.2$). On the other hand, since the charged-particle v_2 is believed to has no dependence on rapidity in the midrapidity region [222], the reference flow V_2 as a function of Z_{vertex} is expected to be uniform. Figure C.6 (left) shows the comparison between the reference flow V_2 as a function of Z_{vertex} before and after applying the Z_{vertex}-dependent NUA corrections. Compared to the V_2 results obtained without applying the NUA corrections, the V_2 magnitude is reduced after correction and its distribution is uniform, except for $Z_{\text{vertex}} < -3$ cm, which is attributed to the disabled NUA corrections. Figure C.7 shows the φ distribution with different Z_{vertex} selections before and after the NUA corrections, which indicates that the φ distribution can be well corrected in most of Z_{vertex} intervals, while in some Z_{vertex} intervals the correction failed, e.g. $-10 < Z_{\text{vertex}} < -3$ cm and $5 < Z_{\text{vertex}} < 10$ cm. This is expected since in these intervals all particles with a given φ are not measured. Finally, considering that an uniform φ distribution and V_2 distribution should be obtained after the NUA corrections, only the events in $-3 < Z_{\text{vertex}} < 5$ cm are selected in this analysis.

The effect of the NUA is also tested with a toy MC. Particles are simulated at generated level with a given V_2, and all these particles can be detected in a perfect detector, i.e. w/o dead zones and NUA. The φ distribution of the particles with V_2 is

$$\frac{\mathrm{dN}}{\mathrm{d}\varphi} \sim 1 + 2V_2\cos(2(\varphi - \Psi_2)), \tag{C.1}$$

where the Ψ_2 is the azimuthal angle of the symmetry plane which is sampling from a uniform distribution. Thus, for a given Z_{vertex} interval, the number of particles is the sampling of the distribution of SPD tracklets. The φ of each particle is sampled from Eq. C.1 and the η is sampled from a uniform distribution in the acceptance of the SPD (-1.5 $< \eta <$ 1.5) used in data. Then all particles are analyzed and it is checked which particle is located in the dead zone of the $\eta - \varphi$ map shown in Fig. C.4. If this is the case, this particle is rejected, otherwise the particle is used to calculate the Q-vector and obtain V_2, which is labeled as the "V_2 with dead zones". After generating 10000 events in each Z_{vertex} interval, we can get V_2 as a function of Z_{vertex}, as shown in Fig. C.6 (right). The V_2 with dead zones is surprisingly consistent with the V_2 without NUA correction shown in Fig. C.6 (left). It indicates that the detector effects are perfectly reproduced in this MC simulation, and the NUA correction performed as expected.

Transverse Momentum Dependence of NUA

The NUA correction for muon tracks is essential before the calculation of differential cumulants. Except for the multiplicity and trigger dependence of the NUA

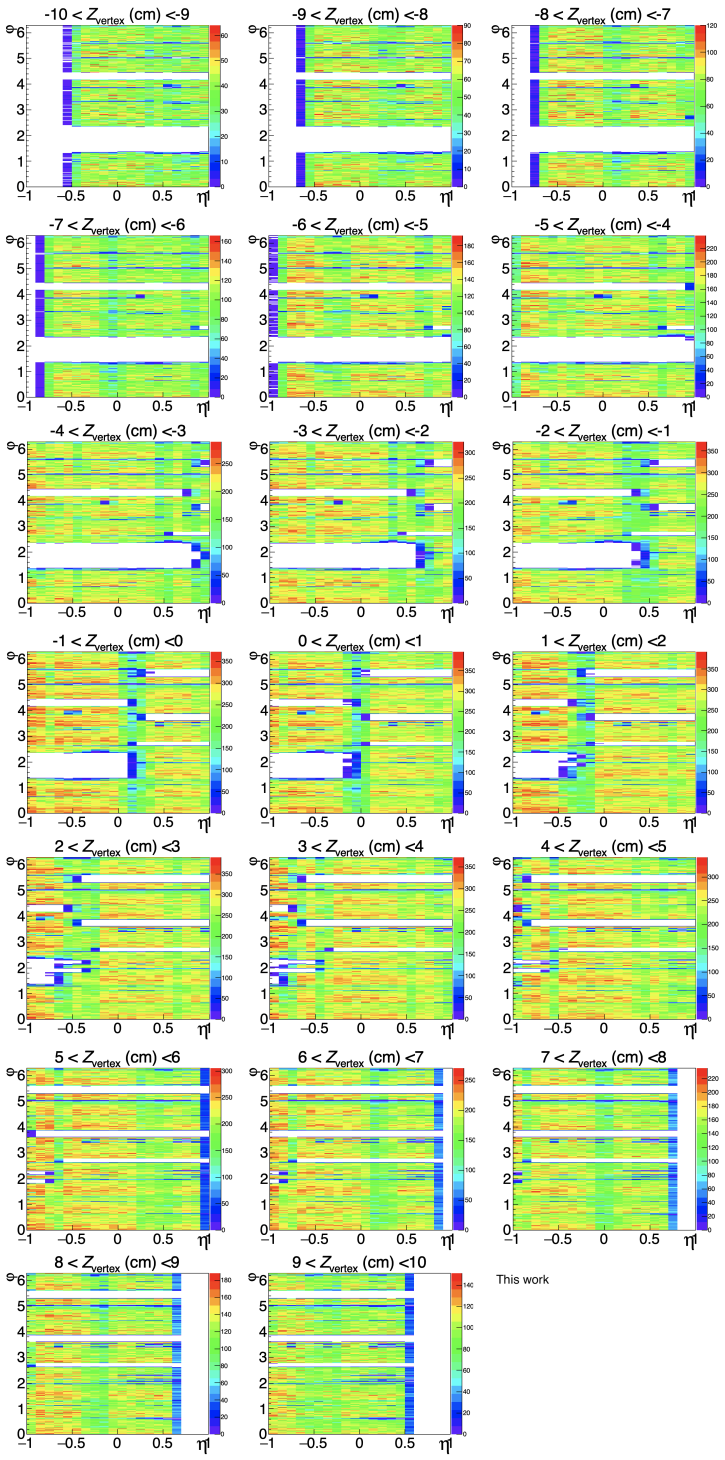

Figure C.4: SPD tracklet η-φ map (η as x-axis, φ as y-axis) in different Z_{vertex} bins for MSL-triggered events in the 0–20% high-multiplicity p–Pb collisions selected with the V0M estimator.

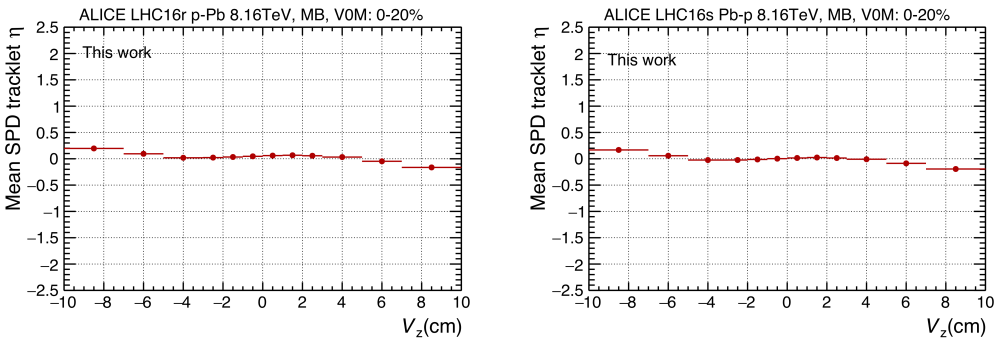

Figure C.5: The average η of SPD tracklets as a function of Z_{vertex} in p–Pb (left) and Pb–p (right) collisions.

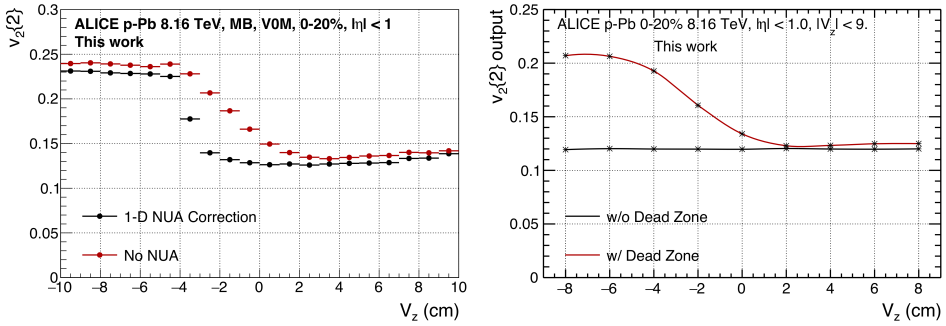

Figure C.6: Left: reference flow V_2 as a function of Z_{vertex} before (red plots) and after (black plots) the NUA corrections are applied. Right: comparison between the reference flow V_2 with and without dead zones in the toy MC.

correction already discussed for SPD tracklets, the p_{T} dependence of NUA correction also needs to be investigated due to the different p_{T} threshold of MSL and MSH triggers. Figure C.8 shows the ratio of the φ distribution within different p_{T} intervals with respect to that in $p_{\text{T}} > 2$ GeV/c and $p_{\text{T}} > 4.5$ GeV/c intervals. It is observed that for MSL-triggered events the p_{T} dependence cannot be ignored for $p_{\text{T}} < 2$ GeV/c, and for MSH-triggered events it has to be considered for $p_{\text{T}} < 4.5$ GeV/c which is expected since the p_{T} trigger threshold for MSH is about 4.2 GeV/c. The same results obtained after the NUA correction are shown in Fig. C.9 and Fig. C.10. As expected, the azimuthal distribution is uniform after such corrections.

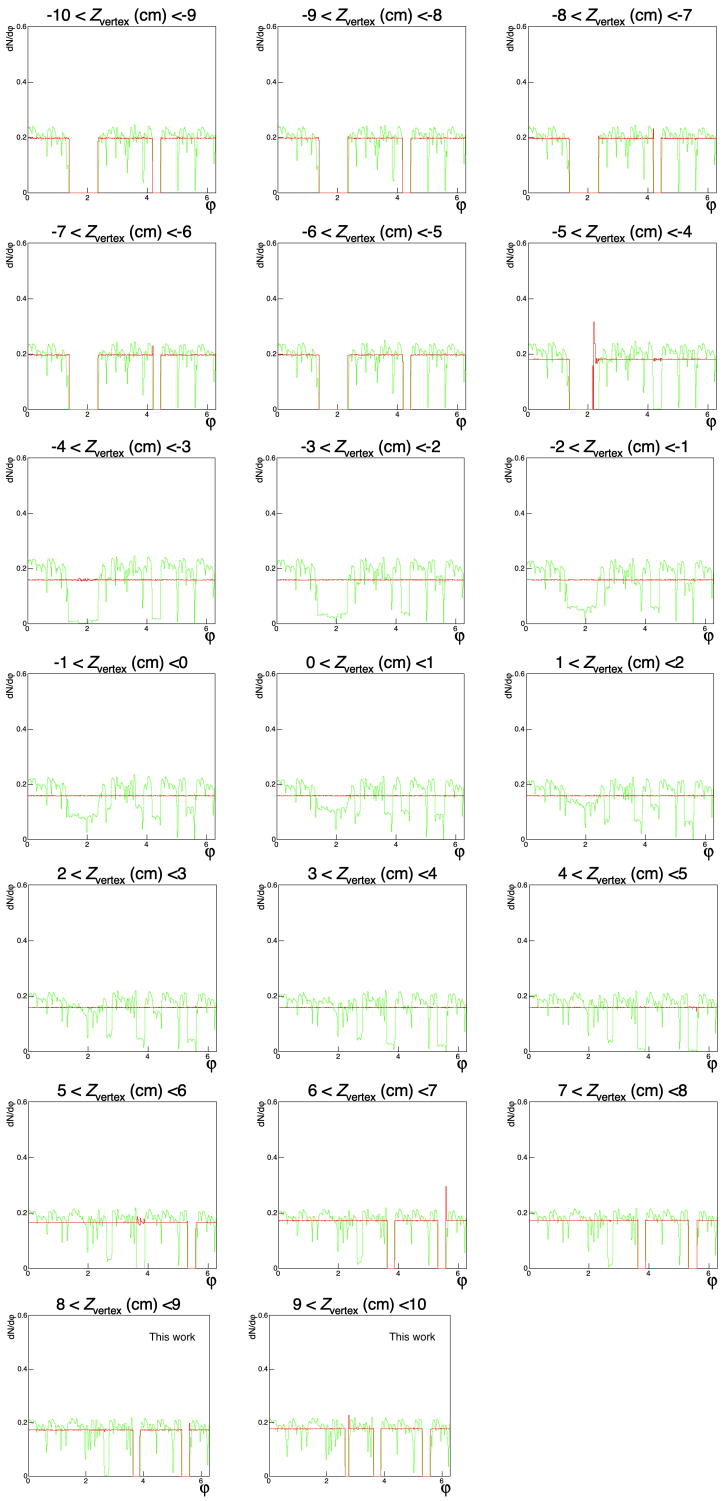

Figure C.7: The φ distribution of SPD tracklets before (green lines) and after (red lines) the NUA correction. The same Z_{vertex} intervals as in Fig. C.4 are employed.

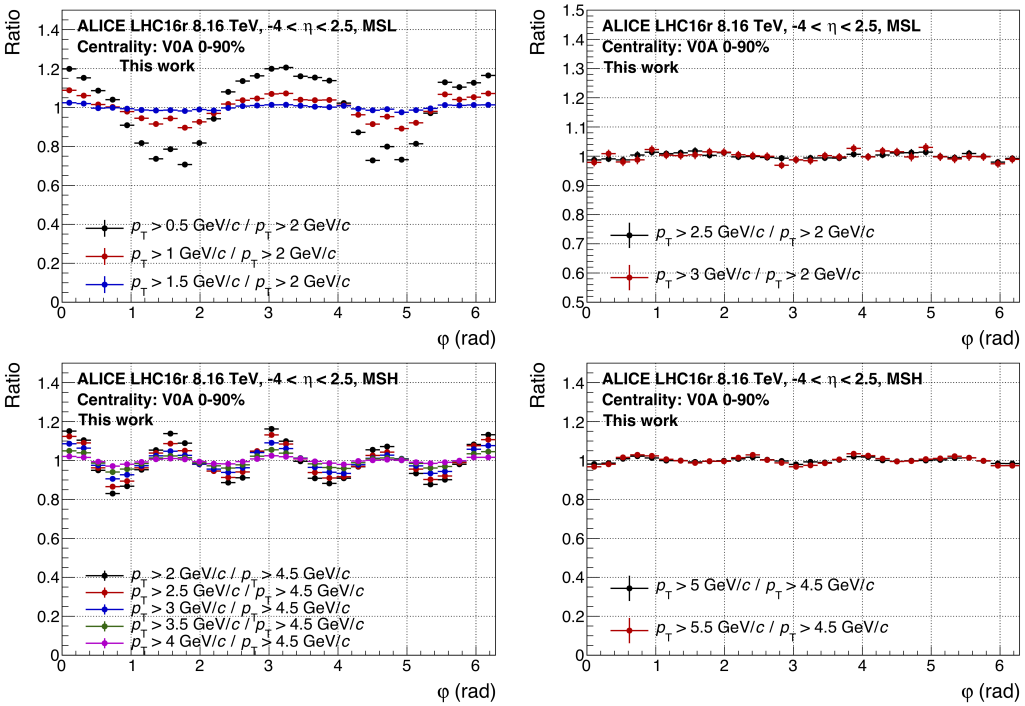

Figure C.8: Ratio of the φ distribution of the muon tracks in various p_{T} intervals with respect to that in $p_{\mathrm{T}} > 2$ GeV/c and $p_{\mathrm{T}} > 4.5$ GeV/c intervals for MSL- (top) and MSH-triggered (bottom) events in 0–90% p–Pb collisions.

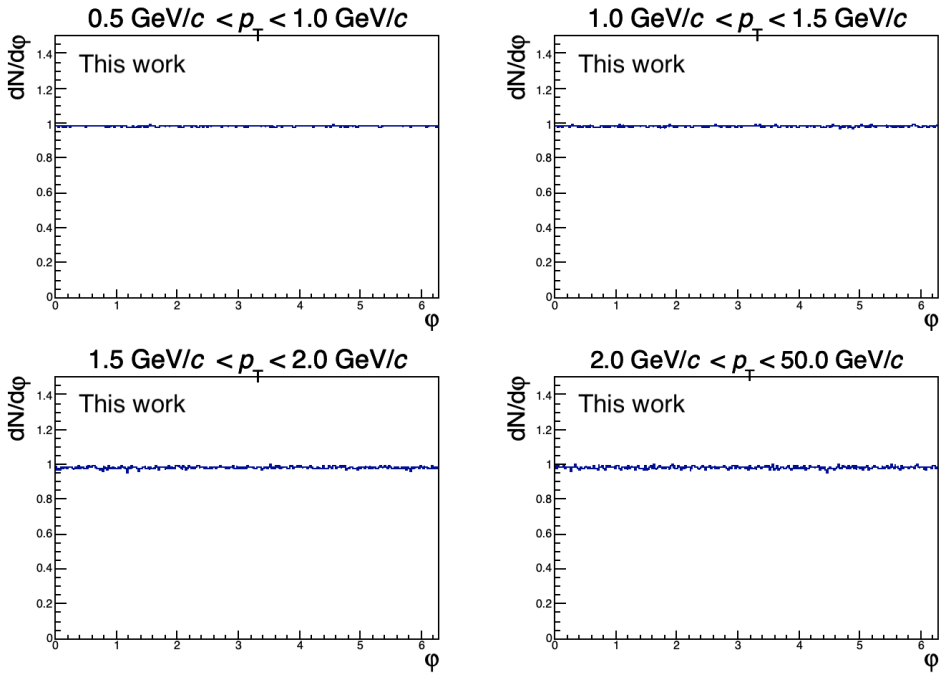

Figure C.9: Muon azimuthal angle φ for MSL-triggered events after the NUA correction in various p_{T} intervals is applied.

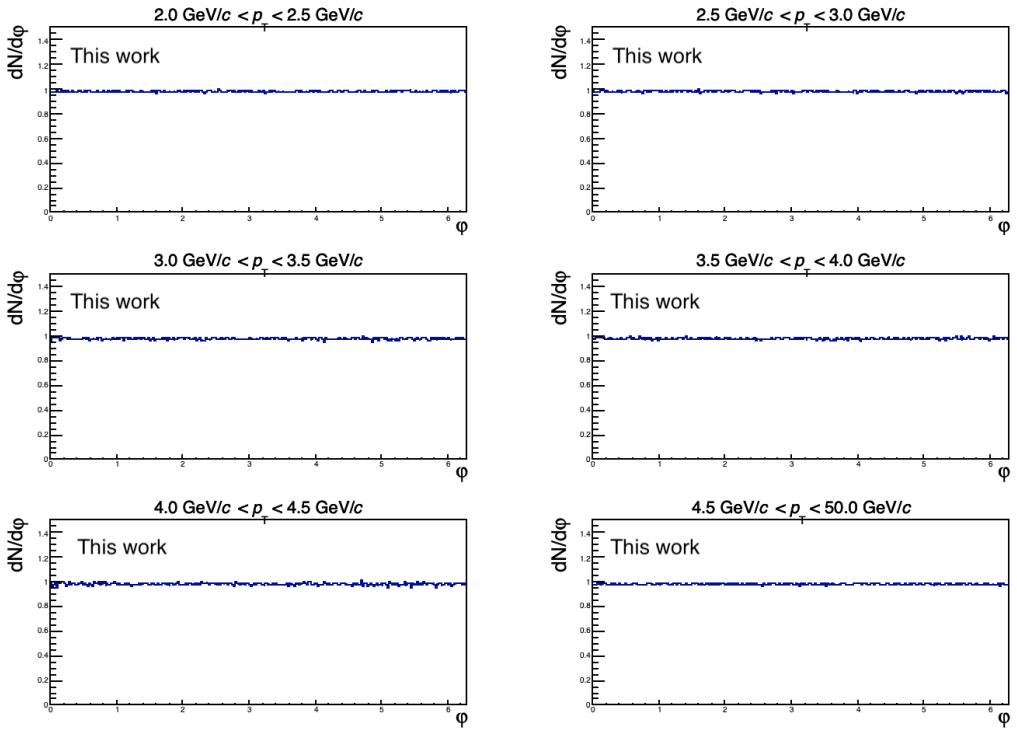

Figure C.10: Muon azimuthal angle φ for MSH-triggered events after the NUA correction in various p_{T} intervals is applied.

Appendix D

The Rivetization of the Measurement of Muons from Heavy-flavour Hadron Decays in pp Collisions at 7 TeV with ALICE

A Short Introduction to RIVET

The experiments at particle colliders (e.g. the LHC) provide many measurements concerning final-state particles, which range from relatively simple production cross sections, to the complicated multiple-differential observables such as the nuclear modification factor, anisotropic flow [223]. In order to understand the underlying physics of these measurements, the results obtained from these measurements need to be compared to theoretical models (e.g.PYTHIA [175] and EPOS-LHC [224]), which aim to generate full events to reproduce the collisions observed by experiments. With the development of these event generators, more and more new model components are added to improve the existing agreement with some results, while some of them may compromise existing agreement with other results. To overcome this challenge, numerous comparisons between published experimental results and models are needed [225].

Robust Independent Validation of Experiment and Theory (RIVET) is such a generator-agnostic framework to provide an universal way to reproduce the experimental results based on the output of Monte Carlo event generators. A set of tools to compute physics objects with robust and standard definitions and an extensive library of analyses are implemented in this framework, and the direct comparison between data and model can be straightforward [223]. Figure D.1 shows how RIVET connects the experimental analyses to theory in a typical physics program. One can see that the comparisons between experimental results and models performed with the RIVET analysis are back loop to the phenomenological models. This type of feedback loop is widely used for development of Monte-Carlo event generators, as well as their validation and tuning [225–227]. Besides, RIVET is widely used by the LHC experiments regarded as a part of their analysis and interpretation toolkit [228–230], and also in studies for future experiments [231, 232]. It has also been used for development of new analysis techniques including for instance machine

learning, jet substructure, pile-up suppression [233, 234].

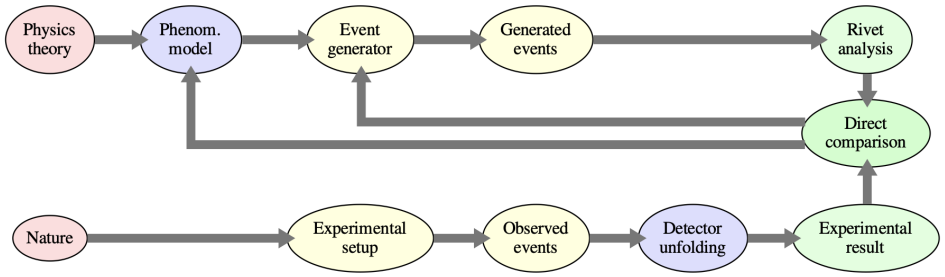

Figure D.1: Outline of how RIVET connects experimental analyses to theory and validation, with the typical workflow of a physics program. The figure is extracted from [225].

The core of the RIVET framework is a C++ shared library, supplemented C++ plugin libraries containing abundant ($\sim$ 1000) published measurements performed in particle colliders, which are regularly updated in the RIVET webpage [235]. The events simulated by generators are stored in the HepMC format [236], which are used as the inputs of a RIVET analysis. The RIVET framework read these inputs and then reproduces the selected analysis as well as produces comparison plots to the published data, which are stored in files with a particular format, so-called Yoda file [223]. For the execution of a RIVET analysis, the projection is an important concept. A projection is a stateful code object inheriting from the `RIVET::Projection` class, which is used to extract a set of specific physical observables from generated events, e.g. the final-state particles meeting specific kinematic or particle identification requirements, event centralities, Q-vectors... These implementations need to be repeated for each particle in data analysis, while in RIVET, they can be easily achieved by calling pre-defined projections. In addition, the projections can be reused across analyses from different experiments, which help to centralise the processing and calculation of common physics objects for MC simulations.

As shown in Fig. D.2, a RIVET analysis can be split into three parts, implemented as separate member functions in an analysis class:

- **Initialization** The method `init()` is run once at the beginning, it is used to set up the analysis. In this method, the histograms can be initialized with appropriate types and binning via `RIVET::book()` function. For the implementation on a published analysis, the better way to book the histograms is to let RIVET take the histogram details from the reference data directly. Besides, all projections required for the analysis can be defined here.

- **Analysis** The method `analyze(const RIVET::Event&)` is run for each event during the execution loop. That concerns the calculations of variables at each event. The main analysis procedures are performed here with the applications of projections and the histograms are filled.

- **Finalization** The method `finalize()` is called once at the end of the anal-

ysis. The users can apply the normalization or scaling of histograms here. Observables averaged over all events are also computed at this stage. This step is important for merging the physics quantities obtained from multiple Monte-Carlo runs correctly, for instance the production cross section, and the R_{AA}.

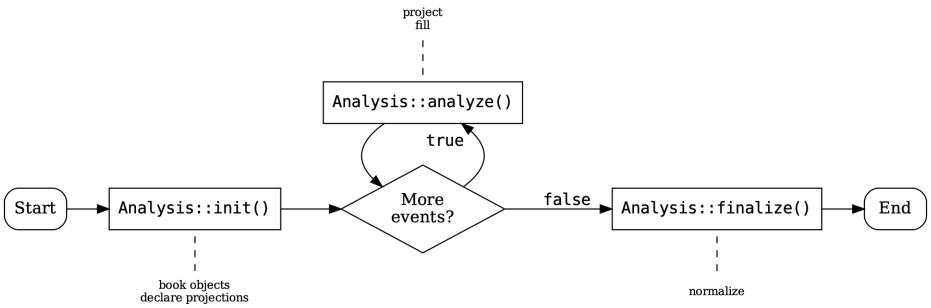

Figure D.2: The illustration of the RIVET analysis class. The figure is taken from [225].

The Development of RIVET-plugin

During the LHC Run 1 and Run 2, many excellent measurements of leptons from heavy-flavour hadron decays in both large and small collision systems with ALICE were performed. They provided new insights in the understandings of the production of heavy quarks and their interactions with the QGP medium [56, 181, 182, 187]. However, there is no any released Rivet-plugins related to the measurements of leptons from heavy-flavour hadron decays with ALICE. In order to fill the gap in the field, we developed the RIVET-plugin (so-called **rivetization**) for the measurement of muons from heavy-flavour hadron decays in pp collisions at $\sqrt{s_{\mathrm{NN}}} = 7$ TeV with ALICE.

This measurement was published in [237]. Figure D.3 shows the p_{T}-differential and rapidity-differential production cross section of muons from heavy-flavour hadron decays in pp collisions at 7 TeV. In addition, the p_{T}-differential production cross section of muons from heavy flavour decays is also measured in five rapidity regions, as shown in Fig. D.4. As described in [237], the muons from charm and beauty hadron decays are obtained after the subtraction of the background muons from the inclusive muons measured in muon spectrometer. The estimation of background muons is based on the PYTHIA simulations [226], as shown in Fig. D.5. Three main background contributions are subtracted:

- **Decay muons** The muons from primary $\pi^{\pm}$ and $\mathrm{K}^{\pm}$ dacays (the main contribution) and other meson and baryon decays (e.g. J/Ψ);
- **Secondary muons** The muons from secondary light-hadron decays produced inside the front absorber.

- **Hadrons** The punch-through hadrons and secondary hadrons escaping the front absorber and crossing the tracking chambers, which are wrongly reconstructed as muons.

The muons from $W^{\pm}$ and Z^0 decays, which cannot be neglected for $p_T \gtrsim 15$ GeV/c, are not considered since the p_T range of interest is limited to 12 GeV/c in this analysis.

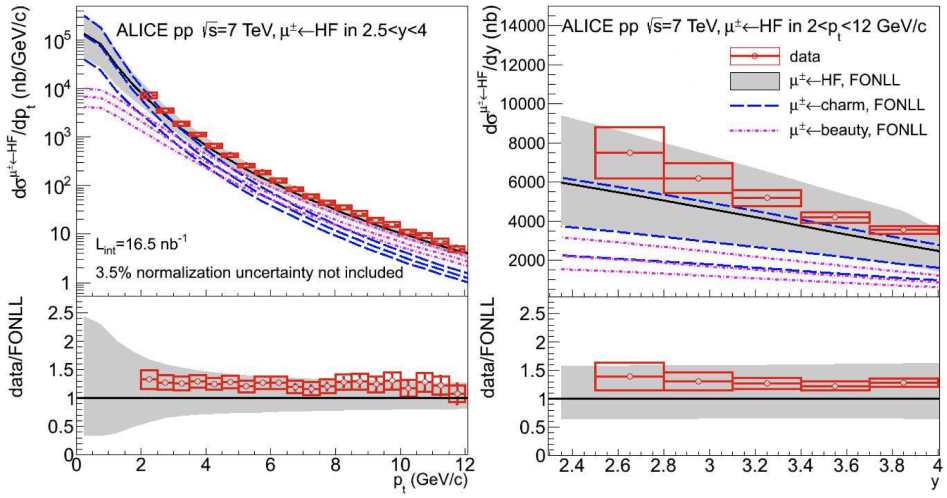

Figure D.3: Left: p_T-differential production cross section of muons from heavy flavour decays in the rapidity range 2.5< y <4. Right: rapidity-differential production cross section of muons from heavy flavour decays, in the range 2< p_T <12 GeV/c. The figures are extracted from [237].

In order to reproduce the measurements shown in Fig. D.3 and Fig. D.4 with the RIVET framework, we need to develop the equivalent procedures applied to the data analysis within the RIVET framework. The first step is to extract the final state muons at forward rapidity (2.5< y <4) in the p_T interval 2< p_T < 12 GeV/c. An `IdentifiedFinalState` projection is defined, and seven histograms which have same binning as that in data are booked in the `init()` method. The second step is to check the mother particles of each muon produced in each event. Only muons from charm or beauty hadron decays are selected, then the corresponding histograms are filled. The final step is to normalize the histograms to the cross section with the unit nanobarn, in order to be consistent with Fig. D.3 and Fig. D.4. The code about the `analyze()` function is shown in Fig. D.6.

In order to test the RIVET-plugin, 160 million events generated with the PYTHIA 8 event generator (tune Monash2013) [226] are used as the inputs of the RIVET analysis. Figures D.7 and D.8 show the comparison between data and RIVET results. One can see that the production cross section of muons from heavy-flavour hadron decays obtained in PYTHIA 8 with the RIVET framework has same trend as that in data, while the magnitude in PYTHIA 8 is systematically higher, which is also observed in previous measurements from ATLAS [238].

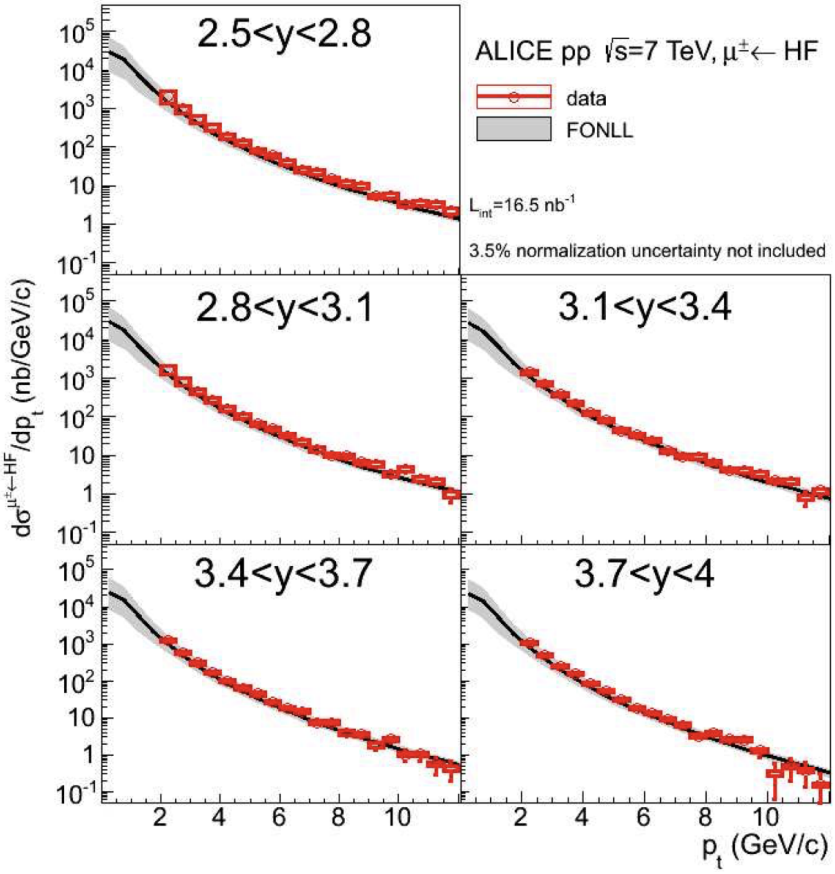

Figure D.4: p_{T}-differential production cross section of muons from heavy flavour decays in five rapidity regions. Figure is extracted from [237].

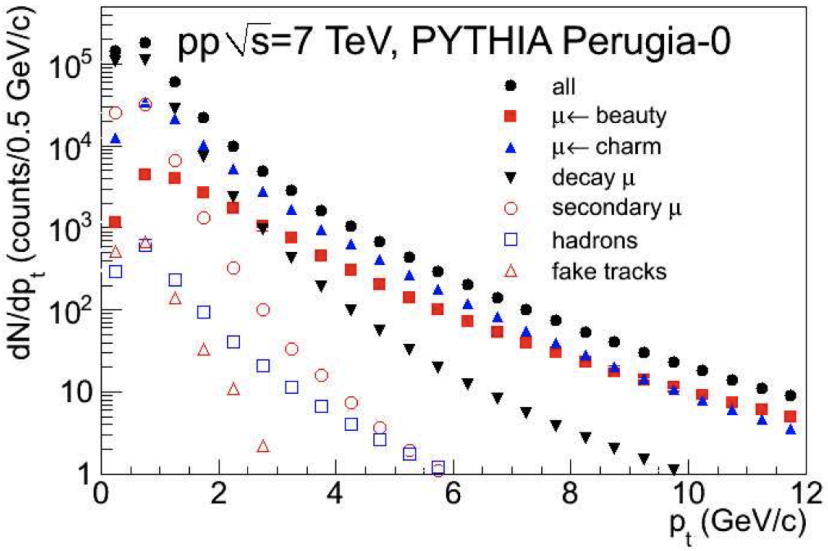

Figure D.5: Transverse momentum distribution of reconstructed tracks in the muon spectrometer obtained from a PYTHIA simulation of pp collisions at 7 TeV. Figure is extracted from [237].

In addition, two further cross checks are implemented in the RIVET analysis. The first one is the calculation of the cross section of muons from light-flavour hadron decays in RIVET analysis, and the comparison to the PYHTHA 8 simulation shown in Fig. D.5. In this case, only muons from primary light hadron (e.g. the pions and kaons) decays are selected. Figure D.9 (left) shows the p_{T}-differential production cross section of muons from heavy-flavour and light-flavour hadron decays. One can notice that both the magnitude and trends are comparable to those in PYTHIA 8 simulation, and previously evidenced in the PYTHIA 6 simulation [237]. The second check is the calculation of the production cross section of muons from charm- and beauty-hadron decays in the RIVET analysis, as shown in Fig. D.9. One can see that the muons from charm-hadron decays dominate at $p_{\mathrm{T}} \lesssim 4$ GeV/c region, while in the $p_{\mathrm{T}} \gtrsim 4$ GeV/c region, the muons from beauty-hadron decays are the main contribution to the yield of muons from heavy-flavour hadron decays. A similar behaviour is observed in FONLL calculations shown in Fig. D.3 (left). Based on these cross checks, we can claim that the RIVET-plugin that we developed is valid to extract the muons from heavy-flavour hadron decays in pp collisions at 7 TeV with ALICE.

Outlook

The first rivetization of the measurement of the production of leptons from heavy-flavour hadrons decays with ALICE has been successfully implemented through my service work. It creates an example for the separation of muons from heavy-flavour and light-flavour hadron decays. This first rivetization will be also

```
void analyze(const Event& event) {
  const FinalState& muons      = apply<FinalState>(event, "IFS");
  bool IsFromHF; bool IsFromLight;
  if (muons.empty()) vetoEvent;
  for (const Particle& p_muon : muons.particles()) {

    ConstGenParticlePtr pmother = p_muon.genParticle();
    ConstGenVertexPtr ivertex = pmother->production_vertex();
    IsFromHF = false; IsFromLight = false;

    while (ivertex) {
      vector<ConstGenParticlePtr> inparts = HepMCUtils::particles(ivertex, Relatives::PARENTS);
      int n_inparts = inparts.size();
      if (n_inparts < 1) break;
      pmother = inparts[0];
      int mother_pid = abs(pmother->pdg_id());

      int flv = 0;
      if(mother_pid == 2212) break; // They are incoming protons
        if(mother_pid == 15) {IsFromHF = false; break;}  // They Tau parents
        if(mother_pid == 443) {IsFromHF = false; break;}  // They are JPsai
      if(mother_pid >= 100 && mother_pid < 1000)
      {
       flv = mother_pid/100%10;
      }
      else if(mother_pid >= 1000 && mother_pid < 10000)
      {
       flv = mother_pid/1000%10;
      }
      else
      {
       break;                      // They are quarks and gluons
      }
      if(flv < 4)              {IsFromLight = true; /*cout<< mother_pid << endl;*/}
      if(flv == 4 || flv == 5) {IsFromHF = true; /*cout<< mother_pid << endl;*/}
      ivertex = pmother->production_vertex();
    }

    if(IsFromHF && !IsFromLight)
    {
     //cout << "HF" << endl;
     _histPtHFmuon->fill(p_muon.pT()*GeV);
     _histRapHFmuon->fill(p_muon.rap()*GeV);

     if(p_muon.rap()< 2.8)      _histPtHFmuon_Rap1->fill(p_muon.pT()*GeV);
     else if(p_muon.rap()< 3.1) _histPtHFmuon_Rap2->fill(p_muon.pT()*GeV);
     else if(p_muon.rap()< 3.4) _histPtHFmuon_Rap3->fill(p_muon.pT()*GeV);
     else if(p_muon.rap()< 3.7) _histPtHFmuon_Rap4->fill(p_muon.pT()*GeV);
     else                       _histPtHFmuon_Rap5->fill(p_muon.pT()*GeV);
    }
  }
}
```

Figure D.6: A part of code of the RIVET analysis.

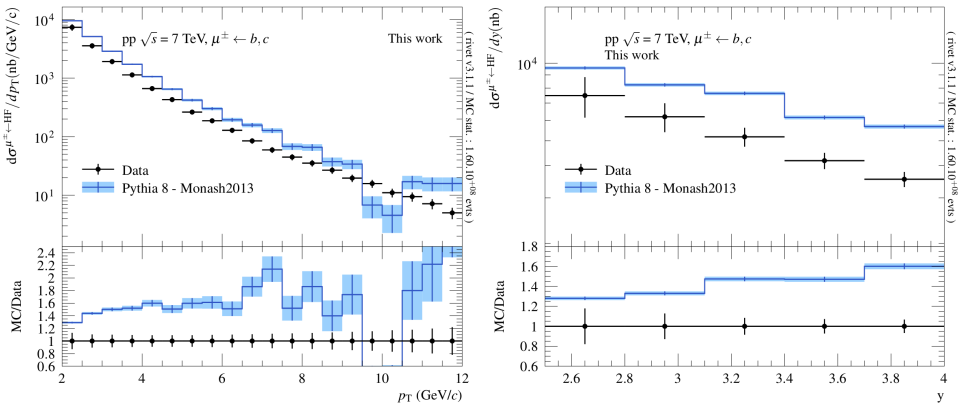

Figure D.7: The comparison of p_{T}- (left) and rapidity-differential (right) production cross section of muons from heavy-flavour hadron decays between the data and PYTHIA 8. The data points are from [237].

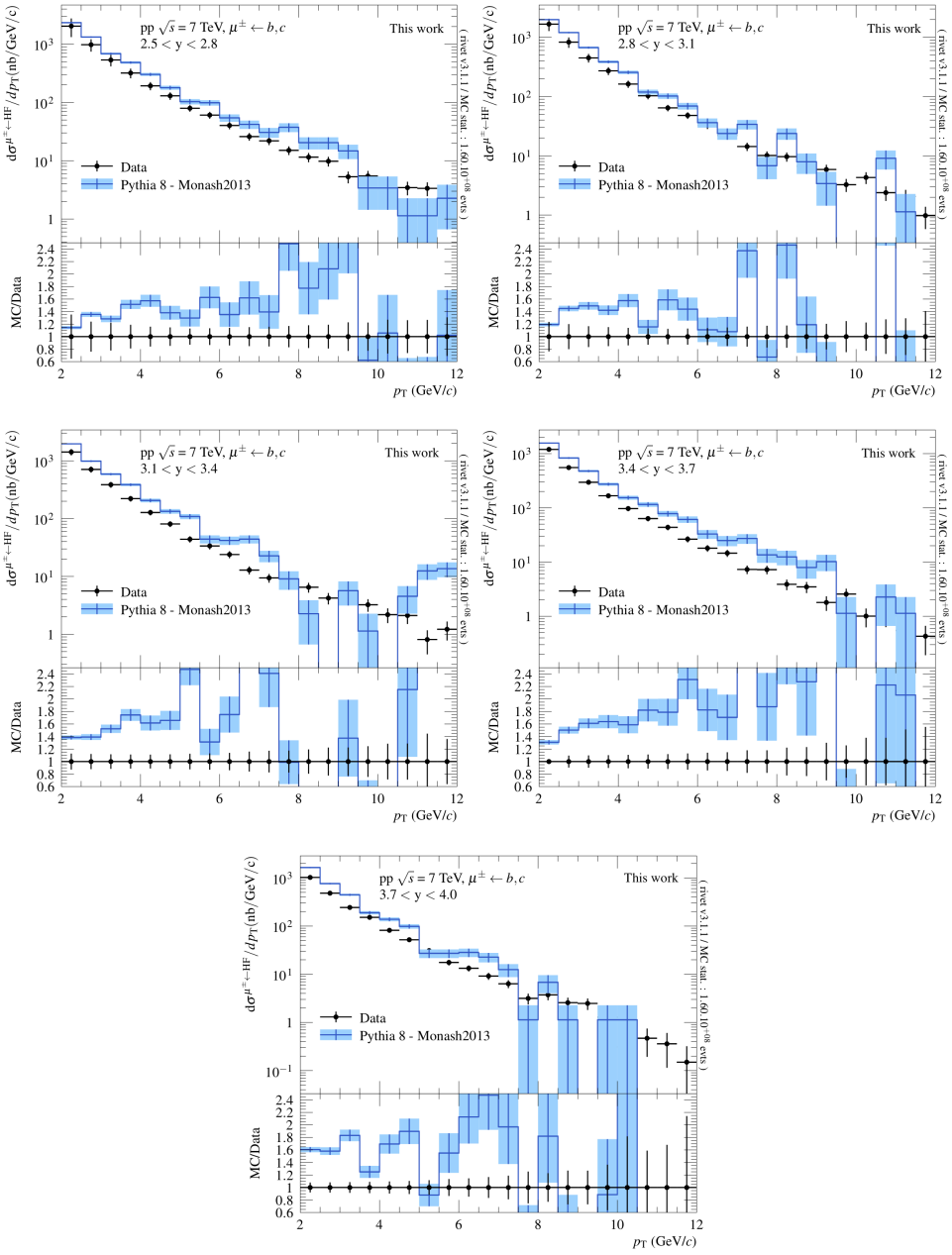

Figure D.8: The comparison of p_T-differential production cross section of muons from heavy-flavour hadron decays in five rapidity regions between the data and PYTHIA8. The data points are from [237].

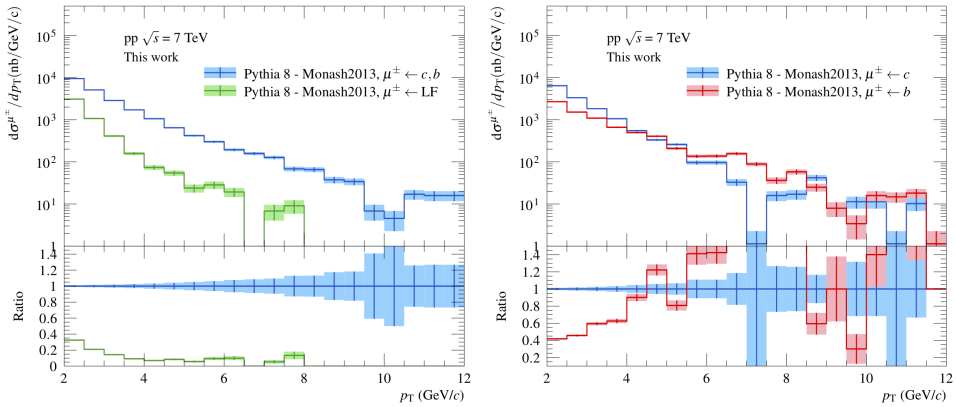

Figure D.9: Left: the p_{T}-differential production cross section of muons from heavy-flavour hadron and light-flavour hadron decays in PYTHIA 8 with RIVET analysis. Right: the p_{T}-differential production cross section of muons from beauty-hadron and charm-hadron decays in PYTHIA 8 with RIVET analysis.

used as a pilot for the development of more complicated RIVET-plugins in the future, e.g. the multi-differential measurements of R_{AA} and v_2 of muons and electrons from heavy-flavour hadron decays in various collision systems.

Bibliography

[1] J. M.A.F.R.S., "Xl. cathode rays", *The London, Edinburgh, and Dublin Philosophical Magazine and Journal of Science* **44** no. 269, (1897) 293–316. https://doi.org/10.1080/14786449708621070. (Cited on page 1.)

[2] **ATLAS** Collaboration, G. Aad *et al.*, "Observation of a new particle in the search for the Standard Model Higgs boson with the ATLAS detector at the LHC", *Phys. Lett. B* **716** (2012) 1–29, arXiv:1207.7214 [hep-ex]. (Cited on pages 1 and 51.)

[3] **CMS** Collaboration, S. Chatrchyan *et al.*, "Observation of a New Boson at a Mass of 125 GeV with the CMS Experiment at the LHC", *Phys. Lett. B* **716** (2012) 30–61, arXiv:1207.7235 [hep-ex]. (Cited on pages 1 and 51.)

[4] W. Heisenberg, "Über quantentheoretische umdeutung kinematischer und mechanischer beziehungen.", *Zeitschrift für Physik* **33** 879–893. (Cited on page 1.)

[5] M. Born and P. Jordan, "Zur quantenmechanik", *Zeitschrift für Physik* **34** 858–888. (Cited on page 1.)

[6] M. Born, W. Heisenberg, and P. Jordan, "Zur quantenmechanik. ii.", *Zeitschrift für Physik* **35** 557–615. (Cited on page 1.)

[7] A. Einstein, "Zur Elektrodynamik bewegter Körper. (German)[On the electrodynamics of moving bodies]", *Annalen der Physik* **322** no. 10, (1905) 891–921. (Cited on page 1.)

[8] J. Wilkinson, "Analysis of D^0 and D^{*+}-meson production in pp and p–Pb collisions with ALICE at the LHC", May, 2016. http://cds.cern.ch/record/2214133. Presented 29 Jul 2016. (Cited on pages xxv and 2.)

[9] C. Nave, "The color force", *HyperPhysics. Georgia State University, Department of Physics. Retrieved 2012-04-02* . http://hyperphysics.phy-astr.gsu.edu/hbase/Forces/color.html. (Cited on page 2.)

[10] P. W. Higgs, "Broken symmetries and the masses of gauge bosons", *Phys. Rev. Lett.* **13** (Oct, 1964) 508–509. https://link.aps.org/doi/10.1103/PhysRevLett.13.508. (Cited on page 3.)

[11] W. Commons, "Standard model of elementary particles", 2021. https://commons.wikimedia.org/w/index.php?title=File:Standard_Model_of_Elementary_Particles.svg&oldid=609231940. (Cited on pages xi and 3.)

[12] K. N. and, "Review of particle physics", *Journal of Physics G: Nuclear and Particle Physics* **37** no. 7A, (Jul, 2010) 075021. (Cited on page 3.)

[13] A. Festanti, "Measurement of the D^0 meson production in Pb–Pb and p–Pb collisions with the ALICE experiment at the LHC.", Feb, 2016. http://cds.cern.ch/record/2057663. (Cited on pages xi, 4 and 10.)

[14] **Particle Data Group** Collaboration, K. A. Olive *et al.*, "Review of Particle Physics", *Chin. Phys. C* **38** (2014) 090001. (Cited on pages xi and 5.)

[15] H. D. Politzer, "Asymptotic Freedom: An Approach to Strong Interactions", *Phys. Rept.* **14** (1974) 129–180. (Cited on page 5.)

[16] K. G. Wilson, "Confinement of quarks", *Phys. Rev. D* **10** (Oct, 1974) 2445–2459. https://link.aps.org/doi/10.1103/PhysRevD.10.2445. (Cited on page 6.)

[17] **HotQCD** Collaboration, A. Bazavov *et al.*, "Equation of state in (2+1)-flavor QCD", *Phys. Rev. D* **90** (2014) 094503, arXiv:1407.6387 [hep-lat]. (Cited on page 6.)

[18] H. Caines, "The search for critical behavior and other features of the qcd phase diagram - current status and future prospects", *Nuclear Physics A* **967** (2017) 121–128. The 26th International Conference on Ultra-relativistic Nucleus-Nucleus Collisions: Quark Matter 2017. (Cited on pages xi and 7.)

[19] J. Schukraft, "Little bang at big accelerators: Heavy ion physics from AGS to LHC", *AIP Conf. Proc.* **531** no. 1, (2000) 3–15. (Cited on page 7.)

[20] C. Cockell, "Astrobiology and the Search for Extraterrestrial Intelligence", 2020. https://www.my-mooc.com/zh/mooc/astrobiology-and-the-search-for-extraterrestrial-life/. (Cited on pages xi and 7.)

[21] M. L. Miller, K. Reygers, S. J. Sanders, and P. Steinberg, "Glauber modeling in high energy nuclear collisions", *Ann. Rev. Nucl. Part. Sci.* **57** (2007) 205–243, arXiv:nucl-ex/0701025. (Cited on pages xi, 8, 9, 10 and 75.)

[22] M. Strickland, "Anisotropic Hydrodynamics: Three lectures", *Acta Phys. Polon. B* **45** no. 12, (2014) 2355–2394, arXiv:1410.5786 [nucl-th]. (Cited on pages xi, 10 and 11.)

[23] B. Müller, "Investigation of Hot QCD Matter: Theoretical Aspects", *Phys. Scripta T* **158** (2013) 014004, arXiv:1309.7616 [nucl-th]. (Cited on pages xi and 11.)

[24] C. Loizides, "Jet physics in ALICE", 2005. http://cds.cern.ch/record/816827. (Cited on page 12.)

[25] J. W. Cronin, H. J. Frisch, M. J. Shochet, J. P. Boymond, P. A. Piroue, and R. L. Sumner, "Production of Hadrons with Large Transverse Momentum at 200 GeV and 300 GeV.", *Phys. Rev. Lett.* **31** (1973) 1426–1429. (Cited on pages 13 and 31.)

[26] **ALICE** Collaboration, S. Acharya *et al.*, "Z-boson production in p-Pb collisions at $\sqrt{s_{\rm NN}} = 8.16$ TeV and Pb-Pb collisions at $\sqrt{s_{\rm NN}} = 5.02$ TeV", *JHEP* **09** (2020) 076, arXiv:2005.11126 [nucl-ex]. (Cited on page 13.)

[27] **CMS** Collaboration, S. Chatrchyan *et al.*, "Measurement of isolated photon production in pp and Pb–Pb collisions at $\sqrt{s_{\rm NN}} = 2.76$ TeV", *Phys. Lett. B* **710** (2012) 256–277, arXiv:1201.3093 [nucl-ex]. (Cited on page 13.)

[28] **CMS** Collaboration, S. Chatrchyan *et al.*, "Study of W boson production in Pb–Pb and pp collisions at $\sqrt{s_{\rm NN}} = 2.76$ TeV", *Phys. Lett. B* **715** (2012) 66–87, arXiv:1205.6334 [nucl-ex]. (Cited on page 13.)

[29] T. Renk, "Physics probed by the $p_{\rm T}$ dependence of the nuclear suppression factor", *Phys. Rev. C* **88** no. 1, (2013) 014905, arXiv:1302.3710 [hep-ph]. (Cited on pages xi, 13 and 14.)

[30] K. C. Zapp, F. Krauss, and U. A. Wiedemann, "A perturbative framework for jet quenching", *JHEP* **03** (2013) 080, arXiv:1212.1599 [hep-ph]. (Cited on pages xi, 13 and 14.)

[31] **ALICE** Collaboration, S. Acharya *et al.*, "Transverse momentum spectra and nuclear modification factors of charged particles in pp, p–Pb and Pb–Pb collisions at the LHC", *JHEP* **11** (2018) 013, arXiv:1802.09145 [nucl-ex]. (Cited on pages xi, xx, 14, 32, 143, 165 and 166.)

[32] **ALICE** Collaboration, J. Adam *et al.*, "Measurement of jet suppression in central Pb–Pb collisions at $\sqrt{s_{\rm NN}} = 2.76$ TeV", *Phys. Lett. B* **746** (2015) 1–14, arXiv:1502.01689 [nucl-ex]. (Cited on pages xi and 14.)

[33] A. Andronic *et al.*, "Heavy-flavour and quarkonium production in the LHC era: from proton–proton to heavy-ion collisions", *Eur. Phys. J. C* **76** no. 3, (2016) 107, arXiv:1506.03981 [nucl-ex]. (Cited on page 15.)

[34] J. C. Collins, D. E. Soper, and G. Sterman, "Heavy particle production in high-energy hadron collisions", *Nuclear Physics B* **263** no. 1, (1986) 37–60. (Cited on page 15.)

[35] B. A. Kniehl, G. Kramer, I. Schienbein, and H. Spiesberger, "Hadroproduction of D and B mesons in a massive VFNS", *AIP Conf. Proc.* **792** no. 1, (2005) 867–870, arXiv:hep-ph/0507068. (Cited on page 15.)

[36] B. A. Kniehl, G. Kramer, I. Schienbein, and H. Spiesberger, "Collinear subtractions in hadroproduction of heavy quarks", *Eur. Phys. J. C* **41** (2005) 199–212, arXiv:hep-ph/0502194. (Cited on page 15.)

[37] M. Cacciari, M. Greco, and P. Nason, "The p_{T} spectrum in heavy flavor hadroproduction", *JHEP* **05** (1998) 007, arXiv:hep-ph/9803400. (Cited on pages 15, 90, 101, 139 and 140.)

[38] M. Cacciari, S. Frixione, N. Houdeau, M. L. Mangano, P. Nason, and G. Ridolfi, "Theoretical predictions for charm and bottom production at the LHC", *JHEP* **10** (2012) 137, arXiv:1205.6344 [hep-ph]. (Cited on pages 15 and 139.)

[39] **ALICE** Collaboration, B. Abelev *et al.*, "Measurement of electrons from beauty-hadron decays in pp collisions at $\sqrt{s} = 7$ TeV", *Phys. Lett. B* **721** (2013) 13–23, arXiv:1208.1902 [hep-ex]. [Erratum: Phys.Lett.B 763, 507–509 (2016)]. (Cited on page 15.)

[40] M. Cacciari, M. L. Mangano, and P. Nason, "Gluon PDF constraints from the ratio of forward heavy-quark production at the LHC at $\sqrt{s} = 7$ and 13 TeV", *Eur. Phys. J. C* **75** no. 12, (2015) 610, arXiv:1507.06197 [hep-ph]. (Cited on page 16.)

[41] **ALICE** Collaboration, S. Acharya *et al.*, "Measurement of D^0, D^+, D^{*+} and $\mathrm{D}_{\mathrm{s}}^+$ production in pp collisions at $\sqrt{s} = 5.02$ TeV with ALICE", *Eur. Phys. J. C* **79** (Jan, 2019) 388. 32 p, arXiv:1901.07979. https://cds.cern.ch/record/2653801. (Cited on pages xi and 16.)

[42] **ALICE** Collaboration, S. Acharya *et al.*, "Production of muons from heavy-flavour hadron decays in pp collisions at $\sqrt{s} = 5.02$ TeV", *JHEP* **09** (2019) 008, arXiv:1905.07207 [nucl-ex]. (Cited on pages xi, 16, 86, 90, 92, 95 and 96.)

[43] S. Cao, G.-Y. Qin, and S. A. Bass, "Heavy-quark dynamics and hadronization in ultrarelativistic heavy-ion collisions: Collisional versus radiative energy loss", *Phys. Rev. C* **88** (2013) 044907, arXiv:1308.0617 [nucl-th]. (Cited on pages xi, 17, 18 and 21.)

[44] R. Baier, Y. L. Dokshitzer, A. H. Mueller, S. Peigne, and D. Schiff, "Radiative energy loss of high-energy quarks and gluons in a finite volume quark-gluon plasma", *Nucl. Phys. B* **483** (1997) 291–320, arXiv:hep-ph/9607355. (Cited on page 18.)

[45] R. Baier, Y. L. Dokshitzer, A. H. Mueller, S. Peigne, and D. Schiff, "Radiative energy loss and p_{T} broadening of high-energy partons in nuclei", *Nucl. Phys. B* **484** (1997) 265–282, arXiv:hep-ph/9608322. (Cited on page 18.)

[46] M. Djordjevic and M. Gyulassy, "Where is the charm quark energy loss at RHIC?", *Phys. Lett. B* **560** (2003) 37–43, arXiv:nucl-th/0302069. (Cited on page 19.)

[47] Y. L. Dokshitzer and D. E. Kharzeev, "Heavy quark colorimetry of QCD matter", *Phys. Lett. B* **519** (2001) 199–206, arXiv:hep-ph/0106202. (Cited on page 19.)

[48] M. Djordjevic and M. Djordjevic, "Predictions of heavy-flavor suppression at 5.1 TeV Pb+Pb collisions at the CERN Large Hadron Collider", *Phys. Rev. C* **92** no. 2, (2015) 024918, arXiv:1505.04316 [nucl-th]. (Cited on pages xx, 20, 100 and 165.)

[49] J. Xu, J. Liao, and M. Gyulassy, "Bridging Soft-Hard Transport Properties of Quark-Gluon Plasmas with CUJET3.0", *JHEP* **02** (2016) 169, arXiv:1508.00552 [hep-ph]. (Cited on pages xx, 20 and 165.)

[50] J. Xu, A. Buzzatti, and M. Gyulassy, "Azimuthal jet flavor tomography with CUJET2.0 of nuclear collisions at RHIC and LHC", *JHEP* **08** (2014) 063, arXiv:1402.2956 [hep-ph]. (Cited on page 20.)

[51] J. Xu, J. Liao, and M. Gyulassy, "Consistency of Perfect Fluidity and Jet Quenching in semi-Quark-Gluon Monopole Plasmas", *Chin. Phys. Lett.* **32** no. 9, (2015) 092501, arXiv:1411.3673 [hep-ph]. (Cited on pages xx, 20 and 165.)

[52] **ALICE** Collaboration, J. Adam *et al.*, "Measurement of electrons from heavy-flavour hadron decays in p-Pb collisions at $\sqrt{s_{\rm NN}} = 5.02$ TeV", *Phys. Lett. B* **754** (2016) 81–93, arXiv:1509.07491 [nucl-ex]. (Cited on page 20.)

[53] **CMS** Collaboration, A. M. Sirunyan *et al.*, "Nuclear modification factor of $\rm D^0$ mesons in PbPb collisions at $\sqrt{s_{\rm NN}} = 5.02$ TeV", *Phys. Lett. B* **782** (2018) 474–496, arXiv:1708.04962 [nucl-ex]. (Cited on pages xi and 21.)

[54] **ALICE** Collaboration, S. Acharya *et al.*, "Prompt $\rm D^0$, $\rm D^+$, and $\rm D^{*+}$ production in Pb–Pb collisions at $\sqrt{s_{\rm NN}} = 5.02$ TeV", *JHEP* **01** (2022) 174, arXiv:2110.09420 [nucl-ex]. (Cited on pages xi and 21.)

[55] **ALICE** Collaboration, S. Acharya *et al.*, "Measurement of electrons from semileptonic heavy-flavour hadron decays at midrapidity in pp and Pb–Pb collisions at $\sqrt{s_{\rm NN}} = 5.02$ TeV", *Phys. Lett. B* **804** (2020) 135377, arXiv:1910.09110 [nucl-ex]. (Cited on pages xii, 21 and 100.)

[56] **ALICE** Collaboration, B. Abelev *et al.*, "Production of muons from heavy flavour decays at forward rapidity in pp and Pb–Pb collisions at $\sqrt{s_{\rm NN}} = 2.76$ TeV", *Phys. Rev. Lett.* **109** (2012) 112301, arXiv:1205.6443 [hep-ex]. (Cited on pages xii, xv, xvi, 21, 86, 90, 96, 105, 106, 169 and 189.)

[57] S. Plumari, V. Minissale, S. K. Das, G. Coci, and V. Greco, "Charmed Hadrons from Coalescence plus Fragmentation in relativistic nucleus-nucleus collisions at RHIC and LHC", *Eur. Phys. J. C* **78** no. 4, (2018) 348, arXiv:1712.00730 [hep-ph]. (Cited on page 21.)

[58] M. Lisovyi, A. Verbytskyi, and O. Zenaiev, "Combined analysis of charm-quark fragmentation-fraction measurements", *Eur. Phys. J. C* **76** no. 7, (2016) 397, arXiv:1509.01061 [hep-ex]. (Cited on pages xii and 22.)

[59] "Parton fragmentation and string dynamics", *Physics Reports* **97** no. 2, (1983) 31–145. (Cited on page 22.)

[60] S. Ferreres-Solé and T. Sjöstrand, "The space–time structure of hadronization in the Lund model", *Eur. Phys. J. C* **78** no. 11, (2018) 983, arXiv:1808.04619 [hep-ph]. (Cited on page 22.)

[61] M. Bahr *et al.*, "Herwig++ Physics and Manual", *Eur. Phys. J. C* **58** (2008) 639–707, arXiv:0803.0883 [hep-ph]. (Cited on pages xii and 22.)

[62] **ALICE** Collaboration, S. Acharya *et al.*, "Λ_c^+ Production and Baryon-to-Meson Ratios in pp and p-Pb Collisions at $\sqrt{s_{NN}}$=5.02 TeV at the LHC", *Phys. Rev. Lett.* **127** no. 20, (2021) 202301, arXiv:2011.06078 [nucl-ex]. (Cited on pages xii and 22.)

[63] **ALICE** Collaboration, S. Acharya *et al.*, "Production of charged pions, kaons, and (anti-)protons in Pb–Pb and inelastic pp collisions at $\sqrt{s_{\rm NN}}$ = 5.02 TeV", *Phys. Rev. C* **101** no. 4, (2020) 044907, arXiv:1910.07678 [nucl-ex]. (Cited on pages 22 and 91.)

[64] **ALICE** Collaboration, B. B. Abelev *et al.*, "K^0_S and Λ production in Pb-Pb collisions at $\sqrt{s_{NN}}$ = 2.76 TeV", *Phys. Rev. Lett.* **111** (2013) 222301, arXiv:1307.5530 [nucl-ex]. (Cited on page 22.)

[65] V. Minissale, S. Plumari, and V. Greco, "Charm hadrons in pp collisions at LHC energy within a coalescence plus fragmentation approach", *Phys. Lett. B* **821** (2021) 136622, arXiv:2012.12001 [hep-ph]. (Cited on page 23.)

[66] M. He and R. Rapp, "Charm-Baryon Production in Proton-Proton Collisions", *Phys. Lett. B* **795** (2019) 117–121, arXiv:1902.08889 [nucl-th]. (Cited on page 23.)

[67] **ALICE** Collaboration, S. Acharya *et al.*, "Constraining hadronization mechanisms with $\Lambda_{\rm c}^+/{\rm D}^0$ production ratios in Pb-Pb collisions at $\sqrt{s_{\rm NN}}$ = 5.02 TeV", arXiv:2112.08156 [nucl-ex]. (Cited on pages xii and 23.)

[68] U. Heinz, C. Shen, and H. Song, "The viscosity of quark-gluon plasma at RHIC and the LHC", *AIP Conf. Proc.* **1441** no. 1, (2012) 766–770, arXiv:1108.5323 [nucl-th]. (Cited on page 24.)

[69] H. Song and U. W. Heinz, "Multiplicity scaling in ideal and viscous hydrodynamics", *Phys. Rev. C* **78** (2008) 024902, arXiv:0805.1756 [nucl-th]. (Cited on page 24.)

[70] P. Romatschke and U. Romatschke, "Viscosity Information from Relativistic Nuclear Collisions: How Perfect is the Fluid Observed at RHIC?", *Phys. Rev. Lett.* **99** (2007) 172301, arXiv:0706.1522 [nucl-th]. (Cited on page 24.)

[71] B. V. Jacak and B. Muller, "The exploration of hot nuclear matter", *Science* **337** no. 6092, (2012) 310–314. (Cited on pages xii and 25.)

[72] **ALICE** Collaboration, K. Aamodt *et al.*, "Harmonic decomposition of two-particle angular correlations in Pb–Pb collisions at $\sqrt{s_{\rm NN}} = 2.76$ TeV", *Phys. Lett. B* **708** (2012) 249–264, arXiv:1109.2501 [nucl-ex]. (Cited on pages xii, 25 and 26.)

[73] **ALICE** Collaboration, K. Aamodt *et al.*, "Higher harmonic anisotropic flow measurements of charged particles in Pb–Pb collisions at $\sqrt{s_{\rm NN}} = 2.76$ TeV", *Phys. Rev. Lett.* **107** (2011) 032301, arXiv:1105.3865 [nucl-ex]. (Cited on pages xii, 25 and 26.)

[74] J. Noronha-Hostler, M. Luzum, and J.-Y. Ollitrault, "Hydrodynamic predictions for 5.02 TeV Pb–Pb collisions", *Phys. Rev. C* **93** no. 3, (2016) 034912, arXiv:1511.06289 [nucl-th]. (Cited on page 25.)

[75] H. Niemi, K. J. Eskola, R. Paatelainen, and K. Tuominen, "Predictions for 5.023 TeV Pb–Pb collisions at the CERN Large Hadron Collider", *Phys. Rev. C* **93** no. 1, (2016) 014912, arXiv:1511.04296 [hep-ph]. (Cited on pages xii, 25, 26 and 28.)

[76] **ALICE** Collaboration, J. Adam *et al.*, "Anisotropic flow of charged particles in Pb–Pb collisions at $\sqrt{s_{\rm NN}} = 5.02$ TeV", *Phys. Rev. Lett.* **116** no. 13, (2016) 132302, arXiv:1602.01119 [nucl-ex]. (Cited on pages xii and 27.)

[77] **CMS** Collaboration, A. M. Sirunyan *et al.*, "Azimuthal anisotropy of charged particles with transverse momentum up to 100 GeV/c in Pb–Pb collisions at $\sqrt{s_{\rm NN}} = 5.02$ TeV", *Phys. Lett. B* **776** (2018) 195–216, arXiv:1702.00630 [hep-ex]. (Cited on pages xii and 28.)

[78] D. Molnar and S. A. Voloshin, "Elliptic flow at large transverse momenta from quark coalescence", *Phys. Rev. Lett.* **91** (2003) 092301, arXiv:nucl-th/0302014. (Cited on page 26.)

[79] **ALICE** Collaboration, S. Acharya *et al.*, "Anisotropic flow of identified particles in Pb–Pb collisions at $\sqrt{s_{\rm NN}} = 5.02$ TeV", *JHEP* **09** (2018) 006, arXiv:1805.04390 [nucl-ex]. (Cited on pages xii, 29 and 150.)

[80] **ALICE** Collaboration, S. Acharya *et al.*, "Transverse-momentum and event-shape dependence of D-meson flow harmonics in Pb–Pb collisions at $\sqrt{s_{\rm NN}} = 5.02$ TeV", *Phys. Lett. B* **813** (2021) 136054, arXiv:2005.11131 [nucl-ex]. (Cited on pages xiii and 30.)

[81] M. L. Mangano and B. Nachman, "Observables for possible QGP signatures in central pp collisions", *Eur. Phys. J. C* **78** no. 4, (2018) 343, arXiv:1708.08369 [hep-ph]. (Cited on page 27.)

[82] M. Arneodo, "Nuclear effects in structure functions", *Phys. Rep.* **240** (Jun, 1992) 301–393. 152 p. https://cds.cern.ch/record/238916. (Cited on page 29.)

[83] M. Akrami and A. Mirjalili, "Comparing optimized renormalization schemes for QCD observables", *Phys. Rev. D* **101** no. 3, (2020) 034007, arXiv:1912.08938 [hep-ph]. (Cited on page 29.)

[84] K. J. Eskola, P. Paakkinen, H. Paukkunen, and C. A. Salgado, "EPPS16: Nuclear parton distributions with LHC data", *Eur. Phys. J. C* **77** no. 3, (2017) 163, arXiv:1612.05741 [hep-ph]. (Cited on page 29.)

[85] K. Eskola, P. Paakkinen, H. Paukkunen, and C. Salgado, "Epps16: nuclear parton distributions with LHC data", *The European Physical Journal C* **77** (12, 2016) . (Cited on pages xiii and 31.)

[86] "The ratio of the nucleon structure functions f_2^N for iron and deuterium", *Physics Letters B* **123** no. 3, (1983) 275–278. https://www.sciencedirect.com/science/article/pii/0370269383904379. (Cited on page 30.)

[87] K. Saito and T. Uchiyama, "Effect of the fermi motion on nuclear structure functions and the EMC effect", *Zeitschrift für Physik A Atoms and Nuclei* **322** (1985) 299–307. (Cited on page 30.)

[88] F. Gelis, E. Iancu, J. Jalilian-Marian, and R. Venugopalan, "The Color Glass Condensate", *Ann. Rev. Nucl. Part. Sci.* **60** (2010) 463–489, arXiv:1002.0333 [hep-ph]. (Cited on page 31.)

[89] **ALICE** Collaboration, B. Abelev *et al.*, "Pseudorapidity density of charged particles in p–Pb collisions at $\sqrt{s_{\rm NN}} = 5.02$ TeV", *Phys. Rev. Lett.* **110** no. 3, (2013) 032301, arXiv:1210.3615 [nucl-ex]. (Cited on pages xiii, 31 and 32.)

[90] I. Helenius, K. J. Eskola, H. Honkanen, and C. A. Salgado, "Impact-Parameter Dependent Nuclear Parton Distribution Functions: EPS09s and EKS98s and Their Applications in Nuclear Hard Processes", *JHEP* **07** (2012) 073, arXiv:1205.5359 [hep-ph]. (Cited on page 32.)

[91] **ALICE** Collaboration, B. Abelev *et al.*, "Transverse momentum distribution and nuclear modification factor of charged particles in p–Pb collisions at $\sqrt{s_{\rm NN}} = 5.02$ TeV", *Phys. Rev. Lett.* **110** no. 8, (2013) 082302, arXiv:1210.4520 [nucl-ex]. (Cited on pages xiii and 33.)

[92] **CMS** Collaboration, V. Khachatryan *et al.*, "Measurement of long-range near-side two-particle angular correlations in pp collisions at $\sqrt{s}$ =13 TeV", *Phys. Rev. Lett.* **116** no. 17, (2016) 172302, arXiv:1510.03068 [nucl-ex]. (Cited on pages xiii, 33 and 34.)

[93] **ALICE** Collaboration, B. B. Abelev *et al.*, "Long-range angular correlations of π, K and p in p–Pb collisions at $\sqrt{s_{\rm NN}}$ = 5.02 TeV", *Phys. Lett. B* **726** (2013) 164–177, arXiv:1307.3237 [nucl-ex]. (Cited on pages xiii, xix, 34, 35, 114, 115, 116, 156 and 157.)

[94] C. Shen, U. Heinz, P. Huovinen, and H. Song, "Radial and elliptic flow in Pb+Pb collisions at the Large Hadron Collider from viscous hydrodynamic", *Phys. Rev. C* **84** (2011) 044903, arXiv:1105.3226 [nucl-th]. (Cited on page 34.)

[95] **CMS** Collaboration, A. M. Sirunyan *et al.*, "Measurement of prompt D^0 meson azimuthal anisotropy in Pb–Pb collisions at $\sqrt{s_{\rm NN}}$ = 5.02 TeV", *Phys. Rev. Lett.* **120** no. 20, (2018) 202301, arXiv:1708.03497 [nucl-ex]. (Cited on page 34.)

[96] **CMS** Collaboration, A. M. Sirunyan *et al.*, "Elliptic flow of charm and strange hadrons in high-multiplicity p–Pb collisions at $\sqrt{s_{\rm NN}}$ = 8.16 TeV", *Phys. Rev. Lett.* **121** no. 8, (2018) 082301, arXiv:1804.09767 [hep-ex]. (Cited on pages xiii and 35.)

[97] **ALICE** Collaboration, S. Acharya *et al.*, "Investigations of Anisotropic Flow Using Multiparticle Azimuthal Correlations in pp, p–Pb, Xe–Xe, and Pb–Pb Collisions at the LHC", *Phys. Rev. Lett.* **123** no. 14, (2019) 142301, arXiv:1903.01790 [nucl-ex]. (Cited on pages xiii, 34 and 35.)

[98] **ATLAS** Collaboration, G. Aad *et al.*, "Transverse momentum and process dependent azimuthal anisotropies in $\sqrt{s_{\rm NN}}$ = 8.16 TeV p+Pb collisions with the ATLAS detector", *Eur. Phys. J. C* **80** no. 1, (2020) 73, arXiv:1910.13978 [nucl-ex]. (Cited on pages xiii, xx, 36, 143, 163 and 164.)

[99] Z. Citron *et al.*, "Report from Working Group 5: Future physics opportunities for high-density QCD at the LHC with heavy-ion and proton beams", *CERN Yellow Rep. Monogr.* **7** (2019) 1159–1410, arXiv:1812.06772 [hep-ph]. (Cited on page 36.)

[100] A. Bilandzic, C. H. Christensen, K. Gulbrandsen, A. Hansen, and Y. Zhou, "Generic framework for anisotropic flow analyses with multiparticle azimuthal correlations", *Phys. Rev. C* **89** no. 6, (2014) 064904, arXiv:1312.3572 [nucl-ex]. (Cited on pages 37 and 45.)

[101] A. M. Poskanzer and S. A. Voloshin, "Methods for analyzing anisotropic flow in relativistic nuclear collisions", *Phys. Rev. C* **58** (Sep, 1998) 1671–1678.

https://link.aps.org/doi/10.1103/PhysRevC.58.1671. (Cited on pages 37, 38 and 47.)

[102] M. Luzum and J.-Y. Ollitrault, "Eliminating experimental bias in anisotropic-flow measurements of high-energy nuclear collisions", *Phys. Rev. C* **87** no. 4, (2013) 044907, arXiv:1209.2323 [nucl-ex]. (Cited on page 37.)

[103] **ATLAS** Collaboration, G. Aad *et al.*, "Measurement of the azimuthal anisotropy for charged particle production in $\sqrt{s_{\mathrm{NN}}} = 2.76$ TeV lead-lead collisions with the ATLAS detector", *Phys. Rev. C* **86** (2012) 014907, arXiv:1203.3087 [hep-ex]. (Cited on page 38.)

[104] **CMS** Collaboration, S. Chatrchyan *et al.*, "Measurement of the elliptic anisotropy of charged particles produced in Pb–Pb collisions at $\sqrt{s_{\mathrm{NN}}}$=2.76 TeV", *Phys. Rev. C* **87** no. 1, (2013) 014902, arXiv:1204.1409 [nucl-ex]. (Cited on page 38.)

[105] **STAR** Collaboration, C. Adler *et al.*, "Elliptic flow from two and four particle correlations in Au+Au collisions at $\sqrt{s_{\mathrm{NN}}} = 130$ GeV", *Phys. Rev. C* **66** (2002) 034904, arXiv:nucl-ex/0206001. (Cited on page 39.)

[106] A. Bilandzic, R. Snellings, and S. Voloshin, "Flow analysis with cumulants: direct calculations", *Phys. Rev. C* **83** (2011) 044913, arXiv:1010.0233 [nucl-ex]. (Cited on pages 40, 41, 42, 43, 44 and 45.)

[107] N. Borghini, P. M. Dinh, and J.-Y. Ollitrault, "A New method for measuring azimuthal distributions in nucleus-nucleus collisions", *Phys. Rev. C* **63** (2001) 054906, arXiv:nucl-th/0007063. (Cited on page 41.)

[108] N. Borghini, P. M. Dinh, and J.-Y. Ollitrault, "Flow analysis from multiparticle azimuthal correlations", *Phys. Rev. C* **64** (2001) 054901, arXiv:nucl-th/0105040. (Cited on pages 41, 45 and 124.)

[109] M. Cacciari and G. P. Salam, "Dispelling the N^3 myth for the k_{T} jet-finder", *Phys. Lett. B* **641** (2006) 57–61, arXiv:hep-ph/0512210. (Cited on page 43.)

[110] I. Selyuzhenkov and S. Voloshin, "Effects of non-uniform acceptance in anisotropic flow measurement", *Phys. Rev. C* **77** (2008) 034904, arXiv:0707.4672 [nucl-th]. (Cited on pages 45 and 147.)

[111] **ATLAS** Collaboration, G. Aad *et al.*, "Measurement of long-range pseudorapidity correlations and azimuthal harmonics in $\sqrt{s_{\mathrm{NN}}} = 5.02$ TeV proton-lead collisions with the ATLAS detector", *Phys. Rev. C* **90** no. 4, (2014) 044906, arXiv:1409.1792 [hep-ex]. (Cited on pages 47 and 116.)

[112] **ATLAS** Collaboration, M. Aaboud *et al.*, "Measurements of long-range azimuthal anisotropies and associated Fourier coefficients for pp collisions at

$\sqrt{s} = 5.02$ and 13 TeV and p+Pb collisions at $\sqrt{s_{\mathrm{NN}}} = 5.02$ TeV with the ATLAS detector", *Phys. Rev. C* **96** no. 2, (2017) 024908, arXiv:1609.06213 [nucl-ex]. (Cited on pages 47, 115 and 155.)

[113] **CMS** Collaboration, A. M. Sirunyan *et al.*, "Studies of charm and beauty hadron long-range correlations in pp and p–Pb collisions at LHC energies", *Phys. Lett. B* **813** (2021) 136036, arXiv:2009.07065 [hep-ex]. (Cited on pages 47 and 139.)

[114] **CMS** Collaboration, S. Chatrchyan *et al.*, "Studies of Azimuthal Dihadron Correlations in Ultra-Central Pb–Pb Collisions at $\sqrt{s_{\mathrm{NN}}} = 2.76$ TeV", *JHEP* **02** (2014) 088, arXiv:1312.1845 [nucl-ex]. (Cited on pages 48, 114 and 173.)

[115] **CMS** Collaboration, V. Khachatryan *et al.*, "Evidence for transverse momentum and pseudorapidity dependent event plane fluctuations in Pb–Pb and p–Pb collisions", *Phys. Rev. C* **92** no. 3, (2015) 034911, arXiv:1503.01692 [nucl-ex]. (Cited on pages 48, 136 and 140.)

[116] **ALICE** Collaboration, J. Adam *et al.*, "Evolution of the longitudinal and azimuthal structure of the near-side jet peak in Pb–Pb collisions at $\sqrt{s_{\mathrm{NN}}} = 2.76$ TeV", *Phys. Rev. C* **96** no. 3, (2017) 034904, arXiv:1609.06667 [nucl-ex]. (Cited on pages xiii and 49.)

[117] L. Evans and P. Bryant, "LHC machine",. https://doi.org/10.1088/1748-0221/3/08/s08001. (Cited on page 51.)

[118] D. Brandt, H. Burkhardt, M. Lamont, S. Myers, and J. Wenninger, "Accelerator physics at LEP",. https://doi.org/10.1088/0034-4885/63/6/203. (Cited on page 51.)

[119] O. S. Bruning, P. Collier, P. Lebrun, S. Myers, R. Ostojic, J. Poole, and P. Proudlock, *LHC Design Report*. CERN Yellow Reports: Monographs. CERN, Geneva, 2004. https://cds.cern.ch/record/782076. (Cited on page 51.)

[120] A. Team, "The four main LHC experiments." Jun, 1999. (Cited on pages xiii and 52.)

[121] **ALICE** Collaboration, J. Adam *et al.*, "Centrality dependence of the charged-particle multiplicity density at midrapidity in Pb–Pb collisions at $\sqrt{s_{\mathrm{NN}}} = 5.02$ TeV", *Phys. Rev. Lett.* **116** no. 22, (2016) 222302, arXiv:1512.06104 [nucl-ex]. (Cited on page 52.)

[122] **ALICE** Collaboration, B. B. Abelev *et al.*, "Performance of the ALICE Experiment at the CERN LHC", *Int. J. Mod. Phys. A* **29** (2014) 1430044, arXiv:1402.4476 [nucl-ex]. (Cited on pages xxv, 52, 54 and 71.)

[123] D. Elia, J. Grosse-Oetringhaus, M. Nicassio, and T. Virgili, "The pixel detector based tracklet reconstruction algorithm in ALICE", tech. rep., CERN, Geneva, Nov, 2009. https://cds.cern.ch/record/1225500. (Cited on pages 53, 72 and 109.)

[124] **ALICE** Collaboration, K. Aamodt *et al.*, "The ALICE experiment at the CERN LHC", *JINST* **3** (2008) S08002. (Cited on pages xiv, xxv, 56, 68, 69, 70 and 88.)

[125] **ALICE** Collaboration, B. Abelev *et al.*, "The ALICE TPC, a large 3-dimensional tracking device with fast readout for ultra-high multiplicity events", *Phys. Rev. Lett.* **109** (2012) 112301, arXiv:1205.6443 [hep-ex]. (Cited on pages xiv and 57.)

[126] **ALICE** Collaboration, S. Acharya *et al.*, "The ALICE Transition Radiation Detector: construction, operation, and performance", *Nucl. Instrum. Meth. A* **881** (2018) 88–127, arXiv:1709.02743 [physics.ins-det]. (Cited on pages 58 and 103.)

[127] **ALICE** Collaboration, *ALICE Time-Of-Flight system (TOF): Technical Design Report*. Technical design report. ALICE. CERN, Geneva, 2000. https://cds.cern.ch/record/430132. (Cited on page 58.)

[128] **ALICE** Collaboration, F. Piuz, W. Klempt, L. Leistam, J. De Groot, and J. Schukraft, "ALICE high-momentum particle identification: Technical Design Report",. https://cds.cern.ch/record/381431. (Cited on page 58.)

[129] **ALICE** Collaboration, P. Martinengo, "The ALICE high momentum particle identification system: An overview after the first Large Hadron Collider run", *Nucl. Instrum. Meth. A* **639** (2011) 7–10. (Cited on page 58.)

[130] **ALICE** Collaboration, V. I. Manko, W. Klempt, L. Leistam, J. De Groot, and J. Schukraft, "ALICE Photon Spectrometer (PHOS): Technical Design Report",. https://cds.cern.ch/record/381432. (Cited on page 58.)

[131] **ALICE** Collaboration, D. Blau, "Performance of the ALICE electromagnetic calorimeters in LHC Runs 1 and 2 and upgrade projects", *JINST* **15** no. 03, (2020) C03025, arXiv:2001.02928 [hep-ex]. (Cited on page 59.)

[132] **ALICE** Collaboration, M. Gallio, W. Klempt, L. Leistam, J. De Groot, and J. Schukraft, "ALICE Zero-Degree Calorimeter (ZDC): Technical Design Report",. https://cds.cern.ch/record/381433. (Cited on page 59.)

[133] **ALICE** Collaboration, "ALICE Photon Multiplicity Detector (PMD): Technical Design Report",. https://cds.cern.ch/record/451099. (Cited on page 59.)

[134] **ALICE** Collaboration, "ALICE forward detectors: FMD, TO and VO: Technical Design Report",. https://cds.cern.ch/record/781854. Submitted on 10 Sep 2004. (Cited on pages 60 and 153.)

[135] Christensen *et al.*, "The ALICE Forward Multiplicity Detector", *Int. J. Mod. Phys. E* **16** (2007) 2432–2437, arXiv:0712.1117 [nucl-ex]. (Cited on pages xxv and 60.)

[136] "Dimuon forward spectrometer : Tracking chambers",. https://twiki.cern.ch/twiki/bin/viewauth/ALICE/MuonTracking. (Cited on pages xiv and 61.)

[137] M. Tarhini, "Measurement of Z-boson and J/ψ Production in p–Pb and Pb–Pb Collisions at $\sqrt{s_{\mathrm{NN}}} = 5.02$ TeV with ALICE at the LHC",. https://tel.archives-ouvertes.fr/tel-01691725. (Cited on pages xiv, 62, 64 and 65.)

[138] P. Rosnet, "The muon spectrometer of the ALICE experiment at LHC",. (Cited on pages xiv and 62.)

[139] D. Stocco, "Development of the ALICE Muon Spectrometer: preparation for data taking and heavy flavor measurement", 2008. https://cds.cern.ch/record/1322408. Presented on Aug 2008. (Cited on page 65.)

[140] R. Arnaldi *et al.*, "The ALICE Dimuon Trigger: Overview and Electronics Prototypes", *Nucl. Instrum. Methods Phys. Res., A* **456** (Dec, 1999) 126–31. 11 p. https://cds.cern.ch/record/426379. (Cited on pages xiv, 66 and 67.)

[141] **ALICE** Collaboration, "ALICE dimuon forward spectrometer: Technical Design Report",. https://cds.cern.ch/record/401974. (Cited on pages xiv and 66.)

[142] **ALICE** Collaboration, C. W. Fabjan, L. Jirden, V. Lindestruth, L. Riccati, D. Rorich, P. Van de Vyvre, O. Villalobos Baillie, and H. de Groot, "ALICE trigger data-acquisition high-level trigger and control system: Technical Design Report",. https://cds.cern.ch/record/684651. (Cited on page 67.)

[143] C. Zampolli, F. Carminati, and A. Colla, "The SHUTTLE: the ALICE Framework for the extraction of the conditions Data",. (Cited on page 70.)

[144] M. Ivanov, "The ALICE data-flow: from calibration, to QA, through reconstruction",. https://indico.cern.ch/event/442390/contributions/1096053/attachments/1289986/1920811/LHCP_MarianIvanov_v12.pdf. (Cited on pages xiv and 71.)

[145] R.Fruhwirth, "Application of Kalman filtering to track and vertex fitting", *Nuclear Instruments and Methods in Physics Research Section A: Accelerators, Spectrometers, Detectors and Associated Equipment* **262** no. 2, (1987) 444–450. (Cited on page 72.)

[146] **ALICE** Collaboration, "The ALICE definition of primary particles",. https://cds.cern.ch/record/2270008. (Cited on page 73.)

[147] A. Maire, "Measurement of production of multi-strange baryons in proton-proton collisions with the ALICE at the LHC", 2011. https://cds.cern.ch/record/1490315. Presented 13 Oct 2011. (Cited on pages xiv, 74 and 145.)

[148] F. Grosa, "Strange and non-strange D-meson production in pp, p-Pb, and Pb-Pb collisions with ALICE at the LHC", 2020. https://cds.cern.ch/record/2713513. Presented 11 Feb 2020. (Cited on page 75.)

[149] **ALICE** Collaboration, B. Abelev *et al.*, "Centrality determination of Pb–Pb collisions at $\sqrt{s_{\rm NN}}$ = 2.76 TeV with ALICE", *Phys. Rev. C* **88** no. 4, (2013) 044909, arXiv:1301.4361 [nucl-ex]. (Cited on pages xiv, 75 and 76.)

[150] **ALICE** Collaboration, J. Adam *et al.*, "Centrality dependence of particle production in p–Pb collisions at $\sqrt{s_{\rm NN}}$= 5.02 TeV", *Phys. Rev. C* **91** no. 6, (2015) 064905, arXiv:1412.6828 [nucl-ex]. (Cited on pages xiv, 76, 77, 78, 137 and 170.)

[151] **ALICE** Collaboration, B. Abelev *et al.*, "Upgrade of the ALICE Experiment: Letter Of Intent", *J. Phys. G* **41** (2014) 087001. (Cited on pages 77 and 79.)

[152] P. Antonioli *et al.*, "INFN What Next: Ultra-relativistic Heavy-Ion Collisions", arXiv:1602.04120 [nucl-ex]. (Cited on page 77.)

[153] **ALICE** Collaboration, D. Colella, "ALICE ITS Upgrade for LHC Run 3: Commissioning in the Laboratory", *JPS Conf. Proc.* **34** (2021) 010004, arXiv:2012.01564 [physics.ins-det]. (Cited on page 79.)

[154] **ALICE** Collaboration, A. Ferretti, "The ALICE Experiment Upgrades", 1, 2022. arXiv:2201.08871 [physics.ins-det]. (Cited on pages xiv, 79 and 80.)

[155] A. L. Gera, "Upgrade of the ALICE Time Projection Chamber for the LHC Run 3", *PoS* **EPS-HEP2019** (2020) 102, arXiv:2004.10520 [physics.ins-det]. (Cited on page 79.)

[156] S. Siddhanta, "Muon physics at forward rapidity with the ALICE detector upgrade", *Nuclear Physics A* **982** (2019) 947–950. https://www.sciencedirect.com/science/article/pii/S0375947418303154.

The 27th International Conference on Ultrarelativistic Nucleus-Nucleus Collisions: Quark Matter 2018. (Cited on pages xiv, 80, 81 and 82.)

[157] **ALICE** Collaboration, P. Antonioli, A. Kluge, and W. Riegler, "Upgrade of the ALICE Readout and Trigger System", tech. rep., Sep, 2013. https://cds.cern.ch/record/1603472. (Cited on page 81.)

[158] Arnaldi *et al.*, "Front-end electronics for the RPCs of the ALICE dimuon trigger", *IEEE Transactions on Nuclear Science* **52** no. 4, (2005) 1176–1181. (Cited on page 81.)

[159] "Technical Design Report for the Muon Forward Tracker", tech. rep., Jan, 2015. https://cds.cern.ch/record/1981898. (Cited on pages xxv, 82 and 83.)

[160] S. Acharya, "First look at Pilot Run with MFT",. https://indico.cern.ch/event/1017729/contributions/4680177/attachments/2372313/4051742/20220113_MFT_FirstLook_Shreyasi.pdf. (Cited on pages xiv, 83 and 84.)

[161] **ALICE** Collaboration, "Upgrade of the ALICE Time Projection Chamber",. https://cds.cern.ch/record/1622286. (Cited on page 83.)

[162] **ALICE** Collaboration, C. Zampolli, "ALICE data processing for Run 3 and Run 4 at the LHC", *PoS* **ICHEP2020** (2021) 929, arXiv:2012.04391 [physics.ins-det]. (Cited on page 84.)

[163] **ALICE** Collaboration, S. Acharya *et al.*, "Measurement of D^0, D^+, D^{*+} and D_s^+ production in Pb–Pb collisions at $\sqrt{s_{NN}} = 5.02$ TeV", *JHEP* **10** (2018) 174, arXiv:1804.09083 [nucl-ex]. (Cited on page 85.)

[164] Z. Zhang, "Open heavy-flavour measurements via muons in proton-proton and nucleus-nucleus collisions with the ALICE detector at the CERN-LHC",. http://www.theses.fr/2018CLFAC077/document. (Cited on pages 86 and 89.)

[165] "Muon QA: LHC11h",. https://indico.cern.ch/event/165414/contributions/250499/attachments/200146/280941/muonQA.pdf. (Cited on page 88.)

[166] "Muon QA: LHC15o muon calo pass1",. https://twiki.cern.ch/twiki/pub/ALICE/MuonPbPbQA2015/muonQA_LHC15o_muon_calo_pass1.pdf. (Cited on page 88.)

[167] **ALICE** Collaboration, B. Abelev *et al.*, "Measurement of the Cross Section for Electromagnetic Dissociation with Neutron Emission in Pb–Pb Collisions at $\sqrt{s_{NN}} = 2.76$ TeV", *Phys. Rev. Lett.* **109** (2012) 252302, arXiv:1203.2436 [nucl-ex]. (Cited on page 88.)

[168] **ALICE** Collaboration, P. Cortese, "Performance of the ALICE Zero Degree Calorimeters and upgrade strategy", *J. Phys.: Conf. Ser.* **1162** (2019) 012006. 8 p. https://cds.cern.ch/record/2715341. (Cited on page 88.)

[169] **ALICE** Collaboration, J. Adam *et al.*, "J/ψ suppression at forward rapidity in Pb–Pb collisions at $\sqrt{s_{\mathrm{NN}}} = \mathbf{5.02}$ TeV", *Phys. Lett. B* **766** (2017) 212–224, arXiv:1606.08197 [nucl-ex]. (Cited on page 90.)

[170] **ALICE** Collaboration, S. Acharya *et al.*, "Studies of J/ψ production at forward rapidity in Pb–Pb collisions at $\sqrt{s_{\mathrm{NN}}} = 5.02$ TeV", *JHEP* **02** (2020) 041, arXiv:1909.03158 [nucl-ex]. (Cited on pages 90 and 95.)

[171] **ALICE** Collaboration, M. Chojnacki, "Production of π/K/p in pp and Pb–Pb collisions measured with ALICE", *J. Phys.: Conf. Ser.* **509** (2014) 012041. 4 p. https://cds.cern.ch/record/2026261. (Cited on page 91.)

[172] **ATLAS** Collaboration, G. Aad *et al.*, "Measurement of charged-particle spectra in Pb+Pb collisions at $\sqrt{s_{\mathrm{NN}}} = 2.76$ TeV with the ATLAS detector at the LHC", *JHEP* **09** (2015) 050, arXiv:1504.04337 [hep-ex]. (Cited on page 92.)

[173] T. Sjostrand, S. Mrenna, and P. Z. Skands, "PYTHIA 6.4 Physics and Manual", *JHEP* **05** (2006) 026, arXiv:hep-ph/0603175. (Cited on pages 92, 93 and 139.)

[174] R. Engel, J. Ranft, and S. Roesler, "Hard diffraction in hadron–hadron interactions and in photoproduction", *Phys. Rev. D* **52** (1995) 1459–1468, arXiv:hep-ph/9502319. (Cited on page 92.)

[175] T. Sjostrand, S. Mrenna, and P. Z. Skands, "A Brief Introduction to PYTHIA 8.1", *Comput. Phys. Commun.* **178** (2008) 852–867, arXiv:0710.3820 [hep-ph]. (Cited on pages 92 and 187.)

[176] X.-N. Wang and M. Gyulassy, "HIJING: A Monte Carlo model for multiple jet production in pp, p–A and A–A collisions", *Phys. Rev. D* **44** (1991) 3501–3516. (Cited on page 93.)

[177] R. Brun, F. Bruyant, F. Carminati, S. Giani, M. Maire, A. McPherson, G. Patrick, and L. Urban, *GEANT: Detector Description and Simulation Tool; Oct 1994*. CERN Program Library. CERN, Geneva, 1993. http://cds.cern.ch/record/1082634. Long Writeup W5013. (Cited on pages 93, 122 and 175.)

[178] S. Alioli, P. Nason, C. Oleari, and E. Re, "NLO vector-boson production matched with shower in POWHEG", *JHEP* **07** (2008) 060, arXiv:0805.4802 [hep-ph]. (Cited on page 93.)

[179] **ALICE** Collaboration, S. Acharya *et al.*, "Energy dependence of forward-rapidity J/ψ and ψ(2S) production in pp collisions at the LHC",

Eur. Phys. J. C **77** no. 6, (2017) 392, arXiv:1702.00557 [hep-ex]. (Cited on page 95.)

[180] **ALICE** Collaboration, "Centrality determination in heavy ion collisions",. http://cds.cern.ch/record/2636623. (Cited on page 96.)

[181] **ALICE** Collaboration, S. Acharya *et al.*, "Production of muons from heavy-flavour hadron decays at high transverse momentum in Pb–Pb collisions at $\sqrt{s_{\rm NN}}$ = 5.02 and 2.76 TeV", *Phys. Lett. B* **820** (2021) 136558, arXiv:2011.05718 [nucl-ex]. (Cited on pages xv, xvi, xxv, 97, 98, 100, 101, 102, 169 and 189.)

[182] **ALICE** Collaboration, S. Acharya *et al.*, "Production of muons from heavy-flavour hadron decays in p–Pb collisions at $\sqrt{s_{\rm NN}}$ = 5.02 TeV", *Phys. Lett. B* **770** (2017) 459–472, arXiv:1702.01479 [nucl-ex]. (Cited on pages xvi, 97, 105, 106, 169 and 189.)

[183] M. He, R. J. Fries, and R. Rapp, "Heavy Flavor at the Large Hadron Collider in a Strong Coupling Approach", *Phys. Lett. B* **735** (2014) 445–450, arXiv:1401.3817 [nucl-th]. (Cited on page 99.)

[184] Z.-B. Kang, F. Ringer, and I. Vitev, "Effective field theory approach to open heavy flavor production in heavy-ion collisions", *JHEP* **03** (2017) 146, arXiv:1610.02043 [hep-ph]. (Cited on page 99.)

[185] M. Nahrgang, J. Aichelin, P. B. Gossiaux, and K. Werner, "Influence of hadronic bound states above T_c on heavy-quark observables in Pb+Pb collisions at at the CERN Large Hadron Collider", *Phys. Rev. C* **89** no. 1, (2014) 014905, arXiv:1305.6544 [hep-ph]. (Cited on page 99.)

[186] **ALICE** Collaboration, S. Acharya *et al.*, "Measurements of low-p_T electrons from semileptonic heavy-flavour hadron decays at mid-rapidity in pp and Pb–Pb collisions at $\sqrt{s_{\rm NN}}$ = 2.76 TeV", *JHEP* **10** (2018) 061, arXiv:1805.04379 [nucl-ex]. (Cited on page 100.)

[187] **ALICE** Collaboration, J. Adam *et al.*, "Elliptic flow of muons from heavy-flavour hadron decays at forward rapidity in Pb–Pb collisions at $\sqrt{s_{\rm NN}}$ = 2.76 TeV", *Phys. Lett. B* **753** (2016) 41–56, arXiv:1507.03134 [nucl-ex]. (Cited on pages xvi, 105, 106 and 189.)

[188] M. L. Mangano, P. Nason, and G. Ridolfi, "Heavy-quark correlations in hadron collisions at next-to-leading order", *Nuclear Physics B* **373** no. 2, (1992) 295–345. (Cited on page 105.)

[189] "https://twiki.cern.ch/twiki/bin/view/ALICE/AliDPGtoolsPhysSel",. (Cited on page 107.)

[190] **ALICE** Collaboration, J. Adam *et al.*, "Forward-central two-particle correlations in p–Pb collisions at $\sqrt{s_{\rm NN}}$ = 5.02 TeV", *Phys. Lett. B* **753**

(2016) 126–139, arXiv:1506.08032 [nucl-ex]. (Cited on pages xviii, 112, 114, 119, 121, 122, 136, 139, 140, 159, 170 and 173.)

[191] **ALICE** Collaboration, B. Abelev *et al.*, "Long-range angular correlations on the near and away side in p–Pb collisions at $\sqrt{s_{\rm NN}} = 5.02$ TeV", *Phys. Lett. B* **719** (2013) 29–41, arXiv:1212.2001 [nucl-ex]. (Cited on pages 114, 115 and 116.)

[192] **ALICE** Collaboration, B. B. Abelev *et al.*, "Multiplicity dependence of jet-like two-particle correlation structures in p–Pb collisions at $\sqrt{s_{\rm NN}}$=5.02 TeV", *Phys. Lett. B* **741** (2015) 38–50, arXiv:1406.5463 [nucl-ex]. (Cited on page 118.)

[193] **ALICE** Collaboration, S. Acharya *et al.*, "Search for collectivity with azimuthal J/ψ-hadron correlations in high multiplicity p–Pb collisions at $\sqrt{s_{\rm NN}} = 5.02$ and 8.16 TeV", *Phys. Lett. B* **780** (2018) 7–20, arXiv:1709.06807 [nucl-ex]. (Cited on page 119.)

[194] **ATLAS** Collaboration, M. Aaboud *et al.*, "Correlated long-range mixed-harmonic fluctuations measured in *pp*, *p*+Pb and low-multiplicity Pb+Pb collisions with the ATLAS detector", *Phys. Lett. B* **789** (2019) 444–471, arXiv:1807.02012 [nucl-ex]. (Cited on page 122.)

[195] S. Roesler, R. Engel, and J. Ranft, "The Monte Carlo event generator DPMJET-III", in *International Conference on Advanced Monte Carlo for Radiation Physics, Particle Transport Simulation and Applications (MC 2000)*, pp. 1033–1038. 12, 2000. arXiv:hep-ph/0012252. (Cited on pages 122 and 139.)

[196] M. Masera, G. Ortona, M. G. Poghosyan, and F. Prino, "Anisotropic transverse flow introduction in monte carlo generators for heavy ion collisions", *Phys. Rev. C* **79** (Jun, 2009) 064909. https://link.aps.org/doi/10.1103/PhysRevC.79.064909. (Cited on pages 122 and 175.)

[197] R. J. Barlow, "Practical Statistics for Particle Physics", *CERN Yellow Rep. School Proc.* **5** (2020) 149–197, arXiv:1905.12362 [physics.data-an]. (Cited on pages 122, 152 and 162.)

[198] B. Collaboration, "Recommended statistical procedures for Babar.", http://www.slac.stanford.edu/BFROOT/www/Statistics/Report/report.ps. (Cited on page 123.)

[199] B. Efron, "The Jackknife, the bootstrap and other resampling plans",. https://cds.cern.ch/record/98913. Lectures given at Bowling Green State Univ., June 1980. (Cited on page 132.)

[200] **ALICE** Collaboration, S. Acharya *et al.*, "Charged-particle pseudorapidity density at mid-rapidity in p–Pb collisions at $\sqrt{s_{\rm NN}} = 8.16$ TeV", *Eur. Phys. J. C* **79** no. 4, (2019) 307, arXiv:1812.01312 [nucl-ex]. (Cited on page 137.)

[201] **ALICE** Collaboration, S. Acharya *et al.*, "Azimuthal anisotropy of heavy-flavor decay electrons in p–Pb collisions at $\sqrt{s_{\rm NN}} = 5.02$ TeV", *Phys. Rev. Lett.* **122** no. 7, (2019) 072301, arXiv:1805.04367 [nucl-ex]. (Cited on pages xviii, 139, 140 and 170.)

[202] C. Zhang, C. Marquet, G.-Y. Qin, S.-Y. Wei, and B.-W. Xiao, "Elliptic flow of heavy quarkonia in p–A collisions", *Phys. Rev. Lett.* **122** no. 17, (2019) 172302, arXiv:1901.10320 [hep-ph]. (Cited on pages xviii, 139 and 140.)

[203] C. Zhang, C. Marquet, G.-Y. Qin, Y. Shi, L. Wang, S.-Y. Wei, and B.-W. Xiao, "Collectivity of heavy mesons in proton-nucleus collisions", *Phys. Rev. D* **102** no. 3, (2020) 034010, arXiv:2002.09878 [hep-ph]. (Cited on pages xviii, 139 and 140.)

[204] **ALICE** Collaboration, S. Acharya *et al.*, "D-meson azimuthal anisotropy in midcentral Pb–Pb collisions at $\sqrt{\mathbf{s}_{\rm NN}} = \mathbf{5.02}$ TeV", *Phys. Rev. Lett.* **120** no. 10, (2018) 102301, arXiv:1707.01005 [nucl-ex]. (Cited on page 139.)

[205] Z.-W. Lin, C. M. Ko, B.-A. Li, B. Zhang, and S. Pal, "A Multi-phase transport model for relativistic heavy ion collisions", *Phys. Rev. C* **72** (2005) 064901, arXiv:nucl-th/0411110. (Cited on pages xxi, 139, 166 and 167.)

[206] L. He, T. Edmonds, Z.-W. Lin, F. Liu, D. Molnar, and F. Wang, "Anisotropic parton escape is the dominant source of azimuthal anisotropy in transport models", *Phys. Lett. B* **753** (2016) 506–510, arXiv:1502.05572 [nucl-th]. (Cited on pages 140 and 166.)

[207] **ALICE** Collaboration, S. Acharya *et al.*, "Constraints on jet quenching in p–Pb collisions at $\sqrt{s_{\rm NN}} = 5.02$ TeV measured by the event-activity dependence of semi-inclusive hadron-jet distributions", *Phys. Lett. B* **783** (2018) 95–113, arXiv:1712.05603 [nucl-ex]. (Cited on pages 143 and 166.)

[208] **ALICE** Collaboration, S. Acharya *et al.*, "Energy dependence and fluctuations of anisotropic flow in Pb–Pb collisions at $\sqrt{s_{\rm NN}} = 5.02$ and 2.76 TeV", *JHEP* **07** (2018) 103, arXiv:1804.02944 [nucl-ex]. (Cited on pages xviii, xix, xx, 144, 146, 147, 164 and 165.)

[209] **ALICE** Collaboration, J. Adam *et al.*, "Azimuthal anisotropy of charged jet production in $\sqrt{s_{\rm NN}} = 2.76$ TeV Pb–Pb collisions", *Phys. Lett. B* **753** (2016) 511–525, arXiv:1509.07334 [nucl-ex]. (Cited on pages xxi, 147, 165, 166 and 167.)

[210] **ALICE** Collaboration, E. Abbas *et al.*, "J/ψ elliptic flow in Pb–Pb collisions at $\sqrt{s_{\rm NN}} = 2.76$ TeV", *Phys. Rev. Lett.* **111** (2013) 162301, arXiv:1303.5880 [nucl-ex]. (Cited on page 150.)

[211] Y. Sekiguchi, "The measurement of FMD v_2 in p–Pb collisions at 5.02 TeV",. https://alice-notes.web.cern.ch/system/files/notes/analysis/743/2019-10-20-ALICE_analysis_note.pdf. (Cited on page 154.)

[212] **ALICE** Collaboration, Y. Sekiguchi, "Measurement of long-range two- and multi-particle correlations by ALICE", *Nucl. Phys. A* **1005** (2021) 121795. (Cited on page 157.)

[213] Z.-W. Lin and L. Zheng, "Further developments of a multi-phase transport model for relativistic nuclear collisions", *Nucl. Sci. Tech.* **32** no. 10, (2021) 113, arXiv:2110.02989 [nucl-th]. (Cited on pages 161 and 166.)

[214] Z.-B. Kang, R. Lashof-Regas, G. Ovanesyan, P. Saad, and I. Vitev, "Jet quenching phenomenology from soft-collinear effective theory with Glauber gluons", *Phys. Rev. Lett.* **114** no. 9, (2015) 092002, arXiv:1405.2612 [hep-ph]. (Cited on pages xx and 165.)

[215] Y.-T. Chien, A. Emerman, Z.-B. Kang, G. Ovanesyan, and I. Vitev, "Jet Quenching from QCD Evolution", *Phys. Rev. D* **93** no. 7, (2016) 074030, arXiv:1509.02936 [hep-ph]. (Cited on pages xx and 165.)

[216] M. Djordjevic, B. Blagojevic, and L. Zivkovic, "Mass tomography at different momentum ranges in quark-gluon plasma", *Phys. Rev. C* **94** no. 4, (2016) 044908, arXiv:1601.07852 [nucl-th]. (Cited on pages xx and 165.)

[217] E. Bianchi, J. Elledge, A. Kumar, A. Majumder, G.-Y. Qin, and C. Shen, "The x and Q^2 dependence of $\hat{q}$, quasi-particles and the JET puzzle", arXiv:1702.00481 [nucl-th]. (Cited on pages xx and 165.)

[218] C. Andrés, N. Armesto, M. Luzum, C. A. Salgado, and P. Zurita, "Energy versus centrality dependence of the jet quenching parameter $\hat{q}$ at RHIC and LHC: a new puzzle?", *Eur. Phys. J. C* **76** no. 9, (2016) 475, arXiv:1606.04837 [hep-ph]. (Cited on pages xx and 165.)

[219] C. Loizides, J. Kamin, and D. d'Enterria, "Improved Monte Carlo Glauber predictions at present and future nuclear colliders", *Phys. Rev. C* **97** no. 5, (2018) 054910, arXiv:1710.07098 [nucl-ex]. [Erratum: Phys.Rev.C 99, 019901 (2019)]. (Cited on page 165.)

[220] H. Li, Z.-W. Lin, and F. Wang, "Charm quarks are more hydrodynamic than light quarks in final-state elliptic flow", *Phys. Rev. C* **99** no. 4, (2019) 044911, arXiv:1804.02681 [hep-ph]. (Cited on pages xxi, 166 and 167.)

[221] A. Bzdak and G.-L. Ma, "Elliptic and triangular flow in p+Pb and peripheral Pb–Pb collisions from parton scatterings", *Phys. Rev. Lett.* **113** no. 25, (2014) 252301, arXiv:1406.2804 [hep-ph]. (Cited on page 166.)

[222] **CMS** Collaboration, A. M. Sirunyan *et al.*, "Pseudorapidity and transverse momentum dependence of flow harmonics in p–Pb and Pb–Pb collisions", *Phys. Rev. C* **98** no. 4, (2018) 044902, arXiv:1710.07864 [nucl-ex]. (Cited on page 181.)

[223] C. Bierlich *et al.*, "Robust Independent Validation of Experiment and Theory: Rivet version 3", *SciPost Phys.* **8** (2020) 026, arXiv:1912.05451 [hep-ph]. (Cited on pages 187 and 188.)

[224] T. Pierog, I. Karpenko, J. M. Katzy, E. Yatsenko, and K. Werner, "EPOS LHC: Test of collective hadronization with data measured at the CERN Large Hadron Collider", *Phys. Rev. C* **92** no. 3, (2015) 034906, arXiv:1306.0121 [hep-ph]. (Cited on page 187.)

[225] C. Bierlich *et al.*, "Confronting experimental data with heavy-ion models: RIVET for heavy ions", *Eur. Phys. J. C* **80** no. 5, (2020) 485, arXiv:2001.10737 [hep-ph]. (Cited on pages xxii, 187, 188 and 189.)

[226] P. Skands, S. Carrazza, and J. Rojo, "Tuning PYTHIA 8.1: the Monash 2013 Tune", *Eur. Phys. J. C* **74** no. 8, (2014) 3024, arXiv:1404.5630 [hep-ph]. (Cited on pages 187, 189 and 190.)

[227] **CMS** Collaboration, V. Khachatryan *et al.*, "Event generator tunes obtained from underlying event and multiparton scattering measurements", *Eur. Phys. J. C* **76** no. 3, (2016) 155, arXiv:1512.00815 [hep-ex]. (Cited on page 187.)

[228] **ATLAS** Collaboration, G. Aad *et al.*, "Charged-particle multiplicities in pp interactions measured with the ATLAS detector at the LHC", *New J. Phys.* **13** (2011) 053033, arXiv:1012.5104 [hep-ex]. (Cited on page 187.)

[229] **ALICE** Collaboration, J. Adam *et al.*, "Measurement of pion, kaon and proton production in proton–proton collisions at $\sqrt{s} = 7$ TeV", *Eur. Phys. J. C* **75** no. 5, (2015) 226, arXiv:1504.00024 [nucl-ex]. (Cited on page 187.)

[230] **ATLAS** Collaboration, G. Aad *et al.*, "Differential top-antitop cross-section measurements as a function of observables constructed from final-state particles using pp collisions at $\sqrt{s} = 7$ TeV in the ATLAS detector", *JHEP* **06** (2015) 100, arXiv:1502.05923 [hep-ex]. (Cited on page 187.)

[231] B. Chokoufé Nejad, W. Kilian, J. M. Lindert, S. Pozzorini, J. Reuter, and C. Weiss, "NLO QCD predictions for off-shell $t\bar{t}$ and $t\bar{t}H$ production and decay at a linear collider", *JHEP* **12** (2016) 075, arXiv:1609.03390 [hep-ph]. (Cited on page 187.)

[232] M. Chala, R. Gröber, and M. Spannowsky, "Searches for vector-like quarks at future colliders and implications for composite Higgs models with dark matter", *JHEP* **03** (2018) 040, arXiv:1801.06537 [hep-ph]. (Cited on page 187.)

[233] A. Butter *et al.*, "The Machine Learning landscape of top taggers", *SciPost Phys.* **7** (2019) 014, arXiv:1902.09914 [hep-ph]. (Cited on page 188.)

[234] P. Hansen, J. W. Monk, and C. Wiglesworth, "A wavelet based pile-up mitigation method for the LHC upgrade", arXiv:1812.07412 [hep-ph]. (Cited on page 188.)

[235] "Rivet webpage",. https://rivet.hepforge.org/analyses.html. (Cited on page 188.)

[236] M. Dobbs and J. B. Hansen, "The HepMC C++ Monte Carlo event record for High Energy Physics", *Computer Physics Communications* **134** no. 1, (2001) 41–46. (Cited on page 188.)

[237] **ALICE** Collaboration, B. Abelev *et al.*, "Heavy flavour decay muon production at forward rapidity in proton–proton collisions at $\sqrt{s} = 7$ TeV", *Phys. Lett. B* **708** (2012) 265–275, arXiv:1201.3791 [hep-ex]. (Cited on pages xxii, 189, 190, 191, 192, 193 and 194.)

[238] **ATLAS** Collaboration, G. Aad *et al.*, "Measurements of the electron and muon inclusive cross-sections in proton-proton collisions at $\sqrt{s} = 7$ TeV with the ATLAS detector", *Phys. Lett. B* **707** (2012) 438–458, arXiv:1109.0525 [hep-ex]. (Cited on page 190.)

Publication list

1. **Production of muons from heavy-flavour hadron decays at high transverse momentum in Pb–Pb collisions at $\sqrt{s_{\rm NN}}$ = 5.02 and 2.76 TeV**
   ALICE Collaboration, PC members: X. Zhang (chair), Z. Zhang, S. Tang, N. Bastid, P. Crochet, D. Zhou
   Phys. Lett. B 820 (2021) 136558

2. **Measurements of azimuthal anisotropies at forward and backward rapidity with muons in high-multiplicity p–Pb collisions at $\sqrt{s_{\rm NN}}$ = 8.16 TeV**
   ALICE Collaboration, PC members: N. Bastid (chair), S. Tang, X. Zhang, N. Bastid, P. Crochet, D. Zhou
   within internal ALICE review, aiming for *Phys. Lett. B*

3. **Azimuthal anisotropy of jet particles in p–Pb and Pb–Pb collisions at $\sqrt{s_{\rm NN}}$ = 5.02 TeV**
   ALICE Collaboration, PC members: S. Tang (chair), C. Cheshkov, X. Zhang, N. Bastid
   within internal ALICE review, aiming for *Phys. Rev. Lett*

4. **Recent results on azimuthal anisotropies of open heavy-flavour particles with ALICE at the LHC**
   S.Tang (for the ALICE collaboration), Quark Matter 2019 conference proceedings
   Nuclear Physics A 1005 (2021) 121768

5. **Measurement of jet-particle v_2 in p–Pb and Pb–Pb collisions at 5.02 TeV with ALICE at LHC**
   S.Tang (for the ALICE collaboration), EPS2021 conference proceedings
   PoS EPS-HEP2021 (2022) 313

6. As a member of the ALICE collaboration ($\sim$ 106)

Analysis notes

1. S. Tang, et al, Open heavy-flavour hadron decay muon v_2 in p–Pb/Pb–p collisions at $\sqrt{s_{\rm NN}}$ = 8.16 TeV with ALICE, ALICE-ANA-778

2. S. Tang, et al, Measurement of Charge Particle v_2 in Jets in p–Pb/Pb–Pb collisions at 5.02 TeV with ALICE, ALICE-ANA-1101

3. S. Tang, et al, Production of muons from heavy-flavour hadron decays at forward rapidity in Pb–Pb collisions at $\sqrt{s_{\rm NN}}$ = 5.02 TeV and and pp collisions at $\sqrt{s}$ = 5.02 TeV, ALICE-ANA-519

Presentations list

1. S. Tang (for the ALICE collaboration), "Recent results on azimuthal anisotropies of open heavy-flavour particles with ALICE at the LHC", QM2019, The 28th International Conference on Ultra-relativistic Nucleus-Nucleus Collisions, Nov. 3-9, 2019, Wuhan, China

2. S. Tang (for the ALICE collaboration), "Measurement of jet-particle v_2 in p–Pb and Pb–Pb collisions at 5.02 TeV with ALICE at LHC", European Physical Society Conference on High Energy Physics, July. 27th, 2021, online

3. S. Tang (for the ALICE collaboration), "Open heavy-flavour hadron decay muon v_2 in p-Pb collisions at 8.16 TeV with ALICE at LHC", QM2019, The 28th International Conference on Ultra-relativistic Nucleus-Nucleus Collisions, Nov. 3-9, Wuhan, China (poster)

4. S. Tang (for the ALICE collaboration), "The Measurement of jet-particle v_2 in p-Pb collisions at 5.02 TeV with ALICE at the LHC", The 6th. International Conference on Initial Stages of high-energy nuclear Collisions, Jan. 10th, 2021 (poster)

5. S. Tang (for the ALICE collaboration), "Open heavy-flavour hadron decay muon v_2 in p–Pb collisions at 8.16 TeV with ALICE at LHC", 148th LHCC, CERN (Geneve), Nov.18th, 2021 (poster)

6. S. Tang (for the ALICE collaboration), "Azimuthal anisotropy with muons and jet associated particles in small collision systems with ALICE", 13th France China Particle Physics Laboratory Workshop (FCPPL2021), 14th Dec. 2021, online

7. S. Tang (for the ALICE collaboration), "Study of Elliptic Flow of Open-Heavy Flavour Decay Leptons", The 7th Asian Triangle Heavy-Ion Conference, November 3-6, 2018, USTC, Hefei, China

8. S. Tang (for the ALICE collaboration), "Study of Elliptic Flow of Muons in p-Pb/Pb-p Collisions at 8.16 TeV ", International Muon Workshop, 26 February-2 March, 2018, AMU Aligarh and Agra, India

9. S. Tang (for the ALICE collaboration), "Elliptic Flow of Inclusive Muons in p-Pb/Pb-p Collisions at 8.16 TeV", International Muon Workshop, 1st April-5th April, 2019, Cape Town, South Africa

10. S. Tang (for the ALICE collaboration), "Open Heavy-flavour Decay Muon Flow in Small Systems with ALICE", Rencontres QGP-France, July 1-4, 2019, Etretat, France

11. S. Tang (for the ALICE collaboration), "Open Heavy-flavour Measurements at Forward Rapidity", ALICE Physics Week, July 22-26, 2019, Prague, Czech Republic

12. S. Tang (for the ALICE collaboration), "Elliptic Flow of Inclusive Muons in p-Pb Collisions at 8.16 TeV", ALICE Physics Forum, Dec.18th, 2019, CERN

13. S. Tang (for the ALICE collaboration), "The measurement of charged-particle v_2 in Jet in p-Pb/Pb-Pb Collisions at 5.02 TeV", ALICE Physics Forum, Apr. 21st, 2021

14. Presentations in meetings of the ALICE Collaboration ($\sim$60)

Résumé détaillé en français

Ce manuscript représente le travail de thèse, réalisé auprès de l'expérience ALICE au CERN, et ayant pour objectif la mesure des muons de décroissance des hadrons charmés et beaux aux grandes rapidités et des particules associées aux jets aux rapidités centrales dans les collisions Pb–Pb à une énergie dans le centre de masse $\sqrt{s_{\rm NN}} = 2.76$ et 5.02 TeV et p–Pb à $\sqrt{s_{\rm NN}} = 5.02$ et 8.16 TeV. Ce résumé débute par une introduction sur l'étude des collisions d'ions lourds et des systèmes de petite dimension. Il s'en suit une description du détecteur ALICE. La stratégie d'analyse est brièvement présentée et les résultats obtenus sont discutés et confrontés à des prédictions théoriques.

Introduction

Collisions d'ions lourds et étude expérimentale du plasma de quarks et gluons

Les collisions d'ions lourds à haute énergie représentent un champ de recherche qui fait l'objet d'une activité intense depuis la fin des années 80. Le but est d'étudier les propriétés d'un nouvel état de la matière, le plasma de quarks et de gluons (QGP), qui se forme dans des conditions extrêmes de température et de pression. La théorie de l'interaction forte, la Chromodynamique Quantique, prédit que la température critique et la densité d'énergie critique correspondant à la transition de phase vers le QGP sont respectivement $T_{\rm c} = 154 \pm 9$ MeV et $\varepsilon_{\rm c} = 0,34 \pm 0.16$ GeV/fm^3. De telles conditions sont souvent qualifiées d'extrêmes. En unités courantes, elles correspondent à une densité de 10^{15}g/cm^3 et une température de 10^{12}K. Ces conditions sont celles dans lesquelles baignait l'univers quelques microsecondes après le big bang. Le QGP peut être créé en laboratoire en faisant entrer en collision des noyaux lourds, tels que l'or ou le plomb, préalablement accélérés à des vitesses proches de celle de la lumière. De telles collisions entre ions lourds, dites ultra-relativistes, permettent d'étudier les propriété d'un système de matière partonique dense et chaud.

La Figure 10 présente l'évolution spatio-temporelle d'une collision d'ions lourds ultra-relativistes qui peut être résumée comme suit :

- **Etat initial :** Les noyaux sont accélérés à des vitesses proche de la vitesse de la lumière. Dans le référentiel du laboratoire, ils sont applatis dans la direction du faisceau en raison de la contraction de Lorentz. Aux énergies du LHC, le facteur de contraction de Lorentz est $\gamma \sim 1500$. Les noyaux sont alors comprimés dans $\sim 0,01$ fm, d'où leur aspect en forme de crèpe. Les nucléons des deux noyaux entrant en collision sont appelés les participants. Leur nombre total est noté $N_{\rm part}$. Les autres nucléons sont appelés les spectateurs. Le nombre total d'interactions binaires est noté $N_{\rm coll}$. La distance entre le centre des noyaux en collision dans la direction perpendiculaire aux faisceaux est appelée

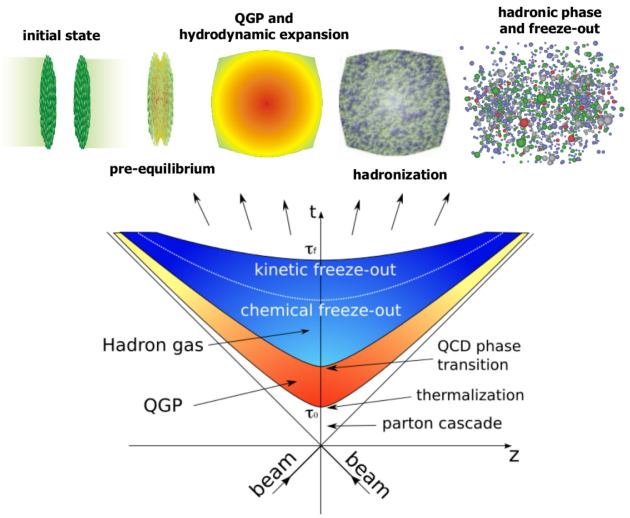

Figure 10: Représentation schématique de l'évolution spatio-temporelle d'une collision d'ions lourds ultra-relativistes.

le paramètre d'impact et noté b. Le degré de centralité de la collision peut être estimé de façon purement géométrique au moyen du modèle de Glauber optique.

- **Pré-équilibre :** La collision se produit dans la région de recouvrement des noyaux en collision et une grande quantité d'énergie est déposée au voisinage du point d'impact. Des partons sont produits dans cet environnement de haute densité d'énergie au moyen de processus durs ($\tau \sim 0$). L'état de pré-équilibre dure pendant un temps typique de $\tau \sim 1$ fm/c. Les particules de grand moment transverse (jets, quarks lourds et photons) sont principalement produites pendant cette phase. En particulier, les quarks charmés sont produits sur une échelle de temps de $1/2m_{\mathrm{Q}} \sim 0,1$ fm/c.

- **QGP :** Si la densité d'énergie est suffisamment élevée, le système atteint le QGP, phase de déconfinement caractérisée par des degrés de liberté quarkoniques et gluoniques. Cette phase dure pendant un temps typique de l'ordre de 10 fm/c aux énergies du LHC.

- **Hadronisation et freeze-out :** Le système se détend et se refroidit. La température décroît en deçà de la température critique T_{c}. Il en résulte une transition de phase entre le QGP et un gaz hadronique. Durant cette étape, des sous-systèmes QGP et gaz hadronique peuvent co-exister. Les interactions inélastiques entre hadrons continuent jusqu'au freeze-out chimique après lequel les interactions élastiques entre hadrons continuent jusqu'au freeze-out cinétique. Finalement, les particules produites (hadrons et leptons principalement) sont identifiées par les détecteurs.

Jusqu'à maintenant plusieurs expériences de collisions d'ions lourds ultra-

relativistes ont été menées auprès du SPS (Super Proton Synchrotron) et du LHC (Large Hadron Collider) au CERN (Centre Européen pour la Recherche Nucléaire) et auprès du RHIC (Relativistic Heavy Ion Collider) au BNL (Brookhaven National Laboratory) aux Etats Unis. De nombreuses signatures de la formation du QGP en laboratoire ont été obtenues. Parmi les signatures historiques, nous avons citer l'abondance des hadrons produits lors des collisions, l'augmentation de l'étrangeté, l'écoulement collectif et l'atténuation des jets de particules.

Les sondes dures, comme par exemple les quarks lourds (charme et beauté) et jets de particules, figurent parmi les sondes les plus pertinentes du QGP. Ils sont produits dans les processus durs aux tous premiers instants de la collision et se propagent ensuite dans le milieu dense et chaud produit dans les collisions en interagissant avec ses constituants. Ces interactions résultent en une perte d'énergie via des radiations de gluons et/ou des diffusions élastiques. Des prédictions théoriques indiquent que cette perte d'énergie dépend de la densité du milieu, de la distance parcourue par le parton dans le milieu et de la saveur du parton. La perte d'énergie est souvent appelée atténuation des jets ou *jet quenching*. A cause de la dépendance en masse et en charge de couleur des pertes d'énergie on s'attend à ce que ces dernières soient plus importantes pour les partons légers que pour les partons lourds suivant $\Delta E_{\mathrm{g}} > \Delta E_{\mathrm{u,d,s}} > \Delta E_{\mathrm{c}} > \Delta E_{\mathrm{b}}$. Expérimentalement, les effets de perte d'énergie peuvent être mis en évidence au moyen du facteur de modification nucléaire R_{AA}. Ce dernier est défini comme le rapport du taux de production d'une certaine particule mesuré dans les collisions noyau-noyau sur celui mesuré dans les collisions proton-proton puis multiplié par le nombre de collisions nucléon-nucléon dans la classe de collisions noyau-noyau considérée. En l'absence de perte d'énergie résultant du QGP, $R_{\mathrm{AA}} = 1$ à grand p_{T} tandis qu'un $R_{\mathrm{AA}} < 1$ reflète la perte d'énergie décrite ci-dessus. L'ordonnancement des pertes d'énergie des partons se traduit aussi par une hiérarchisation des facteurs de modification nucléaire à grand p_{T} : $R_{\mathrm{AA}}(\mathrm{g}) < R_{\mathrm{AA}}(\mathrm{u,d,s}) < R_{\mathrm{AA}}(\mathrm{c}) < R_{\mathrm{AA}}(\mathrm{b})$.

Le R_{AA} des particules chargées, mésons D, J/ψ (prompt et non-prompt) et pions mesuré à mi-rapidité dans les collisions Pb–Pb centrales à $\sqrt{s_{\mathrm{NN}}} = 5{,}02$ TeV est présenté sur la Figure 11. Cette observable est maximale pour des impulsions transverses de l'ordre de 2 GeV/c. Le R_{AA} décroît ensuite avec p_{T} dans l'intervalle $2 \lesssim p_{\mathrm{T}} \lesssim 7$ GeV/c. Une forte suppression ($R_{\mathrm{AA}} \sim 0,15$ pour les pions) est observée dans cette région où la hiérarchisation des R_{AA} est mise en évidence. Finalement le R_{AA} atteint 0.4 pour $p_{\mathrm{T}} \approx 50$ GeV/c.

L'asymétrie azimutale est aussi une observable clé pour l'étude des propriétés du QGP. Dans les collisions semi-centrales, la zone de recouvrement des noyaux en collision est anisotrope. Cette anisotropie spatiale initiale se reflète en une anisotropie de la distribution de impulsions finales des particules produites. La distribution azimutale des particules produites peut être décomposée en une série de Fourier de l'angle azimutal via l'équation (1) où Ψ_n est l'angle du plan de réaction de l'harmonique d'ordre n et v_n est l'amplitude pour l'harmonique n défini dans l'équation (2). Le coefficient v_2, l'écoulement elliptique, présente en particulier des sensibilités au comportement collectif du milieu produit aux faibles $\mathrm{p_T}$ et aux effets de perte d'énergie pour les grands $\mathrm{p_T}$. Les coefficients d'ordre supérieur, v_3 et v_4 en particulier, donnent

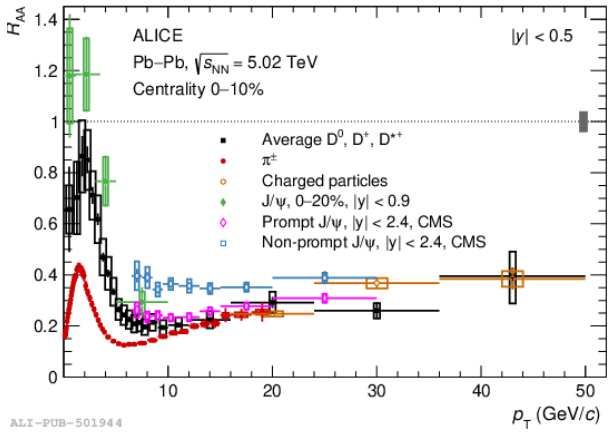

Figure 11: Facteur de modification R_{AA} de différentes particules en fonction de p_{T} dans les collisions Pb–Pb centrales à $\sqrt{s_{\mathrm{NN}}} = 5{,}02$ TeV.

des informations concernant les fluctuations dans l'état initial. Diverses méthodes expérimentales sont utilisées pour extraire les coefficients v_2 comme la méthode du plan de réaction, les corrélations à deux particules, les cumulants à multi-particules, le produit scalaire et la méthode des *Lee-Yang zeroes*.

$$\frac{dN}{d\varphi} \propto 1 + 2\sum_{n=1}^{\infty} v_n \cos[n(\varphi - \Psi_n)], \tag{1}$$

$$v_n = < \cos[\mathrm{n}(\varphi - \Psi_n)] > \tag{2}$$

La Figure 12 montre l'évolution des coefficients v_2 et v_3 fonction de p_{T} dans les collisions Pb–Pb centrales et semi-centrales à $\sqrt{s_{\mathrm{NN}}} = 5.02$ TeV pour différentes particules. Comme attendu, le coefficient v_2 est plus important dans les collisions semi-centrales. Dans la région des faibles p_{T}, on observe que l'écoulement elliptique des mésons D est plus faible que celui des pions et protons, comme attendu d'un système hydrodynamique en expansion radiale. Dans la zone des p_{T} intermédiaires ($5 < p_{\mathrm{T}} < 8$ GeV/c) on observe que $v_2(\mathrm{D}) \sim v_2(\pi^{\pm}) < v_2(\mathrm{p})$ et que à plus grand p_{T} le v_2 est indépendant de la particule produite. Ce comportement résulte respectivement de la production de particules via le mécanisme de coalescence et de la dépendance de la perte d'énergie à la distance parcourue par le parton dans le milieu. Le coefficient v_3 suit la même évolution en fonction de p_{T} que v_2 mais avec une amplitude plus faible.

Les collision nucléon–noyau

La compréhension et la caractérisation du plasma de quarks et gluons formé dans les collisions d'ions lourds (collisions Pb–Pb au LHC) nécessite une connaissance détaillée des systèmes légers, tels que les collisions pp et p–Pb. Il est notamment

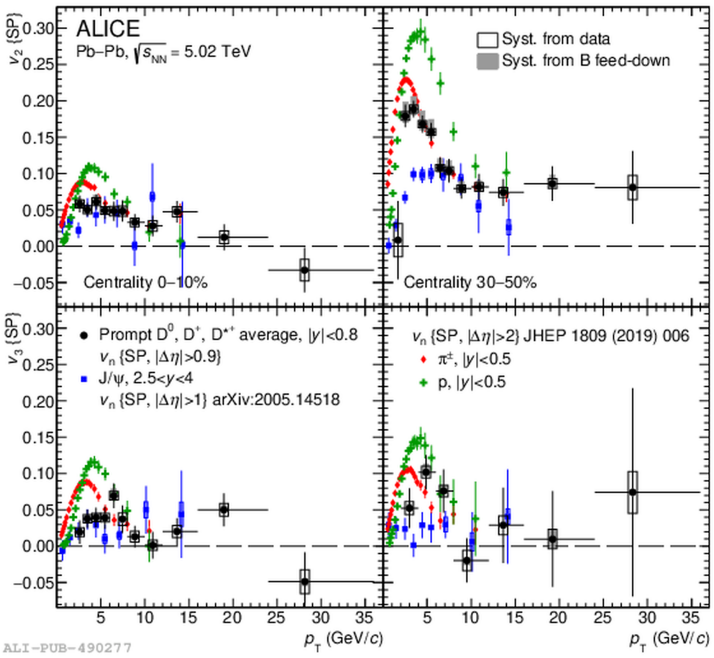

Figure 12: Mesure des coefficients v_2 (haut) et v_3 (bas) de différentes particules dans les collisions Pb–Pb centrales (gauche) et semi-centrales (droite) à $\sqrt{s_{\mathrm{NN}}}$ = 5,02 TeV.

essentiel de pouvoir quantifier les effets nucléaires dits froids qui ne sont pas directement engendrés par la présence du QGP. Ces effets nucléaires froids peuvent être évalués au moyen des collisions nucléon-noyau (p–Pb au LHC) en supposant qu'un système dense et chaud n'est pas produit dans ces collisions. Ces effets nucléaires froids concernent la modification des fonctions de distribution de partons (PDF) du noyau de Pb. Nous avons aussi l'effet Cronin résultant de multiples diffusions élastiques qui conduisent à un élargissement de la distribution en p_{T} des partons et au renforcement de la production de particules produites dans la région des p_{T} intermédiaires. Un autre possible effet nucléaire froid est la perte cohérente d'énergie ou la perte radiative d'energie des partons dans un milieu froid. Cet effet tend à diminuer la production de particules.

La Figure 13 présente le facteur de modification nucléaire R_{pPb} des particules chargées émises dans l'intervalle en pseudo-rapidité $|\eta_{\mathrm{cms}}| < 0,3$ pour les collisions p–Pb à $\sqrt{s_{\mathrm{NN}}} = 5{,}02$ TeV. Alors que le R_{pPb} est maximum dans l'intervalle $2 < p_{\mathrm{T}} < 6$ GeV/c (effet Cronin), il devient compatible avec l'unité dans la région des grands p_{T} confirmant que la forte suppression des taux de production des particules produites dans les collisions Pb–Pb centrales est dûe au milieu dense et chaud créé dans ces collisions.

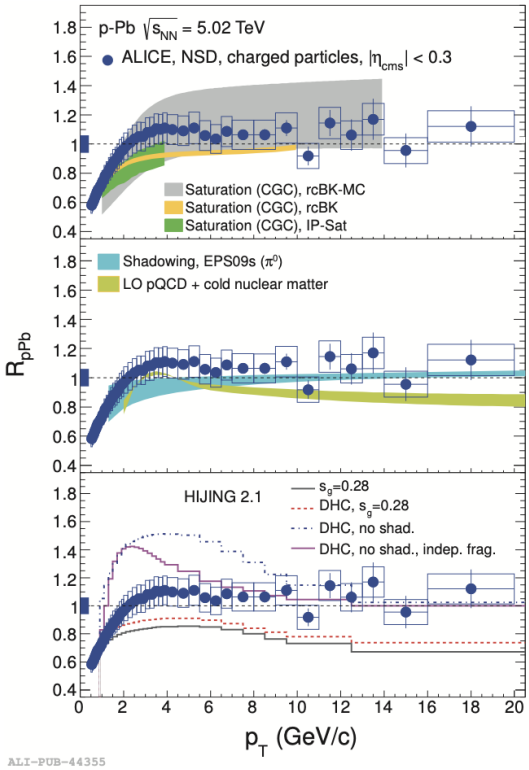

Figure 13: Facteur de modification nucléaire des particules chargées émises dans l'intervalle $|\eta_{\mathrm{cms}}| < 0,3$ dans les collisions p–Pb à $\sqrt{s_{\mathrm{NN}}} = 5{,}02$ TeV. Les données sont comparées à diverses prédictions théoriques.

Les collisions p–Pb sont aussi intensivement étudiées depuis la mise en évidence d'effets collectifs similaires à ceux observés dans les collisions d'ions lourds et attribués à la présence du QGP. En effet, une anisotropie azimutale quantifiée via le coeeficient v_2 est observée, comme illustré sur la Figure 14. L'origine de ces effets dans les petits systèmes est encore fortement débatue.

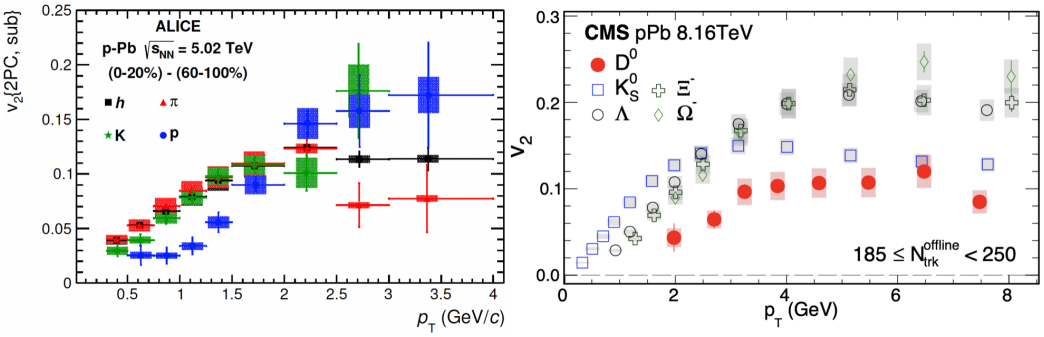

Figure 14: Coefficient v_2 en fonction de p_{T} pour différentes particules émises à mi-rapidité dans les collisions centrales p–Pb à $\sqrt{s_{\mathrm{NN}}} = 5{,}02$ TeV (gauche) et 8,16 TeV (droite).

L'expérience ALICE

Le détecteur ALICE (*A Large Ion Collider Experiment*) a été concu pour étudier le QGP produit dans les collisions d'ions lourds aux énergies du LHC. La collaboration ALICE se compose de 2042 membres de 172 instituts répartis dans 40 pays. Le détecteur ALICE (Figure 15) est optimisé pour supporter les importantes multiplicités de particules attendues dans les collisions d'ions lourds. Il est constitué i) d'une partie centrale (tonneau central) utilisée pour la reconstruction du vertex primaire, la trajectographie des particules chargées, l'identification des électrons, photons, hadrons et détection des gerbes hadroniques, ii) d'un spectromètre pour la mesure des muons dans la région avant, et iii) de détecteurs globaux fournissant des informations sur les collisions comme la multiplicité, la centralité de la collision et le plan de réaction. Ces détecteurs globaux sont aussi utilisés dans le système de déclenchement et pour la réjection du bruit de fond.

Les principaux détecteurs qui ont été utilisés dans les analyses sont présentés brièvement ci-dessous :

- la chambre à projection temporelle (TPC, *Time Projection Chamber*) est un détecteur gazeux cylindrique entourant l'ITS. La TPC assure la reconstruction des trajectoires des particules chargées de 0,1 à 100 GeV/c ainsi que leur quantité de mouvement, permet de reconstruire les vertex de désintégration et d'identifier les particules chargées avec une résolution allant jusqu'à 5,5% ;
- le système de trajectographie interne (ITS, *Inner Tracking System*) se compose de six couches de détecteurs en silicone. Les deux couches les plus internes

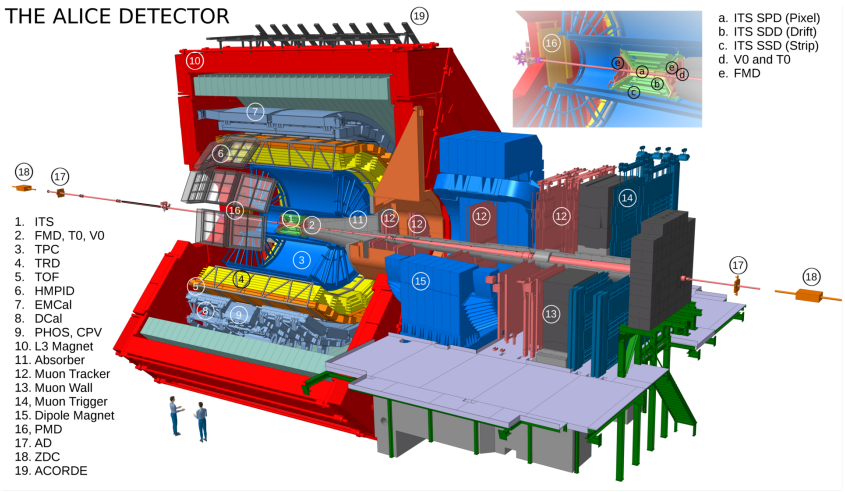

Figure 15: Vue schématique du détecteur ALICE.

constituent le SPD (*Silicon Pixel Detector*). L'ITS est utilisé pour reconstruire le vertex d'interaction et les vertex secondaires, et assiste la chambre à projection temporelle pour la reconstruction et identification des particules chargées ;

- le spectromètre à muons permet la mesure des quarkonia, des hadrons de saveurs lourdes, des résonances de basse masse ainsi que des bosons W et Z dans leur canal de désintégration (di)muonique dans le domaine en pseudo-rapidité $-4 < \eta < -2,5$;

- le V0 constitué de deux hodoscopes de scintillateurs sert de déclencheur. Il est aussi utilisé pour la réjection du bruit de fond, l'évaluation de la centralité de la collision et la mesure de la luminosité ;

- le calorimètre à zéro degré (ZDC, *Zero Degree Calorimeter*) est formé de deux calorimètres placés de part et d'autre du point d'interaction pour la détection de protons et neutrons le long de la ligne de faisceau. Il est utilisé notamment pour la caractérisation des collisions ;

- le détecteur de multiplicité à petit angle (FMD, *Forward Multiplicity Detector*) est utilisé dans cette thèse pour la mesure du coefficient v_2 des particules associées aux jets.

Le spectromètre à muons d'ALICE (Figure 16) est composé d'un absorbeur frontal (pour réduire le bruit de fond), d'un blindage des faisceaux (pour protéger les détecteurs des particules provenant des faisceaux), d'un aimant dipolaire (qui permet de courber les trajectoires des particules chargées), de 5 stations de tracking (pour la reconstruction des traces) et de 2 stations de trigger (pour l'identification des muons et le déclenchement). Un mur de fer de 1,2 m est placé devant les stations de trigger pour protéger le système de trigger des hadrons "punch-through".

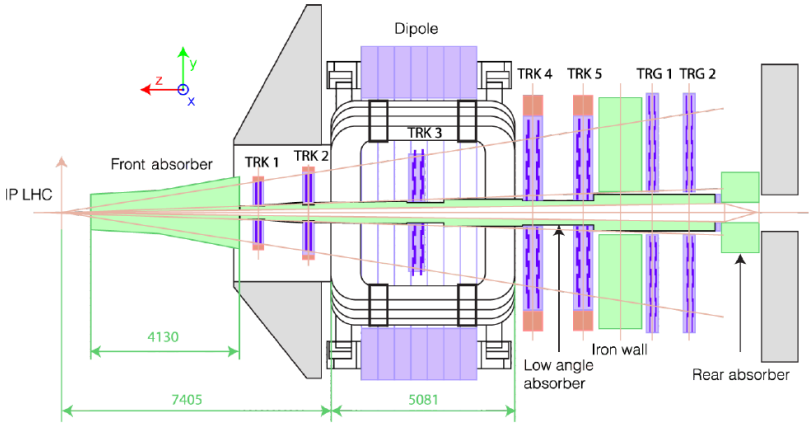

Figure 16: Vue schématique du spectromètre à muons d'ALICE.

De plus, un absorber arrière est placé derrière les stations de trigger pour protéger le système des particules dans les faisceaux et arrivant dans la direction opposée au point d'interaction.

L'environnement d'analyse hors ligne d'ALICE comprend *AliRoot* et *AliPhysics* et exploite les fonctionalités fournies par l'environnement ROOT. Cet environnement permet d'effectuer toutes les tâches, telles que simulation, reconstruction, calibration, alignement, visualisation et analyse, visant à extraire les informations de physique des mesures expérimantales.

Cette thèse utilise les détecteurs de la partie centrale d'ALICE, TPC et ITS en particulier, pour étudier l'asymétrie azimutale des particules chargées associées aux jets. Les résultats utilisant ls spectromètre à muons concernent la production de muons issus de la désintégration des hadrons de saveurs lourdes dans les collisions Pb–Pb à $\sqrt{s_{\rm NN}} = 2,76$ et $5,02$ TeV ainsi que la mesure de l'asymétrie azimutale des muons dans les collisions p–Pb à $\sqrt{s_{\rm NN}} = 8,16$ TeV.

Résultats et discussions

Mesure de la production des muons issus de la désintégration des hadrons charmés et beaux

Cette analyse, publiée dans la revue *PLB 820 (2021) 136558*, utilise l'échanlon de données enregistré par ALICE pendant le run 2015 concernant les collisions Pb–Pb à $\sqrt{s_{\rm NN}} = 5{,}02$ TeV. Pour les comparaisons avec les mesures à plus basse énergie (Pb–Pb à $\sqrt{s_{\rm NN}} = 2{,}76$ TeV), les données enregistrées en 2011 sont utilisées pour étendre le domaine en $p_{\rm T}$ par rapport à celui des résultats déjà publiés. L'analyse de ces échantillons de données est basée sur des événements déclenchés sur la présence de muons qui demandent la coïncidence du déclenchement de biais minimum et la présence d'au moins une trace dans le système de déclenchement des muons avec un

p_{T} supérieur au seuil programmé conduisant à une efficacité de 50%. Les données Pb–Pb ont été collectées avec des seuils en p_{T} de 1 GeV/c (0,5 GeV/c) et 4,2 GeV/c (4,2 GeV/c) à $\sqrt{s_{\mathrm{NN}}}$ = 5,02 (2,76) TeV. Dans la suite, les échantillons collectés avec le bas et haut seuil en p_{T} sont respectivement appelés MSL et MSH. Le bruit de fond engendré par les faisceaux est réduit hors ligne en utilisant l'information en temps délivrée par les détecteurs V0 et ZDC. Les interactions électromagnétiques sont soustraites en appliquant un seuil à l'énergie déposée dans le ZDC. De plus, seuls les événements avec un vertex primaire situé dans une fenêtre de ± 10 cm le long de la ligne des faisceaux sont considérés. Enfin, les analyses sont limitées aux collisions correspondant à la tranche en centralité 0–90%. Après toutes les coupures de sélection, les échantillons de données Pb–Pb correspondent à une luminosité intégrée d'environ 21.9 (224,8) $\mu\mathrm{b}^{-1}$ et 4 (71) $\mu\mathrm{b}^{-1}$ pour les événements MSL (MSH) respectivement à $\sqrt{s_{\mathrm{NN}}}$ = 5,02 et 2,76 TeV. Les sélections standard sont appliquées aux traces des muons candidats. Ces traces doivent être reconstruites dans l'intervalle en pseudo-rapidité $-4 < \eta < -2,5$ et doivent avoir un angle polaire mesuré à la sortie de l'absorbeur dans l'intervalle $170° < \Theta_{\mathrm{abs}} < 178°$. De plus, les traces sont identifiées comme correspondant à des muons si elle coïncident avec des segments de traces dans le système de déclenchement. Enfin, une sélection sur la distance de la trace au vertex primaire dans le plan transverse pondérée par son impulsion est appliquée pour rejeter le bruit de fond induit par les faisceaux qui subsiste.

Le R_{AA} des muons de désintégration des saveurs lourdes est mesuré de p_{T} = 3 GeV/c à p_{T} = 20 GeV/c dans toutes les classes en centralité de l'intervalle 0–80% à $\sqrt{s_{\mathrm{NN}}}$ = 5,02 TeV et dans la classe en centralité 0–10% à $\sqrt{s_{\mathrm{NN}}}$ = 2,76 TeV en combinant les événements déclenchés MSL et MSH jusqu'à p_{T} = 7 GeV/c et au delà de cette valeur. Dans l'intervalle en p_{T} sélectionné, le bruit de fond qui subsiste et doit être soustrait provient des muons de désintégration des pions et kaons chargés primaires et secondaires pour des p_{T} petits et intermédiaires et des muons de désintégration des W et Z/γ^* à plus haut p_{T}. De plus, une composante de muon de désintégration des J/ψ, bien que relativement faible sur l'ensemble de l'intervalle en p_{T} considéré, est également soustraite. Les taux de production de muons inclusifs dans les collisions Pb–Pb sont corrigés de l'acceptance du détecteur et de l'efficacité de reconstruction et de déclenchement ($A \times \varepsilon$) en utilisant la procedure utilisée pour les analyses précédentes. Cette dernière atteint 90% sans, ou presque, dépendance en p_{T} dans la région explorée pour les événements de type MSL, tandis que pour les événements de type MSH, $A \times \varepsilon$ augmente avec p_{T} et sature à une valeur proche de 90% pour $p_{\mathrm{T}} > 14$ GeV/c. De plus, la dépendance de l'efficacité de reconstruction et de déclenchement à l'occupation du détecteur a été déterminée en injectant les muons (générés) de désintégration des saveurs lourdes dans des événements simulés Pb–Pb de biais minimum. Une diminution de l'efficacité de 6% des collisions périphériques (60–80%) vers les collisions centrales (0–10%), sans dépendence au p_{T}, est observée.

L'estimation de la contribution des muons de désintégration des pions et kaons primaires chargés est basée sur une simulation de type Monte-Carlo ajustée sur les données. Cette contribution diminue avec l'augmentation du p_{T} d'environ 21%

(13%) pour $p_{\mathrm{T}} = 3$ GeV/c à environ 7% (4%) pour $p_{\mathrm{T}} = 20$ GeV/c dans la classe en centralité 60–80% (0–10%). Cette dépendance en p_{T} est relativement faible pour $p_{\mathrm{T}} > 10$ GeV/c. La contribution des muons de désintégration des pions and kaons secondaires est estimée au moyen de simulations complètes avec le générateur HIJING et GEANT3. Cette contribution représente environ 9% de la composante des muons de désintégration des pions et kaons primaires. L'estimation de la contribution des muons de désintégration des bosons Z et des γ^* (processus Drell-Yan), pertinente dans la région des hauts p_{T}, est effectuée au moyen du générateur d'événements POWHEG NLO couplé à PYTHIA 6.4.25. Cette contribution est négligeable pour $p_{\mathrm{T}} < 13$ GeV/c et augmente avec p_{T} et la centralité, passant d'environ 3% (6%) pour $p_{\mathrm{T}} = 14$ GeV/c à 18% (36%) à $p_{\mathrm{T}} = 20$ GeV/c dans la classe de centralité 60–80% (0–10%). Finalement, la contribution des muons de désintégration des J/ψ est aussi estimée au moyen d'une simulation Monte-Carlo utilisant les mesures de J/ψ dans le canal dimuonique. Dans les collisions les plus centrales (0–10%), la contribution relative de ces muons varie de 0.5 à 4 %, la fraction maximale étant atteinte pour des p_{T} intermédiaires ($4 < p_{\mathrm{T}} < 6$ GeV/c). La référence pp de la section efficace de production à la même énergie que celle des collisions Pb–Pb à $\sqrt{s_{\mathrm{NN}}} = 5{,}02$ TeV, indispensable au calcul du facteur de modification nucléaire R_{AA} est publiée (*JHEP 09 (2019) 008*).

L'incertitude systématique sur le R_{AA} des muons de désintégration des saveurs lourdes est évaluée en considérant les sources suivantes: taux de production des muons inclusifs et contributions du bruit de fond dans les collisions Pb–Pb, référence pp et normalisation dans les collisions pp et Pb–Pb.

Pour une comparaison directe avec les mesures effectuées à plus basse énergie dans le même domaine en p_{T}, les données Pb–Pb collectées à $\sqrt{s_{\mathrm{NN}}} = 2{,}76$ TeV ont été analysées. Comme présenté dans la suite, ceci permet d'étendre considérablement le domaine en p_{T} du R_{AA} des muons de désintégration des saveurs lourdes qui était précédemment limité à $4 < p_{\mathrm{T}} < 10$ GeV/c. Une telle amélioration est rendue possible grace à la luminosité supérieure et à l'utilisation du déclencheur à haut p_{T}. La stratégie pour extraire les taux de production des muons de désintégration des saveurs lourdes dans les collisions Pb–Pb à $\sqrt{s_{\mathrm{NN}}} = 2{,}76$ TeV est similaire à celle utilisée à $\sqrt{s_{\mathrm{NN}}} = 5{,}02$ TeV. La section efficace différentielle en p_{T} des muons de désintégration des saveurs lourdes dans les collisions pp à $\sqrt{s_{\mathrm{NN}}} = 2{,}76$ TeV dans l'intervalle en rapidité $2{,}5 < y < 4$ qui est utilisée pour le calcul du R_{AA} est celle publiée dans l'intervalle $3 < p_{\mathrm{T}} < 10$ GeV/c. Elle est extrapolée jusqu'à $p_{\mathrm{T}} = 20$ GeV/c en utilisant le rapport entre les données et les calculs "fixed-order plus next-to-leading logarithms" (FONLL).

Le R_{AA} différentiel en p_{T} des muons de désintégration des saveurs lourdes dans l'intervalle en rapidité $2.5 < y < 4$ dans les collisions Pb–Pb à $\sqrt{s_{\mathrm{NN}}} = 5.02$ TeV est présenté sur la Figure 17 pour les collisions centrales (0–10%), semi-centrales (20-40%) et périphériques (60-80%). Une augmentation de la suppression du taux de production de muons en fonction de la centralité par rapport à la référence pp multipliée par la fonction de recouvrement nucléaire moyenne est clairement observée. Cette suppression est maximale aux p_{T} intermédiaires, dans l'intervalle $6 < p_{\mathrm{T}} < 8$

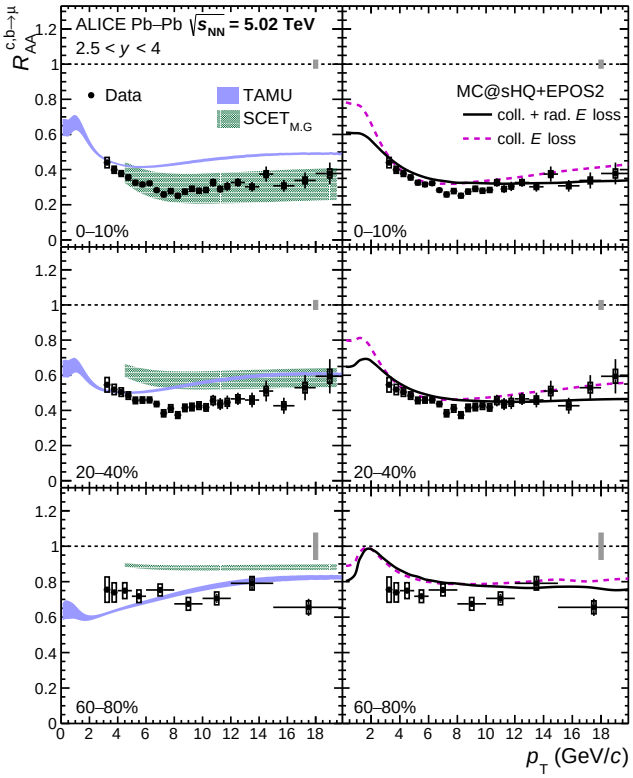

Figure 17: Facteur de modification nucléaire en fonction de p_{T} pour les muons de désintégration des saveurs lourdes aux rapidité avant ($2,5 < y < 4$) dans les collisions Pb–Pb centrales (0–10%, haut), semi-centrales (20–40%, milieu) et périphériques (60–80%, bas) à $\sqrt{s_{\mathrm{NN}}} = 5{,}02$ TeV. Les incertitudes statistiques (barres verticales) et les incertitudes systématiques (boites) sont montrées. Les boites centrées à $R_{\mathrm{AA}} = 1$ représentent les incertitudes de normalisation. Les barres horizontales représentent la taille des bins. Gauche : le R_{AA} est comparé à plusieurs prédictions de modèles de transport. Droite : le R_{AA} est comparé avec les prédictions du modèle MC@sHQ+EPOS2.

GeV/c, et atteint un facteur d'environ 3 pour les collisions les plus centrales. La suppression devient plus petite pour les petits p_{T} et ne présente pas de dépendance importante à p_{T} pour $p_{\mathrm{T}} > 10$ GeV/c. Dans les collisions p–Pb à $\sqrt{s_{\mathrm{NN}}}$, où la formation d'un QGP étendu n'est pas attendue, le facteur de modification nucléaire R_{pPb} des muons de désintégration des saveurs lourdes a été observé être compatible avec l'unité dans l'intervalle en p_{T} considéré. Ceci confirme que la forte suppression observée dans les collisions Pb–Pb est induite par des effets dans l'état final. Le R_{AA} est comparé avec les prédictions de différents modèles de transport. Dans le modèle TAMU, les interactions sont décrites uniquement par des collisions élastiques tandis que le modèle MC@sHQ+EPOS2 incorpore des effect radiatifs et collisionnels ou seulement collisionnels. Le modèle SCET implémente les radiations de gluons induites par le milieu au moyen d'une fonction simplifiée avec des masses de quark finies. Ces modèles considèrent une modification nucléaire des PDF (EPS09). En plus de la fragmentation, une contribution d'hadronisation via la recombinaison des quarks est également incluse dans tous les modèles à l'exception de SCET. Tandis que les modèles MC@sHQ+EPOS2 et SCET reproduisent convenablement le R_{AA} dans les collisions centrales, le modèle TAMU sous-estime la suppression à grand p_{T} ($p_{\mathrm{T}} > 6$ GeV/c). Ceci indique l'importance de la perte d'énergie par effets radiatifs et collisionnels des quarks lourds pour expliquer la dépendance en p_{T} du R_{AA} sur l'ensemble de l'intervalle en p_{T}. On observe une tendance pour tous les modèles, à l'exception de MC@sHQ+EPOS2, de mal décrire le R_{AA} dans les collisions périphériques et/ou dans la région des p_{T} bas et intermédiaires. Une comparaison du R_{AA} des muons de désintégration des saveurs lourdes dans les collisions centrales (0–10%) Pb–Pb à $\sqrt{s_{\mathrm{NN}}} = 2{,}76$ et 5,02 TeV est présentée sur la Figure 18.

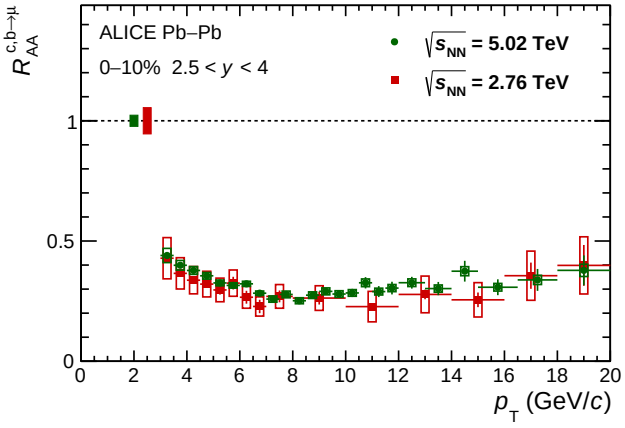

Figure 18: Comparaison du facteur de modification nucléaire des muons de désintégration des saveurs lourdes à rapidité avant ($2.5 < y < 4$) dans les collisions centrales Pb–Pb à $\sqrt{s_{\mathrm{NN}}} = 5{,}02$ TeV (symboles noirs) et $\sqrt{s_{\mathrm{NN}}} = 2{,}76$ TeV (symboles rouges). Les incertitudes statistiques (barres verticales) et les incertitudes systématiques (boites) sont montrées. Les boites centrées à $R_{\mathrm{AA}} = 1$ représentent l'incertitude liée à la normalisation. Les barres horizontales représentent la taille des bins.

L'amélioration de la précision sur la mesure à $\sqrt{s_{\rm NN}} = 5{,}02$ TeV par rapport à celle à $\sqrt{s_{\rm NN}} = 2{,}76$ TeV est clairement visible, l'incertitude systématique étant fortement réduite par rapport aux résultats déjà publiés. Ceci s'explique par la meilleure performance du détecteur à $\sqrt{s_{\rm NN}} = 5{,}02$ TeV et aussi par le fait que les données pp à cette même énergie ont été collectées quelques jours seulement avant la prise de données en mode Pb–Pb, ce qui permet de traiter les incertitudes systématiques sur la réponse du détecteur comme partiellement corrélées entre les deux systèmes. Cette comparaison montre que les suppressions mesurées aux deux énergies sont compatibles compte tenu des incertitudes, comme déjà observé dans la région de rapidité centrale pour les mésons D prompt et pour les J/ψ à rapidité avant. Cette similarité entre les résultats obtenus à deux énergies différentes s'explique par l'applatissement des spectres en $p_{\rm T}$ et l'augmentation de la température du système. Le premier effet ci-dessus provoque la diminution de la suppression, tandis que le second induit une augmentation de celle-ci.

Mesure des anisotropies azimutales des muons dans les collisions p–pb à $\sqrt{s_{\rm NN}} = 8{,}16$ TeV

Les résultats utilisent les données p–Pb et Pb–p à $\sqrt{s_{\rm NN}} = 8{,}16$ TeV collectées en 2016 avec ALICE respectivement aux rapidités avant $(2,03 < y_{\rm cms} < 3,53)$ et arrière $(-4,46 < y_{\rm cms} < -2,96)$. Les résultats sont obtenus avec la méthode des corrélations à deux particules et, pour la première fois dans le secteur des saveurs lourdes, avec les cumulants d'ordre deux implémentant une procédure pour corriger les inéfficacités et non-uniformités du détecteur. Comme pour la mesure des muons de décroissance des hadrons charmés et beaux, l'analyse utilise les événements déclenchés sur la présence de muons. Les données ont été collectées avec des seuils en $p_{\rm T}$ de 0,5 GeV/c (MSL) et 4,2 GeV/c (MSH). Les données MSL and MSH sont utilisées respectivement pour $p_{\rm T} < 2$ GeV/c et $p_{\rm T} > 2$ GeV/c. La contribution de pile-up est négligeable après utilisation des informations délivrées par le SPD et V0 et d'un algorithme pour identifier les vertex multiples. Le bruit de fond engendré par les faisceaux est réduit hors ligne en utilisant l'information en temps délivrée par les détecteurs V0 et ZDC. De plus, seuls les événements avec un vertex primaire situé dans une fenêtre de ± 7 cm le long de la ligne des faisceaux sont considérés. Une condition plus stricte est nécessaire avec la méthode des cumulants (vertex primaire compris entre -5 et 3 cm). Enfin, les analyses sont limitées aux collisions correspondant à la tranche en centralité 0–90%. Après toutes les coupures de sélection, les échantillons de données MSL (MSH) correspondent à une luminosité intégrée d'environ 0,22 (5,8) nb^{-1} et 0,22 (8,2) nb^{-1} pour les collisions p–Pb et Pb–p. Les sélections standard discutées dans le paragraphe 3.1 sont appliquées aux traces des muons candidats. Les segments de traces mesurés avec le SPD sont sélectionnés dans la région en pseudo-rapidité $|\eta| < 1$ avec une condition sur la dépendance de η à la position longitudinale du vertex. Finalement, la différence entre les angles azimutaux des *clusters* dans les deux couches du SPD est inférieure à 5 mrad afin de réduire la contribution de fausses traces et traces secondaires. Des procédures sophistiquées basées sur les corrélations dans les collisions de faibles

multiplicités sont développées pour soustraire les effets *nonflow*" et des études approfondies sont effectuées pour évaluer les incertitudes systématiques.

La Figure 19 présente le coefficient v_2 des muons en fonction de p_{T} dans les collisions de grandes multiplicités p–Pb (gauche) et Pb–p (droite) à $\sqrt{s_{\mathrm{NN}}} = 8{,}16$ TeV obtenu avec les corrélations deux à deux et les cumulants d'ordre deux. La multiplicité est obtenue avec le détecteur V0. L'anisotropie azimutale (coefficient v_2) des muons est mesurée pour la première fois dans un grand intervalle en impulsion tranverse ($0.5 < p_{\mathrm{T}} < 10$ GeV/c). Les deux méthodes donnent des résultats similaires dans les deux régions en rapidité. On observe d'abord une augmentation du signal jusqu'à $p_{\mathrm{T}} \sim 2$ GeV/c puis il s'en suit une diminution du signal. On peut aussi noter une tendance vers une légère augmentation du signal à grand p_{T} avec les cumulants dans les collisions Pb–p. Il est aussi intéressant de noter que le signal est sensiblement plus grand dans les collisions Pb–p que p–Pb. Cela peut s'expliquer par des effets de décorrélation du vecteur *flow* dans les différentes régions en rapidité. Dans le domaine en p_{T} considéré, la contribution des muons de désintégration des pions et kaons domine à bas p_{T} ($p_{\mathrm{T}} < 2$ GeV/c) alors qu'à plus haut p_{T} ce sont les muons de décroissance des hadrons charmés et beaux qui sont prépondérants. Dans l'intervalle $2 < p_{\mathrm{T}} < 6$ GeV/c, le coefficient v_2 est positif avec une significance comprise, suivant la technique utilisée, entre 4.7σ–12σ (7.6σ–11.9σ) dans les collisions p–Pb (Pb–p). Ces résultats suggèrent donc un comportement collectif des quarks lours dans ces collisions p–Pb/Pb–p de grandes multiplicités. Des résultats similaires sont aussi obtenus en utilisant d'autres estimateurs de multiplicité.

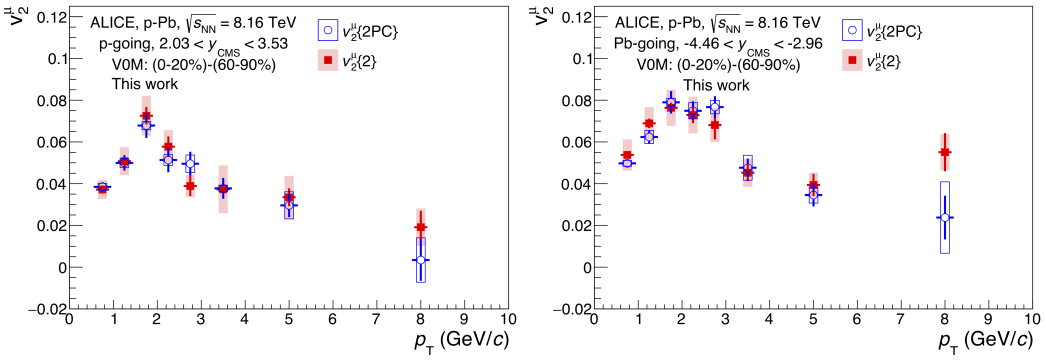

Figure 19: Mesure différentielle en p_{T} du coefficient v_2 des muons dans les collisions p–Pb (gauche) et Pb–p (droite) à $\sqrt{s_{\mathrm{NN}}} = 8{,}16$ TeV obtenue avec une méthode de corrélations deux à deux et les cumulants d'ordre deux.

Afin de d'interpréter les anisotropies azimutales observées pour les muons et progresser dans la compréhension des effets collectifs observés dans les petits systèmes, des comparaisons avec diverses prédictions théoriques sont réalisées. Les comparaisons avec la version *string-melting* du modèle de transport AMPT (*a multiphase transport model*) et des prédictions CGC (*Color Glass Condensate*) sont reportées respectivement sur les Figures 20 et 21. La figure 20 montre que le modèle AMPT génère un signal v_2 positif pour toutes les sources de muons considérées dans les

deux régions en rapidité. Les prédictions montrent un bon accord avec les données. On peut cependant noter que le modèle sur-estime sensiblement les données dans les collisions Pb–p. Cette comparaison suggère que les anisotropies azimutales proviennent du mécanisme d'échappement anisotropique de partons dans lequel les partons ont une plus grande probabilité de s'échapper le long du plus petit axe de la zone d'interaction.

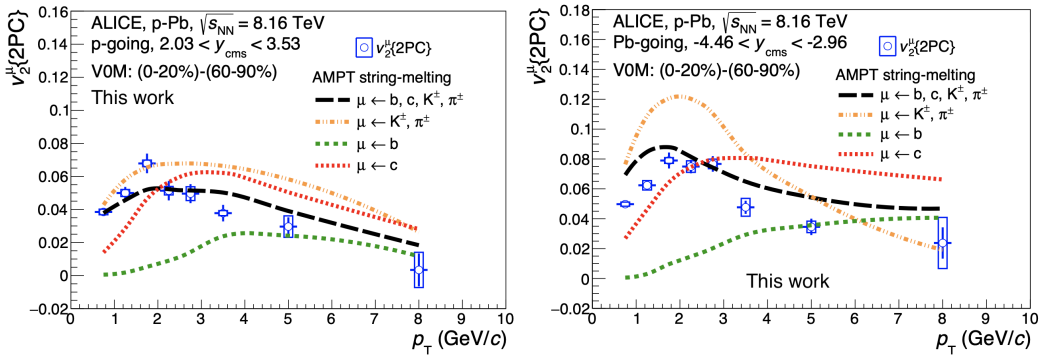

Figure 20: Comparaison de la mesure différentielle du coefficient v_2 des muons dans les collisions p–Pb (gauche) et Pb–p (droite) à $\sqrt{s_{\rm NN}}$ = 8,16 TeV avec les prédictions du modèle AMPT.

La comparaison avec les prédictions based sur le CGC est présentée sur la Figure 21 et concerne les collisions p–Pb. Les prédictions sont disponibles pour les muons de décroissance des hadrons charmés et beaux et la combinaison des deux sources de muons. On observe que les corrélations dans l'état initial génèrent un signal v_2 positif pour les muons de décroissance du charme. L'amplitude du coefficient v_2 est maximale à $p_{\rm T} \sim 2$ GeV/c et est de 0,09. L'amplitude du signal v_2 des muons de désintégration des hadrons beaux est plus faible, sa valeur maximale étant de 0,03. Les prédictions reproduisent qualitativement les données au delà de 2 GeV/c où la contribution des muons de désintégration de pions et kaons n'est pas prépondérante. Cette comparaison indique de possibles contributions d'effets dans l'état initial sur la mesure des anisotropies azimutales (coefficient v_2) des muons issus de la décroissance des hadrons charmés et beaux.

Mesure des anisotropies azimutales des particules associées aux jets dans les collisions p–Pb et Pb–Pb à $\sqrt{s_{\rm NN}}$ = 5,02 TeV

Les anisotropies azimutales des particles associées aux jets (particules des jets) aux rapidités centrales sont mesurées pour la première fois dans les collisions p–Pb et Pb–Pb à $\sqrt{s_{\rm NN}}$ = 5.02 TeV dans la région $0.5 < p_{\rm T} < 8$ GeV/c. Le coefficient v_2 est extrait via une nouvelle technique utilisant les corrélations multi-particules. Pour cette étude, les événements minimum bias sont analysés. Seuls les événements avec un vertex primaire situé dans une fenêtre de ± 10 cm le long de la ligne des faisceaux sont considérés. Les résultats dans les collisions p–Pb et Pb–Pb sont obtenus respectivement dans la région des hautes multiplicités (0–10%) et dans

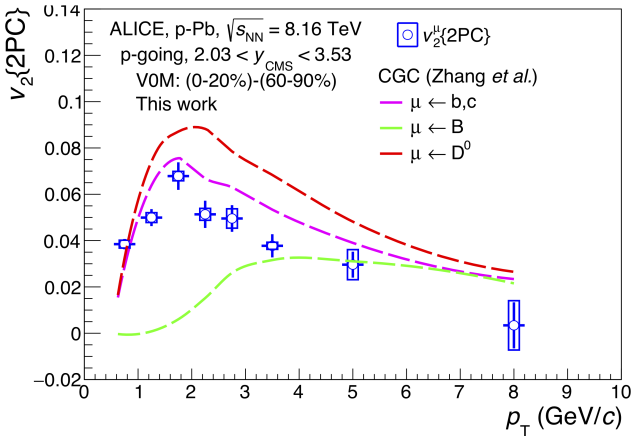

Figure 21: Comparaison de la mesure différentielle du coefficient v_2 des muons dans les collisions p–Pb à $\sqrt{s_{\rm NN}} = 8{,}16$ TeV avec les prédictions du modèle CGC.

la tranche en centralité 20–60%. Les informations des détecteurs TPC et ITS sont utilisées pour la reconstruction des traces dans la région cinématique $p_{\rm T} > 0.5$ GeV/c et $|\eta| < 0.8$. Le FMD, dont l'acceptance est limité ici à $-3,2 < \eta < -1,8$ et $1,8 < \eta < 4,8$, est utilisé pour construire les corrélations à trois particules.

L'analyse comprend i)la construction de corrélations à deux particules (particules chargées à mi-rapidité considérées comme particules *trigger* et particules associées), ii) extraction du pic correspondant aux particules associées aux jets (le signal, *near-side jet peak*) et le bruit de fond par un fit la fonction de corrélation à deux particules, iii) calcul du v_2 des particules *trigger* dans les paires de particules en utilisant des corrélations à trois particules dans les collisions p–Pb et la méthode du produit scalaire avec la technique des trois sous-événements dans les collisions Pb–Pb, et iv) extraction des v_2 de particules des jets (signal) en fonction du $p_{\rm T}$ (des particules *trigger*) avec une fonction d'ajustement à deux composantes qui prend en compte la contribution relative des jets et du bruit de fond pour le calcul du v_2 de la paire de particules. La soustraction des effets *nonflow* dans les collisions p–Pb repose sur l'étude des collisions de faibles multiplicités. Le v_2 des particules chargées est également calculé via la technique des trois sous-événements. Les incertitudes relatives évaluées par des études approfondies sont respectivement de 11,2–34,3% (1,6–10,1%) et 4,4–25% ($< 7,3$%) pour les particules associées aux jets et les particules chargées dans les collisions p–Pb (Pb–Pb).

La Figure 22 (gauche) présente le v_2 des particules des jets en fonction de $p_{\rm T}$ à mi-rapidité ($|\eta| < 0,8$) pour différents intervalles en $p_{\rm T}^{\rm assoc}$ des particules associées, dans les collisions p–Pb de multiplicités élevées (0–10%) à $\sqrt{s_{\rm NN}} = 5,02$ TeV. Le coefficient v_2 des particules chargées inclusives est également reporté à des fins de comparaison. Un signal v_2 positif est observé pour les particules des jets avec une signification de $2{,}6\sigma$–$6{,}8\sigma$ pour $p_{\rm T} < 5$ GeV/c, selon la gamme en $p_{\rm T}$ des particules associées. Le v_2 mesuré est indépendant de $p_{\rm T}$ et s'élève à $\sim 0,04$. En revanche, le

coefficient v_2 des particules chargées est plus grand et montre une nette dépendance en p_{T}. Le signal v_2 augmente jusqu'à $p_{\mathrm{T}} \sim 3$ GeV/c où il atteint une valeur maximale de $\sim 0,13$ puis diminue jusqu'à des valeurs similaires à celles mesurées avec les particules des jets. Une comparison avec le v_2 des particules des jets et particules chargées dans les collisions Pb–Pb semi-centrales est également reportée. Dans ces collisions Pb–Pb, le v_2 des particules des jets diminue avec l'augmentation de p_{T} et converge vers le v_2 des particules chargées inclusives pour $p_{\mathrm{t}} \gtrsim 7$ GeV/c. Ces valeurs de v_2 non nulles mesurées à grand p_{T} sont attribuées à des effets de perte d'énergie dans le milieu. Les résultats publiés par ALICE pour les jets reconstruits dans des collisions semi-centrales (30–50%) Pb–Pb à $\sqrt{s_{\mathrm{NN}}} = 2,76$ TeV complètent les mesures actuelles jusqu'à $p_{\mathrm{T}} = 90$ GeV/c. Notons que le v_2 des particules chargées dans les collisions Pb–Pb est pondéré par un facteur empirique de 0,6 afin d'être en accord avec la même mesure à $p_{\mathrm{T}} \lesssim 3$ GeV/c dans les collisions p–Pb. Ce facteur est également appliqué au v_2 des particules des jets et des jets reconstruits dans les collisions Pb–Pb, peut refléter les anisotropies spatiales légèrement différentes et les multiplicités plus importantes dans les collisions Pb–Pb. Après cette pondération, le v_2 des particules associées aux jets dans les collisions p–Pb a une amplitude comparable au v_2 de ces mêmes particules et des jets reconstruits dans les collisions Pb–Pb à grand p_{T} ($p_{\mathrm{T}} \gtrsim 10$ GeV/c). Ces résultats obtenus dans les collisions Pb–Pb sont attribués aux effets de pertes d'énergie dans le milieu. Dans la région $2 < p_{\mathrm{T}} \lesssim 6$ GeV/c, le v_2 mesurée dans les collisions Pb–Pb peut être une conséquence du fort couplage entre les partons durs et le *bulk*.

Le coefficient v_2 positif mesuré pour les particules des jets dans les collisions p–Pb sans aucune indication de *jet quenching* suggère que d'autres effets contribuent au comportement collectif mis en évidence dans ce "petit" système. Afin de mieux comprendre l'origine de ce $v_2 > 0$ mesuré dans les collisions p–Pb de multiplicités élevées, une comparaison avec les calculs AMPT (option *string-melting* activée) est présentée sur la Figure 22 (droite) pour les particules des jets et particules chargées. Dans ce modèle, le v_2 est calculé suivant la même procédure d'analyse qu'avec les données. Les calculs AMPT reproduisent qualitativement les tendances expérimentales, prédisant un $v_2 > 0$ pour les particules des jets et d'amplitude plus faible que pour les particules chargées. Cependant, le modèle AMPT surestime la mesure du v_2 des particules des jets et montre une dépendance en p_{T}, tout en fournissant un bon accord avec le v_2 des particules chargées. Le v_2 des quarks u et d comme obtenu avec les calculs AMPT ne présente aucune dépendance significative en p_{T} dans la région $p_{\mathrm{T}} < 2$ GeV/c, et son amplitude est similaire à celle mesurée pour les particules des jets pour $p_{\mathrm{T}} > 3$ GeV/c. Par conséquent, ces résultats suggèrent que les anisotropies azimutales dans les collisions p–Pb peuvent être attribuées au mécanisme d'échappement anisotrope des partons tandis que dans les collisions Pb–Pb elles sont générées par l'expansion hydrodynamique du milieu. Le mécanisme de coalescence lors de l'hadronisation peut aussi expliquer en partie les plus grandes valeurs de v_2 obtenues avec le modèle AMPT.

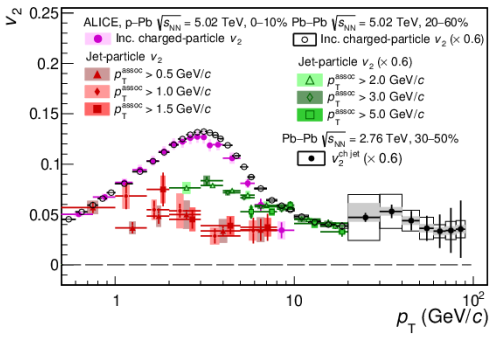

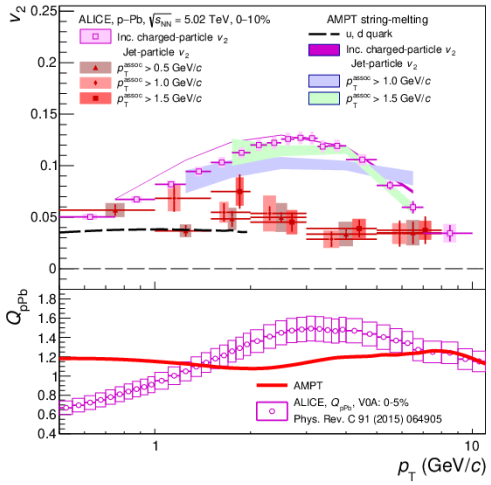

Figure 22: Gauche: comparaison du coefficient v_2 des particules des jets en fonction de p_{T} pour différents $p_{\mathrm{t}}^{\mathrm{assoc}}$ avec le v_2 des particules chargées dans les collisions p–Pb (0–10%) et Pb–Pb (20–40%) à $\sqrt{s_{\mathrm{NN}}} = 5,02$ TeV. Le v_2 des jets reconstruits dans les collisions Pb–Pb à $\sqrt{s_{\mathrm{NN}}} = 2,76$ TeV est également reporté. Les resultats dans les collisions Pb–Pb sont pondérés par un facteur de 0,6. Droite, haut : Comparaisons des résultats du v_2 obtenus dans les collisions p–Pb pour les particules des jets et les particules chargées avec les calculs AMPT. Droite, bas : comparaison du facteur de modification nucléaire Q_{pPb} des particules chargées obtenu dans les collisions p–Pb avec les calculs AMPT.

Conclusion

Le facteur de modification nucléaire R_{AA} différentiel en p_{T} des muons de désintégration des saveurs lourdes a été mesuré dans la région de rapidité avant pour la première fois sur un grand intervalle en p_{T} ($3 < p_{\mathrm{T}} < 20$ GeV/c) pour plusieurs classes de centralité des collisions Pb–Pb à $\sqrt{s_{\mathrm{NN}}} = 5{,}02$ TeV. Une forte suppression de la production de ces muons, atteignant un facteur 3 dans les collisions les plus centrales (0–10%), a été mis en évidence. La suppression devient plus faible pour les collisions moins centrales. La forte suppression mesurée dans la région des grands p_{T} indique que les quarks beaux perdent une fraction importante de leur énergie dans le milieu. La suppression observée dans les collisions centrales est comparable à celle mesurée à plus basse énergie ($\sqrt{s_{\mathrm{NN}}} = 2{,}76$ TeV). Le R_{AA} est correctement reproduit par des modèles de transport qui implémentent les pertes d'énergie radiative et collisionnelle dans le milieu. Cette mesure du R_{AA}, qui bénéficie d'une incertitude considérablement réduite par rapport aux mesures précédentes, apporte de nouvelles possibilités pour contraindre fortement les paramètres des modèles de transport.

Des effets collectifs, similaires à ceux observés dans les collisions d'ions lourds, ont été mis en évidence dans les collisions p–Pb et Pb–p. Afin de progresser dans la compréhension de ces effets collectifs, les anisotropies azimutales (coefficient v_2) ont été étudiées au moyen des muons dans les collisions de grandes multiplicités p–Pb et Pb-p. Un coefficient v_2 positif est mesuré pour la première fois dans un grand domaine en p_{T} pour les muons avec une significance plus grande que 4.6σ (7.6σ) dans la région $2 < p_{\mathrm{T}} < 6$ GeV/c dans les collisions p-Pb (Pb–p) en utilisant les corrélations à deux particules et les cumulants d'ordre deux. Les prédictions AMPT qui prennent en compte le mécanisme d'échappement anisotropique de partons reproduisent la mesure du v_2 des muons. Des prédictions basées sur le CGC indiquent de possibles contributions d'effets dans l'état initial.

Un coefficient $v_2 > 0$ est aussi mesuré pour la première fois dans les collisions p–Pb de grandes multiplicités pour les particules associées aux jets dans l'intervalle $0.5 < p_{\mathrm{T}} < 8$ GeV/c avec une nouvelle technique utilisant les corrélations à trois particules. Un signal v_2 positif et indépendant de p_{T} est observé avec une significance atteignant $6{,}8\sigma$ à petits p_{T} dans les collisions p–Pb. L'amplitude du signal est plus faible que celle mesurée dans les collisions Pb–Pb. Les prédictions AMPT pour les collisions p–Pb sont en accord qualitatif avec la mesure de v_2 de particules chargées et génèrent un v_2 positif pour les particules des jets. Ces nouveaux résultats apportent des informations importantes concernant la compréhension des anisotropies azimutales observées pour les particules des jets dans les collisions p–Pb.

Acknowledgments

This thesis could not have been finished without the great assistance from many people.

I am extremely thankful to my supervisors Daicui Zhou, Xiaoming Zhang in China and Philippe Crochet, Nicole Bastid in France, for their invaluable advice, continuous support, and patience during my PhD study. Their immense knowledge and abundant experience have encouraged me in all the time of my academic research. I am specially grateful for the great support from Philippe Crochet and Nicole Bastid to my life in Clermont-Ferrand, especially during the Covid-19 pandemics such a tough time.

I would also thank Cvetan Cheshkov, who shared me a lot of excellent ideas for my PhD work. In addition, I want to thank many ALICE colleagues I. Altsybeev, A. Bilandzic, A. Dainese, A. Dubla, L. Fabbietti, L. Graczykowski, A. Grelli, E. Kryshen, A. Maire, Y.-X. Mao, A. Ohlson, H. Pei, A. Rossi, D. Sarkar, Y. Sekiguchi, A. Silva, J. Schukraft, A. Uras, Z.-B. Yin, M.-R. Zhao, Y. Zhou for their nice suggestions and discussions.

My appreciation also extends to my laboratory colleagues in the ALIEC group in LPC, S. Acharya, V. Bogdan, P.Dupieux, A. Francisco, X. Lopez, F. Manso, S. Porteboeuf, V. Ramillien, G. Taillepied for their assistance to my research.

Many thanks are also extended to Y.-G. Ma, P.-F. Zhuang, L.-W. Chen, C. Cheshkov, A. Ohlson and Z.-B. Yin, who agree to be the member of committee of my PhD defense.

I would like to express gratitude to my friends and classmates in CCNU, H. Alfanda, M. Anaam, F. Bin, M.-K. Cai, T.-T. Cheng, P.-Y. Cui, Y.-C. Ding, T. Fang, F. Fan, C. Guo, W.-D. Guo, M. Hamid, Y.-Z. Hou, A. Khan, N. Li, X.-L. Li, D.-H. Liu, H.-Q. Wang, Z.-Y. Wang, X.-Y. Peng, B.-Y. Xia, L. Xu, R. Xu, M.-L. Zhang, M.-Y. Zhang, B. Zhang, Y. Zhu, Y.-J. Zhou, who directly or indirectly have lent their hand in this thesis.

My profound thanks go to my parents, for their tremendous support and hope they had given to me. I must express my warmest and missing to my grandfather, who always encourage and support me, however passed away one month before my finishing this thesis.

Finally, I want to sincerely thank my wife, for her unfailing support and continuous encouragement throughout these years. "You are apple of my eye". Thank you.

Siyu Tang
January 1st, 2022
Clermont-Ferrand, France

Abstract

The main aim of ultrarelativistic heavy-ion collisions is the study of a state of strongly-interacting matter at high energy density and temperature, known as the quark-gluon plasma (QGP). Hard probes, for example heavy flavours and jets, play an important in the investigation of the properties of the QGP since they are created at the early stage of the collision and suffer the whole evolution of the system. The nuclear modification factor $R_{\rm AA}$ and the second-order azimuthal anisotropy coefficient v_2 are amongst the most important observables to address the properties of the QGP. The interest in hard probe measurements in small collision systems, like pp and p–Pb, have been for a long time limited to the possibility of providing tests of perturbative quantum chromodynamics, measurements of cold-matter effects in the nuclear medium, and the baseline for observations of hot-medium effects in heavy-ion collisions. However, such measurements have recently gained additional interest due to the possibility of observing final-state like effects typically attributed, in Pb-Pb collisions, to the presence of QGP. The orgin of such effects is still debated. This thesis is dedicated to the study of heavy flavours via the semi-muonic decay channel at forward rapidity and jet particles at midrapidy in p–Pb and Pb–Pb collisions with the ALICE detector at the LHC. A significant suppression of the yields of muons from heavy-flavour hadron decays which reaches a factor of about three, is observed at forward rapidity ($2.5 < y < 4$) in the 10% most central Pb–Pb collisions at $\sqrt{s_{\rm NN}} = 2.76$ and 5.02 TeV. This suppression is compatible with a large heavy-quark in-medium energy loss. The precise $R_{\rm AA}$ measurements have the potential to constrain model calculations. The v_2 coefficient of inclusive muons extracted with the two-particle correlation method and two-particle cumulants in high-multiplicity p–Pb collisions at $\sqrt{s_{\rm NN}} = 8.16$ TeV is found positive with a significance of 4.7σ ($2.03 < y_{\rm cms} < 3.53$) and 7.6σ ($-4.46 < y_{\rm cms} < -2.96$) in the region $2 < p_{\rm T} < 6$ GeV/c dominated by the contribution of muons from heavy-flavour hadron decays. The results are compared with models implementing initial-state effects, and with a multi-phase transport model (AMPT). The results impose new constraints on the theoretical interpretations of the collective behaviour in small collision systems. The azimuthal anisotropy of particles associated with jets (jet particles) is measured at midrapidity ($|y| < 0.8$) in Pb–Pb and p–Pb collisions at $\sqrt{s_{\rm NN}} = 5.02$ TeV, based on novel three-particle correlation technique. The v_2 of jet particles measured for the first time at the LHC in high-multiplicity p–Pb collisions is found to be positive. Comparisons with the jet-particle v_2 in Pb–Pb collisions and with the inclusive charged-particle v_2 in both collision systems, as well as with AMPT calculations are also discussed. The results provide stringent constraints on the understanding of the origin of collectivity in small collision systems.

Keywords: ALICE, quark-gluon plasma (QGP); heavy-ion collisions, small collision systems, heavy flavours, jet particles, azimuthal anisotropy, nuclear modification factor, multi-particle correlation techniques, cumulants.

Résumé

Les collisions d'ions lourds ultra-relativistes ont pour objectif l'étude d'un état de matière en interaction forte dans des conditions extrèmes de température et de pression, le plasma de quarks et gluons (QGP). Les sondes dures, comme par exemple les saveurs lourdes et jets, ont un rôle important pour l'étude des propriétés du QGP car elles produites aux premiers instants de la collision et participent aux différentes étapes de la collision. Le facteur de modification nucléaire $R_{\rm AA}$ et le second coefficient d'anisotropie azimutale v_2 sont des observables fondamentales pour l'etude des propriétés du QGP. L'intérêt de l'étude des sondes dures dans les systèmes de petite taille, pp et p–Pb, a d'abord été limitée aux tests des calculs perturbatifs de chromodynamique quantique, à l'étude les effets nucléaires froids et à fournir la référence pour les mesures dans les collisions d'ions lourds. Les petits sytèmes font l'objet de nombreuses études depuis la mise en évidence d'effets habituellement attribués à la présence du QGP dans les collisions d'ions lourds, dont l'origine est intensément débattue. Cette thèse est dédiée à l'etude des saveurs lourdes ouvertes via le canal semi-muonique aux grandes rapidités et des particules chargées associées aux jets aux rapidités centrales dans les p–Pb et Pb–Pb avec le détecteur ALICE au LHC. Une importante suppression des taux de production des muons de décroissance des hadrons charmés et beaux d'environ un facteur trois, compatible avec des pertes d'énergie importantes dans le milieu, est observée dans les collisions centrales (0–10%) Pb-Pb à $\sqrt{s_{\rm NN}} = 2.76$ et 5.02 TeV. Les résultats de grande précision apportent des contraintes fortes aux paramètres des modèles. Un coefficient v_2 non nul a été mesuré pour les muons avec les corrélations à deux particules et les cumulants d'ordre deux dans les collisions p–Pb de grandes mutiplicités à $\sqrt{s_{\rm NN}} = 8.16$ TeV. La significance est de 4.6σ ($2.03 < y_{\rm cms} < 3.53$) and 7.6σ ($-4.46 < y_{\rm cms} < -2.96$) dans la region $2 < p_{\rm T} < 6$ GeV/c dominée par la contribution des muons de décroissances des hadrons charmés et beaux. Les résultats sont comparés avec des modèles traitant les effets dans l'état initial de la collision et apportent de nouvelles contraintes pour l'interprétation des effets "collectifs" dans les systèmes de petite taille. Le coefficient v_2 a aussi mesuré à mi-rapidité pour les particules associées aux jets à partir d'une nouvelle technique utilisant les corrélations à trois particules. Ce coefficient mesuré pour la première fois au LHC dans les collisions p–Pb à $\sqrt{s_{\rm NN}} = 5.02$ TeV jusqu'à des faibles impulsions transverses ($p_{\rm T} = 0.5$ GeV/c) est positif. Il est comparé à une mesure similaire dans les collisions semi-centrales Pb–Pb $\sqrt{s_{\rm NN}} = 5.02$ TeV ainsi qu'à la mesure du v_2 des particules chargées dans les deux systèmes. Des comparaisons avec le modèle de transport AMPT sont également discutées. Les résultats apportent des contraintes importantes pour la compréhension de l'origine des effets "collectifs" dans les petits systèmes.

Mots clés : ALICE, plasma de quarks et gluons (QGP), collisions d'ions lourds, petits systèmes en collision, saveurs lourdes, particules associées aux jets, anisotropie azimutale, facteur de modification nucléaire, correlations à plusieurs particules, cumulants.